UNIVERSITY OF TECHNOLOGY SYDNEY

Faculty of Engineering and Information Technology

MODELING AND CONTROL OF SMART STRUCTURES EMBEDDED WITH MAGNETORHEOLOGICAL DEVICES

by

Sayed Ahmed Royel

A THESIS SUBMITTED
IN PARTIAL FULFILLMENT OF THE
REQUIREMENTS FOR THE DEGREE

Doctor of Philosophy

Sydney, Australia

2018

Certificate of Authorship/Originality

I, Sayed Royel declare that this thesis, is submitted in fulfilment of the requirements for the award of Doctor of Philosophy, in the School of Electrical and Data Engineering at the University of Technology Sydney.

This thesis is wholly my own work unless otherwise reference or acknowledged. In addition, I certify that all information sources and literature used are indicated in the thesis.

This document has not been submitted for qualifications at any other academic institution.

This research is supported by the Australian Government Research Training Program.

Production Note:
Signature removed prior to publication.

July 16, 2019

ABSTRACT

MODELING AND CONTROL OF SMART STRUCTURES EMBEDDED WITH MAGNETORHEOLOGICAL DEVICES

by Sayed Ahmed Royel

Dissertation supervised by: Associate Professor Quang Ha

Dr. Ricardo P. Aguilera

Engineering structures are the essence of supporting the development of society. However, quite often do they suffer from hostile dynamic loadings or external disturbances that may affect structural health or function. Modeling and control techniques can be applied to resiliently preserve structural health and function with a low energy cost, which is the main theme of the thesis. Smart structures embedded with semi-active control devices offer a promising solution to the problem, such as the magnetorheological (MR) damper (MRD), pin joint (MRP), and elastomer base isolator (MRE). This study first aims at exploring the solutions to the present problem in system modeling and controller design of MR based systems to effectively damp out unwanted vibrations as well as control the embodied energy level. Multi-variable hysteresis models for these structural members are developed, capable of effectively working in a wide scale of loading amplitude and frequency. The modeling objective is to illustrate the intrinsic nonlinearity with traceable relationships between model parameters and control signals in order to realize the field-controlled method for MR structure systems. Experimental data are obtained from a long-stroke MRD, a recent prototype of MRP and an MRE under different loading conditions for model identification and performance assessment. To achieve robustness, a second-order sliding mode controller is designed and applied to the MRE to provide a real-time feedback control of structures. The performance of the proposed technique is evaluated in the simulation of a seismically excited three-

storey benchmark building model. To exploit the frequency domain advantage, this study also focuses on the cyclic dissipation of vibration-induced energy in the smart devices under a controlled magnetic field to analyze the energy relationships of the smart devices in the structures. A frequency-shaped second-order sliding mode controller (FS2SMC) is designed along with a low-pass filter to implement the desired dynamic sliding surface. The proposed controller can shape the frequency characteristics of the equivalent dynamics for the MR structure against induced vibrations, and hence, dissipate the mechanical energy flow within the devices to prevent structural damage. The energy spectra of a 10-floor building subject to four benchmark earthquakes are analyzed in terms of kinetic, damping, strain, and input energies to illustrate the capability of an energy-efficient embedded structure. The merits of FS2SMC in engineering structures can also be verified in a half-car model for reducing the roll angle while adjusting the spectrum to prevent natural modes of the structure under external excitations.

Dedication

To my parents associate professor *Sayed Jahangir Alam* and *Hafiza Khatun*, wife *Farjana Hoq*, and son *Sayed Shoayb Ibraheem*.

Acknowledgments

It gives me great pride to appreciate all the wonderful, brilliant people who contributed directly, indirectly to make this thesis possible for me. Firstly, I would like to show my gratitude and enormous respect to my supervisor associate professor Quang Ha, who has been there consistently and continuously throughout the whole thesis. His brilliant observations guided me to achieve my goal to complete the process. I would like to convey my deepest appreciation to the through efforts made by my co-supervisor Dr Ricardo Aguilera for his constructive comments, which have helped to improve the control design. I am also thankful towards professor Jianchun Li, Dr Yancheng Li and Dr Yang Yu for providing the experimental data for the magnetorheological (MR) pin joint and MR elastomer base isolator.

In addition, I would like to show my gratitude to all my research colleagues, UTS library staff, and the authors of the articles listed in the reference list. On this opportunity, I dully thank all my family and friends: Fazlul Haque, Minara Begum, Asaduzzaman, Syeda Nusrat, Bibhas, Sayeda Fatema, Sayed Mainuddin, Sadia Soma, Sayed Shibly, Sadia Nira, Aminul Tushar, Fauzia Haque, Ariana, Zarif, Shafin, Saifan, Raja, Fahim, Pavittar and Saklayen as without their contribution my thesis would have not reached the position that it has reached today. I cannot thank enough to all the well-wishers who were, directly and indirectly, related to this thesis.

A great respect and warm thanks to my parents and parents in law for being patient with me and support me in every way possible. My wife, son, brothers and sisters are always there as an inspiration to complete this work, Thank you all!

Sayed A. Royel

Sydney, Australia, 2018.

List of Publications

Journal Papers

J-1. Q. P. Ha, **S. Royel**, and C. Balaguer (2018), "Low-energy Structures Embedded With Smart Dampers," *Energy and Buildings*, vol. 177, pp. 375 - 384, doi: 10.1016/j.enbuild.2018.08.016.

J-2. Q. P. Ha, **S. Royel**, J. Li and Y. Li (2016), "Hysteresis Modeling of Smart Structure MR Devices using Describing Functions," *IEEE/ASME Transactions on Mechatronics*, vol. 21, no. 1, pp. 44 - 50, doi: 10.1109/TMECH.2015.2506539.

J-3. Y. Yu, **S. Royel**, J. Li, Y. Li and Q. P. Ha (2016), "Magnetorheological Elastomer Base Isolator for Earthquake Response Mitigation on Building Structures: Modeling and Second-Order Sliding Mode Control," *Earthquakes and Structures*, vol. 11, no. 6, pp. 943-966, doi: 10.12989/eas.2016.11.6.943.

J-4. Y. Yu, Y. Li, J. Li, X. Gu, and **S. Royel** (2018), "Nonlinear Characterisation of the MRE Isolator Using Binary-coded Discrete CSO and ELM," *International Journal of Structural Stability and Dynamics*, vol 18, no 8, doi: 10.1142/S0219455418400072.

Conference Papers

C-1. **S. Royel**, Q. Ha. and R. P. Aguilera (2018), "Frequency-Shaped Second-Order Sliding Mode Control for Smart Suspension Systems," *Proc. IEEE International Conference on Control, Automation, Robotics and Vision*, pp. 907-912, Singapore, Nov. 18 - 21, doi: 10.1109/ICARCV.2018.8581139.

C-2. **S. Royel** and Q. Ha (2017), "Frequency Shaped Sliding Mode Control of Magnetorheological Smart Structure Systems," *Proc. IEEE International Confer-*

ence on Mechatronics, pp. 117–122, Gippsland, Australia, Feb. 13-15, doi: 10.1109/ICMECH.2017.7921090.

C-3. **S. Royel**, Y. Yu, Y. Li, J. Li and Q. P. Ha (2015), "A Hysteresis Model and Parameter Identification for MR Pin Joints using Immune Particle Swarm Optimization," *Proc. IEEE International Conference on Automation Science and Engineering*, pp. 1319-1324, Gothenburg, Sweden, Aug. 24 - 28, doi: 10.1109/CoASE.2015.7294281.

C-4. **S. Royel**, Z. Movassaghi, N. M. Kwok and Q. P. Ha (2012), "Smart Structures Using MR dampers with Second Order Sliding Mode Control," *Proc. IEEE International Conference on Control, Automation and Information Science*, pp. 170-175, Ho Chi Minh, Vietnam, Nov. 26 - 29, 2012, doi: 10.1109/IC-CAIS.2012.6466580.

Contents

7   Low-Energy Structures Embedded with Smart Dampers 144

List of Figures

List of Tables

Notation

$\mathbb{N}, \mathbb{Z}, \mathbb{R}, \mathbb{C}$	the field of natural, integers, real and complex numbers
$\mathbb{R}^+$	the set of strictly positive real numbers
$\mathbb{C}^-$	the open left half of the complex plane, i.e. $\{z \in \mathbb{C} : \text{Re}[z] < 0\}$
$\text{Re}[z](\text{Im}[z])$	the real (imaginary) part of a complex variable z
$\mathbb{R}^n$	the n-dimensional Euclidean space
$\mathbb{R}^{n \times m}$	the set of real matrices with n rows and m columns
$\mathbf{I}^{n \times n}(\mathbf{0}^{n \times n})$	the $n \times n$ identity (zero) matrix
$A^{\text{T}}(x^{\text{T}})$	the transpose of a matrix A (a vector x)
A^{-1}	the inverse of a nonsingular square matrix A
$\lambda(A)$	the spectrum of the non-defective matrix A, i.e. the set of eigenvalues
$\text{diag}(a_1, \ldots, a_n)$	a diagonal matrix with diagonal elements a_1 to a_n
$\text{dist}(p, M)$	the distance from a point $p \in \mathbb{R}^n$ to a set $M \subseteq \mathbb{R}^n$
B_p	the closed ball of radius p with center at the origin is defined by $\{x \in \mathbb{R}^n \mid \|x\| \leq p\}$; p is a nonnegative real number
$f : S_1 \to S_2$	the function f mapping a set S_1 into a set S_2
$f^{-1}(\cdot)$	the inverse of a function $f(\cdot)$
$f'(\cdot)$	the first derivative of a real-valued function $f(\cdot)$
$\text{sgn}(\cdot)$	the signum function
$\text{sat}(\cdot)$	the saturation function
$\tanh(\cdot)$	the hyperbolic tangent function

$\dot{x}$	the first derivative of x with respect to time
$\ddot{x}(\dddot{x})$	the second (third) derivative of x with respect to time
$x^{(r)}$	the rth derivative of x with respect to time
$j = \sqrt{-1}$	the imaginary unit
$|p|$	the absolute value of a scalar p
p_{m}	the minimal value of a positive scalar p
p_{M}	the maximal value of a positive scalar p
$\|x\|$	the Euclidean norm (or 2-norm) of a vector x
$\|\cdot\|_1$	the 1-norm
max (min)	maximum (minimum)
sup	supremum, the least upper bound
inf	infimum, the greatest lower bound
$\forall$	for all
$\in$	belongs to
$\exists$	there exists
$\subset$	subset of
$\rightarrow$	tends to
$\Rightarrow$	implies that
$\equiv$	identically equal
$\approx$	approximately equal
$\Leftrightarrow$	equivalent to, if and only if
$:=$	equal to by definition
(xx)	equation number xx in the thesis
[xx]	reference number xx in the bibliography

Abbreviation

1(2) SMC	First (Second)-order sliding mode control
1(3)D	One (Three) dimensional
DF	Describing function
CE	Control energy
DE	Damping energy
DFG	Describing function gain
DFP	Describing function phase
dof	Degree-of-freedom
DI	Differential inclusion
FDF	Fractional-order describing function
FFOA	Fruit fly optimization algorithm
FRF	Frequency response function
FSSMC	Frequency-shaped (FS) sliding mode control
FS2SMC	Frequency-shaped second-order sliding mode control
FTSMC	Fast terminal sliding mode control
GSMC	Global sliding mode control
HCM	Half car model
HE	Hysteretic energy
HIS	Hydraulically interconnected system
HOSMC	Higher-order sliding mode control
IE	Input energy

IMPM	Inverse mode participation matrix
IMTM	Inverse modal transformation matrix
IPSO	Immune particle swarm optimization
KE	Kinetic energy
LC	Lyapunov-based control
LPF	Low-pass filter
LQR	Linear quadratic regulator
LUT	Look up table
MR	Magnetorheological
MRF	Magnetorheological fluid
MRD	Magnetorheological damper
MRP	Magnetorheological pin joint
MRE	Magnetorheological elastomer base isolator
RMSE	Root means square error
NTSMC	Nonsingular terminal sliding mode control
SAC	Semi-active (SA) control
SE	Strain energy
SISO	Single input single output
SMC	Sliding mode control
TF	Transfer function
TSMC	Terminal sliding mode control
UC	Uncontrolled case

Chapter 1

Introduction

1.1   Background

Civil structures can serve as buildings, bridges, towers, stadiums, tunnels, dams, roads, railways, or pipelines, see Figure 1.1 [1]. Civil infrastructures are the basis for supporting the development of a society and a productive economy. However, quite often do they suffer from harsh environments and severe dynamic loadings that may affect the structural health or function. The failure of the structures could be catastrophic and have subsequent social and psychological impacts. To enhance the safety (strength and stability), serviceability (stiffness) and resilience of civil engineering structures, structural vibration control and structural health monitoring technologies have been developed in the past three or four decades [2]-[5].

The most common civil engineering structures are buildings. Life cycle cost analysis for energy-aware buildings can be evaluated based on energy consumption, assessment of environmental impact or natural hazards, and prediction of structural or non-structural damage [6, 7]. Various elements either surface bonded or equipped with energy-efficient features of the building structures likely experience different levels of damage subject to external dynamic loadings such as seismic events or gusty winds, depending on the specific geographic region where the structures are situated [8]. Thereby, it may increase future costs associated with post-event repair or replacement to maintain structural health or reinstate an acceptable level. Studies have shown that cumulative damage cost can be higher than energy-efficient features and accordingly payback time for building energy efficiency investment will
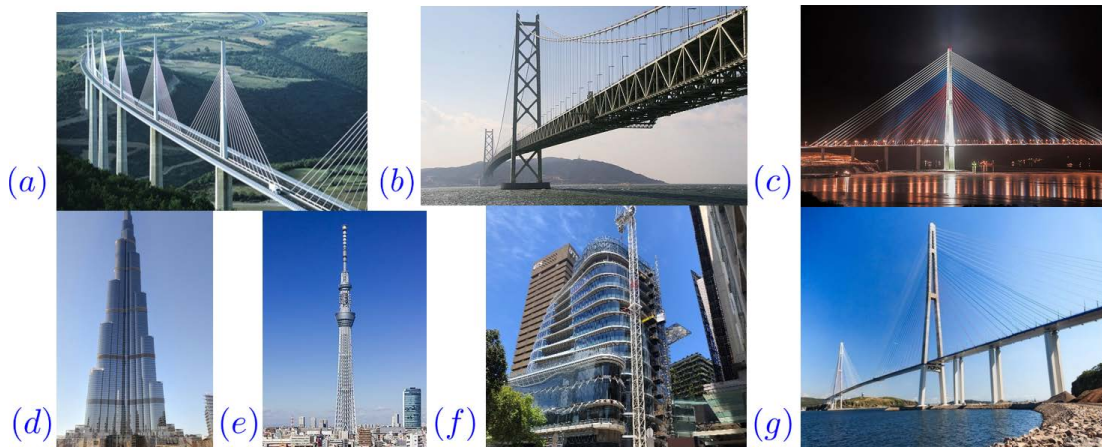
Figure 1.1 : The (a) tallest bridge (Millau Viaduct 343 m); (b) longest suspension bridge (Akashi Kaikyō Bridge 1991 m); (c) longest and widest multi-pylon cable-stayed bridge (Jiaxing-Shaoxing Sea Bridge 10138 m); (d) tallest building (Burj Khalifa 828 m); (e) tallest tower (Tokyo Skytree 634 m); (f) UTS building 2; (g) longest cable-stayed bridge (Russky Bridge 3100 m) [1].

be prolonged [6, 8].

Modern structures involve not only energy management [9] but also condition assessment and safety management, whereby the integration of modeling, control and health monitoring is of crucial importance [10, 11]. Moreover, taller, slimmer and lighter structures using high-strength materials with the same modulus of elasticity, i.e. less stiff structures, may make them more prone to dynamic loading sources, which cause discomfort and eventually, structural deterioration [2, 12]. Thus, adequate strength and energy dissipation capacity should be rendered in the structure to limit the overall structural motion and shift away its natural frequency from the resonance region under the disturbance excitation to maintain the structural health at a controllable embodied energy level. For example, the structural stiffness and damping can be adjusted whilst keep the amount of material utilized to a minimum.

It is possible to increase the stiffness of a building through selecting an appropriate structural configuration. Damping can be increased through the installation of auxiliary robust damping devices, since the damping characteristics, such as inher-

ent damping, of the core structural system is relatively ambiguous until the building is completed [12]-[15]. Alternatively, damping from external devices can be approximated accurately, thanks to the extensive research conducted in the last decades, which make them a competent solution for mitigating the structural vibration problems in any dynamic application. However, active devices require a large supply of energy, for example in active mass dampers, and power supplies to the actuators are not always guaranteed during an earthquake or when an unexpected dynamic changes occur in the structure. Smart structures embedded with semi-active control devices such as magnetorheological (MR) fluid damper (MRD) [16]-[22], MR elastomer base isolator [23, 24], MR pin joint [25]-[27], offer a promising solution to the problem.

Energy-dissipative semi-active devices

MR devices provide supplementary robust damping for the attenuation of vibrations induced by excitation sources into the structure. Semi-active control systems with smart devices can dissipate vibration energy into heat through the adjustment of damping and stiffness characteristics of the system under a low-power control signal and fail-safe operations. The controlled damping forces always oppose the motion of the structure, hence, promoting stability, as well as reducing the consequence of system uncertainties [12, 14]. The smart damping concept has been proven to be an effective approach for energy-aware protection of engineering structures by dissipating excess energy into heat through the fluid. This heat is then transferred to the environment by convection and/or conduction [17],[28]-[30].

Various loadings and environmental conditions

The loads on a structure can be static (gravity) or dynamic (wind loads). Generally, dynamic loadings around civil structures can be classified as [3]

1. *Periodic signals*: harmonic and non-harmonic, and

2. *Non-periodic signals*: short duration (blast) and long duration (earthquake).

Dynamic loads can also be categorized as

1. *Deterministic*: when the magnitude, point of application and variation of the load with respect to time is known, and

2. *Non-deterministic (or random or stochastic)*: if the variation of load with respect to time is unknown.

The most common type of loading and environment conditions are [3, 5]:

1. *Dead loads*: the weight of structural members such as beams, columns, floor slabs, ceilings, fixed service equipment, etc.

2. *Live loads*: all the loads on the structure that are not classified as dead loads, for example, highway loads and railway loads on bridges.

3. *Highway loads*: when a bridge carries a variety of moving loads such as cars, buses, and heavy vehicles.

4. *Railway loads*: when a bridge carries the non-stationary loads of railway vehicles.

5. *Wind loads*: wind effects on the structures such as long-span bridges and high-rise buildings.

6. *Earthquake loads*: the ground motion induced by a sudden release of strain energy assembled in the crust and upper mantle (are called the lithosphere) could generate a large inertia force (or seismic force) on a structure.

7. *Impact loads*: when a load is applied over a very short period of time and has a greater effect on the structure than the same load was applied statically.

8. *Temperature effects*: daily and seasonal environmental thermal effects on structural components

9. *Corrosion*: the deterioration of a metal (e.g. reinforcing steel) that results from a reaction with the environment.

Energy distribution of single-support seismic input in structures

In quake-prone areas, building structures often undergo vibrations in response to the ground motion caused by the seismic energy and fail to dissipate inelastic energy due to excessive lateral motion, resulting in structural deformation [31, 32]. These excitations can be categorized into two types, namely

1. *single-support excitation*: all the masses undergo an identical ground motion, and

2. *multi-support excitation*: ground motions are different at different supports.

The level of possible damage of individual structural members, e.g., beams, columns, and roof/floor slabs can be determined by the transmitted external dynamic loading into structural vibrations. The induced input energy (E_i) can then be decomposed into different forms as mechanical output energy (OE), i.e. kinetic (E_k), damping (E_ζ), recoverable elastic strain (E_s) and irrecoverable hysteretic dissipation (E_h) in the structure during a loading event [31, 33].

As demonstrated schematically in Figure 1.2, the n degree-of-freedom (dof) system is represented by a mass m_k at the top of a column, where k_k and c_k denote the stiffness and damping, respectively; subscript ($_k$) refer to the designated floor. Here, the rotation and vertical deflection are neglected. The system has n natural
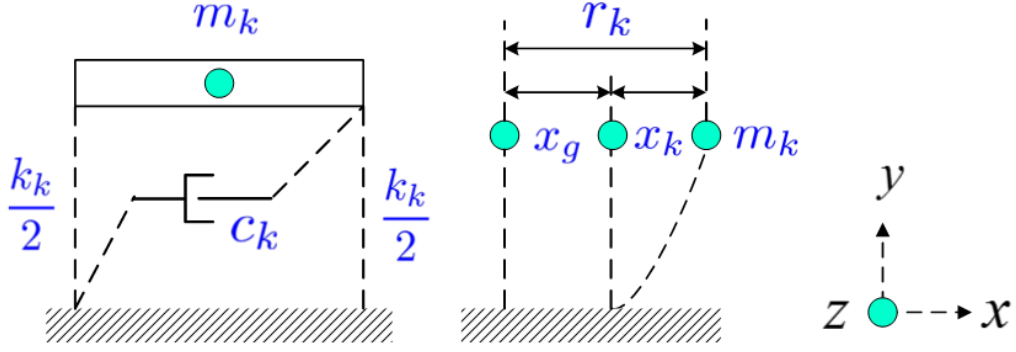
Figure 1.2 : Schematic diagram of the lumped mass distribution of an n-dof system with single-support excitation; $k = 1, 2, \cdots, n$.

frequencies and n modal vectors. $x_k = r_k - x_g$, $k = 1, 2, \cdots, n$, denotes the relative displacement between the ground and each mass; r_k describes the vibrational absolute displacements of each floor; and x_g is the absolute ground displacement. The earthquake input energy (IE) transmitted into the system from the ground motion can then be expressed through the conservation of energy relationship [34]:

$$E_k + E_\zeta + E_s + E_h = E_i, \tag{1.1}$$

where the kinetic energy (KE) reflects the work of the inertia force. The damping energy (DE) is the work of the damping force. The elastic strain energy (SE) represents the portion of the IE stored in the structure in the form of elastic strain. The hysteretic energy (HE) is the energy dissipated through the hysteretic action and is associated with the damage potential of the structure. The derivation of (1.1) is given in Section 7.2, in which nonlinear effects of the n-dof structure are neglected. Also, the floor is assumed to be axially rigid. However, both moving and equivalent fixed-base system give the same relative displacement [31, 34].

Resonance phenomenon

Engineering structures can serve as buildings, bridges, vehicle, ships, or airplanes. Most engineering structures have fixed natural frequencies. When a structure is ex-

(a) The Millennium bridge.

(b) Energy-dissipative dampers.

Figure 1.3 : The 325 m long London Millennium footbridge over the river Thames and renonance phonomenon [35].

cited by external forces whose frequencies are close to the natural frequencies, the effects of dynamic loadings are amplified and the system becomes unstable. To illustrate this resonance phenomenon, we take the following incident as an example. The London Millenium footbridge (see Figure 1.3) experienced an alarming swaying motion on its opening day on 10 June 2000. The bridge started to wobble under the wind- and pedestrian-induced movements. As a large crowd of people started to adjust themselves to the bridge movement, they became synchronized, and the bridge started to wobble even more. The synchronous lateral excitation experienced on the bridge because some of its natural modes are similar to the sideways component of pedestrian footsteps. The bridge was closed for almost two years while modifications were made by adding 37 fluid-viscous dampers and 52 tuned mass dampers to eliminate the horizontal and vertical motions, respectively [35].

1.2   Research objectives

- This study first aims at exploring the solutions to the present problem in system modeling and controller design of MR based systems to effectively damp out unwanted vibrations as well as control the embodied energy level.

Our goal is to employ the hysteretic MR devices to dissipate the induced IE E_i imparted to the structure by injecting a small control energy (CE) E_i for magnetization. By controlling the capability of absorbing excitation energy via the use of smart MR fluid yield stress, we could able to mitigate the overall structural vibrations. A low-energy smart structure can then be achieved to withstand dynamic loading source. To do so, we aim to

1. analyze the energy relationships of a building structure embedded with smart dampers and

2. design a robustly stabilizing control law to resiliently preserve structural health and function with a low energy cost during extreme events or severe loadings.

- A drawback that hinders practical applications of these smart mechatronic devices is the modeling of the complex hysteretic input-output (I/O) relationship of the overall device characteristics. Therefore, the modeling objective here is to

3. illustrate the intrinsic nonlinearity with traceable relationships between model parameters and control signals in order to realize the field-controlled method for MR based systems, and

4. facilitate the semi-active structural system analysis in the frequency domain by obtaining the frequency response functions of the structure.

1.3   Thesis organization

- *Chapter 2: Literature Survey*

This chapter presents a brief survey of the structural control systems, smart materials and devices. The background materials and design methods of the

sliding mode control and frequency-shaped control approaches are also given in this chapter.

- *Chapter 3: Magnetorheological Devices*

  In this chapter, the dissipation and energy-related aspects in the smart fluid damper for analysis of low-energy resilient structures embedded with semi-active control devices are investigated. This chapter also focuses to develop multi-variable hysteresis models for smart structural members which are capable of effectively working in a wide scale of loading amplitude and frequency. We herein considered two fluid based devices, namely the MR damper (MRD) and MR pin joint (MRP), and a polymer medium device, namely MR elastomer base isolator (MRE). The particle swarm optimization (PSO) algorithm is employed to identify the optimal model parameters. The relationships between model parameters and applied magnetic fields are also explored.

- *Chapter 4: Frequency-based modeling of MR devices*

  After introducing some background materials, the hysteresis modeling of MR devices in the frequency domain by using the describing function (DF) method are presented in Sections 4.3 to 4.6. Moreover, these models propose the explicit relationships of the frequency-dependent DFs (gain and phase) for mechatronic intelligent devices with their magnetization current, to facilitate the MR based mechatronic system analysis in the frequency domain.

- *Chapter 5: Second-order Sliding Mode Control of MR Smart Structure Systems*

  In this chapter, based on the proposed hysteresis model with current-dependent parameters, a second-order sliding mode controller (2SMC) is designed and applied to the smart devices to provide a real-time feedback control of smart structures. To deal with high nonlinearity in the hysteretic I/O relationships and to achieve strong robustness of the control system against any dy-

namic loading sources and other uncertainties, the sliding mode methodology is adopted. The last sections of this chapter include verification and feasibility of the proposed technique.

- *Chapter 6: Frequency-Shaped Structural Control*

  The modal decomposition and frequency analysis of smart structures using the DFs are reported in Section 6.2. In Section 6.3, the design method of frequency-shaped sliding mode controller (FSSMC) and some simulation results obtained with the proposed technique are discussed. Design of a frequency-shaped second-order sliding mode controller (FS2SMC) is demonstrated in Section 6.4 by means of exploiting second-order low-pass filter (LPF) to model the dynamic sliding surface to shape the frequency characteristics of the equivalent dynamics.

- *Chapter 7: Low-energy Structure Embedded with Smart Dampers*

  This chapter is outlined as follows. After the introduction, the energy equations for a building structure embedded with smart devices are studied in Section 7.2. Energy distribution of earthquake input energy in the structure is derived using the absolute motion and relative motion. A frequency-shaped second-order sliding mode controller (FS2SMC) is then proposed and designed for buildings embedded with smart devices in Section 7.3 to inject a small amount of control energy to dissipate vibration energy induced by external disturbances to the structure. Section 7.4 presents the application and simulation results obtained with the proposed approach for a 10-floor building. Section 7.5 presents a discussion on the energy flow in the structure embedded with smart devices in the presence of external disturbances. A short summary of the chapter is given in Section 7.6.

- *Chapter 8: Thesis Contributions, Conclusions and Future Works*

This chapter presents a summary of the results drawn from this study, the main contribution and recommendations for future research. Finally, the last section of this dissertation includes appendices containing the relevant supporting documents and bibliography.

Chapter 2

Literature Survey

2.1 Smart Structures

Smart structures employ smart material actuators that allow the adjustment of system parameters (damping or stiffness) as well as of system responses (shape or strain) in a controlled manner. Various types of actuators and sensors, for example, smart materials (piezoelectric, electrostrictive, magnetostrictive, or thermoresponsive materials), smart fluids (electro- or magneto-rheological fluids), shape memory alloys, fiber optics, smart polymers and gels, are being considered for different applications [36]-[41]. They can be integrated with main structures by surface bonding or embedding without causing any significant changes in the structural mass or stiffness of the system. The most diverse applications of smart structures technology range from space systems to fixed-wing and rotary-wing aircraft, civil and mechanical structures, machine tools, automotive, and medical systems [36]-[38]. Their applications to various systems are progressing to control vibration, noise, shock, aeroelastic stability, damping, shape change, and stress distribution. Figure 2.1 defines various type of structure [37, 38]:

- *Adaptive structures* such as conventional aircraft wings with flaps and ailerons, and rotor blades with servo-flaps, have distributed actuators to alter characteristics in a prescribed manner, and may not have sensors.

- *Sensory structures* have distributed sensors to monitor the characteristics of the structure (health monitoring). Sensors may detect mechanical properties

(displacement strains), electromagnetic properties, temperature, and extent of damage or failure.

- *Controlled structures* intersect both adaptive and sensory structures (see Figure 2.1). These structures contain actuators, sensors, and a feedback control system to actively control the structural characteristics.

- *Active structures* are a subset of controlled structures. Integrated actuators and sensors have load carrying capability (structural functionality).

- *Smart or intelligent structures* are a subset of active and controlled structures as shown in Figure 2.1. Smart structures can automatically and intelligently react to external dynamic loadings such as seismic events, strong winds, destructive waves and vibration shocks. They also has the capability to respond to a changing internal environment such as damage or failure. A smart structure system is the integration of actuator, sensors, computing and signal processing units with structural components. It is a distributed parameter system that employs sensors and actuators at different locations on the structure and command the actuators by analysing the sensors' response using one or more microprocessors, and bring the system to equilibrium. Figure 2.2 illustrates the generalized functional diagram for the smart structure [36].

2.2   Structural Control Systems

Structural control systems can be grouped into four basic categories: (a) passive, (b) active, (c) semi-active and (d) hybrid control systems, as listed in Table 2.1 [3, 4, 13],[42]-[44]. Passive systems may also be classified as: (a1) material based dissipation systems (e.g. viscous and visco-elastic dampers), and (a2) additional mass generating counteracting inertia forces (e.g. tuned mass dampers and tuned liquid dampers). Passive control systems are simpler, less expensive but often less
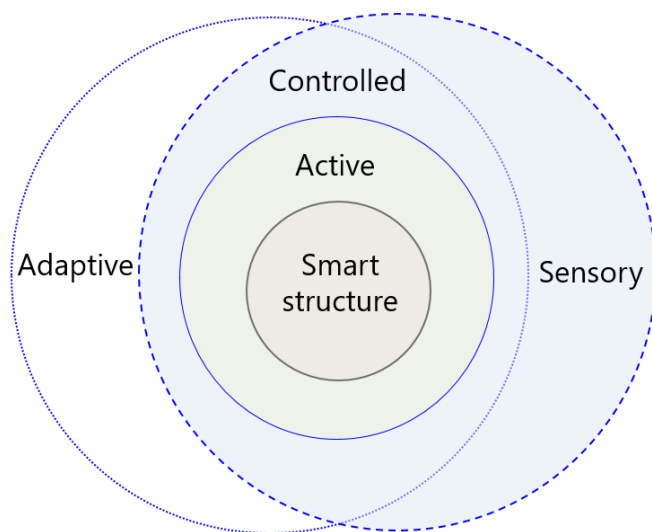
Figure 2.1 : Schematic view of a set of structures.
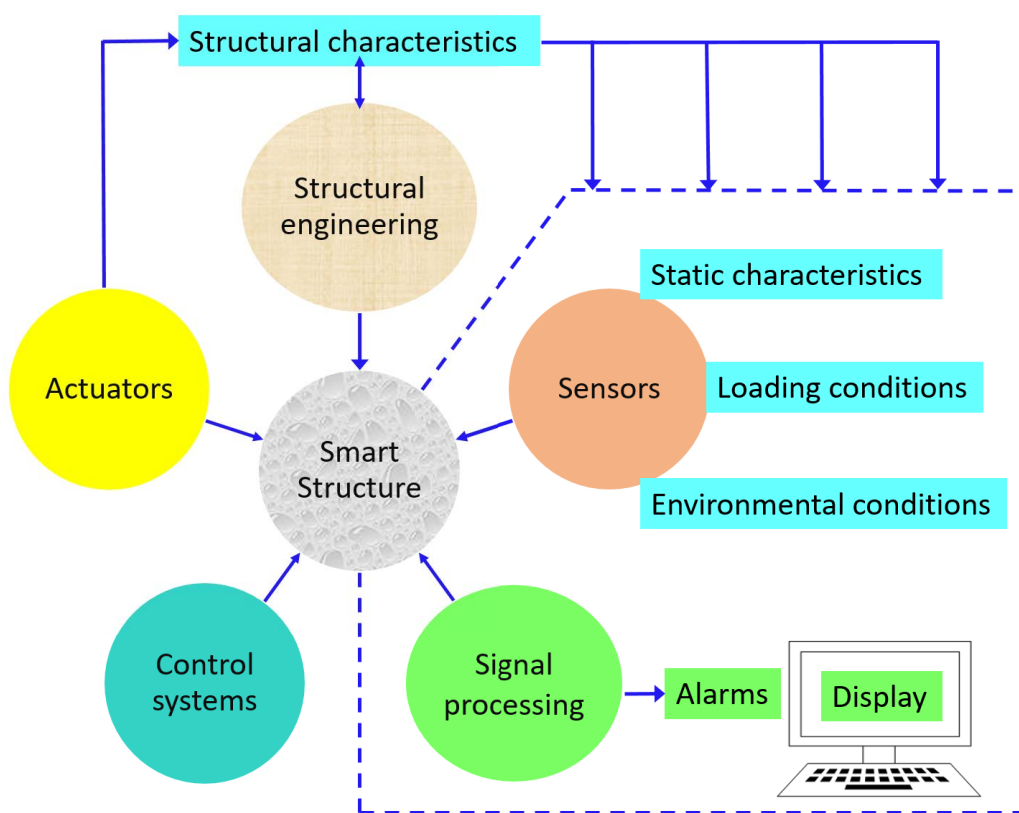
Figure 2.2 : Functional summary of the smart structure.

effective and less adaptive. Active control systems use devices capable of generating counteracting external forces to the structure. However, a major drawback of the active control system is their power failure during the earthquake. Hybrid control systems are the combination of the previous two types (active and passive control system). Semi-active control systems have been developed to combine the best features of active and passive control systems with a prominent property of being adjusted in real time without injecting energy into the controlled system. The power supply to the actuators is not always guaranteed during the earthquake, thus semi-active control is a preferable choice. In the following, structural control systems are briefly presented.

2.2.1 Passive control systems

Passive systems employ passive energy-dissipating devices which respond to the motion of structure to dissipate vibratory energy in the structural systems. Two principles are utilized to dissipate vibratory energy: (i) convert kinetic energy to heat energy and (ii) transfer energy among vibration modes. Passive control systems do not require an external power source, which may be interrupted during earthquake, and no need to measure response and carry out feedback. Hence, they are simple, less expensive, and their maintenance is relatively easy. However, the limitations of these device methods are not being able to adapt structural changes, varying usage patterns and loading conditions.

Example of passive systems including passive base isolation, viscoelastic dampers, viscous fluid dampers, metallic yield dampers, friction dampers, tuned mass dampers (TMDs) and tuned liquid dampers (TLDs). TMDs can be categorized as (a) sliding type, (b) bearing mounted type and (c) pendulum type. Pendulum type TMDs can be further classified as (c1) single pendulum type, (c2) multi-stepped pendulum type and (c3) inverted pendulum type. TLDs can be grouped into two general categories:

Table 2.1 : Classification of structural vibration control.

Structural vibration control				
Intelligent control			Passive control	
Active	Semi-active	Hybrid	Seismic isolation	Energy dissipation
Active base isolation, Active mass driver, Active bracing, Other active control systems	Variable orifice damper, Variable friction damper, Variable stiffness damper, Controllable TMD, TLD, ER dampers, MR dampers, MR elastomer devices, SA impact damper, Shape memory alloy (SMA) dampers	Hybrid mass damper, Hybrid base isolation, Hybrid damper actuator bracing control,	Sliding isolation, Lead-Rubber bearings, Elastomeric bearings, Elastomeric & sliding bearings	Hysteretic devices (such as metallic damper, friction damper), Viscoelastic devices (such as solid damper, fluid damper), Re-centering devices, Phase transformation damper, Dynamic vibration absorbers (such TMD, TLD), Other energy dissipators

(a) tuned sloshing dampers (TSDs) and (b) tuned liquid column dampers (TLCDs).

2.2.2   Active control systems

The active control mechanisms have been developed to minimize the effect of environmental loads. Active control systems require a certain amount of external power or energy to drive the actuators in order to accomplish the control objective and impart forces on the structure. However, power supplies to the actuators are not always guaranteed during an earthquake or when an unexpected dynamic changes occur in the structure. An active control system can measure and estimate the response over the entire structure to determine appropriate control action. Example of such strategies include active tendon systems, active bracing system, active tuned mass damper/drive, active base isolation systems and active aerodynamic appendage mechanism.

2.2.3   Semi-active control systems

Semi-active control systems have been developed to exploit the best features of both passive and active control systems with a prominent property of being adjusted in real time without injecting energy into the controlled system. The performance of semi-active control system is bounded by passive and active control system. The basic configuration of semi-active control system is similar to active control system, except they have a unique device, which can represent both active and passive device's features. Therefore, semi-active control devices are frequently referred to as controllable passive dampers. The semi-active control systems utilize the motion of a structure to develop control forces through the adjustment of damping and/or stiffness characteristics of the system under a low operation energy level. These forces always oppose the motion of the structure, hence, promoting stability, as well as reducing the consequence of the uncertainty of intrinsic damping [12, 14]. They have several advantages such as low operating power requirements, simplicity,
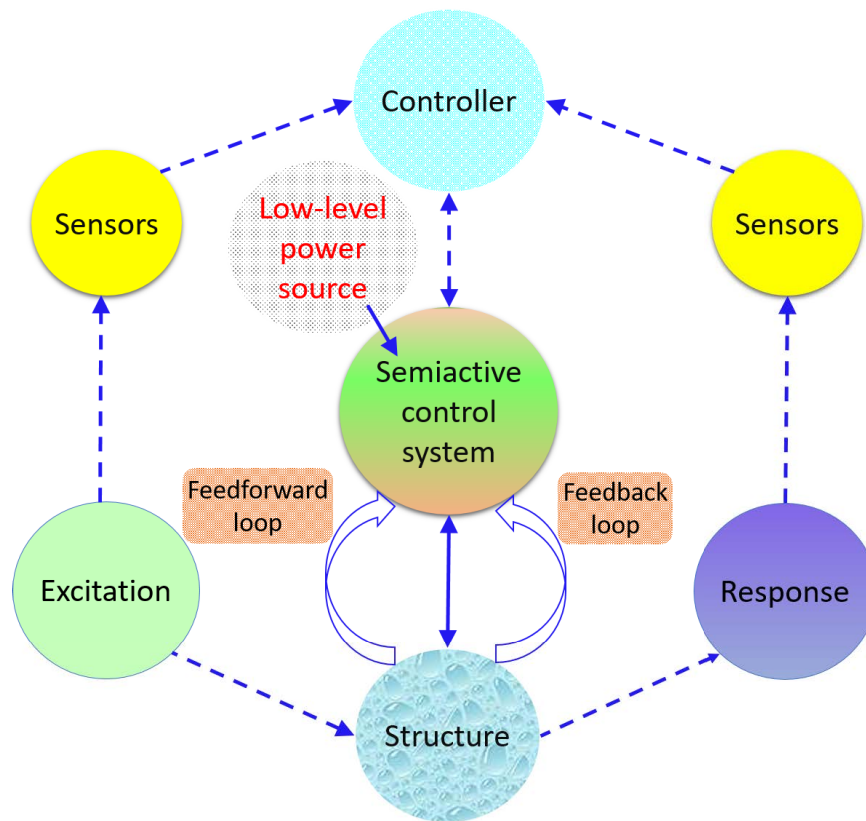
Figure 2.3 : Schematic diagram of semi-active control systems.

easily maintainable, environmental robustness and their properties can be varied dynamically. Figure 2.3 shows the schematic diagram of a typical semi-active control system. Typical examples of such devices include variable orifice fluid dampers, variable friction dampers, controllable friction devices, variable stiffness devices, controllable liquid dampers, controllable impact dampers and controllable fluid (e.g. Electro-rheological, Magneto-rheologcal) dampers [42, 45].

2.2.4 Hybrid control systems

A hybrid control system is the one that employs a combination of two or more passive or active control devices. Since, there are multiple control devices operating, a hybrid control system can alleviate some of the limitations that exist when each system (i.e. passive, active) is acting alone. Hence, a higher level of performance

is possibly achievable, although it is often also more complicated. Typically these systems include hybrid mass damper systems, hybrid base isolation systems and hybrid damper-actuator bracing systems.

2.2.5 Smart structure control systems

A smart structure system equipped with magnetorheologcal (MR) devices has the potential to satisfy all requirements of low-cost, robustness and reliability against various dynamic loading sources. The effects of dynamic sources such as those induced by earthquakes and strong winds on civil engineering structures, considered as external disturbances, as well as high nonlinearity of the MR devices due to hysteresis and saturation due to their physical constraints of pose difficult issues for structural control using these devices. To this end, effort has been paid to develop various structural control algorithms. The structural control strategies applied to the control of civil and mechanical engineering structures can be classified as [19],[46]-[55]:

- *Optimal control* such as clipped optimal control, bang-bang control, linear quadratic (LQ) regulator (LQR)/ Gaussian (LQG),

- *Independent mode space control* such as modal control based on state space and modal control based on equation of motion,

- *Robust control* such as $\mathcal{H}_{\infty}$ control, Lyapunov theory based control, sliding mode control (SMC),

- *Predictive control* such as adaptive predictive control, model based predictive control in which each control solution may be suitable only for specific type of structure.

2.3   Smart Materials and Magnetorheological Devices

2.3.1   Smart materials

Smart materials are the materials that receive, transmit, or process a stimulus and respond by producing a useful effect that may include a signal that the materials are acting upon it, for example, strain, stress, temperature, electric field, magnetic field, hydrostatic pressure, different types of radiation, chemicals (including pH stimuli), and other forms of stimuli. Typical examples of such intelligent materials are piezoelectric materials, electrostrictive materials, magnetostrictive materials, pH-sensitive materials, thermoresponsive materials, light-sensitive materials, electrorheological fluids, magnetorheological fluids, shape memory alloys, smart polymers, hydrogels, smart catalysts [39, 40, 45, 56]. One of the important features of smart materials is their inclusion in smart structures. A summary of smart materials is given in Table 2.2.

2.3.2   Magnetorheological devices

Magnetorheological (MR) material is a type of intelligent material with the behaviours and properties of rheology, which are able to be continuously, quickly and reversibly adjusted when external magnetic field is applied. Based on this distinct merit, the MR-based devices, such as MR squeeze film dampers (SFDs), MR variable stiffness air springs, MR dampers (MRDs), MR pin joints (MRPs), and MR absorbers (MRAs), have been developed as controllable smart components installed in the engineering structures for vibration alleviation and mitigation when structures are subjected to external hazard excitations, i.e. strong wind, earthquake, vibration shock and destructive wave. As a novel smart material, MR elastomer (MRE) has the benefits of both MR material and elastomer, i.e. quick response, controllable and reversible mechanical property.

Table 2.2 : Summary of smart materials.

Smart materials	Comments
Piezoelectric	− exhibit a linear relationship between electric and mechanical variables
Electrostrictive	− show a quadratic relationship between mechanical stress and the square of electrical polarization
Magnetostrictive	− response as material deformation when stimulated by a magnetic field
Elastorestrictive	− mechanical equivalent of electrorestrictive and magnetorestrictive materials − exhibit high hysteresis between stress and strain
Electrorheological	− rheological or viscous properties of these fluids, which are usually uniform dispersions or suspensions of particles within a fluid, are changed instantly through the application of an electric field
Magnetorheological	− magnetic equivalent of electrorheological fluids
Shape memory alloys (SMAs)	− able to remember and recover from large strains without permanent deformation, the most well-known form of transformation behavior exploited in SMAs is thermally induced shape change
pH-sensitive	− example includes the acids, bases, and indicators (change color as a function of pH and the action is reversible)
Other smart materials	− such as thermoresponsive, light-sensitive, smart polymers, smart gels, smart catalysts
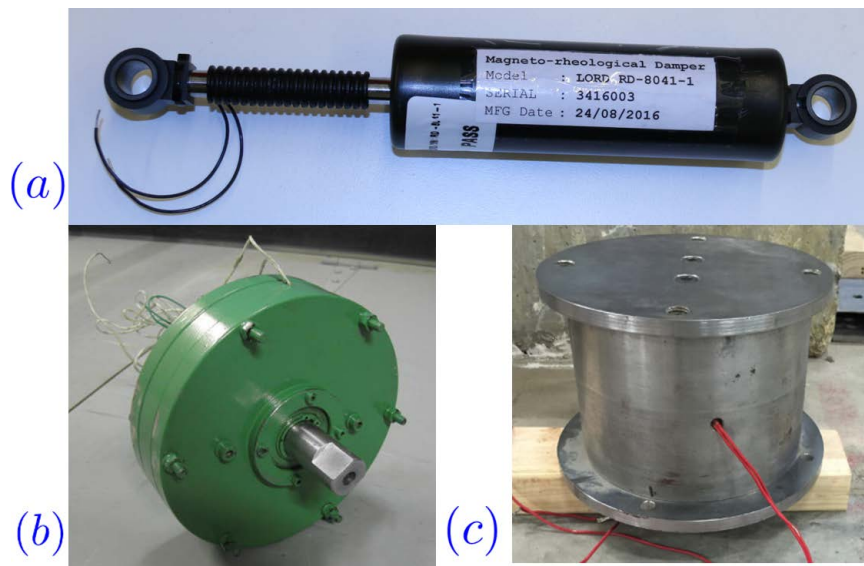
Figure 2.4 : MR device photos: (a) MRD, (b) MRP and (c) MRE base isolator.

Figure 2.4(a), (b) and (c), respectively, shows photographs of an MRD, an MRP and an MRE. There is a large number of technical papers addressing various applications of these smart structural members. In civil engineering, energy-dissipative devices have been utilized to design semi-active smart control system for protecting civil infrastructure against wind and earthquake loads. The most diverse applications of these smart devices include seismic response mitigation of civil/mechanical structures [22, 52],[57]-[59], vibration & shock attenuation of suspension systems [50], vehicle seat suspensions [60], wind-induced vibration control of wind turbines [61], control of aircraft vibration due to landing impacts/runway excitations, MR passenger protection systems, prosthetic-artificial knee damper, or noise and vibration reduction of washing machines [16].

In an MRD, highly concentrated magnetizable particles in a non-magnetic carrier, such as silicon oil, are aligned with the applied magnetic field such that the yield stress of the fluid is changeable to form a semi-solid, see Figure 2.5. Consequently, when a current is supplied to the magnetizing coil built in the piston or on the damper housing, a controllable damping force is produced, which can be used by an

(a)   (b)
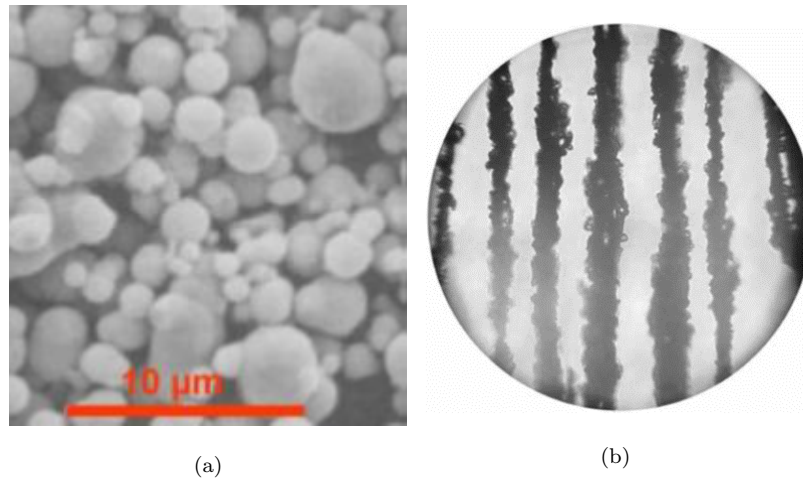
Figure 2.5 : Smart MR fluid with (a) no magnetic field and (b) an applied magnetic field [62].

approximately tuned feedback controller to suppress structural vibrations induced by any dynamic loading. The viscosity of the fluid is thus adjustable by altering the electric current applied to the coil. The principle of operation of an MRP remains the same as MRD. Semi-active MRPs also use smart MR fluid, which is a magnetic analog of electrorheological (ER) fluid. MRP is a rotational structural member compared to its family members, and can be considered as shear-mode rotational damper. Hence, it can be employed for mitigating rotary deflections in structures.

Generally, the MRE is made of three principle ingredients: elastomer matrix, polarized magnetic particles and silicon oils. When the MRE is supplied with external magnetic field, its mechanical properties, such as elasticity modulus and damping, will be greatly improved. It is able to avoid the problems of poor stability, sedimentation and particle wearing existing in MR fluid. Because of this inherent feature, the MRE exhibits the huge potentiality in the field of vibration and shock mitigation of mechanical or civil infrastructure.

2.3.3 Mathematical models of MR devices

Although MR material and MR-based devices are significantly promising in the field of structural vibration control, the major aporia that affects their practical implementations is the modeling of their unique dynamics with high nonlinearity and inherent hysteresis. In the past several decades, various numerical models have been proposed to model hysteretic smart devices, which can be divided into quasi-static and dynamic models. Even though quasi-static models can satisfactorily emulate the relationship between force and displacement of damper, they are not competent to depict the nonlinear force-velocity relationship of the device. This drawback can be tackled by dynamic models. Up to now, several models have been proposed in the literature based on various methods. Generally, these models are classified as parametric and nonparametric models [19, 44, 57],[63]-[71]:

1. *Parametric models*: The models are expressed by an algebraic function whose parameters are determined rheologically, and gained via the conclusive method belongs to the parametric models. Typically examples of parametric models are Bingham models (nonlinear Bingham plastic model, modified Bingham plastic model, Gamato and Filisko model, three-element model), Dahl models (viscous Dahl model, modified Dahl model), Kelvin–Voigt model, Lu-Gre model, Bouc-Wen models (simple Bouc-Wen model, modified Bouc-Wen model, nonsymmetrical Bouc-Wen model, current dependent Bouc-Wen model, current-frequency-amplitude dependent Bouc-Wen model), strain stiffening model, bi-viscous models (hysteretic bi-viscous model, modified bi-viscous model, lumped parametric bi-viscous model), viscoelastic-plastic model, static hysteresis model, stiffness-viscosity-elasto-slide (SVES) model, temperature phenomenal model with mass element, polynomial model, sigmoid function model, equivalent model, hydromechanical model, and phase transition model.

2. *Non-parametric models*: The soft computing techniques contribute to the development of non-parametric models, in which the dynamical behaviour of the devices cannot be described by the specific mathematical expressions. Non-parametric models are based on the performance of a specific device. Typically these models include orthogonal Chebyshev polynomials, neural networks model, neuro-fuzzy model.

2.4 Sliding Mode Control

A challenging requirement for structural control systems remains strong robustness in face of system uncertainties and external disturbances. For this, sliding mode (SM) control (SMC) is known as a discontinuous robust control [72]-[82]. To develop understanding about the fundamental mathematical concepts of SMC, some background information and common design methods of the SMC theory are presented in the following.

2.4.1 Background

SMC is a specific type of variable structure control system (VSCS) [78, 79]. SMC forcibly confines the system's states to a user-chosen sliding surface (is called equivalent dynamics) by varying the control structure with infite frequency on both sides of the desired hyperplane in the state space. Hence, the ultimate trajectory does not exist entirely within one control structure, instead it slides along the boundaries of the control structures. The motion of the system as it slides along these boundaries is called a SM and the geometrical locus consisting of the boundaries is called the sliding (hyper) surface.

SMC alters a possibly higher-order problem into a first-order stabilization problem that of controlling the distance from the system state to the manifold so that the distance is zero or as close as to that the actuators can obtain. The striking

feature of SMC is its insensitivity to parametric uncertainty and disturbances during the SM [72, 77].

At first, a sliding surface is designed such that the reduced order model has convergence properties and independent of the model uncertainty. The nth order sliding manifold can be defined as the static intersection in the state space by

$$\sigma(x) = \mathcal{S}x = x_n + \sum_{k=1}^{n-1} \rho_k x_k, \ x \in \mathbb{R}^n, \tag{2.1}$$

where the vector $\mathcal{S} = [\rho_1, \cdots, \rho_{n-1}, 1]$. The parameters ρ_1 to ρ_{n-1} are chosen such that the characteristic equation,

$$s^{n-1} + \cdots + \rho_2 s + \rho_1 = 0,$$

has all roots with negative real parts where s is the Laplace operator [80]-[82]. For example, if $n = 3$, then

$$\sigma(x) = \rho_1 x_1 + \rho_2 x_2 + x_3, \tag{2.2}$$

to satisfy the condition that the polynomial $s^2 + \rho_2 s + \rho_1$ is Hurwitz, i.e., the eigen values of $\sigma(x) = s^2 + \rho_2 s + \rho_1 = 0$ should have a negative real part. Hence, we can obtain $s^2 + 2\lambda s + \lambda^2 = 0$ for a positive scalar $\lambda > 0$ in $(s + \lambda)^2 = 0$ which gives $\rho_2 = 2\lambda$ and $\rho_1 = \lambda^2$.

The vector $\mathcal{S}$ consist of coefficients that describe the sliding surface in terms of the state vector x. The value of σ represents the distance of the point from the sliding surface, therefore $\sigma = 0$ implies the point is on the sliding surface. Now from (2.1), we have

$$\sigma(x) = \rho_1 x_1 + \rho_2 x_2 + \cdots + \rho_{n-1} x_{n-1} + x_n = 0$$

$$\Rightarrow x_n = -\rho_1 x_1 - \rho_2 x_2 - \cdots + \rho_{n-1} x_{n-1}$$

$$\Rightarrow \dot{x}_n = -\rho_1 x_2 - \rho_2 x_3 - \cdots - \rho_{n-2} x_{n-1} + \sum_{k=1}^{n-1} \rho_{n-1} \sigma_k x_k.$$

Thus, the entire dynamics of the system is governed by the sliding surface parameters $\mathcal{S}$ only, i.e., the system dynamics are independent of system parameters.

Secondly, the control gain is constructed (can be obtained based on the generalized Lyapunov stability theory), which can use only the information on the bounds of uncertain variables, to drive all trajectories on to the manifold in finite time and remain on it thereafter. The average of the high-frequency switching induces the control which ensures the conditon $\dot{\sigma} = 0$ [80]-[82]. Since the polynomial is Hurwitz, once on the sliding manifold, the trajectories will go to zero with a transient behavior characterized by the selected $\rho_1, \ldots, \rho_{n-1}$.

Filippov continuation method

The VSCS dynamics is characterized by differential equation with discontinuous right-hand side. Filippov first proposed a solution for this type of system [83]. Since sliding surface occurs on the discontinuity surface, the state motion vector lies on a tangential surface, and according to Fillipov if the velocity vector on one side of the sliding surface is f_+ and on the other side of the surface is f_-, then the resultant vector f_0 is formed by the convex sum of the two column vectors $(f_+, \ f_-)$:

$$\dot{x} = f_0(x, t)$$
$$f_0 := \alpha f_+ + (1 - \alpha) f_-, \quad 0 < \alpha < 1 \tag{2.3}$$

where parameter α depends on the directions and magnitudes of the vectors $(f_+, \ f_-)$ and the gradient of the sliding surface σ, see Figure 2.6

SMC based on reaching law

The closed-loop system behavior under SMC can be categorized into two phases: *reaching phase* and *sliding phase* [84]-[86]. The reaching phase drive system to maintain a stable manifold and the sliding phase drive system guarantees slide to equilibrium. Four types of reaching laws: *general reaching law, constant rate reaching law, exponential reaching law,* and *power rate reaching law* are briefly presented in the following.
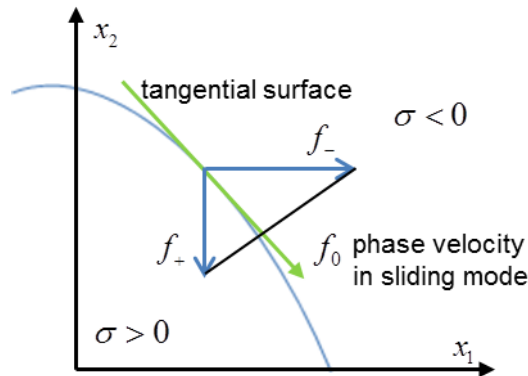
Figure 2.6 : Schematic representation of Filippov's definition.

(*R1.*) *General reaching law*: The dynamics of the switching function can be specified by the differential equation as

$$\dot{\sigma} = -\eta \operatorname{sgn}(\sigma) - \kappa f(\sigma), \ \eta > 0, \ \kappa > 0,$$

$$\sigma f(\sigma) > 0, \ f(0) = 0, \ \forall \sigma \neq 0,$$

(2.4)

where $\operatorname{sgn}(\cdot)$ denotes the signum function, defined as

$$\operatorname{sgn}(\sigma) := \begin{cases} -1, & \text{if } \sigma < 0, \\ 0, & \text{if } \sigma = 0, \\ 1, & \text{if } \sigma > 0, \end{cases}$$

which has a property

$$\sigma \operatorname{sgn}(\sigma) = |\sigma|. \tag{2.5}$$

(*R2.*) *Constant rate reaching law*:

$$\dot{\sigma} = -\eta \operatorname{sgn}(\sigma), \quad \eta > 0, \tag{2.6}$$

where η is the constant rate; too small value of η prolongs the reaching time and too large value of η results in severe chattering.

(*R3.*) *Constant proportional rate or exponential reaching law*:

$$\dot{\sigma} = -\eta \operatorname{sgn}(\sigma) - \kappa \sigma, \ \eta > 0, \ \kappa > 0, \tag{2.7}$$

where the solution of the exponential term $\dot{\sigma} = -\kappa\sigma$ is $\sigma = \sigma(t_0)e^{-\kappa(t-t_0)}$. Hence, when σ is large then the states approaches the switching manifold swiftly.

(*R4.*) *Power rate reaching law*:

$$\dot{\sigma} = -\kappa|\sigma|^{\alpha}\operatorname{sgn}(\sigma), \quad \kappa > 0, \ 0 < \alpha < 1. \tag{2.8}$$

When the state is far away from the switching manifold, the reaching law increases the reaching speed, but when the state is near the manifold, it reduces the rate. The result is a fast and low chattering reaching mode.

It is evident that the above four reaching laws (*R1.*) to (*R4.*) satisfy the sliding condition $\sigma\dot{\sigma} < 0$.

SMC based on quasi-sliding mode

In SMC, the ultimate trajectory does not exist entirely within one control structure, instead it slides along the boundaries of the control structures. Theoretically, the trajectory is supposed to slide on the sliding manifold, but there are delays and imperfections in the switching devices, and unmodeled high-frequency dynamics, which lead to chattering.

Chattering is a small amplitude high-frequency oscillation which appears in the neighborhood of the sliding manifold that results in low control accuracy, high heat losses in electrical circuit and high wear of moving mechanical parts [80, 87]. It can also excite unmodeled high-frequency dynamics which may degrade the system performance and lead to unforeseen instabilities. Therefore, it is one of the main concerns in SMC.

One way to reduce the chattering is to use the quasi-sliding mode method which can make the state lie within a neighbourhood ε. Here, ε is called the boundary layer and a small positive constant. Making the following substitution in the corresponding discontinuous ones: $\operatorname{sgn}(\sigma)$ with a high-slope saturation function $\operatorname{sat}(\sigma/\varepsilon)$,
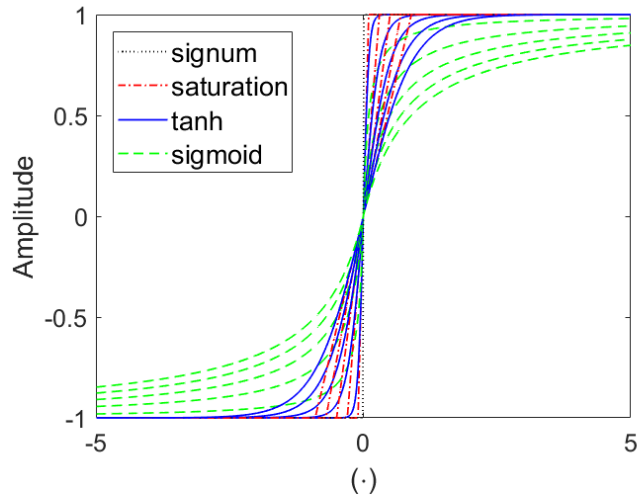
Figure 2.7 : Approximations of sgn($\cdot$) nonlinearity; $\varepsilon = [0.1, 0.3, 0.5, 0.7, 0.9]$. In the limit $\varepsilon \to 0$, saturation, tangent and sigmoid functions approach to signum function.

or sgn(σ) with a hyperbolic tangent function $\tanh(\sigma/\varepsilon)$ or sgn(σ) with a sigmoid-like function $f_\varepsilon(\sigma)$, a continuous control law can be obtained in order to alleviate the chattering phenomena by smoothing out the control discontinuity in a thin boundary layer,

$$B_\varepsilon = \{\|\sigma\| \leq \varepsilon\},$$

neighboring the switching surface [72, 80, 81]. A good approximation of sgn($\cdot$) nonlinearity needs the use of small ε as shown in Figure 2.7.

(*Q1.*) The high-slope saturation function can be defined by

$$\text{sat}\left(\frac{\sigma}{\varepsilon}\right) = \begin{cases} 1, & \text{if } \frac{\sigma}{\varepsilon} > 1, \\ \frac{\sigma}{\varepsilon}, & \text{if } \left|\frac{\sigma}{\varepsilon}\right| \leq 1, \\ -1, & \text{if } \frac{\sigma}{\varepsilon} < -1, \end{cases} \tag{2.9}$$

where $1/\varepsilon$ is the slope of the linear portion of sat($\cdot/\varepsilon$). Outside the boundary layer, the system dynamics are the same as the switching control and inside the boundary layer, the linear feedback control is used.
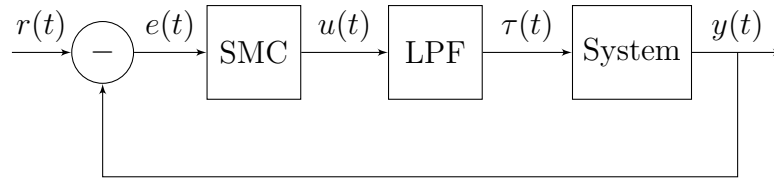
Figure 2.8 : Closed-loop block diagram of the SMC system with LPF.

(*Q2.*) The sigmoid function is

$$f_\varepsilon(\sigma) = \frac{\sigma}{|\sigma| + \varepsilon}, \tag{2.10}$$

where ε is a small positive constant. In the limit $\varepsilon \to 0$, $f_\varepsilon(\cdot)$ approaches point-wise to sgn($\cdot$).

(*Q3.*) The hyperbolic tangent function is

$$\tanh(\sigma/\varepsilon) = \frac{2\exp(\sigma/\varepsilon) - 1}{2\exp(\sigma/\varepsilon) + 1}, \quad \varepsilon > 0. \tag{2.11}$$

The steepness of the hyperbolic tangent function is determined by ε. In the limit $\varepsilon \to 0$, $\tanh(\cdot/\varepsilon)$ approaches to sgn($\cdot$).

SMC based on low pass filter

To reduce the control chattering, sliding mode control system with low pass filter (LPF) can be designed [82, 86]. A block diagram of the SMC system with LPF is shown in Figure 2.8 where $r(t)$, $e(t)$, and $y(t)$ are the reference, error, and output signals, respectively; $u(t)$ is the SMC output; $\tau(t)$ is the practical control input. for example, the transfer function of the low pass filter can be given by

$$T(s) = \frac{\lambda}{s + \lambda} = \frac{\tau(s)}{U(s)} \quad \Rightarrow \quad \dot{\tau} + \lambda\tau = \lambda u, \tag{2.12}$$

where $\lambda > 0$, $U(s)$ and $\tau(s)$ denote the Laplace transform of $u(t)$ and $\tau(t)$, respectively.

Terminal sliding mode control

In conventional SMC, the system states reach equilibrium asymptotically. Thus a nonlinear function or terminal attractor can be added into the design of the sliding upper plane to construct a terminal sliding surface results in the tracking errors on the sliding surface converge to zero in a finite time [88]. In the following, three types of TSMCs: *conventional terminal sliding mode control, fast terminal sliding mode control,* and *nonsingular terminal sliding mode control,* are presented.

Consider a two-dimensional, single-input uncertain nonlinear dynamic system of the form

$$\dot{x}_1 = x_2,$$
$$\dot{x}_2 = h(x) + g(x)u + d(x,t), \tag{2.13}$$

where $x \in \mathbb{R}^2$ is the system state vector, $u \in \mathbb{R}$ is the control input, $h(x)$ and $g(x) \neq 0$ are some smooth nonlinear functions, and $d(x,t)$ is the uncertainties and disturbances. Assume further that

$$|d(x,t)| \leq D, \quad D > 0. \tag{2.14}$$

(*T1.*) *Conventional terminal sliding mode control(TSMC)*: The conventional TSM can be described by the following first-order terminal sliding variable [89]:

$$\sigma = x_2 + \beta x_1^{q/p}, \ \beta > 0, \tag{2.15}$$

where p and q are positive odd integers satisfying the condition $p > q$.

The derivative of (2.15) along the system dynamics (2.13) gives

$$\dot{\sigma} = \dot{x}_2 + \frac{\beta q}{p} x_1^{\frac{q}{p}-1} \dot{x}_1 = h(x) + g(x)u + d(x,t) + \frac{\beta q}{p} x_1^{\frac{q}{p}-1} x_2. \tag{2.16}$$

Suppose that the control law is selected as

$$u = -g^{-1}(x)\left(h(x) + \frac{\beta q}{p} x_1^{\frac{q}{p}-1} x_2 + (D+\mu)\operatorname{sgn}(\sigma)\right) \tag{2.17}$$

where $\mu > 0$, $\frac{q}{p} - 1 < 0$. Thus, when $x_1 = 0$ and $x_2 \neq 0$ a singular problem exits for the conventional terminal controller. From (2.16), we have

$$\dot{\sigma} = d(x,t) - (D + \mu)\operatorname{sgn}(\sigma). \qquad (2.18)$$

Taking $V = \frac{1}{2}\sigma^2$ as a Lyapunov function candidate, we have that

$$\dot{V} = \sigma\dot{\sigma} = d(x,t)\sigma - (D+\mu)\operatorname{sgn}(\sigma)\sigma = d(x,t)\sigma - (D+\mu)|\sigma| \leq -\mu|\sigma|. \qquad (2.19)$$

(*T2.*) *Fast terminal sliding mode control (FTSMC)*: FTSMC can make the system states converge to zero in a finite time [90]. Asymptotical convergence of states under the normal sliding mode is overcome. The convergent characteristic of fast terminal sliding mode control is superior to the conventional SMC. Furthermore, there is no switch function in terminal sliding mode control, therefore, the chattering phenomenon is evitable [90].

For the system (2.13), the fast terminal sliding variable can be described by adding a linear attractor αx_1 into (2.15):

$$\sigma = x_2 + \alpha x_1 + \beta x_1^{\frac{q}{p}}, \qquad (2.20)$$

where $\alpha > 0$, and β, p and q have been defined in (2.15). The variable σ satisfies

$$\dot{\sigma} = h(x) + g(x)u + d(x,t) + \alpha x_2 + \frac{\beta q}{p}x_1^{\frac{q}{p}-1}x_2. \qquad (2.21)$$

Then, for system (2.13), the FTSMC is designed as

$$u = -g^{-1}(x)\left(h(x) + \alpha x_2 + \frac{\beta q}{p}x_1^{\frac{q}{p}-1}x_2 + \phi\sigma + \gamma\sigma^{\frac{q}{p}}\right), \qquad (2.22)$$

where $\phi > 0$, and $\gamma > 0$. Taking $V = \frac{1}{2}\sigma^2$ as a Lyapunov function candidate, we have

$$\dot{V} = \sigma\dot{\sigma} = -\phi\sigma^2 - \gamma\sigma^{\frac{q+p}{p}} + d(x,t)\sigma. \qquad (2.23)$$

Here, $p + q$ is an even number and $-\gamma\sigma^{\frac{q}{p}} + d(x,t)\sigma \leq 0$ satisfied, i.e. $\gamma \geq |\frac{1}{\sigma^{q/p}}|D$. Thus, $\dot{V} \leq 0$.

(*T3.*) *Nonsingular terminal sliding mode control (NTSMC)*: For the system (2.13), to deal with the singular problem of conventional TSMC, the nonsingular terminal sliding variable is given by [91]

$$\sigma = x_1 + \frac{1}{\beta} x_2^{\frac{p}{q}}, \tag{2.24}$$

where β, p and q have been defined in (2.15). Suppose that the NTSMC is designed as

$$u = -g^{-1}(x)\left(h(x) + \frac{\beta q}{p} x_2^{2-\frac{p}{q}} + (D + \mu)\operatorname{sgn}(\sigma)\right), \tag{2.25}$$

where $1 < \frac{p}{q} < 2$, $\mu > 0$.

The derivative of (2.24) along the system dynamics (2.13) satisfies

$$\begin{aligned}
\dot{\sigma} &= x_2 + \frac{p}{\beta q} x_2^{\frac{p}{q}-1} \dot{x}_2 = x_2 + \frac{p}{\beta q} x_2^{\frac{p}{q}-1}\left(h(x) + g(x)u + d(x,t)\right) \\
&= \frac{p}{\beta q} x_2^{\frac{p}{q}-1}\left(d(x,t) - (D+\mu)\operatorname{sgn}(\sigma)\right).
\end{aligned} \tag{2.26}$$

Accordingly,

$$\sigma\dot{\sigma} = \frac{p}{\beta q} x_2^{\frac{p}{q}-1}\left(d(x,t)\sigma - (D+\mu)|\sigma|\right) \le -\mu \frac{p}{\beta q} x_2^{\frac{p}{q}-1}|\sigma| \tag{2.27}$$

where $x_2^{\frac{p}{q}-1} > 0$ as $1 > (\frac{p}{q} - 1) > 0$ when $x_2 \ne 0$.

Global sliding mode control

Global sliding mode control (GSMC) eliminates the attaining motion phase and guarantees that the whole system response is robust. Thus, the drawback of the traditional sliding mode variable structure which has no robustness in the attaining mode is overcome.

The GSMC law can be obtained by formulating a dynamic nonlinear sliding surface equation. The global sliding variable can be designed in conjunction with $f(t)$ for the second-order system (2.13) as [92]

$$\sigma = \dot{e} + \rho e - f(t), \ \rho > 0, \tag{2.28}$$

where the tracking error is $e = x - x_d$ and desired trajectory is x_d. $f(t)$ is a function to be chosen so as to attain at the sliding surface without a reaching phase. For this, the following conditions need to be satisfied:

($C1$) $f(0) = \dot{e}_0 + \rho e_0$, $e_0 = e(t = 0)$,

($C2$) $f(t) \to 0$ as $t \to \infty$,

($C3$) $f'(t)$ exits and is bounded.

Here, conditions ($C1$), ($C2$) and ($C3$) represent the initial distance away from the sliding surface, the asymptotic stability, and the existence of the sliding mode. Thus, $f(t)$ can be selected as $f(t) = f(0)e^{-\kappa t}$, where κ is a positive constant.

Dynamic sliding mode control

Dynamic sliding mode control (DSMC) can be obtained by constructing a switching function (σ_0) in the normal sliding mode into a new dynamic switching function (σ) [86]. The switching function is relative to the first- or higher-order derivative in the control input. It can shift the discontinuous terms into the first- or higher-order derivative in the control input. Hence, a continuous DSM control law is acquired and the chattering phenomenon is mitigated adequately.

Consider a second-order uncertain nonlinear system

$$\dot{x} = h(x) + g(x)u + d(t), \qquad (2.29)$$

where $h(x)$ and $g(x) \neq 0$, $\forall x \in \mathbb{R}^2$, are known smooth functions, $y = x_1$ is the output and $d(t)$ is the uncertainties. Assume that

$$|d(t)| \leq D, \ |\dot{d}(t)| \leq D_d.$$

Now define the sliding function and tracking error as $\sigma_0 = \dot{e} + \rho e$ and $e = y - y_d$,

respectively, where $\rho > 0$. Then,

$$\dot{\sigma}_0 = \ddot{e} + \rho\dot{e} = \ddot{y} - \ddot{y}_d + \rho\dot{e}$$

$$\Rightarrow \ \dot{\sigma}_0 = h(x) + g(x)u + d(t) - \ddot{y}_d + \rho\dot{e}. \tag{2.30}$$

A new dynamic sliding function is then constructed as

$$\sigma = \dot{\sigma}_0 + \lambda\sigma_0 = h(x) + g(x)u + d(t) - \ddot{y}_d + \rho\dot{e} + \lambda\sigma_0 \tag{2.31}$$

where $\lambda > 0$. For $\sigma = 0$, $h(x) + g(x)u + d(t) - \ddot{y}_d + \rho\dot{e} + \lambda\sigma_0 = 0$ is a asymptotically stable, accordingly, $e \to 0$ and $\dot{e} \to 0$.

Suppose that the dynamic controller is selected as

$$v = -g^{-1}(x)\Big(- \frac{d}{dt}h(x) + (\rho + \lambda)\ddot{y}_d + \dddot{y}_d - u\Big(\frac{d}{dt}g(x) + (\rho + \lambda)g(x)\Big)$$
$$- (\rho + \lambda)h(x) - \lambda\rho\dot{e} - \mu\operatorname{sgn}(\sigma)\Big), \tag{2.32}$$

where $v = \dot{u}$ and $\mu > D_d + (\rho + \lambda)D$.

The derivatives of (2.31) along the system dynamics (2.29) gives

$$\dot{\sigma} = \frac{d}{dt}h(x) + u\frac{d}{dt}g(x) + g(x)\dot{u} + \dot{d}(t) - \dddot{y}_d + \rho\ddot{e} + \lambda\dot{\sigma}_0$$
$$= \frac{d}{dt}h(x) + u\frac{d}{dt}g(x) + g(x)v + \dot{d}(t) - \dddot{y}_d + \rho\Big(h(x) + g(x)u + d(t) - \ddot{y}_d\Big)$$
$$+ \lambda\Big(h(x) + g(x)u + d(t) - \ddot{y}_d + \rho\dot{e}\Big)$$
$$= \frac{d}{dt}h(x) - (\rho + \lambda)\ddot{y}_d - \dddot{y}_d + \dot{d}(t) + (\rho + \lambda)d(t) + (\rho + \lambda)h(x) + g(x)v \tag{2.33}$$
$$+ u\Big(\frac{d}{dt}g(x) + (\rho + \lambda)g(x)\Big) + \lambda\rho\dot{e}$$
$$= \dot{d}(t) + (\rho + \lambda)d(t) - \mu\operatorname{sgn}(\sigma).$$

Accordingly,

$$\sigma\dot{\sigma} = \sigma\Big(\dot{d}(t) + (\rho + \lambda)d(t) - \mu\operatorname{sgn}(\sigma)\Big)$$
$$= \sigma\Big(\dot{d}(t) + (\rho + \lambda)d(t)\Big) - \mu|\sigma| \leq \sigma\Big(D_d + (\rho + \lambda)D\Big) - \mu|\sigma| < 0. \tag{2.34}$$

2.4.2 First-order sliding mode control

Consider an nth order nonlinear system of the form

$$
\begin{aligned}
\dot{x}_1 &= x_2, \\
\dot{x}_2 &= x_3, \\
&\vdots \\
\dot{x}_{n-1} &= x_n, \\
\dot{x}_n &= h(x) + g(x)u,
\end{aligned}
\tag{2.35}
$$

with $x \in \mathbb{R}^n$ being the state vector and $u \in \mathbb{R}$ the control input. Assume that $h(x)$ and $g(x)$ are some smooth nonlinear functions and $g(x) \geq g_0 > 0$ for all x. The control objective is for $y(t) = \dot{x}_1(t)$ to track a desired signal $y_d(t)$. Let $e = y - y_d$ be the tracking error. The nth order sliding manifold can be defined by

$$
\sigma(x) = \mathcal{S}e = e^{(n-1)} + \rho_{n-1}e^{(n-2)} + \cdots + \rho_2\dot{e} + \rho_1 e = 0,
\tag{2.36}
$$

with ρ_k, $k = 1, \cdots, n-1$, real positive constants such that the characteristic equation $s^{n-1} + \sum_{k=1}^{n-1} \rho_k s^{k-1} = 0$ is a Hurwitz polynomial, where s is the Laplace operator. The manifold $\sigma(x) = 0$ has dimension $(n-1)$ and the objective of SMC is to steer the trajectory onto this sliding manifold. If x is on the sliding surface defined by $\sigma = 0$, then we have $e^{(n-1)} = -\rho_1 x_1 - \rho_2 x_2 - \cdots - \rho_{n-1}x_{n-1}$. The derivatives of σ satisfies the equation

$$
\begin{aligned}
\dot{\sigma} &= e^{(n)} + \rho_{n-1}e^{(n-1)} + \cdots + \rho_2\ddot{e} + \rho_1\dot{e} \\
&= h(x) + g(x)u - y_d^{(n)} + \rho_{n-1}e^{(n-1)} + \cdots + \rho_2\ddot{e} + \rho_1\dot{e}.
\end{aligned}
\tag{2.37}
$$

Suppose the unknown functions h and g satisfy the following bound

$$
\left| \frac{h(x) - y_d^{(n)} + \rho_{n-1}e^{(n-1)} + \cdots + \rho_2\ddot{e} + \rho_1\dot{e}}{g(x)} \right| \leq \varrho(x, t),
\tag{2.38}
$$

for some known function $\varrho(x,t)$. Now let $V = \frac{1}{2}\sigma^2$ be the Lyapunov function candidate for (2.37). Differentiating V yields

$$\dot{V} = \sigma\dot{\sigma} = \sigma\left(h(x) - y_d^{(n)} + \rho_{n-1}e^{(n-1)} + \cdots + \rho_2\ddot{e} + \rho_1\dot{e}\right) + g(x)\sigma u$$
$$\leq g(x)|\sigma|\varrho(x,t) + g(x)\sigma u \tag{2.39}$$

Suppose that the control law is selected as

$$u = -\beta(x,t)\,\mathrm{sgn}(\sigma) = -\left(\varrho(x,t) + \eta\right)\mathrm{sgn}(\sigma),\ \eta > 0, \tag{2.40}$$

which yields

$$\dot{V} \leq g(x)|\sigma|\varrho(x,t) - g(x)\sigma\left(\varrho(x,t) + \eta\right)\mathrm{sgn}(\sigma) = -g(x)\eta|\sigma| \leq -g_0\eta|\sigma|, \tag{2.41}$$

where g_0 is defined in (2.36).

Now define the function $\chi = \sqrt{2V} = |\sigma|$, which satisfies the differential inequality $\dot{\chi} \leq -g_0\eta$. By integrating the differential inequality over the time interval $0 \leq \tau \leq t$, we have

$$|\sigma(t)| \leq |\sigma(0)| - g_0\eta t, \tag{2.42}$$

which implies that the trajectory reaches the manifold $\sigma = 0$ in finite time. The interesting feature of the control law (2.40) is its robustness with respect to $h(x)$ and $g(x)$, and only need to know the upper bound of $\varrho(x,t)$.

2.4.3 Higher-order sliding mode control

The r-th order sliding mode (r-SM) can be determined by the set [72, 79],[93]-[98]

$$\sigma = \dot{\sigma} = \cdots = \sigma^{(r-1)} = 0,\ r = [r_1, \ldots, r_n], \tag{2.43}$$

where

(i) successive total time derivatives $\sigma, \ldots, \sigma^{(r-1)}$ are continuous functions of x,

(ii) $\sigma = \cdots = \sigma^{(r-1)} = 0$ is a nonempty integral set which consists locally of Filippov's trajectories [83], and

(iii) the Filippov set of admissible velocities at the r-sliding points contains more than one vector.

The r-th derivative $\sigma_1^{(r_1)}, \sigma_2^{(r_2)}, \ldots, \sigma_n^{(r_n)}$ are discontinuous or non existent as a single-valued function of x due to some reason like trajectory nonuniqueness. The vector $r = [r_1, \ldots, r_n]$ is called the sliding order. A SM is called *stable* if the corresponding integral sliding set is *stable*. The motion on r-sliding set (2.43) is said to be the 2-SM when the sliding order is $r = [2, \ldots, 2]$ with $\ddot{\sigma}$ being discontinuous and σ, $\dot{\sigma}$ being continuous functions of x.

Suppose the system is closed by a bounded feedback control prescribed by

$$u_k = U_k(\sigma_k, \dot{\sigma}_k, \ldots, \sigma_k^{(r_k-1)}) \tag{2.44}$$

and associated with a differential inclusion (DI)

$$\sigma_k^{(r)} \in [-\varphi_k, +\varphi_k] + [\kappa_{\mathrm{m}(k)}, \kappa_{\mathrm{M}(k)}]u_k, \tag{2.45}$$

understood in the Filippov's sense, i.e. the right-hand vector set is enlarged at the discontinuity points of (2.44) in order to satisfy certain convexity and semicontinuity properties defined as below [80, 93, 99]:

A DI $\dot{x} \in F(x)$, $x \in \mathbb{R}^n$, is a Filippov DI if the vector set $F(x) \subseteq \mathbb{R}^n$ is nonempty, closed, convex, locally bounded and upper-semicontinuous i.e.

$$\lim_{x \to y}[\sup\{\mathrm{dist}(p, F(y))|p \in F(x)\}] = 0.$$

The origin is an equilibrium point when $0 \in F(x)$. Let $p \in \mathbb{R}^n$ and set $M \subseteq \mathbb{R}^n$ then the distance is defined as $\mathrm{dist}(p, M) = \inf\{|p - a||a \in M\}$.

The function $U_k(\sigma_{r-1})$ is a locally-bounded Borel-measurable function. Now, next step is to find a feedback $u_k = U_k(\sigma_{r-1})$ that all the trajectories of (2.44),

(2.45) converge in finite time to the origin $\sigma_{r-1} = 0$ of the r-sliding phase space $\sigma_k, \dot{\sigma}_k, \ldots, \sigma_k^{(r_k-1)}$.

DI (2.45) $\left(\sigma_k^{(r)} = [-\varphi_k, \varphi_k] + [\kappa_{\mathrm{m}(k)}, \kappa_{\mathrm{M}(k)}]U_k \right.$ with a locally-bounded Lebesgue-measurable right-hand side is replaced by a Filippov DI$\Big)$ is called *globally uniformly asymptotically stable* at zero, if

   (i) it is Lyapunov stable and

  (ii) for any $R > 0$, $\varepsilon = \varepsilon(R) > 0$, $\exists T(R, \varepsilon) > 0$ such that any trajectory starting inside the ball $\mathcal{B}_R$, i.e. $\|\sigma_{r-1}(t_0)\| < R$, enters into a smaller ball $\mathcal{B}_\varepsilon$ after a time period T which is independent of t_0 and remains inside thereafter, equivalently $\|\sigma_{r-1}(t)\| \in \mathcal{B}_\varepsilon$, $\forall t \geq t_0 + T(R, \varepsilon)$. Thereby, $\mathcal{B}_\varepsilon \subseteq \mathcal{B}_R$ in which $\mathcal{B}_\varepsilon = \{q \in B_R | \; \|q(t)\| < \varepsilon\}$, $\mathcal{B}_R = \{q \in \mathbb{R}^n \,|\, \|q(t_0)\| < R\}$ and $\mathcal{D} \subseteq \mathbb{R}^n$.

According to [93]-[96], the stability of the r-sliding lies in if all the trajectories in the phase plan $\sigma_k, \ldots, \sigma_k^{(r_k-1)}$ which pass through a given continuity point of $U_k(\sigma_{r-1})$ are confined between the properly chosen trajectories of

$$\sigma_k^{(r)} = \pm\varphi_k + \kappa_{\mathrm{M}(k)}U_k \text{ and } \sigma_k^{(r)} = \pm\varphi_k + \kappa_{\mathrm{m}(k)}U_k. \tag{2.46}$$

Thereby, the trajectories can be chosen as, if $U_k(\sigma_{r-1}) > 0$, then

$$\sigma_k^{(r)} = \varphi_k + \kappa_{\mathrm{M}(k)}U_k \text{ and } \sigma_k^{(r)} = -\varphi_k + \kappa_{\mathrm{m}(k)}U_k. \tag{2.47}$$

Similarly, when $U_k(\sigma_{r-1}) < 0$ then

$$\sigma_k^{(r)} = -\varphi_k + \kappa_{\mathrm{M}(k)}U_k \text{ and } \sigma_k^{(r)} = \varphi_k + \kappa_{\mathrm{m}(k)}U_k. \tag{2.48}$$

2.5   Frequency-Shaped Control

Engineering structures such as buildings and bridges are built with uncertainties, e.g., the damping characteristics of a structural system is ambiguous until the

structure is completed. Additionally, the construction materials of civil structures subject to degradation over time. Hence, structural health monitoring and control techniques using the structural frequency response functions (FRFs) can be incorporated into structures to enhance their performance, quality and safety [100]-[102]. For instance, weakness or cracks in the building structure, or loosening of structural components, may not be visible in the time domain signal but could appear as discrete frequency spikes in the frequency spectrum. On the other hand, energy-dissipative MR devices can be embedded or surface bonded as components in structural systems to improve their damping and stiffness characteristics under a low energy cost. Moreover, for analysis of the energy flow, dynamic responses of these devices are characterized by frequency-based techniques and excitations can be represented in the frequency domain by their power spectral density functions [21, 103]. The frequency domain approach to structural control allows for a roll-off of the control action at high frequencies and specify the disturbance attenuation over desired bands.

The frequency-shaping (FS) technique to the linear-quadratic (LQ) design was first proposed in [104] with the cost functional expressed via the frequency variable ω. To extend the SMC design to the frequency domain, frequency-shaped (FS) SMC (FSSMC) and discrete-time FSSMC have been developed and applied to various mechanical systems including active vibration control [105, 106], flexible robot manipulators [107]-[110], active suspension system [111], electrohydraulic servo-motor [112], pickup heads in optical disk drives [113], hard disk drives [114] and smart structure [21, 84, 115]. In FSSMC, the sliding surface is modeled by a desired linear operator to suppress frequency components of the SM response in a designated frequency band [87, 110]. According to [110], linear operators can be interpreted as a low-pass filter (LPF) (either as a prefilter, similar to introducing artificial actuator dynamics or as a postfilter, functioning like sensor dynamics) for

shaping the system equivalence dynamics in the frequency domain. The idea has been studied and extended by many researchers, e.g. [106, 116], and given the name *frequency-shaped sliding surface*.

A discrete time approach to the frequency-shaping LQ control using the Parseval's theorem was reported in [111] for active suspension system. A synthesis method for flexible manipulator was proposed in [109]: (*a*) the terminal sliding mode technique was applied to achieve small steady state error and to accelerate the convergence of the sliding mode towards equilibrium and (*b*) frequency shaping approach was employed to reduce the intrinsic resonance modes. An output feedback FSSMC was studied in [115] for damping out structural vibrations, where the system states are implicitly obtained by measuring the output at a faster rate than the control input. The works mentioned in Table 2.3, have not clearly explained on the dissipation of vibration-induced energy in the controlled smart devices. In [21], the frequency domain advantage is taken into account in the framework of semi-active structural control to result in low-energy and resilient structures against dynamic loadings such as earthquakes or gusty winds.

Table 2.3 : Summary of frequency-shaped control methods.

Reference	Control	Application	Comments
1980	FS technique using state feedback to LQ design [104]	robotic manipulator	cost functional expressed via the frequency variable ω.
1988	FS LQ design [117]	robotic manipulator	reported a spectral factorization relationship with FS LQ control problem
1989	discrete FS LQ design [111]	active seat suspension	developed a discrete time approach using the Parseval's theorem
1993	State feedback FSSM [110]	robotic manipulator	to attenuate the effect of unmodelled high frequency dynamics
2000	FS and TSMC [109]	robotic manipulator	to mitigate the inherent resonance modes and to achieve small steady state error
2002	FS technique with recursive backstepping algorithm [116]	linear system	to eliminate the high frequency, high amplitude chattering caused by large feedback gain properties of backstepping algorithm

Reference	Control	Application	Comments
2005	FSSMC [113]	optical disk drives	
2005	FSSMC [106]	active vibration isolation	(i) US Patent 2005/0256613 A1, (ii) takes into account plant uncertainties and payload disturbances (iii) showed FS sliding surface is equivalent to a feedback-feedforward compensation problem
2009	Output feedback FSSM [115]	smart flexible cantilever beam	states are obtained by measuring the output at a faster rate than the control input
2017	H$_\infty$ based FSSMC [114]	hard disk drive	discrete-time FSSMC for high-precision systems with narrow band disturbances
2018	FS2SMC [21]	smart structure	addressed the energy flow in the building structures for control and monitoring

Chapter 3

Magnetorheological Devices

3.1 Introduction

Hysteretic magnetorheological (MR) based devices, such as MR damper (MRD), MR pin joint (MRP) and MR elastomer isolator (MRE), are recognized as smart devices for protection of engineering structures subject to external dynamic loadings such as seismic events, strong winds, destructive waves and vibration shocks. This is due to their advantageous features of controllable mechanical properties, quick response, lower power consumption and fault-safe. Dampers with hysteretic properties can be used to dissipate a large amount of input energy imparted to the structure under the control from a magnetizing current. The embedded smart devices are controlled to adjust mechanical parameters of the seismically or wind excited structure and allow for dissipation of the induced energy with a controllable resisting force over a finite displacement. The heat energy is dissipated through the smart fluid inside the damper housing and harmlessly transferred to the environment via conduction and convection mechanisms. By controlling the capability of absorbing excitation energy through the use of MR fluid yield stress to ultimately mitigate the overall structural vibrations under external excitations, a low-energy smart structure can be achieved to withstand dynamic loading sources. Nevertheless, due to the unique nonlinear nature of these devices, the major challenge is how to design a robust model for structural vibration control. The experimental characterization and cyclic energy dissipation of MR devices are emphasized in the following.
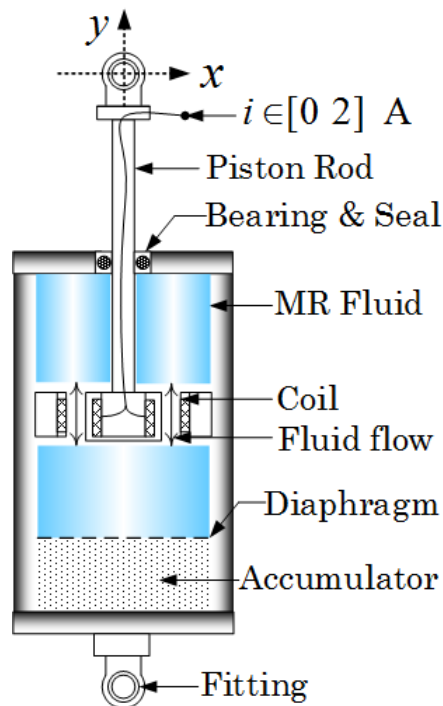
Figure 3.1 : MR damper structure.

3.2 Magnetorheological Damper

To experimentally study the dissipation and energy-related aspects in the magnetorheological (MR) fluid damper (MRD) for analysis of low-energy resilient structures embedded with MRDs, the RD-8041-1 damper manufactured by LORD Corporation is characterized by using a thermal camera. Figure 3.1 shows a schematic diagram of the damper. The damper, which accepts a maximum input current of 2 A at 12 V dc, has a mass of 0.92 kg, an extended length of 24.8 cm and a ±3.7 cm stroke. The key properties of the RD-8041-1 MRD is given in Table 3.1. To thoroughly understand the dynamic features of the MRD, a serious of experiments are conducted in the laboratory.

Table 3.1 : Parameters of the LORD RD-8041-1 MRD.

Typical properties	
Mass	920 gm
Stroke	74 (±37) mm
Extended length	248 mm
Body diameter	42.1 mm
Shaft diameter	10 mm
Response time	< 15 msec
Electrical properties	
Input current	$i \in [0\ 2]$ A
Input voltage	12 VDC
Resistance	5 Ω (7 Ω) at 25°C (71°C)

3.2.1 Experimental setup

A dynamic machine, Instron ElectroPuls$^{\text{TM}}$ E10000, was used to provide sinusoidal signal to the RD-8041-1 damper, located in the Dynamic & Mechanics of Solids Laboratory of the University of Technology Sydney (UTS) as pictorially shown in Figure 3.2. A wide range of displacement waveforms including sine, triangle, trapezoidal, step and pseudo-random can be employed to measure the dynamic responses of an MRD using this test setup.

The damper was mounted between the effectors of the E10000 and moves along the y axis. A wide range of excitation variables: harmonic displacements of the damper rod of $E = \pm 4$, ± 8, ± 12, ± 15 mm and frequencies $f = 0.5$, 1, 2, 3 Hz were considered. This low frequency range was considered to represent the range of essential dynamics of civil structure excitations. The voltage applied to the RD-
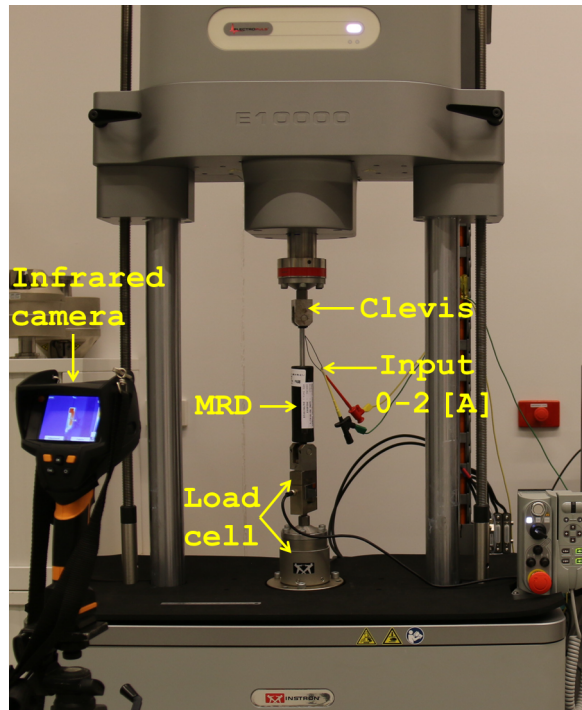
Figure 3.2 : A photograph of the MRD RD-8041-1 test system.

8041-1 were held at constant levels as given in Table 3.2. These voltages correspond to currents $i \in [0\ 2]$ A with an increment of 0.25 A.

A Testo 875-2i thermal camera was utilized to monitor the temperature effect which has certain influences on the MR fluid properties. During the experiments, the damper was ON, stroking the damper piston under a constantly supplied current for a period cause the increase of temperature (see Table 3.2). Since it will be more effective to consider the magnetization current as the control input of MR device-based mechatronic systems, instead of the conventional view of semiactive control using the derivation of damping force.

There are 88 operating cases carried out with twice repetition and the sampling rate was set at 1 kHz for all the tests. The instantaneous displacement and output force were measured along the y axis, and imported into Excel worksheets through the E10000 transducers: a position sensor and a bi-axial Dynacell$^{\text{TM}}$ load cell with a

Table 3.2 : $x = E\sin(2\pi t)$; $E = 4, 8, 12, 15$ mm, $f = 1$ Hz.

Voltage (V)	0	1.04	2.12	3.2	4.28	5.36	6.44	7.52	8.6
Current (A)	0	0.25	0.5	0.75	1	1.25	1.5	1.75	2
Temp. (°C)	25.6	26.7	28.5	30	32.3	35.1	38	40.9	43.9
Test no.	1-4	5-8	9-12	13-16	17-20	21-24	25-28	29-32	33-36

range of ± 10 kN, respectively, using the WaveMatrix$^{\text{TM}}$ user interface. An additional load cell, KPA6110P model with a capacity of 1 ton, was installed in series with the MRD and Dynacell$^{\text{TM}}$ load cell. The experimental readings were filtered by a second-order Butterworth filter. A central difference approximation method was applied to obtain the velocity and acceleration responses from the measured displacement data.

3.2.2 Energy cycle of MR dampers

The damping capacity of smart structures embedded with MRDs depends on the amount of energy dissipated in the devices as a result of their induced hysteretic effect, during a typical vibration cycle while the MRDs operate at a constant magnetic field [17, 29]. The MRD dissipates its cyclic energy in the MR fluid via the formation of a closed-loop mechanical lag in the force-displacement trajectory. Figure 3.3 shows that hysteresis occurring in the damper's dynamic relation between input-output (I/O) variables represents memory effects involving field-dependent friction in the MR fluid suspension, leading to energy dissipation. Notably, in both the force-displacement (Figure 3.3(a)) and force-velocity (Figure 3.3(b)) relationships, hysteresis loops representing intrinsic nonlinearity and complex dynamics of the damper are not zero-centred, which account for the effect of the accumulator at the bottom of the MRD. Therefore, to eliminate the force bias/offset, the MRD

(a) f_{MR} vs x trajectories

(b) f_{MR} vs $\dot{x}$ trajectories
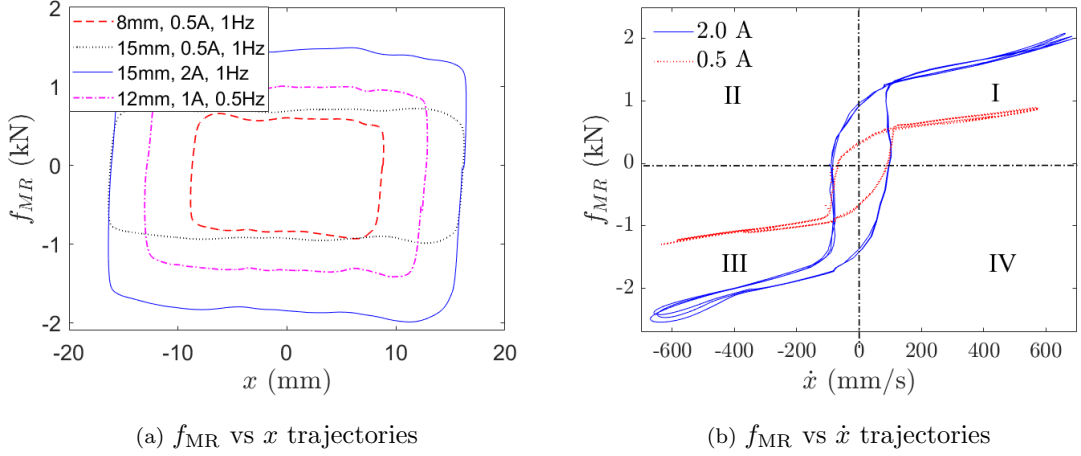
Figure 3.3 : Measured RD-8041-1 hysteresis.

effective stiffness can be defined by

$$k_{\mathrm{MR}} = \frac{f_{\mathrm{MR}}^+ - f_{\mathrm{MR}}^-}{E^+ - E^-},$$

where f_{MR}^+ is the measured force at the maximum positive displacement E^+ and f_{MR}^- is the measured force at the minimum negative displacement E^-.

Let c_{MR}, E_{MR}, f_{MR}, k_{MR}, and ζ_{MR} denote the equivalent damping, dissipated energy, output force function, effective stiffness and damping ratio of the device, respectively. Given periodic displacement $x = E\sin(\omega t)$ and velocity $\dot{x} = E\omega\cos(\omega t)$ of amplitude E and angular frequency $\omega = 2\pi f$, the energy dissipated by an MRD in one vibration period can be given by the area enclosed within the hysteresis loop, as shown for example in Figure 3.4.

The MRD dissipated energy can be expressed as

$$\begin{aligned}
E_{\mathrm{MR}} &= \oint f_{\mathrm{MR}} dx = \int_0^{\frac{2\pi}{\omega}} f_{\mathrm{MR}} \dot{x} dt = \int_0^{\frac{2\pi}{\omega}} c_{\mathrm{MR}} \dot{x}^2 dt \\
&= c_{\mathrm{MR}} \int_0^{\frac{2\pi}{\omega}} (E\omega)^2 \cos^2(\omega t) dt = \frac{c_{\mathrm{MR}}(E\omega)^2}{2} \int_0^{\frac{2\pi}{\omega}} (1 - \sin(2\omega t)) dt \\
&= \frac{c_{\mathrm{MR}}(E\omega)^2}{2} \cdot \frac{2\pi}{\omega} - 0 \\
&= \pi c_{\mathrm{MR}} E^2 \omega = 2\pi^2 f c_{\mathrm{MR}} E^2,
\end{aligned} \tag{3.1}$$
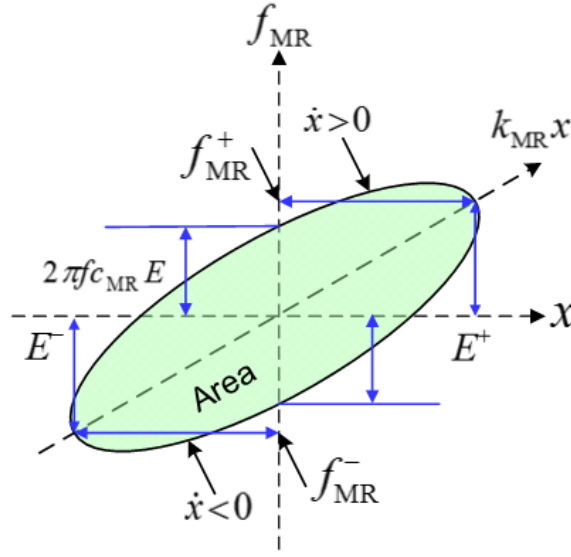
Figure 3.4 : Graphical representation of dissipated-energy per cycle at resonance.

where damping force function

$$f_{\mathrm{MR}} = c_{\mathrm{MR}}\dot{x} = c_{\mathrm{MR}}E\omega\cos(\omega t)$$
$$\Rightarrow f_{\mathrm{MR}} = \pm c_{\mathrm{MR}}\omega\sqrt{E^2 - x^2}$$

(3.2)

and with its conjugate variable, the displacement, lying on an ellipse

$$(\frac{f_{\mathrm{MR}}}{c_{\mathrm{MR}}\omega E})^2 + (\frac{x}{E})^2 = 1$$

(3.3)

depicted in Figure 3.4.

The loss coefficient or damping ratio ζ_{MR} of MRD can be defined as the ratio of damping energy loss per radian divided by the strain energy:

$$\zeta_{\mathrm{MR}} = \frac{2\pi^2 f c_{\mathrm{MR}}E^2}{2\pi(k_{\mathrm{MR}}E^2)}.$$

(3.4)

Thus, we have

$$c_{\mathrm{MR}} = \frac{k_{\mathrm{MR}}\zeta_{\mathrm{MR}}}{\pi f}.$$

(3.5)

Using the concept of equivalent viscous damping and substituting c_{MR} into (3.1) gives

$$E_{\mathrm{MR}} = 2\pi k_{\mathrm{MR}}\zeta_{\mathrm{MR}}E^2 = 2\pi^2 f c_{\mathrm{MR}}E^2.$$

(3.6)

(a) Thermal image

(b) Real image

(c) Histogram shows average $\theta = 43.9°$C

(d) Temperature profile
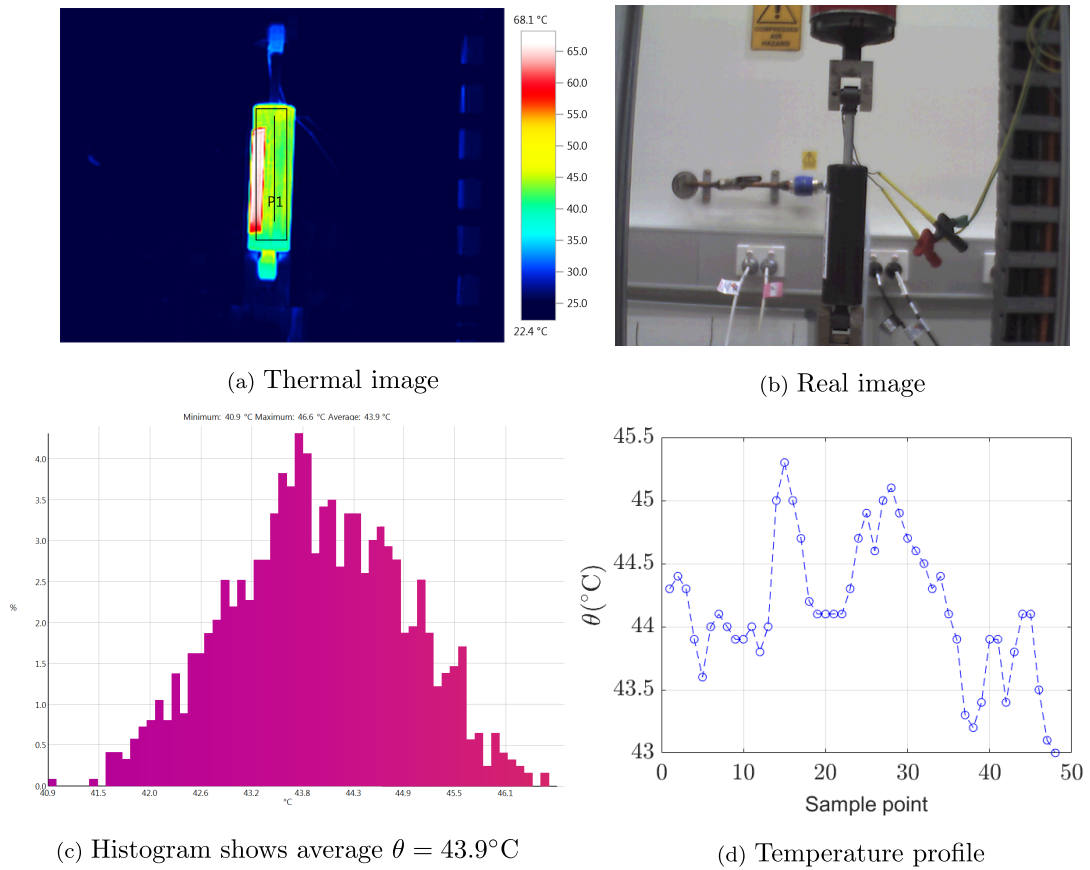
Figure 3.5 : Heat generation in the field-controllable hysteretic MRD.

3.2.3   Dissipation in MR dampers

To record the dissipation of the RD-8041-1 damper in response to the harmonic wave motion $x = E\sin(2\pi f t)$ and magnetic field strength at a magnetization current $i(t)$, we used a Testo 875-2i thermal camera based on the IR-Soft software and Easyclimate software. Figures 3.5(a) and (b) show the thermal and real images for the 5 min heating test when $E = 8$ mm, $f = 2$ Hz and $i = 1$ A. Here high-temperature area refers to the nameplate of the damper. Results of Figures 3.5(c) and (d) indicate that the generated heat can be averaged over the device, since the temperature at every section of the damper (vertical solid line) is nearly the same at a given time. For example, $\theta = 43.9°$C at point P1. It can be seen that, the mechanical energy dissipated in the magnetorheological fluid inside the damper

housing is converted into heat, depending on the magnetic field strength and input excitation variables (stroke and frequency). Thus, an increase in the magnetization current i will result in a temperature rise in the fluid inside the MRD housing, as depicted in Figures 3.6(a) and (b).

Figures 3.6(c) and (d) present the result of the heating tests for different amplitudes and frequencies. As can be seen, the MRD RD-8041-1 is initially at the room temperature of about $\theta = 25.6°$C. At the end of the test, temperature is increased. The results of Figures 3.6(c) and (d) indicate that the heat generated inside the damper not only depends on the applied magnetization current but also depends on the oscillation amplitude and excitation frequency, respectively. In these cases, the loading amplitude varies from 8 mm to 12 mm, frequency varies from 1 Hz to 2 Hz and input current varies from 1 to 1.5 A.

Taking into account also the Joule effect of the coil resistance R, the power P of the system can be given by

$$P = -f_{\mathrm{MR}}(t)\dot{x} - i^2(t)R, \tag{3.7}$$

where $R = 5$ Ω (7 Ω) at the ambient temperature (at 71°C) and $i \in [0\ 2]$A for the damper used in experiments.

The time responses of the energy and power (energy rate) obtained for the hysteresis loops of the conjugate force-displacement and force-velocity trajectories of Figures 3.3(a) and (b) are shown in Figures 3.7(a) and (b), respectively. They indicate that the force-displacement hysteresis progresses along clockwise trajectories while the force-velocity hysteresis follows anticlockwise paths. It can be interpreted from these figures that the MRD attached to a structure stores its elastic energy of the structure via its spring component and when the structural motion and correspondingly the MRD stroke is to reverse their direction, the damper would transfer the energy back to the structure. The energy alterations can be seen at the enclosed

(a) Identified temperature vs current

(b) $i = [1, 1.5]$ A

(c) $E = [8, 12]$ mm

(d) $f = [1, 2]$ Hz
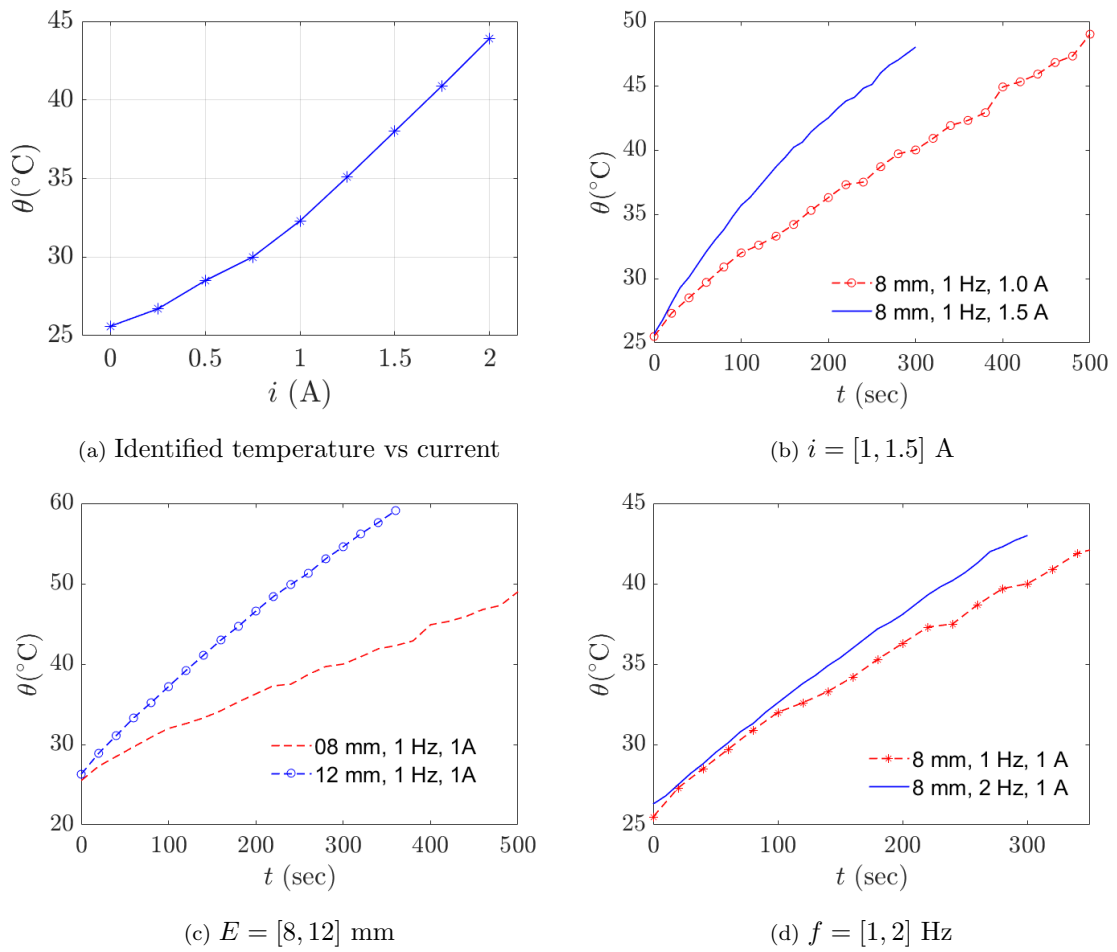
Figure 3.6 : Experimental temperature rise history within MRD due to harmonic wave motion $x = E \sin(2\pi f t)$.

area of quadrants II and IV in Figures 3.3(b) and 3.7(b), that is $-f_{\mathrm{MR}} \cdot \dot{x}$. The corresponding negative values occur in only a short duration,

$$\Delta t_{\mathrm{II}} + \Delta t_{\mathrm{IV}} = 0.042 + 0.048 = 0.09 \text{ sec,}$$

about 18% of one vibration period

$$T = \frac{2\pi}{\omega} = 0.5 \text{ sec,}$$

as shown in Figure 3.7(b). The cyclic dissipation and energy rate of the smart device not only depend on the oscillation amplitude of the MRD stroke, but also vary with

(a) One energy cycle, $2\pi/\omega = 0.5$ s

(b) $x = E\sin(2 \times 2\pi t)$ mm, $i = 2$ A

(c) $x = 8\sin(2 \times 2\pi t)$ mm

(d) $x = 8\sin(2\pi f t)$ mm, $i = 2$ A
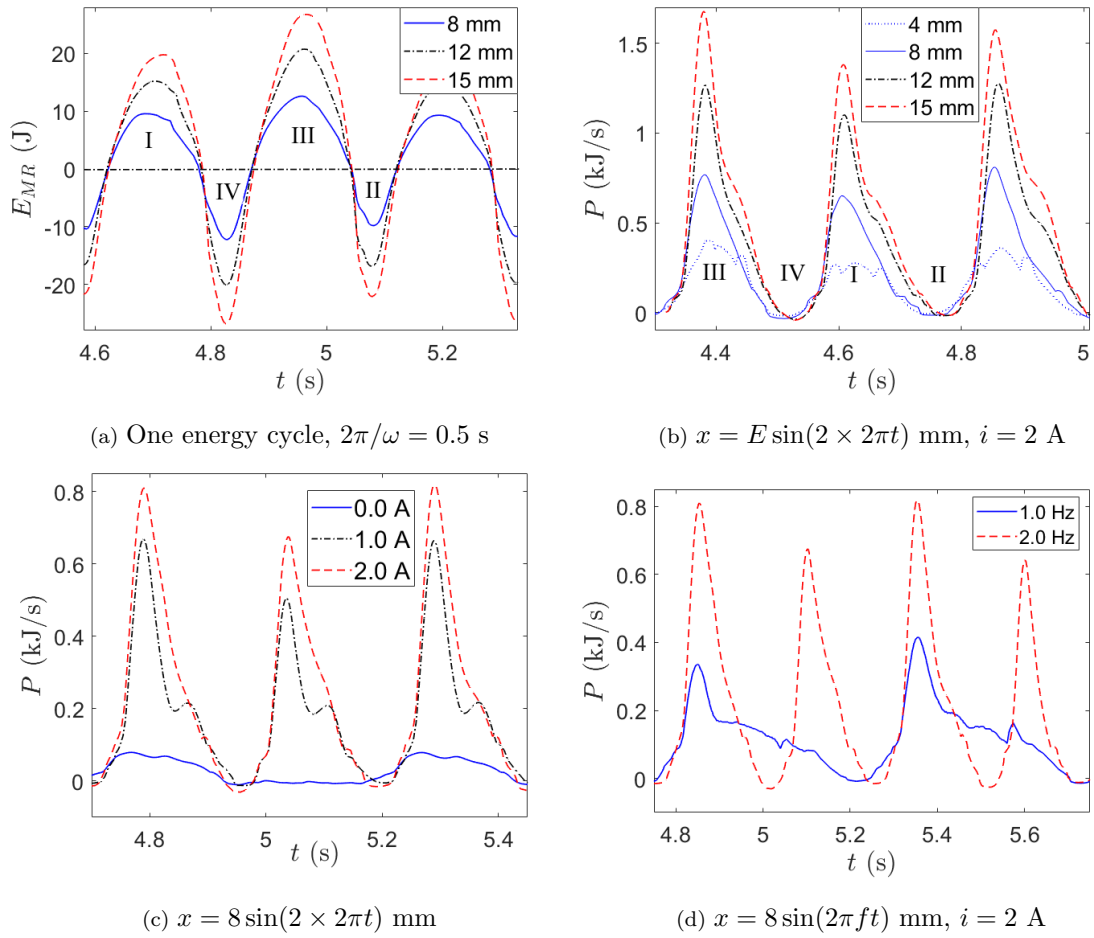
Figure 3.7 : MRD (a) dissipated energy and (b)-(d) energy rate during a vibration cycle operated at a constant magnetic field: $i \in [0\ 2]$ A, $E = [4, 8, 12, 15]$ mm, $f = [0.5, 1, 2, 3]$ Hz, $R = 5\ \Omega$ and $\theta \in [25.6\ 43.9]°$C.

respect to the applied magnetization current and excitation frequency, as shown in Figures 3.7(c) and (d), respectively.

3.3 Magnetorheological Pin Joint

Figure 3.8 shows the corresponding design schematic of the MRP, see Figure 2.4(b). The smart pin joint mainly consists of five components: a rotary thin plate inside the pin joint, a shaft connected to the plate to transfer the joint torque, two uniform housings forming a hollow cavity, MR fluid between the housing and plate,
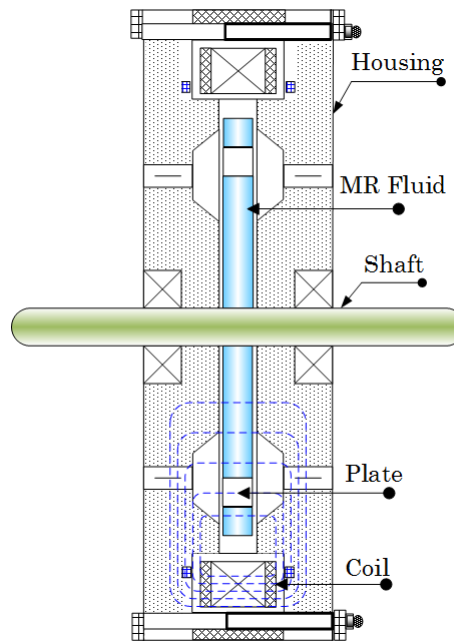
Figure 3.8 : MR pin joint schematic.

and a circular coil producing the required magnetic field. The newly-developed MRP operates in the shear mode, where two parallel plates are moving relative to each other to incur a shear flow. Detailed theoretical modeling analysis, structural parameters, and characterization test setup of the rotary pin joint considered in this section can be found in [26, 27]. Between the plate and the housings is a gap of approximately 1 mm, filled with the MR liquid MRF140CG. The liquid can provide a yield stress of up to 60 kPa at a saturated magnetic flux density of B=1.0 T when the MRP can produce a torque of up to 15 Nm at a saturated current of 2.0 A.

The magnetorheological pin joint (MRP) can be used as a rotational connector at the column-beam connection in a structural frame as shown in Figure 3.9. Its output torque can be adjusted from nearly zero joint moment (pinned) to full capacity (locked), by controlling directly the magnetization current of the circular coil inside the pin joint housing. The smart pin can behave as a free rotating hinge when not magnetized or as a partially or fully fixed joint, hence, the rigidity of the structural connection can be controlled from fully rigid and fully pinned as well as any state
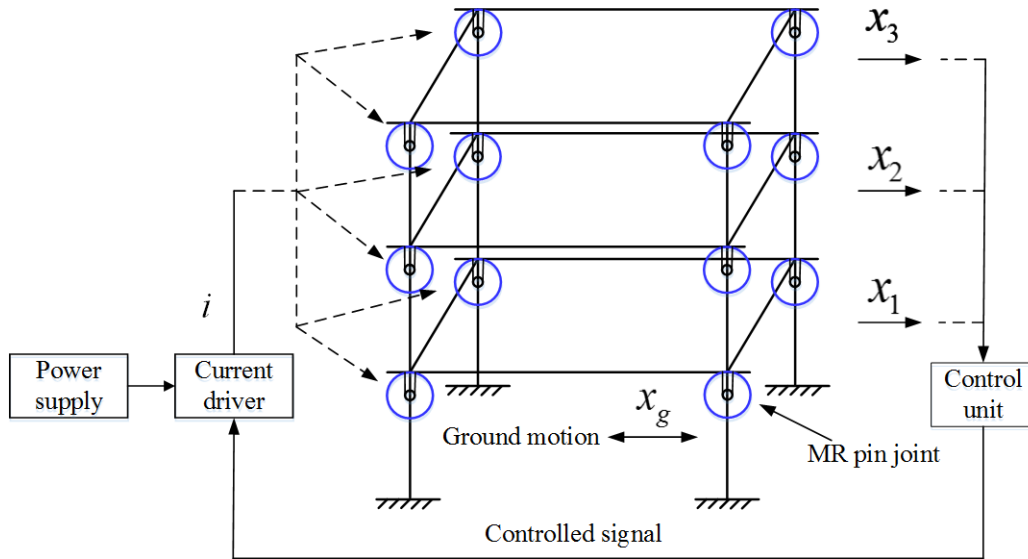
Figure 3.9 : An example of the MRP-embedded structure.

in between. The building structure's natural frequency, therefore, can be shifted further from the resonance region to avoid a structural collapse by resonance.

3.3.1 Experimental setup and device characteristics

In order to characterize the nonlinear hysteretic mechanism of the MRP, a series of dynamic tests have been conducted using 10-tonne, 3 m $\times$ 3 m MTS uni-axial shake table at the Structure Laboratory, University of Technology Sydney (UTS), to provide sinusoidal excitations, shown in Figure 3.10 [25, 27]. During the tests, MRP is fixed to a stand on the floor outside the shake table. Two steel plates fixed to the housing of the device are firmly attached to the shake table by a steel rod. A load cell (capacity of 300 N) and two linear position sensors (LPS) are used to measure the torque, horizontal and vertical displacements of the tip of the MRP steel rod, respectively. In the test, the smart device is driven with a harmonic excitation of four amplitudes, $E = 7.06, 17.65, 28.20, 35.20$ mm, respectively, corresponding to the maximum rotation angle of 2°, 5°, 8° and 10° in a range of frequencies, $f = 1$, 2, 3 Hz. A custom-designed current amplifier was used during the tests to supply
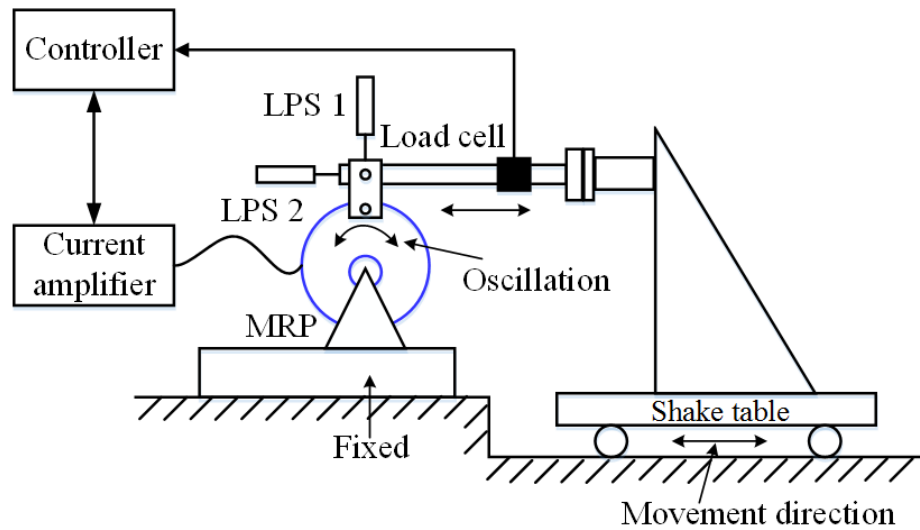
Figure 3.10 : Test setup schematic for dynamic testing of MRP.

currents ($i = 0, 0.5, 1, 1.5, 2$ A) to the magnetic coil of the MRP, hence providing the controlled magnetic field strengths. Data obtained are processed for the modeling purpose. Readings from the attached load cell and two linear position sensors were recorded by the proprietary data acquisition system of a shake table facility. To completely capture the response of the device, the sampling rate was set at 2,048 Hz. The responses of velocity can be calculated from the response of displacement using the differential computation method.

Figures 3.11(a) and (b) show the MRP T versus θ and T versus $\dot{\theta}$ trajectories when $f = 2$ Hz frequency, $E = 7.06$ mm amplitude excitation and supplied with various magnetization current values from 0 A to 2 A, respectively. It is observed that the torque value gradually increases with the ascending magnetic fields. Figures 3.11(c) and (d) show the damping torque plot of the MRP with different applied currents when it is under 28.2 mm amplitude and 1 Hz frequency harmonic loading. It is noticeable that the torque versus shaft angle response in Figure 3.11(c) exhibits highly nonlinear phenomenon while the hysteresis feature is illustrated in the torque versus angular velocity response in Figure 3.11(d). Generally, the generated T is

(a) $f = 2$ Hz, $E = 7.06$ mm

(b) $f = 2$ Hz, $E = 7.06$ mm

(c) $f = 1$ Hz, $E = 28.2$ mm

(d) $f = 1$ Hz, $E = 28.2$ mm
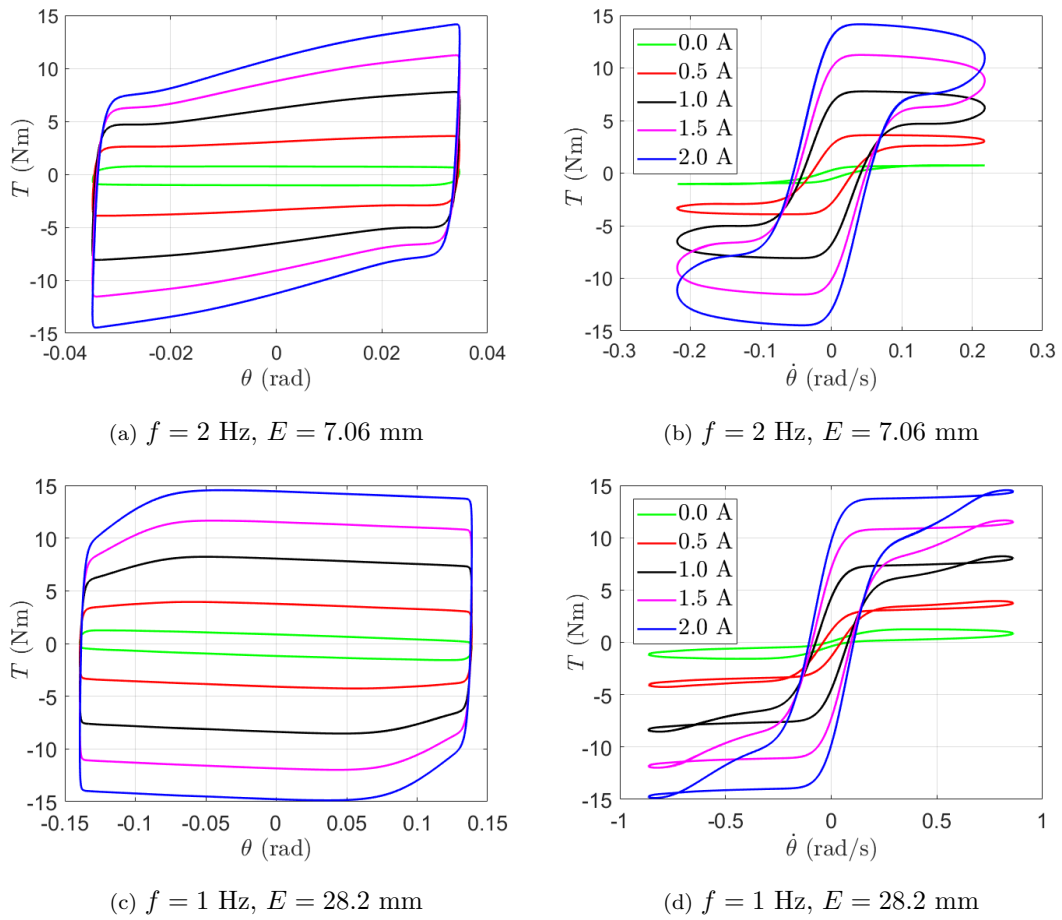
Figure 3.11 : Characteristics of MRP at $i \in [0, \ 2]$ A.

related with the mechanical properties of the MRP. That is why the torque-angle plot is elliptical and the torque-angular velocity loop is the sloped ellipse. When the current value is 0 A, the viscous phenomenon of the device is obvious because of elliptical moment-angular displacement response. Moreover, the slope of the torque-angular velocity curve in the roll off area increases with the increasing magnetic fields. As a result, in order to make full use of this novel device, an accurate model should be developed to describe these features.

3.3.2 Static hysteresis model

A static hysteresis model is proposed in this section to describe the highly-nonlinear hysteretic relationship between the torque and angular velocity in an MRP. In the proposed model, a hyperbolic tangent function is considered for portraying the S-shaped curve and modeling the hysteresis cycle of the MRP torque-angular velocity response. The model contains a hyperbolic function and a Gaussian function, respectively, representing the average hysteresis and the hysteresis thickness. Then, the resulting hysteresis is obtained from the summation of these two curves, namely the mean curve and thickness curve of the hysteresis.

For MRP hysteresis modeling, the experimental reading of MRP damping torque T is depicted against angular velocity $\dot{\theta}$ at $i = 1.5$ A, $f = 2$ Hz with the maximum rotational angle of $10°$ or amplitude $E = 35.20$ mm in Figure 3.12(a). This hysteresis cycle can be described by two curves, namely the upper curve T_1 when $\frac{d\dot{\theta}}{dt} \geq 0$ and the lower curve T_2 when $\frac{d\dot{\theta}}{dt} < 0$. Then the mean value of the hysteresis can be achieved by taking the average of every vertical sector in the hysteresis loop.

$$\bar{X}_i = \frac{1}{n} \sum_{i=1}^{n} (T_{1i} + T_{2i}), \tag{3.8}$$

where i is the index of the angular velocity of the hysteresis curves, T_{1i} and T_{2i} are the corresponding smart MRP torques determined by the angular displacement polarity.

The calculated mean is further described by a hyperbolic tangent curve, which contains only three parameters, as can be seen in Figure 3.12(b), proposed as

$$H(\theta) = \alpha + \beta \tanh(\gamma \dot{\theta}), \tag{3.9}$$

where α, β and γ are the parameters to be identified.

The thickness of the hysteresis can be estimated by taking the mean difference between the two upper/lower traces and the mean of the hysteresis [118]. Figure

(a) Hysteresis cycle

(b) Hysteresis mean curve

(c) Hysteresis thickness curve

(d) $i \in [0, \ 2]$ A from lower to upper cycle
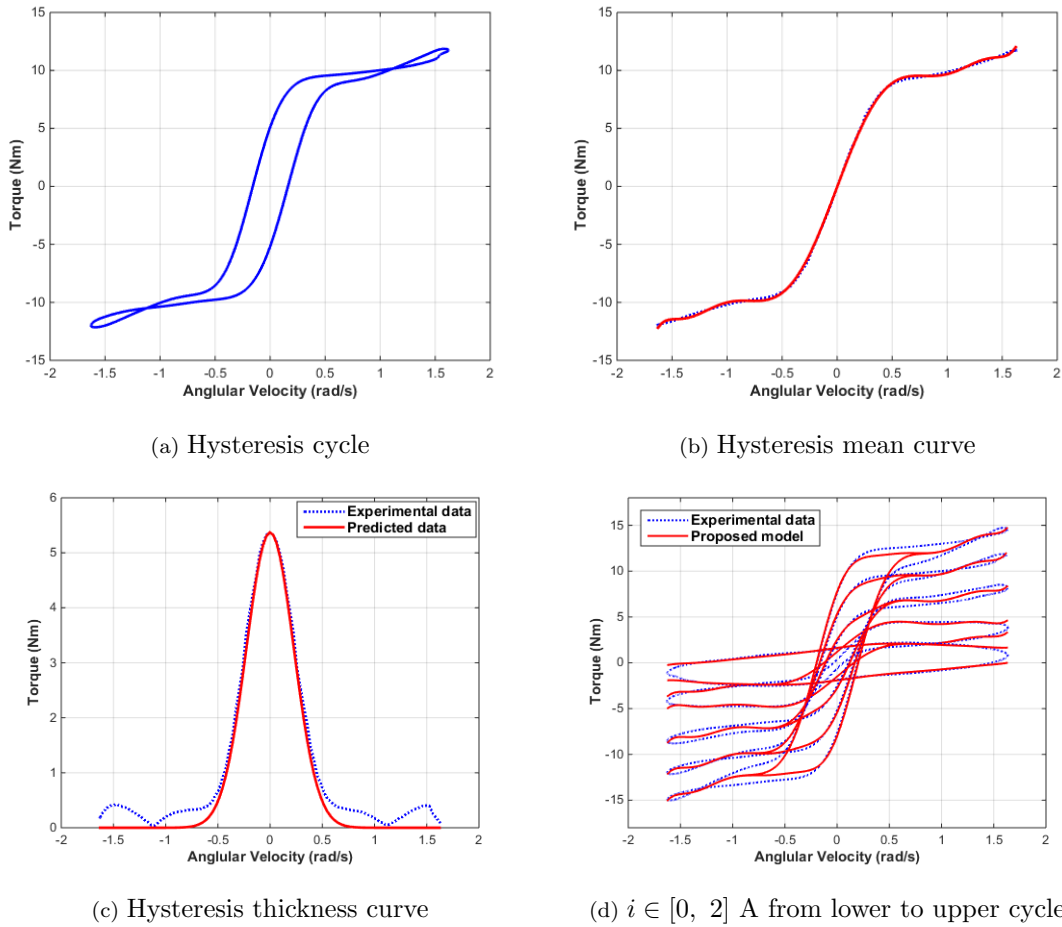
Figure 3.12 : (a)-(c) MRP hysteresis cycle, mean and thickness curve at $i = 1.5$ A, (d) a family of hysteresis by using the proposed model at $f = 2$ Hz, $E = 35.20$ mm.

3.12(c) illustrates the thickness of the hysteresis. The hysteresis thickness can now be written by

$$D_i = \frac{1}{n} \sum_{i=1}^{n} (|T_{1i} - \bar{X}_i| + |T_{2i} - \bar{X}_i|). \tag{3.10}$$

A Gaussian curve is adopted here in order to capture the thickness of the hysteresis more precisely [118]. The Gaussian curve can be defined as

$$G(\theta) = \varphi \exp\left(\frac{-\dot{\theta}^2}{2\sigma^2}\right), \tag{3.11}$$

where φ and σ stand for the vertical scaling factor of the hysteresis and the width of the hysteresis, respectively.
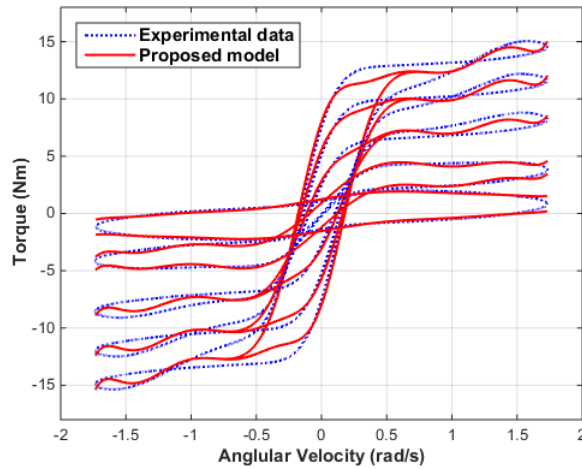
Figure 3.13 : A family of hysteresis by using the proposed model at $i \in [0,\ 2]$ A, $f = 3$ Hz, $E = 28.20$ mm.

Now, by adding and subtracting the two components, (3.9) and (3.11), respectively, the upper hysteresis curve $T_1(\theta)$ and the lower hysteresis curve $T_2(\theta)$ can be obtained. The overall hysteresis loop can be built up by the aggregation of these components, $H(\theta)$ and $G(\theta)$, as plotted in Figure 3.12(d). The proposed MRP hysteresis model can be formulated in the form

$$
T(\theta) = \begin{cases} T_1(\theta): \ H(\theta) + G(\theta) & \text{if } \ddot{\theta} \geq 0 \\ T_2(\theta): \ H(\theta) - G(\theta) & \text{if } \ddot{\theta} < 0 \end{cases}
$$
$$
= \begin{cases} \alpha + \beta\tanh(\gamma\dot{\theta}) + \varphi e^{\frac{-\dot{\theta}^2}{2\sigma^2}} & \text{if } \ddot{\theta} \geq 0 \\ \alpha + \beta\tanh(\gamma\dot{\theta}) - \varphi e^{\frac{-\dot{\theta}^2}{2\sigma^2}} & \text{if } \ddot{\theta} < 0. \end{cases}
\tag{3.12}
$$

A set of five parameters should be identified for the proposed model of MR pin joint and the set of parameters is $\Omega = [\alpha,\ \beta,\ \gamma,\ \varphi,\ \sigma]$. Figure 3.13 shows the comparison of hysteresis cycles from experimental and simulated data at a 3 Hz excitation with a lateral reciprocal displacement of 28.20 mm and five different magnetization current values from 0 to 2 A.
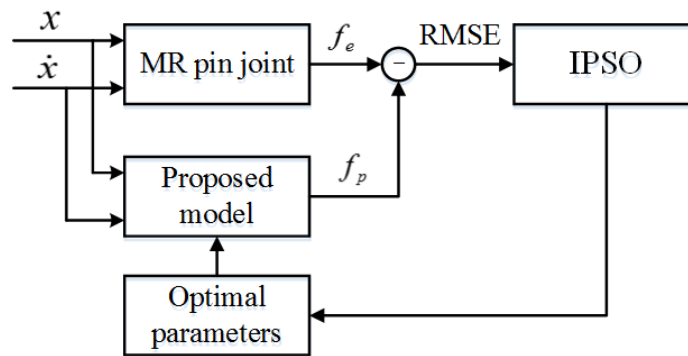
Figure 3.14 : Schematic of model identification.

3.3.3 Model identification using immune particle swarm optimization

The structure for model identification of the MRP is shown in Figure 3.14. The model parameter identification can be considered as solving a minimization optimization problem, in which the root mean square error (RMSE) is adopted as the objective function:

$$Y_{\text{RMSE}} = \sqrt{\frac{1}{n} \sum_{i=1}^{n} \left[y_e(i) - y_p(i) \right]^2}, \tag{3.13}$$

where $y_e(i)$, $y_p(i)$ and n represent the experimental data, predicted data and number of the experimental data, respectively.

The above problem can be solved by the optimization algorithm such as particle swarm optimization (PSO). In the beginning, each particle in the swarm is assigned its own position and velocity. Then, constantly updating information of searching, the whole swarm can quickly arrive at the source in the limited iterations. The specific mathematical expressions of velocity and position updates of i-th particle are given as follows [119]:

$$v_i^{k+1} \leftarrow w v_i^k + c_1 r_1 (p_i - x_i^k) + c_2 r_2 (p_g - x_i^k), \tag{3.14}$$

$$x_i^{k+1} \leftarrow x_i^k + v_i^{k+1}, \tag{3.15}$$

where w, c_1 and c_2 respectively denote the inertia weight factor and acceleration

coefficients, which are usually set as the constants; r_1 and r_2 are two random numbers in the range of $[0,\ 1]$; p_i and p_g denote the individual optimal position of i-th particle and the global optimal position of the whole swarm, respectively.

When the algorithm meets a termination criterion such as maximum iteration number or minimum adaptive threshold, the optimization process stops. Although the PSO has the benefits of simple procedure and easy implementation, its main problem remains being easy to fall into the local optimum. Especially in the later stage of optimization iteration, the convergence rate becomes relatively slow, resulting to the low accuracy of identification results.

Here, to deal with the problem of premature convergence, the biological immune mechanism is applied to the particle update in the standard PSO. Generally, antibody diversity and immune memory are the main features of an immune system [120]. To guarantee the diversity, the antibodies, which have the low concentration and high affinity with the antigen, are prone to be promoted. In contrast, the antibodies with high concentration and low affinity will be restrained. Besides, the immune memory is to reserve part of the antibodies that react to the invading antigen. When the same kind of antigen invades again, the corresponding memory cells will be activated to generate a large number of antibodies. If these two features can be incorporated into the standard PSO, the global search ability of the PSO can be greatly improved in term of a solution to the local optimum problem. If the antibody (particle) has a small concentration, it will be selected with high probability. Or else, a small probability is to be chosen. This operation is able to guarantee the coverage of the antibody (particle) and maintain the individual particles with higher fitness in the meantime, avoiding the premature convergence. The detailed procedure of immune particle swarm optimization is composed of the following steps:

(*Step 1.*) Set the PSO parameters: learning factor $c_1 = c_2 = 1.496$, inertia

weight $w = 0.7298$, maximum iteration $MaxT = 300$ and particle number $N = 50$.

(*Step 2.*) Initialize the optimization problem and randomly generate N particles (antibodies) $x_i = [\alpha, \beta, \gamma, \sigma, \varphi]$ with the velocity v_i to form the particle swarm; $i = 1, 2, \cdots, N$.

(*Step 3.*) Generate the immune memory particles (antibodies): calculate and record the fitness values of individuals in the current swarm as the immune memory particle, and judge whether it meets the stopping rule. If the stopping rule is satisfied, move to *Step 7*. Otherwise, execute *Step 4*.

(*Step 4.*) Randomly generate N new particles by PSO algorithm and M new antibodies by immune algorithm.

(*Step 5.*) Let x_i and $\xi(x_i)$ denote the i-th particle and corresponding fitness value. Now, calculate the selection probabilities p of $N + M$ particles according to

$$P(x_i) = \frac{\sum\limits_{j=1}^{N+M} |\xi(x_i) - \xi(x_j)|}{\sum\limits_{i=1}^{N+M} \sum\limits_{j=1}^{N+M} |\xi(x_i) - \xi(x_j)|}, \tag{3.16}$$

and choose N particles with high probabilities to form new swarm.

(*Step 6.*) Update the particle swarm: compare the new swarm with the immune memory particles and substitute the particles with higher fitness for the previous ones.

(*Step 7.*) Check whether the maximum iteration is obtained, and stop the program if it is satisfied. Otherwise, move to *Step 2*.

3.3.4 Identification results and analysis

In the following parameter identification results are included to validate the effectiveness of the proposed model. Based on the experimental data reported in previous section, the proposed hybrid model can be identified using IPSO. Figures

3.15(a) and (b) give the comparison between experimental measurements and the predicted torques from the proposed model when $i \in [0.5, \ 2]$ A, $E = 7.06$ mm and $f = 3$ Hz. It is noticed that the model can provide the satisfactory agreements with the experimental data from the load cell. Besides, it can be found that the captured torque exhibits the obvious increase with the addition of the applied current. The ascending magnetic field will result in the expansion of the area and slope in the hysteresis responses. Here, the proposed model can depict this phenomenon very well.

Figures 3.15(c) and (d) show the experimental and predicted torque-angular displacement / angular velocity cycles under a 2 Hz sinusoidal excitation with different amplitudes at $i = 1.5$ A. It is noticeable that all the responses are in the irregular rectangular shape with obtuse turns at the top left and bottom right corners. In addition, an obvious phenomenon can be found that the peak moment of the device output mainly depends on the magnetic field applied and the angular velocity has little influence on it. The results of Figures 3.15(c) and (d) confirm that the dynamic responses of the MRP in different excitation amplitudes are perfectly modelled and the current-dependence feature can also be reasonably portrayed by the hybrid model.

The comparison between experimental data and prediction from the model with various excitation frequencies ($f \in [1, \ 3]$ Hz) is illustrated in Figures 3.15(e) and (f). It is clearly seen that when the excitation frequencies are set at 1 Hz and 2 Hz, the torque-angular velocity responses exhibit the peanut shape hysteresis loops. Moreover, the slope and enclosed area of the torque-angular displacement responses almost keep unchanged with the increasing load frequency. The three groups of comparisons verify the performance of the proposed model to depict these features.

To evaluate the superiority of this model over another existing model for the
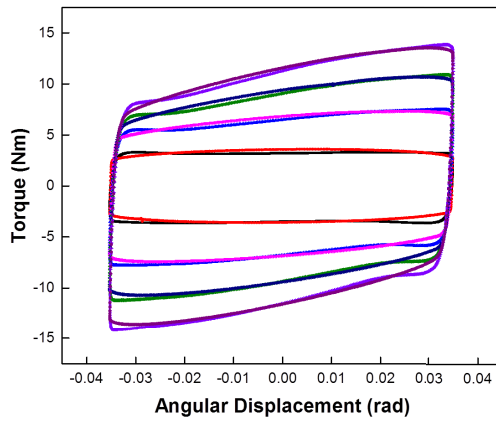
(a) T vs θ trajectories
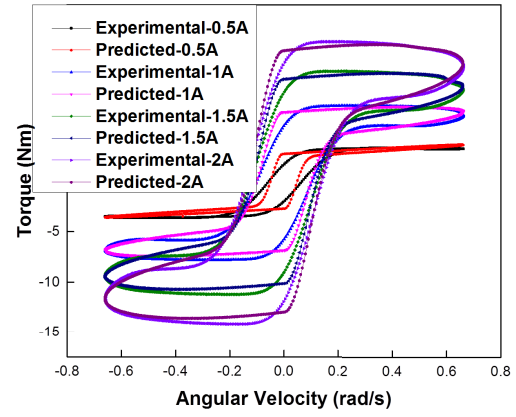
(b) T vs $\dot{\theta}$ trajectories
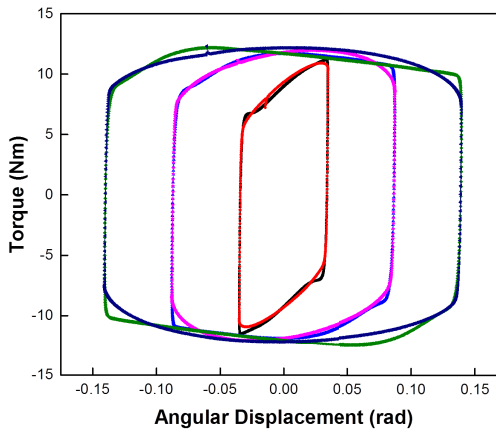
(c) T vs θ trajectories
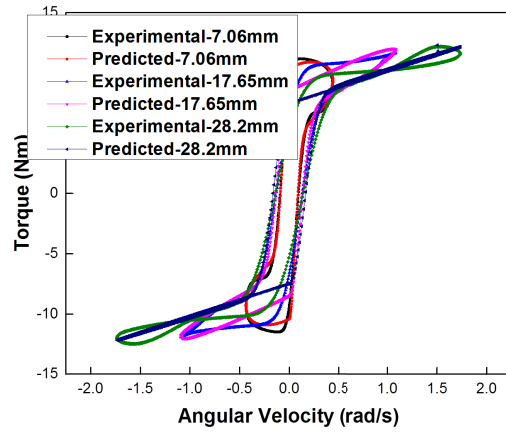
(d) T vs $\dot{\theta}$ trajectories

(e) T vs θ trajectories
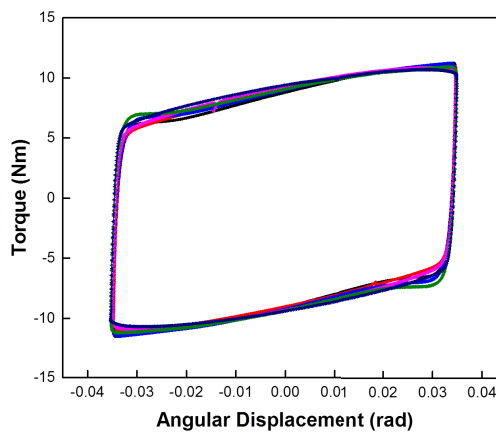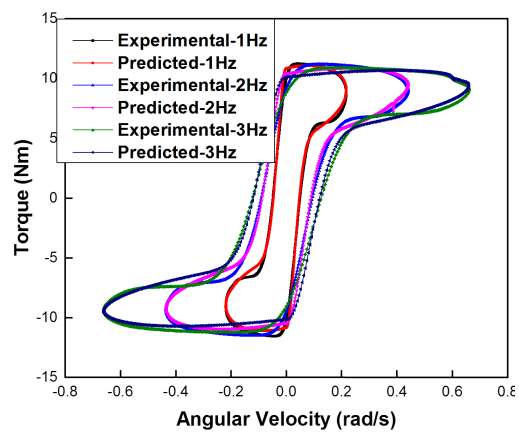
(f) T vs $\dot{\theta}$ trajectories

Figure 3.15 : $x = E\sin(2\pi ft)$; $i \in [0\ 3]$ A, $f \in [1\ 4]$ Hz, $E \in [2\ 8]$ mm.
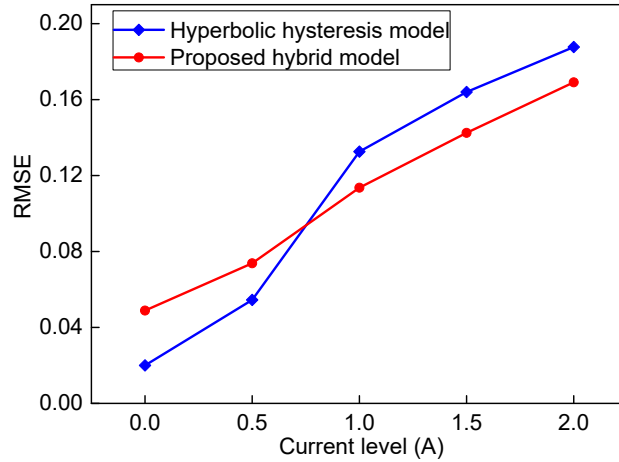
Figure 3.16 : RMSE comparison of the proposed and hyperbolic hysteresis models.

MRP, the comparison with the static hyperbolic hysteresis model has been undertaken in the following. The hyperbolic hysteresis model can be formulated as

$$
\begin{aligned}
T &= c\dot{\theta} + k\theta + \alpha z + T_0, \\
z &= \tanh\left(\beta\dot{\theta} + \delta\,\mathrm{sgn}(\theta)\right),
\end{aligned}
\tag{3.17}
$$

where T is the MRP output torque, θ and $\dot{\theta}$ are shaft angle and rotational velocity, respectively. Coefficients c and k are viscous and stiffness; α is the hysteresis scale factor; internal variable z represents the hysteresis, determined by β and δ. The numerical values of the model parameters are given in Appendix A.3.

Figure 3.16 illustrates the RMSE comparison of the proposed model and hyperbolic hysteresis model at $f = 2$ Hz with the maximum rotational angle of $2°$ or $E = 7.06$ mm. It is obviously seen that when no current or at a low current ($i < 1$ A) applied to the device, the rotational hyperbolic hysteresis model has a smaller RMS error than the proposed hybrid model. However, when the current is elevated to above 1 A, the proposed model is superior to the other one in the comparison of RMS error.
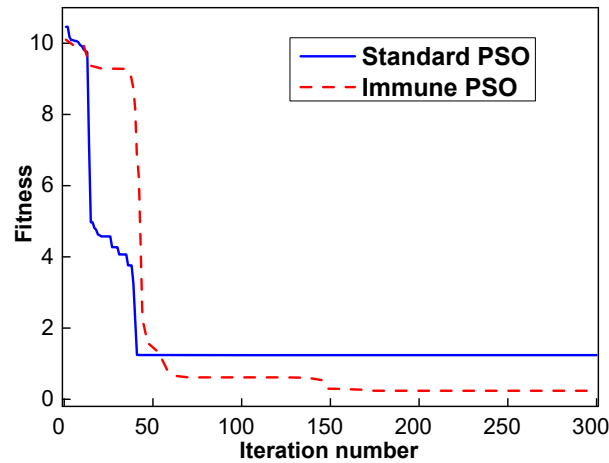
Figure 3.17 : Convergence comparison of two types of PSO.

Eventually, to assess the ability of the IPSO in the dynamic modeling of MR pin joint, the standard PSO is adopted for algorithm performance comparison. To make a fair judgment for two types of PSO, all basic PSO parameters are set as the same values. The test data are selected with the loading condition of 2 Hz frequency, 7.06 mm amplitude and 1.5 A current level. Figure 3.17 demonstrates the variation of fitness with the increasing iteration for the two algorithms. Although the standard PSO has the faster convergence rate than the IPSO, it results in a premature convergence. Unlike the standard PSO, the IPSO has a higher identification accuracy and can prevent the algorithm from falling into the local optimum.

3.4   Magnetorheological Elastomer Base Isolator

Based on the advantages of the magnetorheological elastomer (MRE) material, a new adaptive base isolator was designed by [23, 121, 122] according to the laminated structure of rubber bearing, in which the traditional rubber component is replaced by thin MRE and steel plates so that the shear modulus of the device is able to be varied according to external energized magnetic fields [24, 103],[123]-[126]. Figure
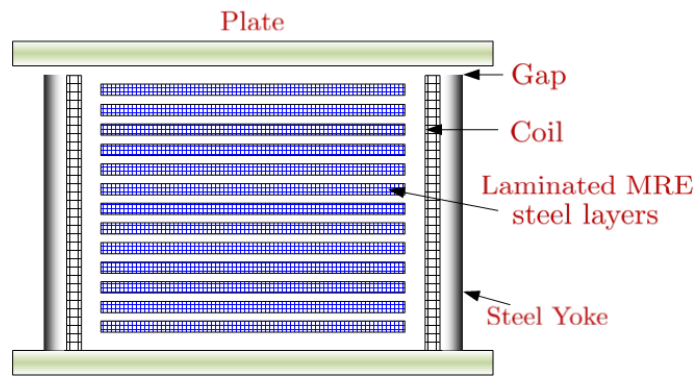
Figure 3.18 : MRE base isolator schematic.

3.18 shows the corresponding design schematic of the real product, see Figure 2.4(c). It can be seen from the figure that, the device design is achieved via the replacement of conventional rubbers with MREs. The core part of the device is the formation of the laminated configuration via alternative vulcanization of MRE sheets and steel plates. There are a total of 25 layers of soft MRE sheets with 120 mm diameter and 1 mm thickness, and 26 layers of steel plates with the same diameter and thickness. The steel sheets are used to provide the isolator with load-carrying capacity in the vertical direction, i.e. weight for the structure.

For the base isolation system, the vibration control performance is mostly dependent on the lateral stiffness of the shear mode device [23]

$$k = \frac{G_s A}{n h_t},$$ (3.18)

where G_s is the shear modulus of elasticity of MR elastomer material, A is the cross-section area of the MR elastomer layers, h_t is the thickness of the elastomer layers and n is the number of elastomer layers in the device. For the squeeze mode MRE, the compressive stiffness of the device can be defined by [23]

$$k = \frac{E_s A}{n h_t},$$ (3.19)

where E_s is the compression modulus of the MRE material.

To ensure the best vibration isolation performance, the lateral stiffness should be carefully calculated and selected. Moreover, a solenoid, made of nonmagnetic support and electromagnetic coil, is deployed outside of the laminated bearing component to produce the constant magnetic field after supplied with DC current. The maximal permissible lateral displacement of the MRE base isolator is 15 mm. Thus without the applied current, the vertical loading support ability of the device is 50 kg. And the axial load carrying capacity will increase with the ascending applied current and descending lateral displacement. Because the axial load carrying capacity is the function of shear modulus of the material and the thickness of the cross-sectional thickness, it can be designed based on the practical application requirement.

3.4.1 Experimental setup and device characteristics

Figure 3.19 displays the experimental setup for device performance testing. A hydraulic vibration table is used to provide the horizontal loading signals for the device, which is fixed on the table and moves with the movement of the vibration table. The displacement sensor, internally connected with the platform of the vibration system, is used to obtain the displacement responses of the device. A force sensor, connected with the top of the isolator, is used to measure the force responses generated. The DC power is used to energize the magnetic coils of the device.

In the test, a large range of excitations with different loading frequencies, amplitudes and applied magnetic fields are selected to drive the isolator. In this work, three types of driven frequencies of 1 Hz, 2 Hz and 4 Hz and three amplitudes of 2 mm, 4 mm and 8 mm are chosen together with four applied current levels of 0 A, 1 A, 2 A and 3 A corresponding to different magnetic fields. To assure that the MRE is tested in the steady condition, more than three cycles of responses (shear force and displacement) are captured for each excitation case. The sampling frequency is set as 256 Hz. To guarantee the stable capacity of the isolator, over 10 cycles of
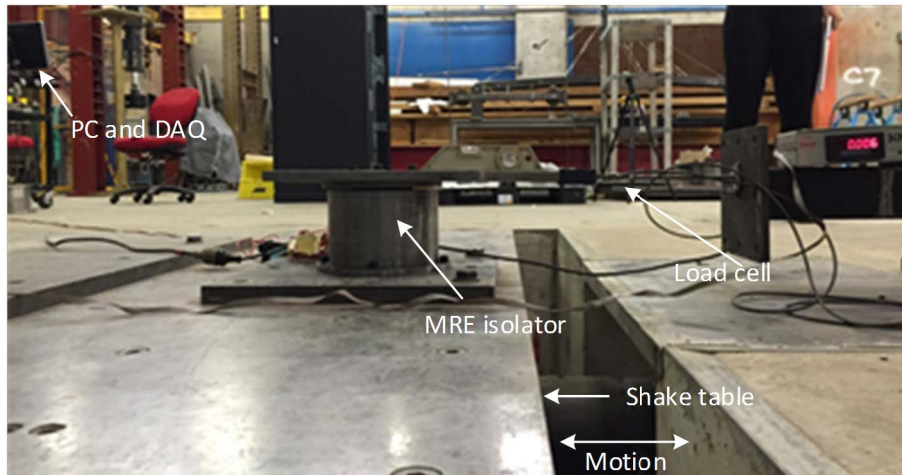
Figure 3.19 : Test setup for dynamic testing of MRE base isolator at UTS.

responses are captured for every loading condition. Moreover, each test is independently repeated five times to guarantee the consistency and accuracy of the result. After obtaining the displacement responses, the velocity responses can be calculated using finite-difference approximation method.

Figure 3.20(a) presents the dynamic force-displacement responses when the device is driven by 2 Hz frequency sinusoidal excitation with 8 mm amplitude for all current levels ranging from 0 A to 3 A. According to this figure, an obvious increment of shear force with the applied magnetic field is observed. It also can be seen that the effective stiffness of the device, denoted as the slope of the response loop, displays a significant increase with the adding current. Figure 3.20(b) gives the effective stiffness values of the device corresponding to different applied currents. The result suggests that the device has a perfect linear relationship between effective stiffness and supplying current, which is beneficial to its practical control application.

(a) Force-displacement responses

(b) Effective stiffness
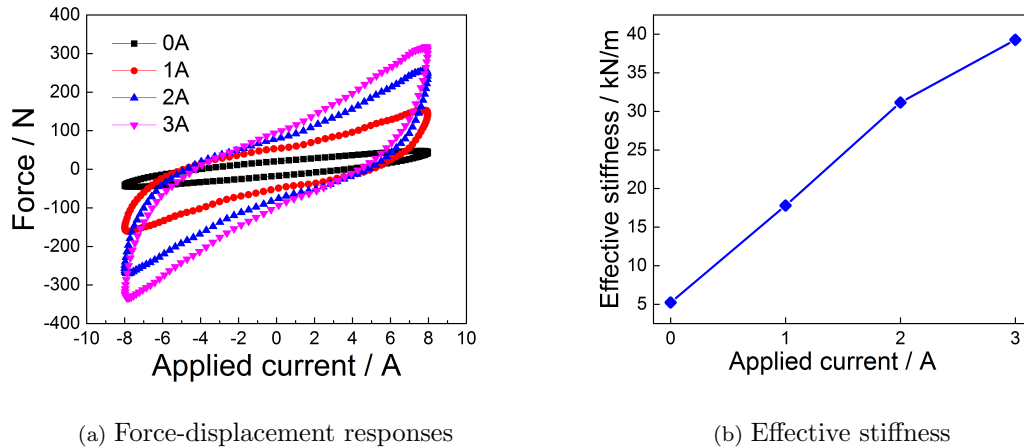
Figure 3.20 : MRE's testing results under $x = 8\sin(2 \times 2\pi t)$ mm.

3.4.2 Hyperbolic hysteresis model

Unlike other complex MRE models with differential equations, we propose a relatively simple mathematical model to capture the nonlinear and hysteretic force-displacement responses of the device. A component-wise added method is applied which includes a viscos dashpot component, a linear spring and a strain stiffening element. We consider a hyperbolic sine function spring to portray the phenomenon of stiffening hardening with the increasing current, and two linear functions to depict the viscos-elastic feature. The proposed hysteresis model can be formulated as

$$F = c_0\dot{x} + k_0 x + \alpha z + F_0, \ \ z = \frac{1 - e^{-2\beta x}}{2e^{-\beta x}}, \tag{3.20}$$

where c_0 and k_0 denote the viscous and stiffness parameters, respectively; α denotes the scale coefficient to control the tendency of strain stiffening; β is the parameter to trim the hysteresis loop; F_0 denotes the force offset of the device and its value can be obtained by calculating the mean value of shear force in one sampling cycle.

Compared with the Bouc-Wen model, the proposed hyperbolic hysteresis model has fewer model parameters to be identified. In addition, the proposed model has much simpler mathematical expression to demonstrate the hysteresis component

than Bouc-Wen model, because there is no any highly nonlinear differential equation in the expression of the proposed model. It is generally known that the numerical integration methods such as Euler method or Runge-Kutta method are employed to solve the differential equation in the Bouc-Wen model. However, these methods belong to the recursive algorithms, which may bring the iteration errors during the calculation process and result in more calculation time meanwhile. As a consequence, the proposed model should have higher accuracy, at least in theory, which is beneficial to the controller development.

3.4.3 Model identification using fruit fly optimization algorithm

The following describes identification of the model parameters according to the measured force-displacement and force-velocity responses of each loading case. Since the proposed model is highly nonlinear in which the parameters are difficult to search by trials, the process of the parameter identification is considered as solving a minimization optimization problem. The key issue of the optimization problem is the selection of the fitness function, which has a significant impact on the final recognition results. The root mean square error (RMSE) between the experimental data and predictions from the proposed model in a sampling cycle is employed as the fitness for parameter identification:

$$obj(\Omega) = \sqrt{\frac{1}{N}\sum_{i=1}^{N}\left[F_i^{exp} - c_0\dot{x}_i - k_0 x_i - \frac{\alpha(1 - e^{-2\beta x_i})}{2e^{-\beta x_i}} - F_0\right]^2}, \qquad (3.21)$$

where $\Omega = [c_0, k_0, \alpha, \beta]$ is the model parameter set to be identified; N is the total number of the experimental data in one sampling cycle; x_i, $\dot{x}_i$ and F_i^{exp} denote the collected displacement, velocity and shear force of the device at ith sampling time point, respectively. If the value of $obj(\Omega)$ approximates to zero, the corresponding result Ω is treated as the optimal solution of the problem.

In the next step, the fruit fly optimization algorithm (FFOA) [127], based on

interactive evolutionary computation method simulated by the food search behavior of fruit fly swarm, is adopted to deal with above optimization problem. Due to the superiority of smell and vision organs, the FFOA can reach the global optimum very quickly and has a better recognition performance over other commonly used swarm algorithms [127]. The procedure of FFOA to identify the model of MRE base isolator can be composed of the following steps:

Step 1. Determine the optimization problem and algorithm parameters: population size N_p and maximal iteration number N_i.

Step 2. Initialize the position of fruit fly swarm (xx, yy).

Step 3. Randomly assign the orientation and scope for food search by the personal fruit fly based on smell organ, expressed as

$$x_i = xx + x_r, \quad y_i = yy + y_r, \tag{3.22}$$

Step 4. Because the information on food source is unknown, the range between ith fly coordinate and the original point $(0,0)$ is calculated first, denoted as d_i. Then calculate the reciprocal of d_i as the model parameter set S_i to be identified according to the following equations

$$d_i = \sqrt{x_i + y_i}, \quad \Omega_i = \frac{1}{d_i}, \tag{3.23}$$

Step 5. Put the Ω_i into the fitness function $Obj(\Omega_i)$ to calculate the smell concentration value $(smell_i)$ of ith fruit fly. After obtaining all the smell concentration values of the swarm, the fruit fly with lowest smell concentration will be picked out and recorded in the system together with concentration value and corresponding coordinate

$$smell_i = Obj(\Omega_i), \quad [smell, \ coordinate = \min(smell_i)], \tag{3.24}$$

Step 6. Record the optimal concentration value and corresponding coordinate. In the meantime, the overall swarm flies towards that optimal position.
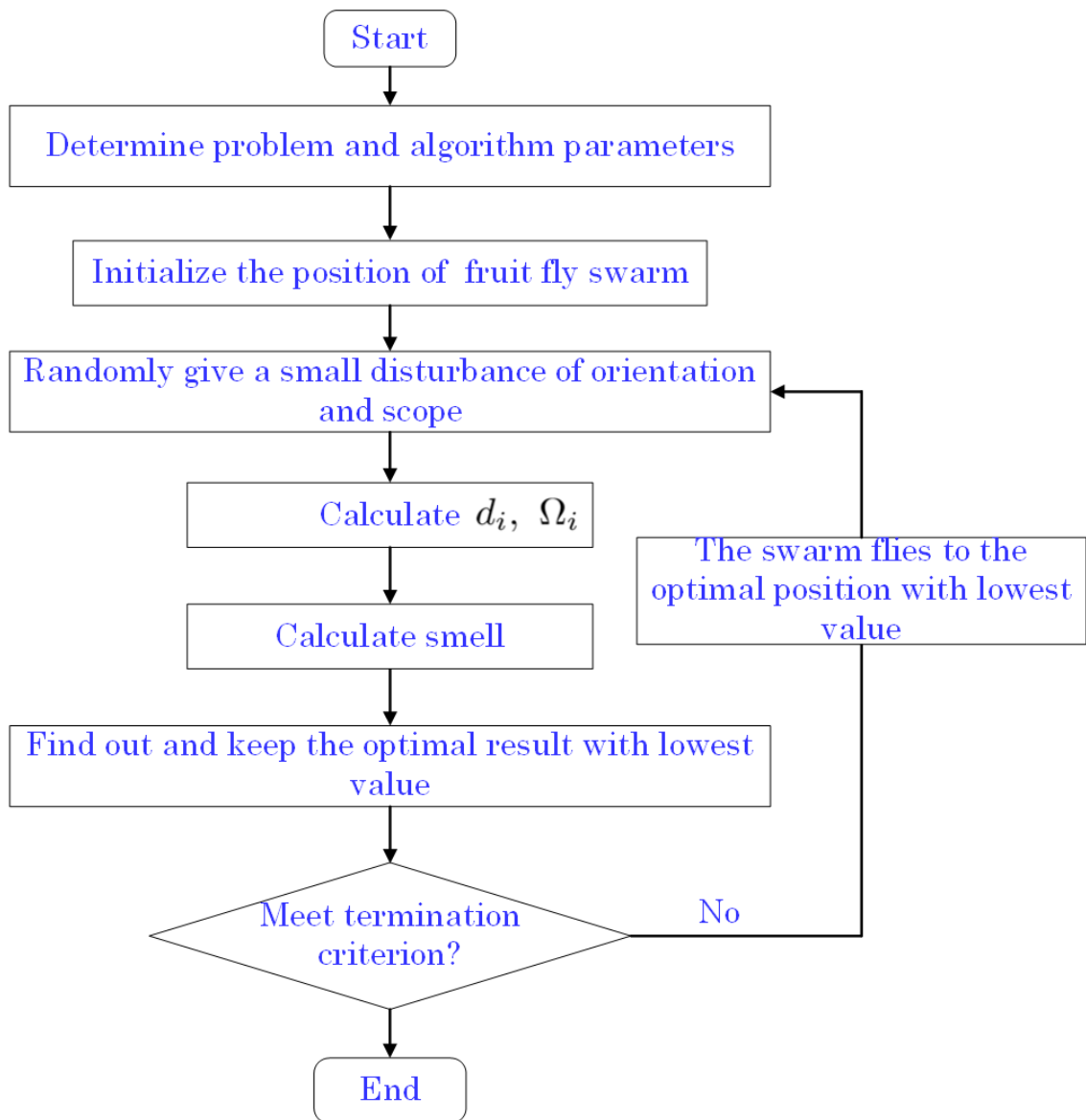
Figure 3.21 : Flow chart of FFOA to identify the hyperbolic hysteresis model.

Step 7. Repeat the *Step 2* to *Step 5.* If the calculated optimal concentration value is lower than the record, update the record through replacing it with the lower value. Otherwise, the record is unchanged. If the iteration number arrives at the maximal iteration, terminate the algorithm. Figure 3.21 illustrates the implementation of FFOA to calculate the parameter values of hyperbolic hysteresis model for MRE base isolator.

(a) Optimal flight path

(b) Fitness variation
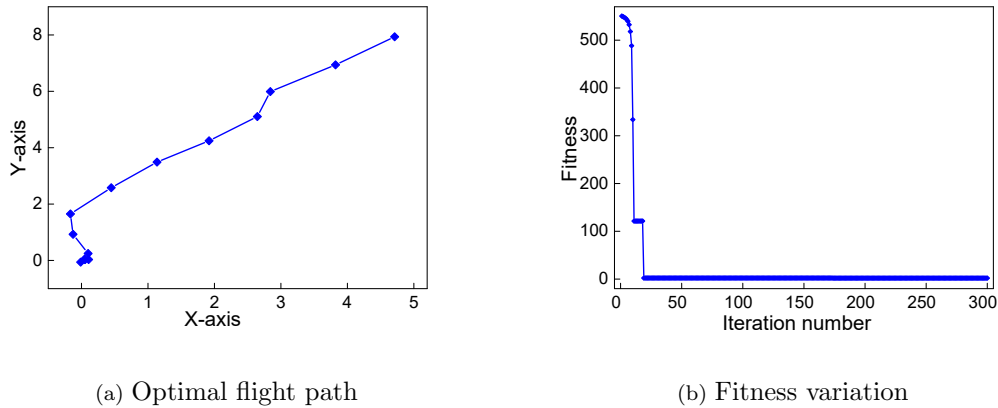
Figure 3.22 : Iteration process of parameter identifiction using FFOA.

3.4.4 Identification results and analysis

The algorithm parameters are set as: $N_p = 50$ and $N_i = 300$. Figure 3.22(a) describes one example of the flight path of fruit fly swarm for the parameter k_0 using FFOA when loading condition is $f = 4$ Hz and $E = 2$ mm. The result demonstrates that this flying path of the fruit fly swarm is relatively steady without any big cornering. The whole swarm can directly fly towards the food source and quickly arrive at that position. Figure 3.22(b) displays the convergence rate of the FFOA during the process of parameter identification. It is obviously seen that after 300 evolution iterations, the convergence rate is able to be obtained at the generation of 20 with the coordinate of $(0.04401, 0.04306)$, and the corresponding parameter values of $k_0 = 16.3818$. The identification results for all loading conditions are given in Table 3.3.

To demonstrate the effectiveness of the proposed model to describe the dynamic behaviours of the device, several comparative studies are conducted according to different loading conditions. The f_{MR} vs x responses of MRE base isolator under the 2 mm amplitude harmonic excitations and 1 A current level are portrayed in Figure 3.23(a) with predictions from the proposed model, while Figure 3.23(b) gives

the corresponding results of f_{MR} vs $\dot{x}$ responses. All the plots are drawn at 1 Hz, 2 Hz and 3 Hz. It seems that three loops in the f_{MR} vs x responses overlap together, which directly demonstrates that the effective stiffness and the maximal shear force are independent of the exciting frequency. Unlike f_{MR} vs x responses, the loops in Figure 3.23(b) have the obvious increments of nonlinear behaviours with the ascending frequency. According to the comparison results, the predictions from the proposed model perfectly agree with the experimental data under different frequency excitations.

Figure 3.23(c) gives a group of comparison between predicted shear force and experimental data when loading the device with the 4 mm amplitude and 2 Hz frequency excitations. It is clearly seen that the proposed model accurately illustrates the strain stiffening phenomenon of the device with the increasing current level. Figure 3.23(d) shows the measured and predicted force-displacement loops acquired through loading the device with the 1 Hz frequency excitation and 3 A applied current. In this case, the loading amplitude varies from 2 mm to 8 mm. An obvious feature to be noticed in this comparison is Mullins effect, in which the increasing excitation amplitude will result in the slight reduction of the effective stiffness. The results also demonstrate the capacity of the proposed model to capture this unique phenomenon of the device.

In order to further demonstrate the superiority of the proposed model over other existing MRE models, it is also compared with the classical Bouc-Wen model in terms of fitting curve, modeling error and running time. Similarly, the Bouc-Wen model is identified using the same experimental data, objective function, optimization algorithm (FFOA) and algorithm parameters as the proposed hyperbolic hysteresis model. Figure 3.23(e) gives the predicted responses from the Bouc-Wen model in the loading condition of the 4 Hz excitation with 3 A current level. The comparison results show that the Bouc-Wen model can provide the perfect agree-

Table 3.3 : Identification results for all the excitation conditions.

Excitation		Parameter	i (A)			
f (Hz)	E (mm)		0 A	1 A	2 A	3 A
1 Hz	2 mm	k_0	4.0958	8.2243	13.1275	23.2931
		c_0	0.3537	2.1711	3.7312	4.2844
		α_0	14.7934	15.2078	26.4769	29.0083
		β_0	0.0622	0.8185	0.8817	0.8720
	4 mm	k_0	2.9999	7.8168	11.8441	19.0549
		c_0	0.3329	1.5603	2.5673	3.0085
		α_0	4.4035	12.5352	29.8296	23.7437
		β_0	0.3036	0.5271	0.4771	0.5692
	8 mm	k_0	2.3289	2.7041	1.4534	15.011
		c_0	0.3062	1.181	1.9238	2.2723
		α_0	14.4578	24.4383	22.1404	21.4932
		β_0	0.1292	0.2838	0.3889	0.3532
2 Hz	2 mm	k_0	1.6444	18.4213	19.049	27.973
		c_0	0.2258	1.1576	1.9599	2.2876
		α_0	8.8277	23.8813	13.6024	24.0823
		β_0	0.4337	0.2823	1.1128	0.8684
	4 mm	k_0	2.6855	10.6519	14.9709	16.5911
		c_0	0.2127	0.8358	1.3552	1.5876
		α_0	11.8971	2.8526	17.5807	39.0569
		β_0	0.2063	0.8528	0.5698	0.4494
	8 mm	k_0	1.6707	9.8401	7.3621	13.9311
		c_0	0.1956	0.6410	1.0154	1.2077
		α_0	8.0351	1.8535	19.772	19.0687
		β_0	0.2562	0.5285	0.3659	0.3742
4 Hz	2 mm	k_0	2.7132	16.3818	21.0926	39.5461
		c_0	0.1464	0.6477	1.0629	1.2206
		α_0	5.5715	3.7949	31.8038	2.8777
		β_0	0.6492	1.2273	0.6403	1.7722
	4 mm	k_0	5.3159	14.9349	17.1666	27.248
		c_0	0.1384	0.4726	0.7372	0.8559
		α_0	5.0829	8.9217	6.6962	7.7418
		β_0	0.2159	0.3741	0.7907	0.7415
	8 mm	k_0	5.4541	5.1195	7.7478	12.457
		c_0	0.1277	0.3664	0.5604	0.6561
		α_0	2.8212	8.6349	21.760	30.503
		β_0	0.1833	0.3952	0.3472	0.3169
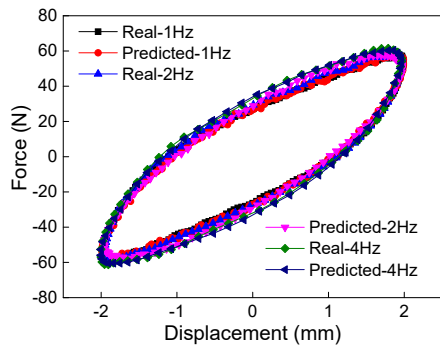
(a) Force-displacement loops
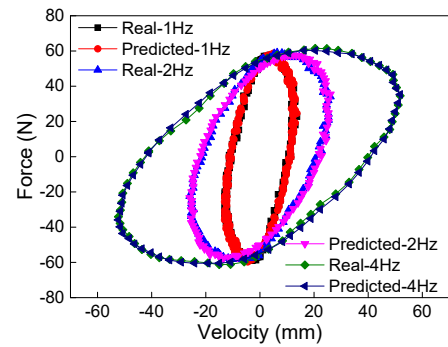
(b) Force-velocity loops
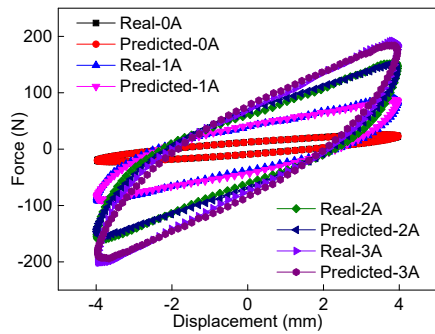
(c) Different driven currents
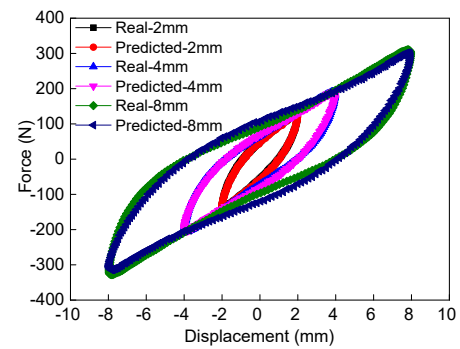
(d) Different loading amplitudes
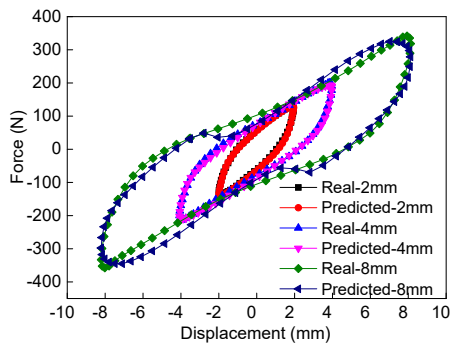
(e) f_{MR} vs x, $f = 4$ Hz, $i = 3$ A
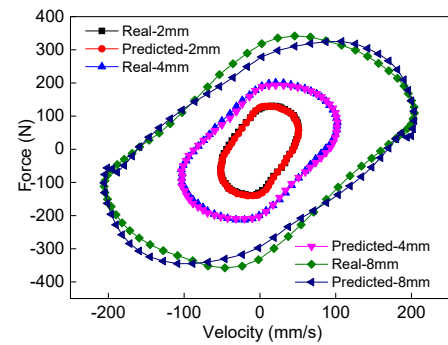
(f) f_{MR} vs $\dot{x}$, $f = 4$ Hz, $i = 3$ A

Figure 3.23 : $x = E\sin(2\pi ft)$; $i \in [0\ 3]$ A, $f \in [1\ 4]$ Hz, $E \in [2\ 8]$ mm.

ments with the experimental data under the condition of small amplitudes (2 mm and 4 mm). However, when the loading amplitude $E \geq 8$ mm, the Bouc-Wen model becomes less efficient as shown in Figure 3.23(f).

The RMS errors between shear forces acquired from the measurements and predictions from both Bouc-Wen and proposed models based on identified parameters are described in Figures 3.24(a) and (b). When no current or low current level is applied to the isolator, two models have the similar RMSEs. Nevertheless, with the increase of the current level, the proposed model shows the higher identification accuracy than the Bouc-Wen model. Figures 3.24(c) and (d) show the running time of both models for the parameter identification under different loading conditions. For each case, the running time descends with the increasing frequency. This is mainly because the complete hysteresis loops with different loading frequencies are made up of different numbers of sampling points. Besides, for the same loading condition, the Bouc-Wen model requires longer running time than the proposed model due to the high nonlinearity in the model together with more parameters to be identified. These results demonstrate that the proposed model is more accurate and efficient for modeling MRE.

The parameters identified from the proposed model with different loading conditions are grouped in accordance with applied current levels. The least square (LS) method is used to calculate these coefficients and the corresponding results are given in Appendix A.2. Finally, a generalized hyperbolic hysteresis model is built, the expression of which is given as follows

$$F = c_0(i)\dot{x} + k_0(i)x + \alpha(i) \cdot \frac{1 - e^{-2\beta(i)x}}{2e^{-\beta(i)x}} + F_0. \qquad (3.25)$$

To evaluate the performance of this generalized field-dependent model, comparative loops are shown in Figure 3.25, in which the measurements are obtained by loading device with the random excitation with maximal input amplitude of 4 mm and 1 A applied current. The comparison results demonstrate that the nonlinear behavior of the device is perfectly captured.

(a) Bouc-Wen model

(b) Proposed model

(c) Bouc-Wen model

(d) Proposed model
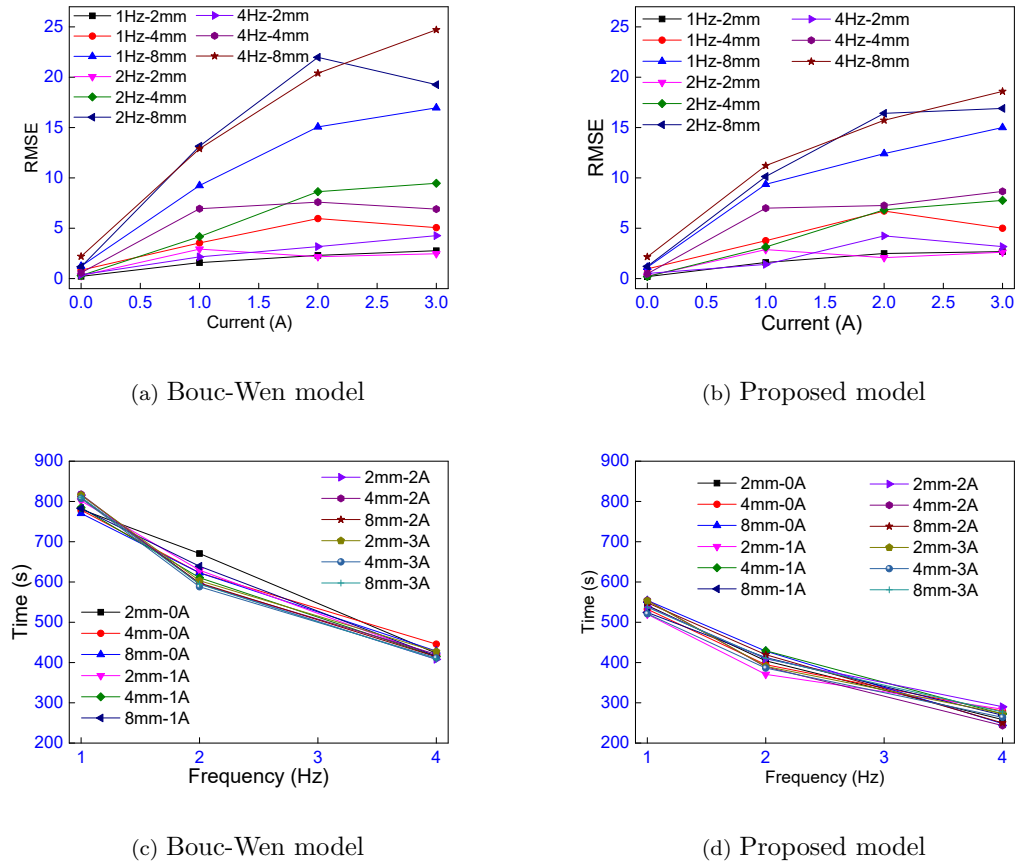
Figure 3.24 : RMSE and running time of model identification using FFOA.

3.5   Summary

This chapter has presented the experimental characterization and cyclic energy dissipation of a laboratory MRD for analysis of low-energy structures integrated with smart dampers. This work also developed novel multi-variable hysteresis models for semi-active structural members, namely smart pin joint using MR fluid and MRE. The curve fitting method is utilized through the combination of the hyperbolic function and Gaussian function for the torque-angular velocity responses of the MRP. For the model parameter identification, the IPSO is implemented due to its ability to deal with the premature convergence problem. Experimental data from a rotary pin joint are used to evaluate the performance of the proposed model.
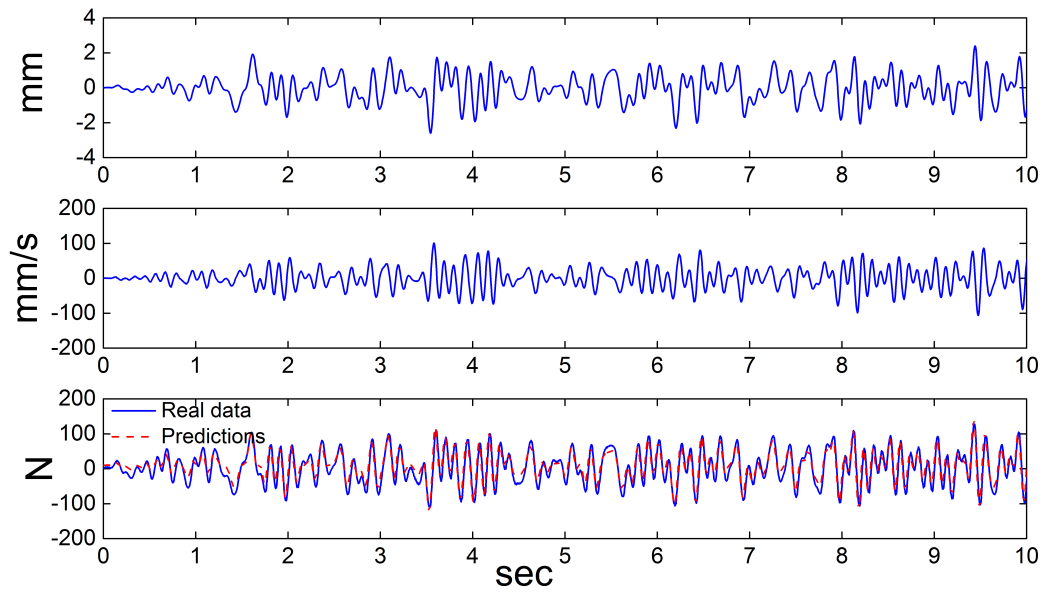
Figure 3.25 : Under random excitation and 1 A current level.

The results show that this model is effective in modeling the hysteretic and non-linear responses of the device with high accuracy. Furthermore, the immune PSO algorithm can avoid the local optimal solution in the process of parameter identification. A new hysteresis model has also been proposed to characterize the MRE base isolator, which is developed for seismic mitigation of building structures via semi-active control. This newly designed model is constituted by a nonlinear spring and a Voigt component connected in a parallel way with the benefits of fewer parameters and simpler expression without any differential equations, compared with classical Bouc-Wen model. Then, based on the experimental data, the model parameters are identified using FFOA, which can be summarized as the functions of applied current.

Chapter 4

Frequency-based modeling of MR devices

4.1 Introduction

One way to deal with a nonlinear system is to linearize it. The standard approach is small-signal linearization, which requires taking the derivative of each nonlinear term and using that slope as the gain of a linear term. However, this method can only illustrates the effects of small variations about the linearization point.

The describing function (DF) technique or the harmonic balance method is a mathematical approach for the design and analysis of systems containing single nonlinearity [81],[128]-[130]. The idea of the DF approach is to replace each nonlinear element with a (quasi) linear descriptor or DF whose gain is a function of input amplitude. As a function of the input excitation variables (stroke and frequency), the DF can be represented in three-dimension (3D) to interpret special properties of nonlinear systems and to allow for a design using frequency characteristics [131]. The DF methodology has been adopted to compute estimates of the amplitude and frequency of the harmonics in a smart actuator control system [132].

The hysteresis model can be considered as representations of nonlinear back-lash, whose DFs have been extensively investigated in [130]. In this chapter, the DF approach was applied to represent hysteresis by a gain and a phase. The DFs gain and phase are allowed to be amplitude E, frequency f, and current i dependent. From the characterizing data, obtained in the previous chapter, a look-up table (LUT) is formed to computationally obtain its DF showing the complicated hysteretic rheological process with respect to the excitation field. The Curve Fitting
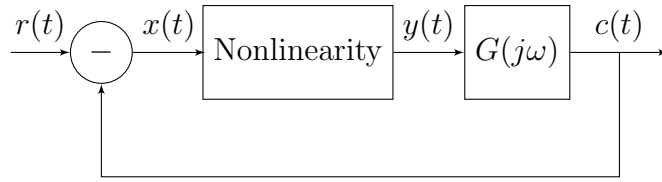
Figure 4.1 : Nonlinear feedback system for DF analysis.

Toolbox (*cftool*) in MATLAB/Simulink is utilized to determine the parameters of the proposed DF model. The fractional-order describing function (FDF) technique [128, 129] has also been applied to improve the fitting accuracy of these models.

4.2   Describing Function

Consider the nonlinear feedback system having one nonlinear element, a linear system with transfer function $G(s)$, the output $c(t)$ and unit feedback, see Figure 4.1 [81, 128]. The reference $r(t)$ is set to zero. Suppose that a sinusoidal signal, $x(t) = E \cos \omega t$, as input of the nonlinear element which is to be linearized. The output of the nonlinear element is a non-sinusoidal function:

$$y(t) = g(E \cos \omega t), \tag{4.1}$$

where E and $\omega = 2\pi f$ represent the amplitude and the angular frequency, respectively. However, $y(t)$ is periodic with the same period as the input and including higher-frequency harmonics besides the fundamental harmonic component. The periodic function $y(t)$ can be expanded by using the Fourier series:

$$y(t) = \sum_{n=1}^{\infty} Y_n \cos(n\omega t + \phi_n), \tag{4.2}$$

in which Y_n and ϕ_n; $n \in [1 \ \infty)$ are respectively the amplitude and the phase shift of the n-th harmonic. In the DF analysis, it is assumed that all the higher-frequency harmonics $Y_n \cos(n\omega t + \phi_n)$; $n \in [2 \ \infty)$ can be neglected as compared with the fundamental component $Y_1 \cos(\omega t + \phi_1)$. This assumption is often valid not only because the higher harmonics have smaller amplitude compared to the first harmonic,

but also most of the systems have low-pass properties, i.e., $|G(j\omega)| \gg |G(jn\omega)|$ for $n \in [2\ \infty)$.

The DF or sinusoidal DF can be defined as the complex ratio of the fundamental component of the nonlinear element by the sinusoidal input. This is given by

$$DF(E,\omega) = \frac{Y_1(E,\omega)e^{j\phi_1(E,\omega)}}{E}, \tag{4.3}$$

including a gain $|DF(E,\omega)| = N(E,\omega)$ and a phase $\angle DF(E,\omega) = \phi_1(E,\omega)$. Generally, the DF is a function of two variables, i.e., $DF(E,\omega)$ when the nonlinear element involves energy (storage or dissipation). Otherwise, the DF is single-valued, only amplitude dependent. The hysteresis of MRD depends also on the magnetization current i. Hence, the DF is amplitude, frequency and current dependent yielding gain $N(E,\omega,i)$ and phase $\phi(E,\omega,i)$. For two nonlinear elements connected in parallel, the DF can be calculated by the sum of the two individual DF, that is DF_1+DF_2. If two nonlinear elements are connected in series, then the DF is obtained by the corresponding DF denoted by DF_{12} where $DF_{12} \neq DF_1 \times DF_2$.

In the case that the nonlinearity is too complicated for an analytical form of (4.3), like the hysteresis of MRD addressed in this paper, the DF can be determined by simulation or numerical integration method. A MATLAB/Simulink computational diagram [131] can be used to implement the DF defined by

$$DF(E,\omega) = \frac{1}{\pi E} \int_0^{2\pi} g(E\cos\omega t)e^{-j\omega t}d\omega t, \tag{4.4}$$

where the current-dependent nonlinear relationship is available in a lookup table (LUT) obtained from characterization tests.

4.3   MRD Describing Function Model

Data recorded from characterization tests (reported in Section 3.2) are used in the computational implementation (4.4) to plot the 3D dependence of gain and phase

(a) $i = 1.25$ A

(b) $i = 1.5$ A

(c) $i = 1.75$ A

(d) $i = 2$ A
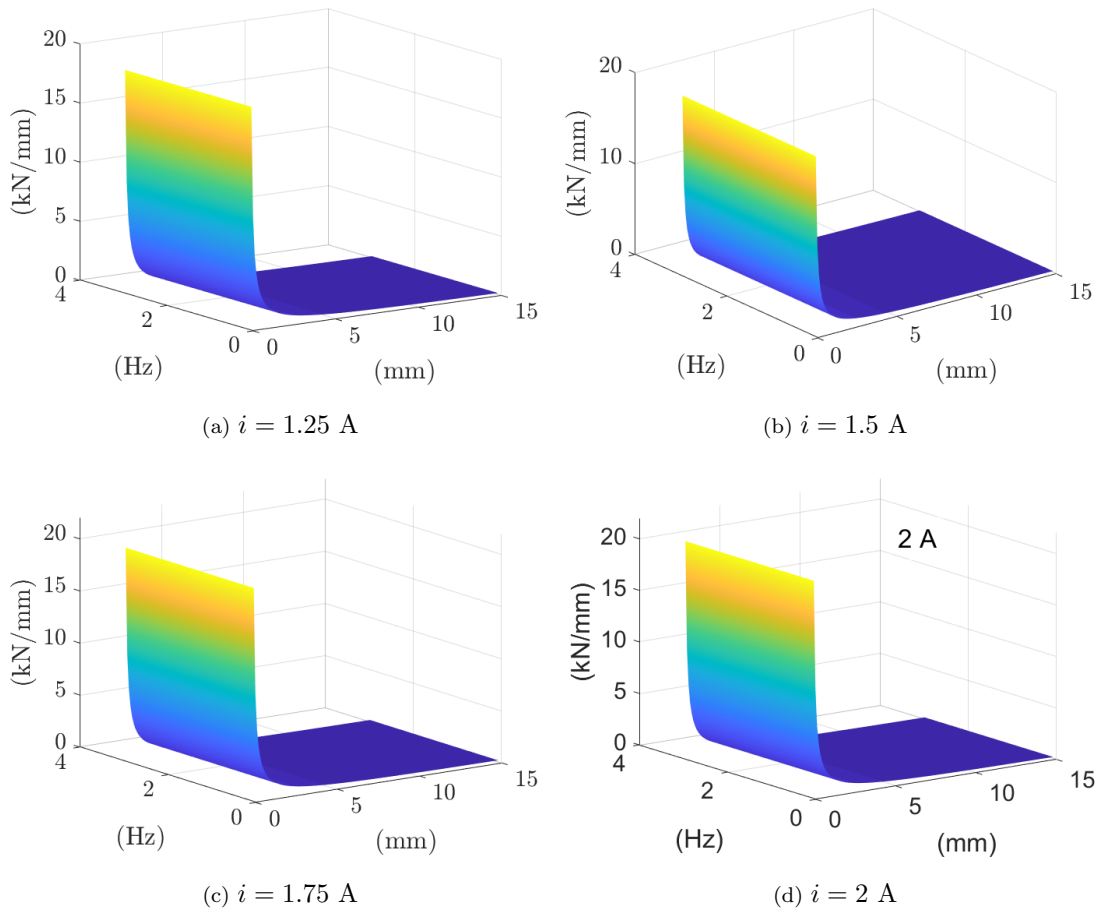
Figure 4.2 : DF gain for MRD hysteresis.

DFs. The magnitude and phase DFs for RD-8041-1 MRD are plotted in Figures 4.2 and 4.3 at different driven currents. In general, the gain $N_D(E, f, i)$ decreases as the amplitude E and/or frequency f increases. On the other hand, the DF gain of MRD increases with the magnetization i within its operational range. Since the DF is a complex quantity, i.e. $N_D e^{j\phi_D}$, DF of MRD exhibits a phase shift ϕ_D as shown in Figure 4.3.

To examine the influence of the external magnetic field on the smart device hysteresis, a family of the gain DFs against amplitude is plotted over the range of current i at $f=2$ Hz, as given in Figure 4.4. It is shown that at the damping force at the output increases substantially with an applied current in the interval $[0.25\ 2]$

(a) $i = 1.25$ A

(b) $i = 1.5$ A

(c) $i = 1.75$ A

(d) $i = 2$ A
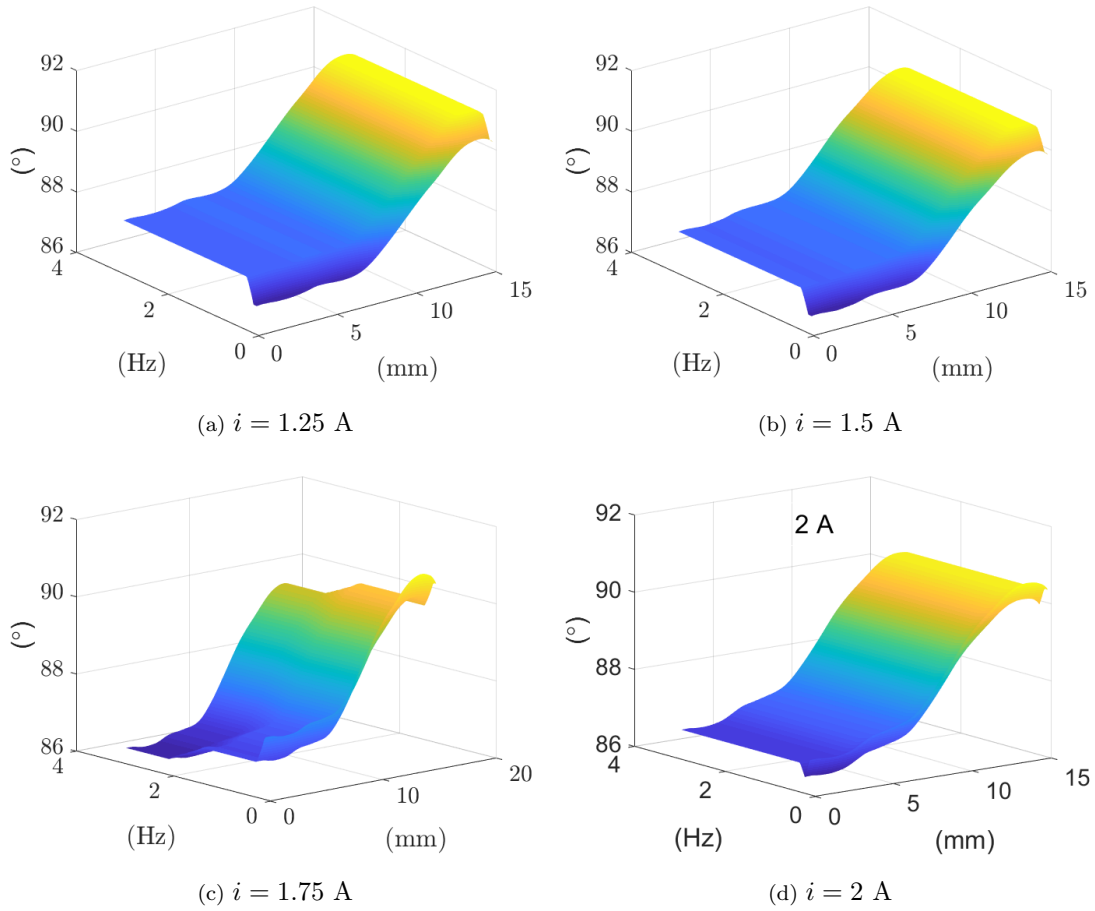
Figure 4.3 : DF phase for MRD hysteresis.

A at a damper stroke less than 12 mm in amplitude. A rational approximation technique yields the following expressions:

$$
\begin{aligned}
N_D(E,f,i) &= \frac{n_0 + n_1 i + n_2 i^2}{E + m_0 + m_1 f} = \frac{0.102 + 2.23i - 1.08i^2}{E - 0.33 + 0.04f}, \\
\phi_D(E,f,i) &= \frac{q_0 + q_1 i + q_2 i^2}{E + p_0 + p_1 f} = \frac{-0.7 + 7.6i - 2.9i^2}{E + 1.9 - 0.08f},
\end{aligned}
\tag{4.5}
$$

where $i \in [0\ 2]$ A, $f \in [0.1\ 3]$ Hz and displacement amplitude $E \in [0.1\ \ 20]$ mm. The goodness-of-fit for these parametric models are judged via R^2 and root-mean square of the error (RMSE) as given in Table 4.1.
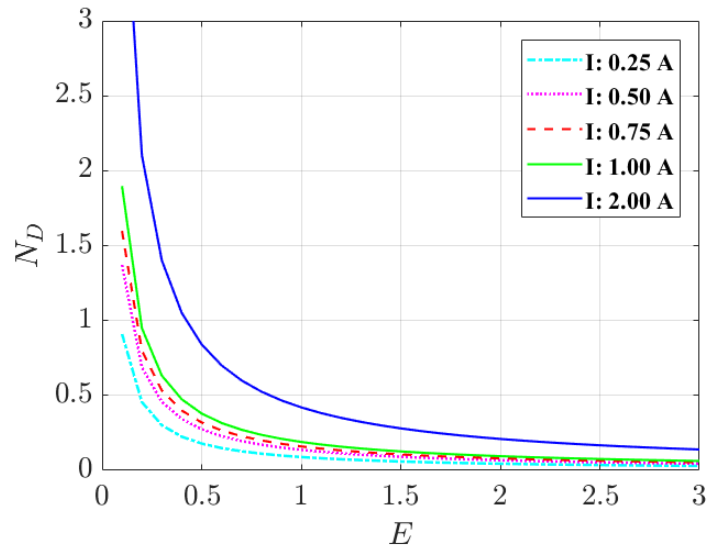
Figure 4.4 : N_D with different currents.

4.4 MRP Describing Function Model

Here, the sinusoidal input is the angular displacement excited by the shake table, and the output is the torque. From experimental data (reported in Section 3.3), the gain and phase DFs of the MRP are shown respectively in Figures 4.5(a) and (b). The input amplitude is normalized at 1.5° on the rotary shaft, corresponding to a 5.3 mm displacement of the plate motion. The gain and phase DFs of the MRP are generally decreasing with respect to the input amplitude. For the gain DF of hysteresis, the excitation frequency appears to have a minor effect on $N(E, f, i)$ as well as $\phi(E, f, i)$.

A family of the DF gain against amplitude with various magnetization currents is shown in Figure 4.5(c), where the DF gain, and hence damping capability of the smart pint joint, is quite uniformly dependent on the applied current in the operating range of less than 2.5 A. The results obtained indicate that the gain for the damping torque increases about 5 Nm/rad according to an increment of 0.5 A of the applied current at a sinusoidal excitation of amplitude 1.5° ($E = 1$ on Figure

(a) MRP DF gain

(b) MRP DF phase

(c) N_P with different currents.
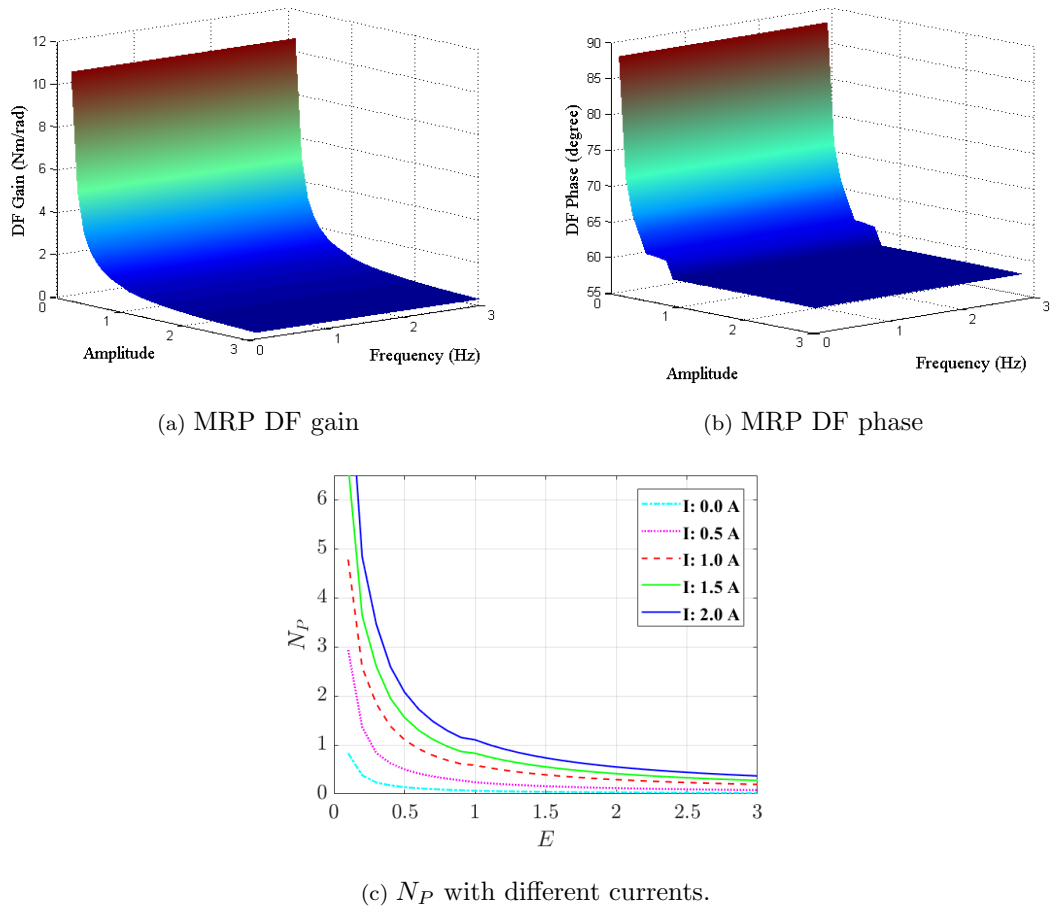
Figure 4.5 : Hysteresis DFs for smart pin joint.

4.5(c)). By curve fitting, the following gain (Nm per degree) and phase (in rad) describing functions, expressed explicitly of amplitude E, frequency f and current i, can be obtained with goodness-of-fit statistics listed in Table 4.1:

$$
\begin{aligned}
N_P(E, f, i) &= \frac{n_0 + n_1 i + n_2 i^2}{E + m_0 + m_1 f} = \frac{0.5 + 5.01i + 0.291i^2}{E - 0.028 + 0.027f}, \\
\phi_P(E, f, i) &= \frac{q_0 + q_1 i + q_2 i^2}{E + p_0 + p_1 f} = \frac{1.82 + 1.16i + 0.08i^2}{E + 0.08 + 0.14f},
\end{aligned}
\tag{4.6}
$$

where $i \in [0 \ \ 3]$ A, $f \in [0.1 \ \ 3]$ Hz, and angular amplitude $E_P \in [0.25° \ \ 4.5°]$.

4.5 MRE Describing Function Model

The prototypical MRE hysteresis DFs can be plotted using experimental data reported in Section 3.4, similarly as for the MRD and MRP. Figures 4.6(a) and

(a) MRE DF gain

(b) MRE DF phase

(c) N_E with different currents

(d) ϕ_E with different currents
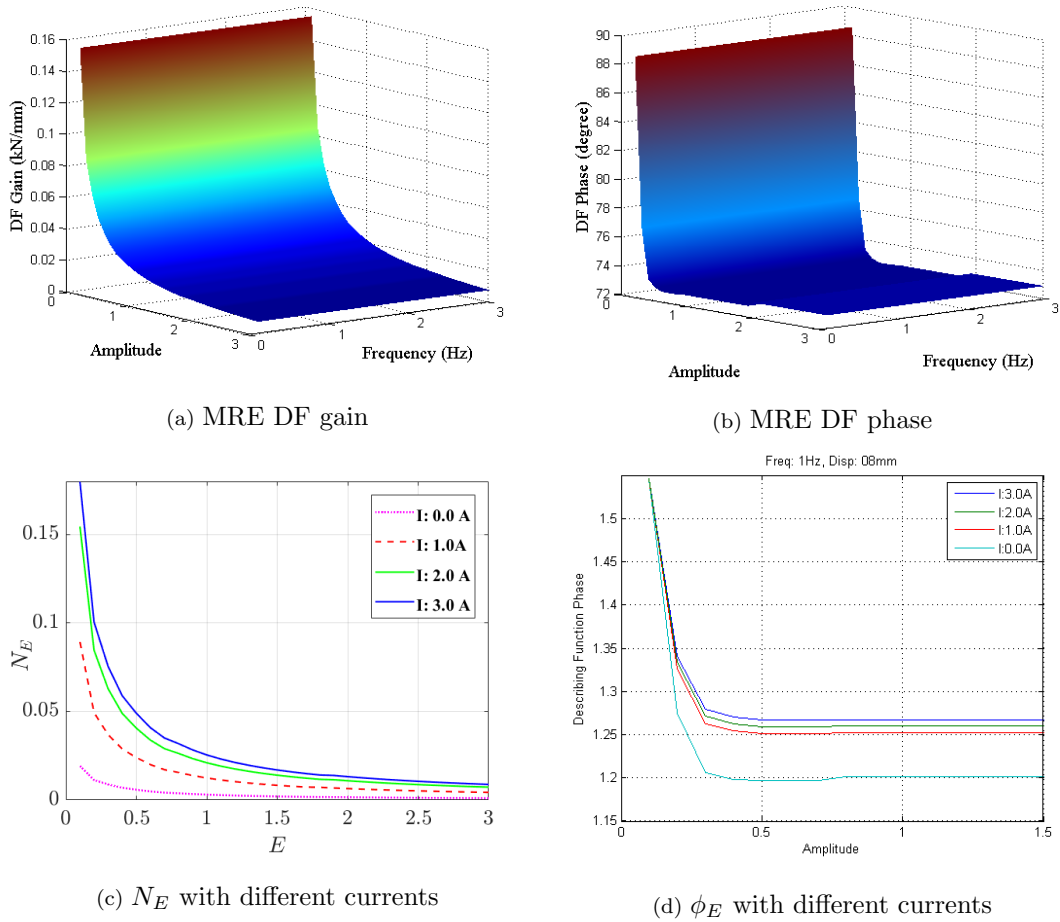
Figure 4.6 : Hysteresis DFs for MRE base isolator.

(b) present respectively the DFs gain and phase of the MRE hysteresis, where the amplitude is normalized at 8 mm per unit and the frequency is in Hz, and the magnetization current $i = 2$ A, corresponding to a magnetic flux density of around 0.28 T. The gain DF exhibiting a typical hyperbolic relation: the lower the amplitude the higher the gain. Within a reasonable range of magnetic field (0.2 T to 0.5 T), a high structural stiffness results from a significant increase of the MRE shear modulus. Consequently, the gain and phase DFs smoothly decrease with respect to the excitation amplitude. To examine the influence of the external magnetic field on the MRE hysteresis, the DFs gain and phase are plotted over a range of current i, as shown in Figures 4.6(c) and (d). The results shown are rather consistent with

Table 4.1 : Goodness-of-fit statistics.

DFs and FDF phase	R^2	RMSE
$N_D(E, f, i)$	0.9503	0.1193
$\phi_D(E, f, i)$	0.9083	0.8725
$N_P(E, f, i)$	0.9981	0.2872
$\phi_P(E, f, i)$	0.9245	0.3945
$N_E(E, f, i)$	0.9512	0.2156
$\phi_E(E, f, i)$	0.9039	0.2873
$\phi_D(\alpha, E, f, i); \ \alpha = 0.91$	0.9533	0.1172
$\phi_P(\alpha, E, f, i); \ \alpha = 0.95$	0.9746	0.0767
$\phi_E(\alpha, E, f, i); \ \alpha = 0.98$	0.9747	0.0845

those of MRD and MRP hysteresis. The following approximations of $N_E(E, f, i)$ and $\phi_E(E, f, i)$ are obtained as the gain and phase DFs for the smart device hysteresis by curve-fitting:

$$
\begin{aligned}
N_E(E, f, i) &= \frac{n_0 + n_1 i + n_2 i^2}{E + m_0 + m_1 f} = \frac{0.25 - 0.16i + 0.058i^2}{E + 0.06 - 0.02f}, \\
\phi_E(E, f, i) &= \frac{q_0 + q_1 i + q_2 i^2}{E + p_0 + p_1 f} = \frac{1.2 + 0.06i - 0.013i^2}{E - 0.086 + 0.01f},
\end{aligned}
\tag{4.7}
$$

where $i \in [0 \ \ 3]$ A, $f \in [0.1 \ \ 5]$ Hz, and displacement amplitude $E_E \in [0.5 \ \ 12]$ mm. The level of accuracy is determined by R^2 and RMSE as given in Table 4.1.

4.6 Fractional-Order DF and Comparison

From the fitness level given in Table 4.1, the DF gain of MR devices appear to achieve a better approximation for their characterized nonlinearity than the DF phase. Since the DF approach is an approximate technique, fractional calculus can be applied here as a mathematical tool to improve the accuracy of the approximated

frequency response of the nonlinearity using DFs. According to [128, 129], the integration in definition (4.4) can be generalized to a non-integer order α by

$$DF(\alpha, E, f, i) = \big[DF(E, f, i)\big]^{\alpha}, \ 0 < \alpha \leq 1. \tag{4.8}$$

By applying a one-dimensional (1D) search for the DF phase of the MR devices, we obtain the fractional order α for $\phi_D(E, f, i)$, $\phi_P(E, f, i)$ and $\phi_E(E, f, i)$ with improved goodness-fit statistics, in terms of R^2 and RMSE, as summarized in Table 4.1.

The proposed DFs are obtained based on our static models for MR device hysteresis. To show their validity, the DFs obtained are compared with the well-known hysteresis models. These include the Bouc-Wen and LuGre models, whose parameters are identified by using a genetic algorithm proposed in [67], and the static model obtained in [27]. Figure 4.7 shows the proposed gain DF (4.6) for MRP at several values of magnetization current in comparison, carried out considering the frequency responses, with those mentioned dynamic and static models for hysteresis. It can be seen that these curves are not much different, but the gain DF from the proposed model and the static model is slightly higher than that from Bouc-Wen and LuGre models since internal dynamics in the MR devices are not considered in our approach.

4.7 Summary

This chapter has presented the frequency based hysteresis modeling of smart devices, including the damper, pin joint and elastomer base isolator. Characterization data obtained display the current-dependent hysteretic relationships between the damping torque (force) and the rotary (linear) displacement. The describing function approach is applied to interpret this intrinsic current-dependent hysteretic dynamics of these devices by a gain and a phase. Approximate closed forms of
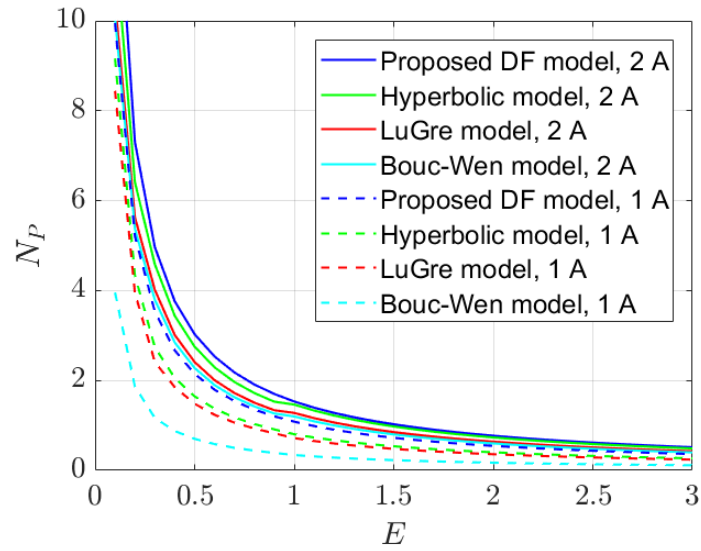
Figure 4.7 : Comparison of gain DFs for MRP hysteresis.

the DF gain and DF phase as functions of amplitude, frequency and current are then proposed using curve-fitting technique, to facilitate the semi-active structural system analysis in the frequency domain.

Chapter 5

Second-order Sliding Mode Control of Smart Structures Using MR Devices

5.1   Introduction

Magnetorheological (MR) material and corresponding devices have attracted widespread attention for their promising application in damping of structural vibrations and controlling the embodied energy level. The energy-dissipative MR device considered herein is a highly adaptive base isolator based on MR elastomer (MRE) material. Using the current-dependent model, developed in Chapter 3, a semi-active controller based on second-order sliding mode control (2SMC or SOSMC) is designed and utilized to provide a real-time feedback control of the device for structural vibration mitigation. The sliding mode methodology is adopted here to deal with intrinsic nonlinearity in the device's dynamic relation between I/O variables and achieve strong robustness of the control system against any dynamic loading sources and other uncertainties. A three-storey building model equipped with two field-controlled MR devices subjected to four benchmark earthquakes: EI-Centro, Kobe, Hachinohe and Northridge, is then used to validate the performance of the controller designed according to the proposed model. The results show that both inter-storey shift and acceleration are minimized therefore verifying the capability of the proposed method in vibration control for civil structures.

5.2 System Model

The n-degree-of-freedom (dof) smart structure integrated with energy-dissipative MREs can be portrayed as an n-storey building structure. The structural sketch of the building structure of mass M, lateral stiffness K, and viscous damping C configured with two identified adaptively tuned MREs is shown in Figure 5.1. The current-dependent MRE devices are rigidly installed underneath the base floor. Thus, the augmented model is an $(n + 1)$-dof system. We assume that the structural motion is sufficiently moderate that nonlinear effects can be neglected, the acceleration disturbance and its time derivative are bounded $\forall t \geq 0$, and $x, \dot{x}, \ddot{x}$ are available for on-line measurement.

Now, the floor motion equation can be written as

$$m_b\ddot{r}_b + c_b(\dot{r}_b - \dot{x}_g) - c_1(\dot{r}_1 - \dot{r}_b) + k_b(r_b - x_g) - k_1(r_1 - y_b) = f_b, \qquad (5.1)$$

where r_b is the absolute displacement of the base floor with respect to an inertial frame, x_g denotes the displacement of the ground that is induced by seismic-like ground acceleration $\ddot{x}_g$. Let $x_k = r_k - x_g$, $k = b, 1, \ldots, n$ describe the relative displacements between the ground and each mass, and contain the dof of the system. Thus, the motion equations of the structure can be written as

$$S_b : m_b\ddot{x}_b + (c_b + c_1)\dot{x}_b - c_1\dot{x}_1 + (k_b + k_1)x_b - k_1x_1 = f_b - m_b\ddot{x}_g$$

$$S_1 : m_1\ddot{x}_1 - c_1\dot{x}_b + (c_1 + c_2)\dot{x}_1 - c_2\dot{x}_2 - k_1x_b + (k_1 + k_2)x_1 - k_2x_2 = -m_1\ddot{x}_g$$

$$S_k : m_k\ddot{x}_k - c_k\dot{x}_{k-1} + (c_k + c_{k+1})\dot{x}_k - c_{k+1}\dot{x}_{k+1} - k_kx_{k-1} \qquad (5.2)$$

$$+ (k_k + k_{k+1})x_k - k_{k+1}x_{k+1} = -m_k\ddot{x}_g$$

$$S_n : m_n\ddot{x}_n - c_n\dot{x}_{n-1} + c_n\dot{x}_n - k_nx_{n-1} + k_nx_n = -m_n\ddot{x}_g.$$

The motion equations of the system can be rewritten in the following matrix form

$$M\ddot{x} + C\dot{x} + Kx = \Gamma f_\Sigma - M\ddot{x}_g, \ x \in \mathbb{R}^{n+1}, \qquad (5.3)$$
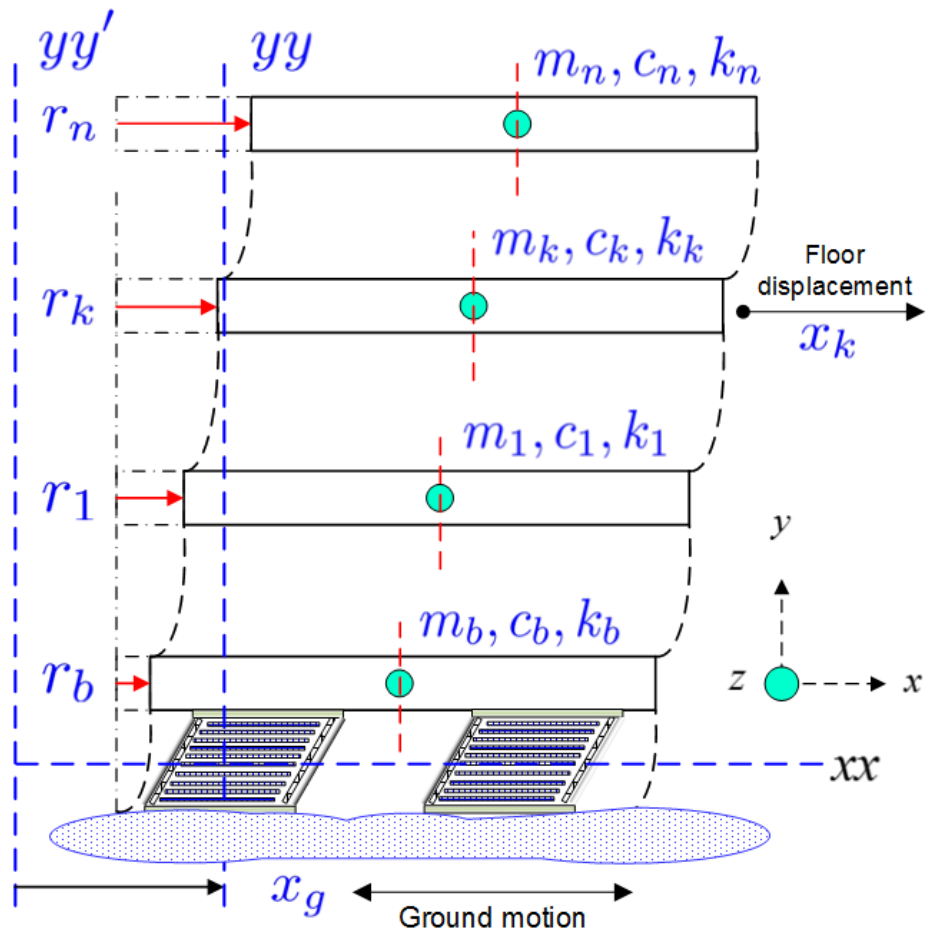
Figure 5.1 : Smart building integrated with MRE base isolators.

where M, C and K denote the mass, damping and stiffness matrices of the system structure, respectively, and can be given by

$$M = \begin{bmatrix} m_b & 0 & 0 & \cdots & 0 \\ 0 & m_1 & 0 & \cdots & 0 \\ 0 & 0 & m_2 & \cdots & 0 \\ \vdots & \vdots & \vdots & \ddots & \vdots \\ 0 & 0 & 0 & \cdots & m_n \end{bmatrix} = M^{\mathrm{T}} > 0,$$

$$C = \begin{bmatrix} c_b + c_1 & -c_1 & 0 & \cdots & \cdots & \cdots & 0 \\ -c_1 & c_1 + c_2 & -c_2 & 0 & \cdots & \cdots & 0 \\ 0 & -c_2 & c_2 + c_3 & -c_3 & \ddots & \cdots & 0 \\ \vdots & 0 & -c_3 & \ddots & \ddots & \ddots & \vdots \\ \vdots & \vdots & \ddots & \ddots & \ddots & -c_{n-1} & 0 \\ \vdots & \vdots & \vdots & \ddots & -c_{n-1} & c_{n-1} + c_n & -c_n \\ 0 & 0 & 0 & \cdots & 0 & -c_n & c_n \end{bmatrix} = C^{\mathrm{T}} \geq 0,$$

and

$$K = \begin{bmatrix} k_b + k_1 & -k_1 & 0 & \cdots & \cdots & \cdots & 0 \\ -k_1 & k_1 + k_2 & -k_2 & 0 & \cdots & \cdots & 0 \\ 0 & -k_2 & k_2 + k_3 & -k_3 & \ddots & \cdots & 0 \\ \vdots & 0 & -k_3 & \ddots & \ddots & \ddots & \vdots \\ \vdots & \vdots & \ddots & \ddots & \ddots & -k_{n-1} & 0 \\ \vdots & \vdots & \vdots & \ddots & -k_{n-1} & k_{n-1} + k_n & -k_n \\ 0 & 0 & 0 & \cdots & 0 & -k_n & k_n \end{bmatrix} = K^{\mathrm{T}} > 0.$$

$f_\Sigma \in \mathbb{R}^n$ denotes the total controllable MRE damping force vector. $\Gamma \in \mathbb{R}^{n \times n}$ is a factor matrix taking into account the location and number of MRE isolators in the structure. The MRE base isolator hyperbolic hysteresis model is

$$f_e = c_e \dot{x}_b + k_e x_b + \alpha \sinh(\beta_e x_b), \tag{5.4}$$

where $c_e = c_{e0} + c_{e1}i$, $k_e = k_{e0} + k_{e1}i$, $\alpha_e = \alpha_{e0} + \alpha_{e1}i$ and $\beta_e = \beta_{e0} + \beta_{e1}i$ [124].

Since the mass matrix is non-singular, (5.3) can be described by

$$\dot{q} = Aq + b(q, i) + D, \tag{5.5}$$

where $q = [x \ \dot{x}]^{\mathrm{T}}$ is a state vector, A represents the $2(n + 1) \times 2(n + 1)$ system matrix depending on the damping and stiffness of the structure, $b(q, i)$ is the non-affine function, and D is the $2(n + 1) \times 1$ disturbance matrix composed of model

uncertainties and external excitation. The first element of stiffness and damping matrices are $k_b + k_1 + 2k_{e0}$ and $c_b + c_1 + 2c_{e0}$, respectively, and all remaining entries are same as that in the matrices K and C.

5.3 SOSMC Design

The standard sliding surface which is the intersection of the hyperplanes defined in the plant states can be written as

$$\sigma = \rho x_b + \dot{x}_b, \tag{5.6}$$

where $\rho > 0$ is a design constant to be chosen to guarantee the closed-loop stability of the system (5.5). The first and second derivative of (5.6) along the trajectories of (5.5) give

$$\dot{\sigma}(t) = \rho \dot{x}_b + \ddot{x}_b, \ \ddot{\sigma}(t) = \rho \ddot{x}_b + \dddot{x}_b.$$

Now, the base floor equation of the system can be rewritten as

$$
\begin{aligned}
m_b \ddot{x}_b &+ (c_b + c_1)\dot{x}_b - c_1 \dot{x}_1 + (k_b + k_1)x_b - k_1 x_1 = -2(c_{e0} + c_{e1}i)\dot{x}_b \\
&- 2(k_{e0} + k_{e1}i)x_b - 2(\alpha_{e0} + \alpha_{e1}i)\sinh\left((\beta_{e0} + \beta_{e1}i)x_b\right) - m_b \ddot{x}_g.
\end{aligned} \tag{5.7}
$$

In the following, the control signal is defined as the time rate of applied current variation to the base isolated building model. We have

$$
\begin{aligned}
m_b \dddot{x}_b = &- (c_b + c_1 + 2c_{e0})\ddot{x}_b + c_1 \ddot{x}_1 - (k_b + k_1 + 2k_{e0})\dot{x}_b + k_1 \dot{x}_1 \\
&- 2(c_{e1}\ddot{x}_b + k_{e1}\dot{x}_b)i - 2(\alpha_{e0} + \alpha_{e1}i)\cosh\left(\beta_e x_b\right)\beta_e \dot{x}_b \\
&- 2\Big(c_{e1}\dot{x}_b + k_{e1}x_b + \alpha_{e1}\sinh\left((\beta_{e0} + \beta_{e1}i)x_b\right) \\
&+ \alpha_e \cosh\left((\beta_{e0} + \beta_{e1}i)x_b\right)\beta_{e1}x_b \Big)\frac{di}{dt} - m_b \dddot{x}_g.
\end{aligned} \tag{5.8}
$$

Hence, the second-order sliding variable is achieved as

$$\ddot{\sigma} = \Phi(t, x_b, i) + \Psi(t, x_b, i)\frac{di}{dt}, \tag{5.9}$$

where

$$\Phi(t, x_b, i) = -m_b^{-1}\Big((c_b + c_1 + 2c_{e0})\ddot{x}_b - c_1\ddot{x}_1 + (k_b + k_1 + 2k_{e0})\dot{x}_b - \\ k_1\dot{x}_1 + 2(c_{e1}\ddot{x}_b + k_{e1}\dot{x}_b)i + 2(\alpha_{e0} + \alpha_{e1}i)\cosh\big(\beta_e x_b\big)\beta_e\dot{x}_b + \\ \lambda\big((c_b + c_1 + 2c_{e0})\dot{x}_b - c_1\dot{x}_1 + (k_b + k_1 + 2k_{e0})x_b - k_1x_1 + \\ 2(c_{e1}\dot{x}_b + k_{e1}\dot{x}_b)i + 2\alpha_e\sinh(\beta_e x_b)\big)\Big) - \dddot{x}_g - \lambda\ddot{x}_g, \tag{5.10}$$

and

$$\Psi(t, x_b, i) = -2m_b^{-1}\Big((\alpha_{e0} + \alpha_{e1}i)\cosh\big(\beta_e x_b\big)\beta_{e1}x_b + c_{e1}\dot{x}_b + \\ k_{e1}x_b + \alpha_{e1}\sinh\big(\beta_e x_b\big)\Big). \tag{5.11}$$

Denoting $u = \frac{di}{dt}$ as the rate of change of MRE current and $\nabla = \frac{\partial}{\partial u}$, the following standard expression will be acquired:

$$\ddot{\sigma} = \Phi(t, x_b, i) + \Psi(t, x_b, i)u, \\ \Phi(t, x_b, i) = \ddot{\sigma}|_{u=0}, \quad \Psi(t, x_b, i) = \nabla\ddot{\sigma} \neq 0, \tag{5.12}$$

where Φ and Ψ meet the following global boundary condition with the concrete values of τ, ϑ_m and ϑ_M:

$$-\tau \leq \Phi(t, x_b, i) \leq \tau, \quad \forall t > 0, \\ 0 < \vartheta_m \leq \Psi(t, x_b, i) \leq \vartheta_M. \tag{5.13}$$

Equations (5.12) and (5.13) provide the following differential inclusion (DI) trajectories to zero for the finite-time convergence:

$$\ddot{\sigma} \in [-\tau, \ \tau] + [\vartheta_m, \ \vartheta_M]u. \tag{5.14}$$

Then, there exists a 2SMC, i.e.

$$u = \frac{di}{dt} = \phi(\sigma, \dot{\sigma}), \tag{5.15}$$

to steer the sliding function σ and its time derivative $\dot{\sigma}$ to 0 asymptotically. Since the DI (5.14), understood in the Filipov sense, insensitive to the original system (5.5), such the controller is obviously robust with respect to any perturbations preserving.

The actual current command to the MRE base isolator is bounded within the range of $0 \leq i \leq i_{\mathrm{M}}$. According to [22, 59], the control current $\kappa(t)$ can be achieved by integrating the feedback control signal $u(t)$. Here, a quasi-continuous controller is adopted, given as follows:

$$
u(t) = \begin{cases} \min[\epsilon, \ \max(-\epsilon, -\xi(\frac{\dot{\sigma}}{|\sigma|^{\frac{1}{2}}} + \mu \operatorname{sgn}(s)))], & \sigma \neq 0, \quad \kappa(t) \leq i_{\mathrm{M}}, \\ -\epsilon \operatorname{sgn}(\dot{\sigma}), & \sigma = 0, \quad \kappa(t) \leq i_{\mathrm{M}}, \\ 0, & \kappa(t) > i_{\mathrm{M}}. \end{cases} \quad (5.16)
$$

where ϵ, ξ and μ are positive constants and satisfy

$$
\rho \vartheta_m - \tau > \frac{\mu^2}{2}, \ \xi \mu > \rho.
$$

The control law (5.16) allows to increase the value of ξ to get closer to the parabola $\dot{s} + |s|^{\frac{1}{2}} \mu \operatorname{sgn}(s) = 0$ without increasing the control magnitude.

Here, due to power constraint and magnetic saturation, the force range of the smart devices is bounded by the maximum force at 2 A and the residual force at 0 A:

$$
i = \int u \, dt. \quad (5.17)
$$

Thereby, the integral state may be inconsistent with the smart device input. We here use a back-information antiwindup technique, in which the difference between the saturated and unsaturated output (control signal) is used to generate a feedback signal to act on the integrator input.

5.4 Simulation Results and Discussion

As an application example, a benchmark three-storey building model of mass M, lateral stiffness K, and viscous damping C configured with two identical MRE base isolators is considered. The current-dependent MRE devices are rigidly installed

underneath the base floor. The three-storey scaled building model parameters are

$$
M = \begin{bmatrix} 98.3 & 0 & 0 \\ 0 & 98.3 & 0 \\ 0 & 0 & 98.3 \end{bmatrix} \text{kg}, \ C = \begin{bmatrix} 175 & -50 & 0 \\ -50 & 100 & -50 \\ 0 & -50 & 50 \end{bmatrix} \text{Ns/m},
$$

$$
K = \begin{bmatrix} 12 & -6.84 & 0 \\ -6.84 & 13.8 & -6.84 \\ 0 & -6.84 & 6.84 \end{bmatrix} \times 10^5 \text{N/m}.
$$

(5.18)

Numerical values of the model parameters as functions of the applied current i are given in the following:

$$
c_e = c_{e0} + c_{e1}i = 339.6 + 576.7i,
$$

$$
k_e = k_{e0} + k_{e1}i = 3343.1 + 5816.1i,
$$

$$
\alpha_e = \alpha_{e0} + \alpha_{e1}i = 8.11 + 4.981i,
$$

$$
\beta_e = \beta_{e0} + \beta_{e1}i = 0.3463 + 0.1322i.
$$

To verify the effectiveness of the designed second order sliding mode controller, four benchmark earthquakes are also adopted to excite the smart structure in simulations, i.e., EI-Centro 1940, Hachinohe 1968, Northridge 1994 and Kobe 1995. Among four earthquake excitations, the former two are representatives of far-field earthquakes with medium ground movements while the latter two are near-field, more grievous seismic events. To make sure the fundamental frequency of smart structure with the main seismic frequency spectrum, the magnitude of four earthquake records are scaled down by 0.5. Accordingly, the passive structure responses would be greatly reinforcement so that the performance of the proposed method would be better verified.

Figure 5.2 illustrates time-history control signal changes of MRE base isolators during the seismic excitations. It is noticeable that all the applied currents continuously vary between 0 A and 2.5 A, which meets the maximum current limitation

(a) El-Centro

(b) Hachinohe

(c) Northridge

(d) Kobe
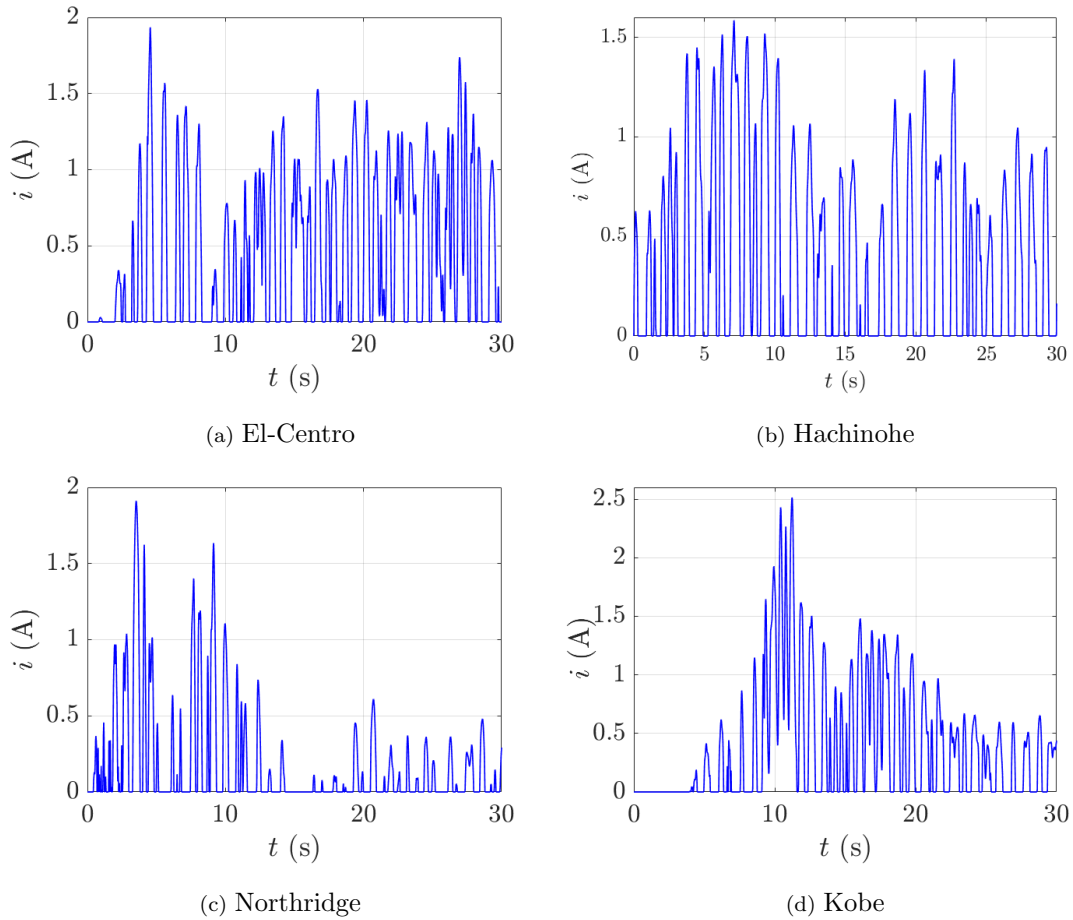
Figure 5.2 : Applied current signals under four earthquake excitations.

requirement ($i = 3$ A). It is mainly because the coils in the isolator will generate a massive source of heat when the isolator is supplied with varied currents, leading to unstable performance of the device.

Floor acceleration is one of the most important responses to represent the effectiveness of earthquake proof of the proposed smart isolation system. Generally, the floor acceleration ascends with the increasing of building level due to the first-mode of the structure subjected to the seismic excitations. As a result, the floor acceleration continuously ascends with the increase of structure level, which means that the maximum acceleration always happens at the top level of the structure. Hence, the acceleration change when the acceleration of the third floor arrives at its peak
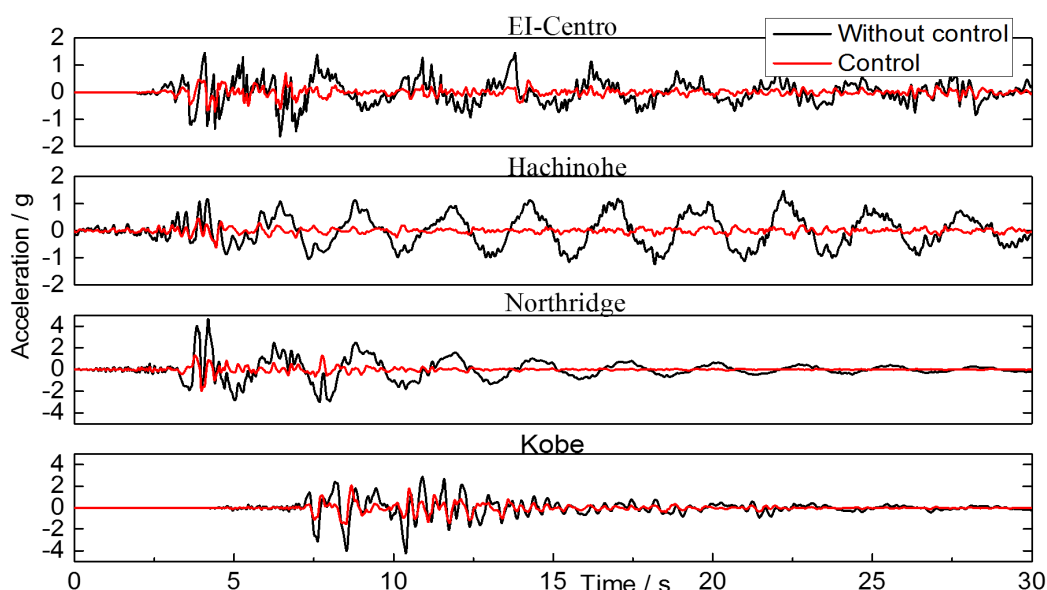
Figure 5.3 : Response comparisons between passive and controlled structures under four earthquake excitations.

value is employed as the evaluation index to assess the intensity of the vibration and deformation of the building. Figure 5.3 presents the time-series top floor acceleration comparison of smart structure with and without the proposed model-based control strategy under four benchmark seismic excitations. The black lines denote the responses of smart structure without control while the red solid line illustrates the responses of smart building with the controller based on the proposed model. From the results in figure, it is clearly seen that with the semi-active control strategy based on the proposed model, the structure is able to remarkably reduce the acceleration responses for all the seismic cases. Especially for El-Centro and Hachinohe earthquakes, the smart structure with the controller is shown more useful than passive structure in restraining the structure vibration.

Apart from the time historical acceleration at the top floor, both inter-storey drift and peak acceleration of all the floors are also significant indices in describing the effectiveness of the controller based on the proposed model. Floor peak acceleration
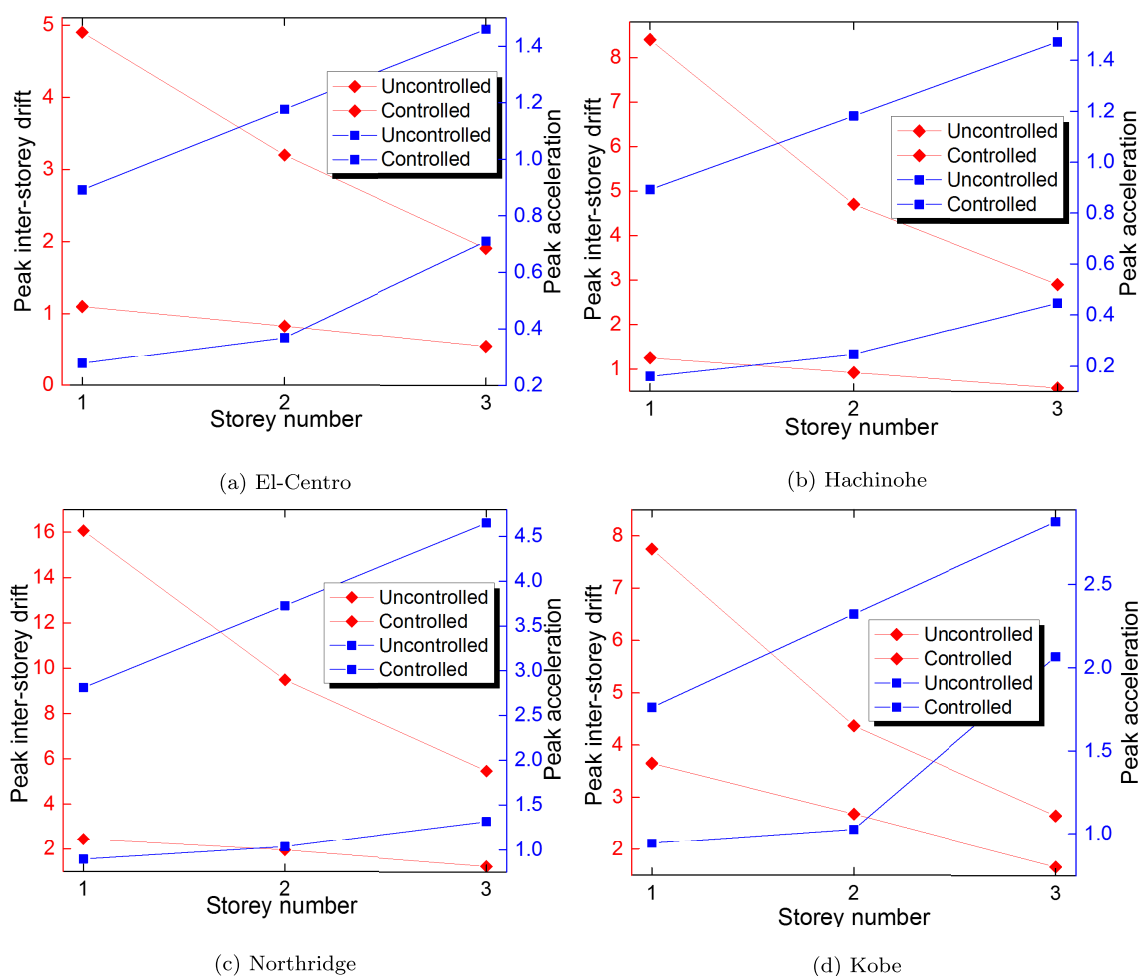
Figure 5.4 : Comparisons of inter-storey drift and peak acceleration at each floor between passive and control structures.

is capable of providing a rough structure configuration with most serious vibration while the inter-storey drift at each floor represents the deformation degree between two neighboring levels.

Figure 5.4 compares both inter-storey drift and peak acceleration of all the floors between passive and controlled smart structure under four earthquake excitations. It is obvious that the floor peak acceleration always rise with the structure height while the inter-storey drift shows the dropping relationship with the floor for all the cases of earthquakes, which accords with previous analysis. Another noteworthy result is that compared with passive structure, the controlled one changes relatively less

in terms of two indices at all floors. These comparisons sufficiently prove that the MRE base isolator together with semi-active control based on proposed model has a promising application prospect in protection and vibration mitigation of building structure.

5.5   Summary

A second-order sliding mode controller, based on the field-dependent model, is proposed to implement semi-active control of MRE isolator. To evaluate its effectiveness, a numerical study was conducted using a three-storey benchmark building model as well as four commonly used seismic excitations. The analysis results showed that the controlled smart structure using the proposed method outperforms the passive structure in terms of floor acceleration and inter-storey drift.

Chapter 6

Frequency-Shaped Structural Control

6.1 Introduction

The dynamic behavior of the structures are characterized by their frequency response functions (FRFs). External dynamic loadings such as seismic events, strong winds and vibration shocks can also be represented in the frequency domain by their power spectral density functions. Thus, frequency domain control approaches allow the designer to deal with these representations of the structural model and excitation, and roll off the control action at high frequencies as well as to specify the disturbance attenuation over the desired frequency range during control design.

While structural FRFs are important for structural control and health monitoring [102], they have a limitation due to inherent nonlinearity of the smart devices embedded in the structure. Therefore, the describing function (DF) model (developed in Chapter 4) is utilized and frequency shaped sliding mode control (FSSMC) is developed to achieve structural resilience and sustainability against nonlinearities, modeling uncertainties and disturbances from dynamic loadings. Simulations are reported for a three-story building model integrated with two identical current-dependent magnetorheological (MR) dampers (MRDs) subject to one dimensional quake-induced vibration to investigate lateral dynamic responses as produced by earthquakes or strong winds.

In the second part of this chapter, design of a frequency-shaped second-order sliding mode controller (FS2SMC) is demonstrated. The second-order sliding mode control method has been adopted here to directly adjust the structural frequency

response and improve robustness performance. The sliding surface is obtained by exploiting a second-order low-pass filter (LPF) to shape the frequency characteristics of the equivalent dynamics. The proposed technique is numerically verified in a half-car model (HCM) with inbuilt active hydraulically interconnected suspension (HIS) system for reducing the roll angle while adjusting the spectrum to prevent natural modes of the structure under external excitations.

6.2   Modeling in the Frequency Domain

Following describes the modeling of current-driven MR device integrated smart structures in the frequency domain. At first, we diagonalized the system matrices via a modal decomposition to obtain a set of n second-order systems in modal coordinates. Then, current-dependent DFs of MR devices are adopted to configure FRFs of displacement.

6.2.1   Modal decomposition

Coupled motion equations

Consider an n degree-of-freedom (dof) structure embedded with n intelligent energy-dissipation devices. The smart structure integrated with auxiliary robust damping devices can be depicted typically in a building structure as shown in Figure 6.1. The n dof structure has n natural frequencies and n modal vectors. The equations of motion of the system can always be arranged as a set of n coupled second-order ordinary differential equations (ODEs) in the shear mode by

$$M\ddot{x}(t) + C\dot{x}(t) + Kx(t) = \Gamma f_{\mathrm{MR}}(x, i) + f_d(t), \qquad (6.1)$$

with zero initial condition $x(t_0) = 0$. Here, $x(t) = [x_1, x_2, \ldots, x_n]^{\mathrm{T}}$ is an n vector with $x_k(t)$ being the structure displacement of a designated level unit; subscript $(_k)$ refer to the designated floor/unit. $\dot{x}$ and $\ddot{x}$ are respectively the velocity and

acceleration array both with n elements. M, C and K are respectively, the mass, damping and stiffness matrices of dimension $n \times n$ and can be given by

$$M = \text{diag}\,(m_k) = M^{\mathrm{T}} > 0; \; k = 1, 2, \ldots, n,$$

$$C = \begin{bmatrix} c_1 + c_2 & -c_2 & 0 & \cdots & \cdots & 0 \\ -c_2 & c_2 + c_3 & -c_3 & 0 & \cdots & 0 \\ 0 & -c_3 & c_3 + c_4 & \ddots & \ddots & \vdots \\ \vdots & 0 & \ddots & \ddots & \ddots & 0 \\ \vdots & \vdots & \ddots & -c_{n-1} & c_{n-1} + c_n & -c_n \\ 0 & 0 & 0 & 0 & -c_n & c_n \end{bmatrix} = C^{\mathrm{T}} \geq 0,$$

and

$$K = \begin{bmatrix} k_1 + k_2 & -k_2 & 0 & \cdots & \cdots & 0 \\ -k_2 & k_2 + k_3 & -k_3 & 0 & \cdots & 0 \\ 0 & -k_3 & k_3 + k_4 & \ddots & \ddots & \vdots \\ \vdots & 0 & \ddots & \ddots & \ddots & 0 \\ \vdots & \vdots & \ddots & -k_{n-1} & k_{n-1} + k_n & -k_n \\ 0 & 0 & 0 & 0 & -k_n & k_n \end{bmatrix} = K^{\mathrm{T}} > 0,$$

where coefficients m_k, c_k and k_k are the k-th unit lumped mass, lateral damping and stiffness, respectively. Factor matrix

$$\Gamma = \begin{bmatrix} \vartheta\gamma_1 & 0 & 0 & \cdots & 0 \\ 0 & \vartheta\gamma_2 & 0 & \cdots & 0 \\ 0 & 0 & \vartheta\gamma_3 & \cdots & 0 \\ \vdots & \vdots & \vdots & \ddots & \vdots \\ 0 & 0 & 0 & \cdots & \vartheta\gamma_n \end{bmatrix} \in \mathbb{R}^{n \times n},$$

represents the location and number of the auxiliary intelligent devices in the structure. ϑ denotes the number of smart devices mounted on each unit and $\gamma_k = 1$ (or 0) if the device is (or is not) attached at the designated unit; $k = 1, 2, \ldots, n.$
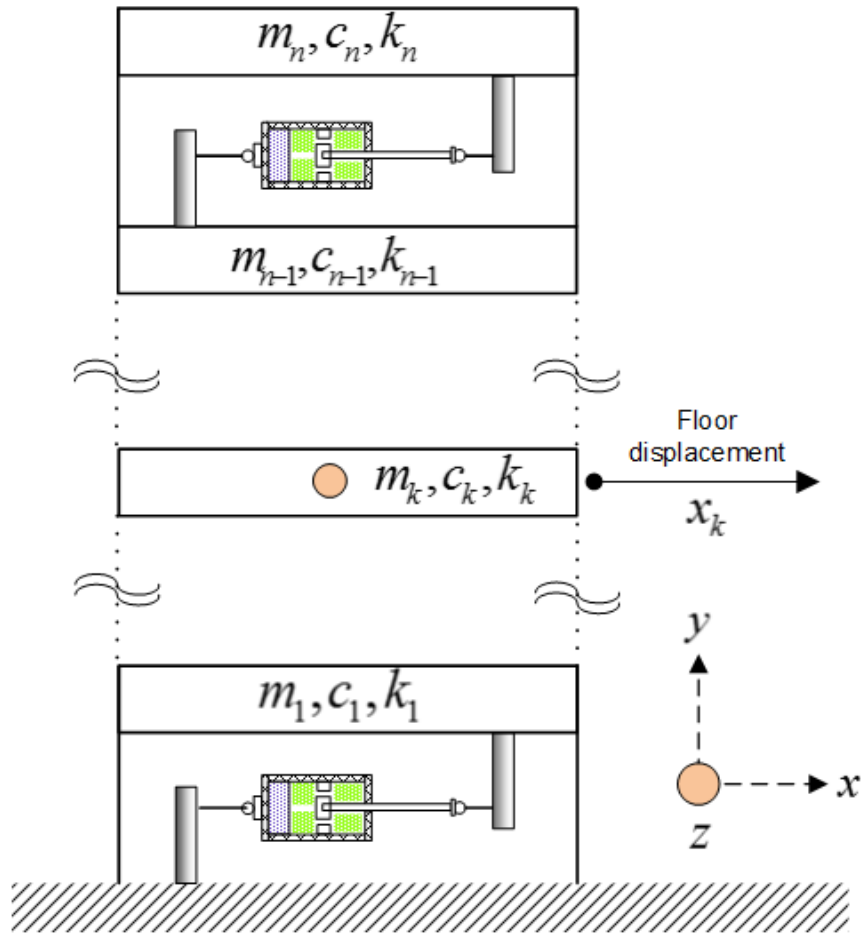
Figure 6.1 : Schematic diagram of the smart structure integrated with auxiliary robust damping devices.

$f_{\mathrm{MR}}(x, i) \in \mathbb{R}^n$ is the damping force vector due to the nonlinear MR device. $f_d(t)$ is the disturbance array with n elements from external dynamic loadings.

Suppose the model (6.1) satisfies the following assumptions:

($A7.1.$) the structure's M is invertible and $M^{-1}K$ has a set of n linearly independent eigenvectors $v_1, v_2, \ldots, v_n$, i.e., all the n eigenvalues $\lambda_k(M^{-1}K)$, $1 \le k \le n$, are distinct and positive.

($A7.2.$) $x \in \mathbb{R}^n, \dot{x} \in \mathbb{R}^n$ and $\ddot{x} \in \mathbb{R}^n$ are available for on-line measurement and

($A7.3.$) the unknown dynamic disturbance $f_d(t)$ and its time-derivative are

bounded for $t \in [t_0 \; \infty)$,

Since the mass matrix is a nonsingular matrix, we multiply (6.1) from the left by M inverse results in

$$\ddot{x} + M^{-1}C\dot{x} + M^{-1}Kx = M^{-1}\Gamma f_{\mathrm{MR}} + M^{-1}f_d. \tag{6.2}$$

The matrix $M^{-1}K$ can be diagonalized as

$$\begin{bmatrix} \frac{k_1+k_2}{m_1} & \frac{-k_2}{m_1} & 0 & \cdots & \cdots & \cdots & 0 \\ \frac{-k_2}{m_2} & \frac{k_2+k_3}{m_2} & \frac{-k_3}{m_2} & 0 & \cdots & \cdots & 0 \\ 0 & \frac{-k_3}{m_3} & \frac{k_3+k_4}{m_3} & \frac{-k_4}{m_3} & \ddots & \cdots & 0 \\ \vdots & 0 & \frac{-k_4}{m_4} & \ddots & \ddots & \ddots & \vdots \\ \vdots & \vdots & \ddots & \ddots & \ddots & \frac{-k_{n-1}}{m_{n-2}} & 0 \\ \vdots & \vdots & \vdots & \ddots & \frac{-k_{n-1}}{m_{n-1}} & \frac{k_{n-1}+k_n}{m_{n-1}} & \frac{-k_n}{m_{n-1}} \\ 0 & 0 & 0 & \cdots & 0 & \frac{-k_n}{m_n} & \frac{k_n}{m_n} \end{bmatrix} = \Phi\Lambda\Phi^{-1}, \tag{6.3}$$

where the orthogonal matrix $\Phi \in \mathbb{R}^{n \times n}$ is the column-wise concatenation of the mode-shape or eigenvectors and the diagonal matrix $\Lambda \in \mathbb{R}^{n \times n}$ is listing the n squared frequencies. The modal transformation matrix Φ and diagonal frequency matrix Λ are given by

$$\Phi = \begin{bmatrix} | & | & \cdots & | \\ v_1 & v_2 & \cdots & v_n \\ | & | & \cdots & | \end{bmatrix} = \begin{bmatrix} v_{11} & v_{12} & \cdots & v_{1n} \\ v_{21} & v_{22} & \cdots & v_{2n} \\ \vdots & \vdots & \ddots & \vdots \\ v_{n1} & v_{n2} & \cdots & v_{nn} \end{bmatrix},$$

$$\Lambda = \begin{bmatrix} \lambda_1 & 0 & 0 & \cdots & 0 \\ 0 & \lambda_2 & 0 & \cdots & 0 \\ 0 & 0 & \lambda_3 & \cdots & 0 \\ \vdots & \vdots & \vdots & \ddots & \vdots \\ 0 & 0 & 0 & \cdots & \lambda_n \end{bmatrix} = \begin{bmatrix} \omega_1^2 & 0 & 0 & \cdots & 0 \\ 0 & \omega_2^2 & 0 & \cdots & 0 \\ 0 & 0 & \omega_3^2 & \cdots & 0 \\ \vdots & \vdots & \vdots & \ddots & \vdots \\ 0 & 0 & 0 & \cdots & \omega_n^2 \end{bmatrix},$$

where ω_k is the umdamped ($C = \mathbf{0}^{n \times n}$) natural frequency of the k-th mode.

Modal coordinates & decoupled second-order ODEs

Since the set of eigenvectors occupies the n-dimensional space of $x(t)$, therefor $x(t)$ can be expressed as a weighted linear combination of the natural mode vectors:

$$
\begin{bmatrix} x_1 \\ x_2 \\ \vdots \\ x_n \end{bmatrix} = \begin{bmatrix} \upsilon_{11} & \upsilon_{12} & \cdots & \upsilon_{1n} \\ \upsilon_{21} & \upsilon_{22} & \cdots & \upsilon_{2n} \\ \vdots & \vdots & \ddots & \vdots \\ \upsilon_{n1} & \upsilon_{n2} & \cdots & \upsilon_{nn} \end{bmatrix} \begin{bmatrix} q_1 \\ q_2 \\ \vdots \\ q_n \end{bmatrix},
\tag{6.4}
$$

$$
\Rightarrow \; x = \sum_{k=1}^{n} \upsilon_k q_k = \Phi q,
$$

$$
\therefore \; q(t) = \Phi^{-1} x(t),
$$

where $q(t) = [q_1, q_2, \ldots, q_n]^{\mathrm{T}}$ is an n vector of the modal coordinate.

Substituting (6.4) into (6.2) yields

$$
\Phi \ddot{q} + M^{-1} C \Phi \dot{q} + \Phi \Lambda \Phi^{-1} \Phi q = M^{-1} \Gamma f_{MR} + M^{-1} f_d
$$

$$
\Rightarrow \ddot{q} + \Phi^{-1} M^{-1} C \Phi \dot{q} + \Lambda q = \Omega f_{\mathrm{MR}} + \Phi^{-1} M^{-1} f_d,
\tag{6.5}
$$

where $\Phi^{-1} M^{-1} \Gamma f_{\mathrm{MR}} = \Omega f_{\mathrm{MR}}$ is denoted as the modal control u.

The damping matrix $\Phi^{-1} M^{-1} C \Phi$ can be assembled by a matrix that is proportional to mass and stiffness,

$$
C = \alpha M + \beta K,
$$

known as Rayleigh or proportional damping [31, 33]. Real scalars α and β are related to damping ratios and frequencies by

$$
\zeta_k = \frac{\alpha}{2\omega_k} + \frac{\beta \omega_k}{2},
$$

where ζ_k is the damping ratio of the k-th mode of vibration. The principal diagonals entry of the damping matrix are

$$
\Phi^{-1} M^{-1} C \Phi_{(kk)} = 2\zeta_k \omega_k
$$

and the modal coupling kr-th elements are assumed as

$$\Phi^{-1}M^{-1}C\Phi_{(kr)} = \mu_{kr}, \ r \neq k, \ 1 \leq (k,r) \leq n.$$

Applying modal transformation, a set of n second-order motion equations decoupled from (6.1) of $2n$-th order can be obtained for each mode k:

$$\ddot{q}_k + 2\zeta_k\omega_k\dot{q}_k + \sum_{r=1,r\neq k}^{n} \mu_{kr}\dot{q}_r + \omega_k^2 q_k = u_k + d_k, \tag{6.6}$$

where d_k represents the k-th elements of the disturbance force vector:

$$d_k = \Phi^{-1}M^{-1}f_d = \Phi^{-1}M^{-1}\Phi\Phi^{-1}f_d = \left[\operatorname{diag}\left(1/m_k\right)\right]\Phi^{-1}f_d. \tag{6.7}$$

6.2.2   Frequency response function

In this section, the hysteretic MR device is replaced by its obtained DF: magnitude $N(E, f, i)$ and phase $\phi(E, f, i)$. We encapsulate the DF model into the system dynamics to obtain responses of MR device-based smart structure in the frequency domain.

Describing function matrix

The MR device hysteresis DFs gain and phase construct a matrix $DF_{\mathrm{MR}} \in \mathbb{C}^{n \times n}$:

$$DF_{\mathrm{MR}} = \begin{bmatrix} \vartheta\gamma_1 N_1 e^{j\phi_1} & \varepsilon_{12} & \varepsilon_{13} & \cdots & \varepsilon_{1n} \\ \varepsilon_{21} & \vartheta\gamma_2 N_2 e^{j\phi_2} & \varepsilon_{23} & \cdots & \varepsilon_{2n} \\ \varepsilon_{31} & \varepsilon_{32} & \vartheta\gamma_3 N_3 e^{j\phi_3} & \cdots & \varepsilon_{3n} \\ \vdots & \vdots & \vdots & \ddots & \vdots \\ \varepsilon_{n1} & \varepsilon_{n2} & \varepsilon_{n3} & \cdots & \vartheta\gamma_n N_n e^{j\phi_n} \end{bmatrix},$$

whose principal diagonal terms

$$DF_{\mathrm{MR}(kk)} = \vartheta\gamma_k N_k e^{j\phi_k}$$

referred to each dof of the structure and off-diagonal components

$$DF_{\mathrm{MR}(kr)} = \varepsilon_{kr} \geq 0, \ r \neq k, \ 1 \leq (k,r) \leq n,$$

represent inter-storey, between the k-th and $(k-1)$-th storeys, damping from smart devices mounted at other storeys. Notably,

$$\varepsilon_{kr} \in [0 \quad \vartheta\gamma_k N_k e^{j\phi_k}]$$

are generally much less than or equal to the k-th diagonal term. Since the damping capability is always predominant at the level where these devices are installed, the DF_{MR} can be considered as diagonally dominant listing only terms $\vartheta\gamma_k N_k e^{j\phi_k}$ and some of the coupling effect from the residual modes due to modal decomposition errors can be reduced implicitly by encompassing it as a part of disturbance d_k (6.7).

Transfer function matrix

When the applied excitation harmonic with an angular frequency ω, the controlled MR devices can be modelled in the frequency domain as $DF_{\mathrm{MR}}Q(j\omega) \in \mathbb{C}^n$

$$\Gamma f_{\mathrm{MR}}(q,i) \rightarrow \begin{bmatrix} \vartheta\gamma_1 N_1 e^{j\phi_1} & \varepsilon_{12} & \varepsilon_{13} & \cdots & \varepsilon_{1n} \\ \varepsilon_{21} & \vartheta\gamma_2 N_2 e^{j\phi_2} & \varepsilon_{23} & \cdots & \varepsilon_{2n} \\ \varepsilon_{31} & \varepsilon_{32} & \vartheta\gamma_3 N_3 e^{j\phi_3} & \cdots & \varepsilon_{3n} \\ \vdots & \vdots & \vdots & \ddots & \vdots \\ \varepsilon_{n1} & \varepsilon_{n2} & \varepsilon_{n3} & \cdots & \vartheta\gamma_n N_n e^{j\phi_n} \end{bmatrix} \begin{bmatrix} q_1(j\omega) \\ q_2(j\omega) \\ q_3(j\omega) \\ \vdots \\ q_n(j\omega) \end{bmatrix}. \tag{6.8}$$

Thus,

$$\left[-\omega^2 + 2j\omega\zeta_k\omega_k + \omega_k^2 \right] q_k(j\omega) + \sum_{r=1, r\neq k}^{n} \mu_{kr} j\omega q_r(j\omega) = -$$
$$\left[\frac{\vartheta\gamma_k N_k e^{j\phi_k}}{m_k} q_k(j\omega) + \sum_{r=1, r\neq k}^{n} \frac{\varepsilon_{kr}}{m_k} q_r(j\omega) \right] + \Upsilon F_d(j\omega), \tag{6.9}$$

where $\Phi^{-1}M^{-1}$ is denoted by Υ.

Equation (6.9) can be written as

$$\left[-\omega^2 + 2j\omega\zeta_k\omega_k + \omega_k^2 + \frac{\vartheta\gamma_k N_k e^{j\phi_k}}{m_k} \right]\Phi^{-1}x_k(j\omega)$$

$$+ \left[\sum_{r=1,r\neq k}^{n} \mu_{kr}j\omega + \sum_{r=1,r\neq k}^{n} \frac{\varepsilon_{kr}}{m_k} \right]\Phi^{-1}x_r(j\omega) = \Upsilon F_d(j\omega). \quad (6.10)$$

The frequency response function (FRF) matrix of displacement $F_d(j\omega) \to X(j\omega)$ can be derived from the relation

$$X(j\omega) = H(j\omega)F_d(j\omega),$$

where $H(j\omega)$ is the FRF matrix of displacement.

Taking the assumption of Rayleigh damping [31, 33] yields:

$$\left[\mathrm{diag}\left(\omega_k^2 - \omega^2 + 2j\omega\zeta_k\omega_k + \frac{\vartheta\gamma_k N_k e^{j\phi_k}}{m_k} \right) \right]\Phi^{-1}X(j\omega) = \Upsilon F_d(j\omega). \quad (6.11)$$

Hence, .

$$H(j\omega) = \Phi\left[\mathrm{diag}\left(\omega_k^2 - \omega^2 + 2j\omega\zeta_k\omega_k + \frac{\vartheta\gamma_k N_k e^{j\phi_k}}{m_k} \right) \right]^{-1}\Upsilon$$

$$\Rightarrow H(j\omega) =$$

$$\Phi\begin{bmatrix} \frac{1}{\omega_1^2-\omega^2+2j\zeta_1\omega\omega_1+\frac{\vartheta\gamma_1 N_1 e^{j\phi_1}}{m_1}} & 0 & \cdots & 0 \\ 0 & \frac{1}{\omega_2^2-\omega^2+2j\zeta_2\omega\omega_2+\frac{\vartheta\gamma_2 N_2 e^{j\phi_2}}{m_2}} & \ddots & \vdots \\ \vdots & 0 & \ddots & 0 \\ 0 & \cdots & 0 & \frac{1}{\omega_n^2-\omega^2+2j\zeta_n\omega\omega_n+\frac{\vartheta\gamma_n N_n e^{j\phi_n}}{m_n}} \end{bmatrix}\Upsilon.$$

$$(6.12)$$

Algebraic manipulation of (6.12) gives

$$H(j\omega) = \sum_{k=1}^{n} \frac{\Phi_k\Upsilon_k^{\mathrm{T}}}{\omega_k^2 - \omega^2 + 2j\omega\zeta_k\omega_k + \frac{\vartheta\gamma_k N_k e^{j\phi_k}}{m_k}}. \quad (6.13)$$

Similarly as of nonlinearities, to configure FRFs for velocity and acceleration as in (6.13), velocity and acceleration need to be considered as input to the nonlinearity to obtain DFs of MR devices [103].

6.3   FSSMC of MR Smart Structure Systems

6.3.1   FSSMC design

To illustrate the control design methodology for the set of n second-order motion equations (6.6) decoupled from (6.1) of $2n$-th order, the following two-dimensional, single-input nonlinear system is now considered:

$$\dot{z} = h(z) + g(z)u, \quad g(z) \geq g_0 > 0, \tag{6.14}$$

where $h(\cdot)$ and $g(\cdot)$, $\forall z \in \mathbb{R}^2$, are some smooth nonlinear functions, g_0 is a lower bound on the function g, and $u \in \mathbb{R}$ is the control input. Our main goal is to design a robustly stabilizing control law. In other words, the control $u = U(z_1, z_2)$ is supposed to constrains the trajectories to the manifold (or surface) $\sigma \equiv 0$ in finite time, i.e. $\lim_{t \to \infty} z_1, z_2 = 0$.

The standard ($\dot{\sigma}$ is discontinuous and σ is continuous functions of z) sliding variable can be expressed by a first-order form

$$\sigma = \mathcal{S}z = \rho z_1 + z_2, \; \mathcal{S} = [\rho \; 1], \; t \geq 0, \tag{6.15}$$

where ρ satisfies the Hurwitz condition, i.e. $\rho > 0$. Suppose that sliding motion is generated in the system at $t_s > 0$. Hence, on this manifold $\sigma \equiv 0$, the governing motion can be written as

$$\dot{z}_1 + \rho z_1 = 0, \; \forall t \geq t_s > 0. \tag{6.16}$$

A solution of (6.16) and its derivative are

$$z_1(t) = z_1(t_s)e^{-\rho(t-t_s)},$$

$$\Rightarrow \dot{z}_1(t) = z_2(t) = -\rho z_1(t_s)e^{-\rho(t-t_s)},$$

in which the rate of convergence can be controlled by choice of a finite positive constant ρ, e.g., if the k-th stiffness and damping of an n-dof structure are known, and denoted respectively by k_k and c_k, then $\rho_k = k_k/c_k$; $k \in [1, \; n]$.

The dynamic sliding variable is designed with a linear operator $L(\cdot)$ which has the interpretation of a low-pass filter (LPF) [106]:

$$\sigma = \mathcal{L}(s)z = L(s)z_1 + z_2, \ \mathcal{L}(s) = [L(s) \ 1], \ t \geq 0, \tag{6.17}$$

where $L(s) = \frac{b_1 s + b_0}{a_1 s + a_0}$ and s is the Laplace operator. The coefficients of the bilinear transfer function are real constants, where the coefficients of the denominator a_0 and a_1 are positive. This is

$$\sigma = \frac{b_1 s + b_0}{a_1 s + a_0} z_1 + z_2. \tag{6.18}$$

Accordingly, the algebraic manipulation of (6.18) yields

$$a_1 \dot{\sigma} + a_0 \sigma = (b_1 s + b_0)z_1 + a_1 \dot{z}_2 + a_0 z_2$$
$$\Rightarrow \dot{\sigma} = \frac{(b_1 s + b_0)z_1}{a_1} + \dot{z}_2 + \frac{a_0}{a_1}(z_2 - \sigma)$$
$$\Rightarrow \dot{\sigma} = \frac{(b_1 s + b_0)z_1}{a_1} + h(z) + g(z)u - \frac{a_0}{a_1}\left(\frac{b_1 s + b_0}{a_1 s + a_0}\right)z_1$$
$$\Rightarrow \dot{\sigma} = \frac{s(b_1 s + b_0)z_1}{a_1 s + a_0} + h(z) + g(z)u.$$

Therefore,

$$\dot{\sigma} = \mathcal{L}(s)z = sL(s)z_1 + h(z) + g(z)u, \ \forall z \in \mathbb{R}^2, \ t \geq 0. \tag{6.19}$$

Suppose that t_R is the attaining time from $\sigma(0) \neq 0$ to $\sigma = 0$:

$$\sigma = L(s)z_1 + z_2 = 0, \quad t \geq t_R. \tag{6.20}$$

Now, the best approximation $\hat{u}$ of the continuous control law that achieves $\dot{\sigma} = 0$ can be obtained as

$$\hat{u} = -\frac{sL(s)z_1 + \hat{h}(z)}{\hat{g}(z)}, \tag{6.21}$$

where $\hat{g}(z)$ and $\hat{h}(z)$ are the estimations of the $g(z)$ and $h(z)$, respectively.

A discontinuous term now can be added to pull the system to the surface as equivalent control $u_E = \hat{u}$ is valid only on the sliding surface. Adding a reaching

control input u_R to (6.21) guarantees that the plant dynamics reach the sliding surface in finite time regardless the presence of uncertainty or nonlinearity.

Substituting $u = u_E + u_R = -\hat{g}(z)^{-1}\big[sL(s)z_1 + \hat{h}(z)\big] + u_R$ into (6.19) results in

$$
\begin{aligned}
\dot{\sigma} &= h(z) + sL(s)z_1 + g(z)\Big[-\frac{\hat{h}(z) + sL(s)z_1}{\hat{g}(z)} + u_R\Big] \\
&= h(z) - \frac{g(z)}{\hat{g}(z)}\hat{h}(z) + sL(s)z_1\Big[1 - \frac{g(x)}{\hat{g}(z)}\Big] + g(x)u_R \\
&= \xi(z) + g(x)u_R,
\end{aligned}
\tag{6.22}
$$

where $\xi(z)$ denotes the perturbation term by

$$
\xi(z) := h(z) - \frac{g(z)}{\hat{g}(z)}\hat{h}(z) + sL(s)z_1\Big[1 - \frac{g(x)}{\hat{g}(z)}\Big].
$$

Assume further that $\xi(z)$ satisfies the following bound

$$
\Big|\frac{\xi(z)}{g(z)}\Big| \leq \varrho(z)
\tag{6.23}
$$

for some known positive definite function $\varrho(z)$. Taking

$$
V = \frac{1}{2}\sigma^2,
\tag{6.24}
$$

a Lyapunov function candidate for $\dot{\sigma} = sL(s)z_1 + h(z) + g(z)u$, we have that

$$
\dot{V} = \sigma\dot{\sigma} = \sigma\big[\xi(z) + g(z)u_R\big] \leq g(z)|\sigma|\varrho(z) + g(z)\sigma u_R.
\tag{6.25}
$$

To achieve the control objective, the robust signal u_R is selected as

$$
u_R = -\beta(z)\,\mathrm{sgn}(\sigma),
\tag{6.26}
$$

with

$$
\beta(z) \geq \varrho(z) + \eta, \ \eta > 0,
\tag{6.27}
$$

so that the term $g(z)\sigma u_R$ is negative and dominates over the residual (positive) term $g(z)|\sigma|\varrho(z)$ when $\sigma \neq 0$, and the net results to force $|\sigma|$ to reach zero. Finally, the control structure is obtained as

$$
u = -\frac{sL(s)z_1 + \hat{h}(z)}{\hat{g}(z)} - \beta(z)\,\mathrm{sgn}(\sigma).
\tag{6.28}
$$

Substituting (6.26) into (6.25) results in

$$
\begin{aligned}
\dot{V} &\leq g(z)|\sigma|\varrho(z) - g(z)\beta(z)\sigma\operatorname{sgn}(\sigma) \\
&\leq g(z)|\sigma|\varrho(z) - g(z)(\varrho(z)+\eta)|\sigma| \\
&\leq -g(x)\eta|\sigma \leq -g_0\eta|\sigma|,
\end{aligned}
\tag{6.29}
$$

where g_0 is defined in (6.14). Now define the function

$$
\chi = \sqrt{2V} = |\sigma|,
\tag{6.30}
$$

which satisfies the differential inequality

$$
\dot{\chi} \leq -g_0\eta.
\tag{6.31}
$$

By integrating the differential inequality over the time interval $0 \leq \tau \leq t$, we obtain

$$
\sqrt{V(t)} \leq \sqrt{V(0)} - \frac{g_0\eta t}{\sqrt{2}}.
\tag{6.32}
$$

Thus $V(t)$ reaches zero in a finite time t_R that is bounded by

$$
t_R \leq \frac{\sqrt{2V(0)}}{g_0\eta}.
\tag{6.33}
$$

During the sliding phase, the motion is completely independent of $g(z)$ and $h(z)$, and we only need the information of the upper bound $\varrho(z)$ which is likely to be smaller than an upper bound on the whole function. As a result, the amplitude of the switching component will be reduced in which η is a positive tuning parameter to be chosen to obtain a desired closed-loop performance.

6.3.2   Application to smart building structures

In the following, the proposed FSSMC strategy is applied to the kth mode of the MRD-embedded structures (6.1) in second-order form (6.6).

We design the sliding surface from (6.18) and (6.19)

$$\sigma_k = L_k(s)q_k + \dot{q}_k = \frac{b_1 s + b_0}{a_1 s + a_0}q_k + \dot{q}_k,$$
$$\Rightarrow \dot{\sigma}_k = \frac{(b_1 s + b_0)q_k}{a_1} + \ddot{q}_k + \frac{a_0}{a_1}(\dot{q}_k - \sigma_k)$$
$$\Rightarrow \dot{\sigma}_k = \frac{(b_1 s + b_0)q_k}{a_1} + \ddot{q}_k - \frac{a_0}{a_1}\left(\frac{b_1 s + b_0}{a_1 s + a_0}\right)q_k \quad (6.34)$$
$$\Rightarrow \dot{\sigma}_k = \frac{s(b_1 s + b_0)q_k}{a_1 s + a_0} + \ddot{q}_k = sL_k(s)q_k + \ddot{q}_k.$$

Recall the plant model (6.6) in modal coordinates

$$\ddot{q}_k + 2\zeta_k\omega_k\dot{q}_k + \sum_{r=1, r\neq k}^{n} \mu_{kr}\dot{q}_r + \omega_k^2 q_k = u_k + d_k. \quad (6.35)$$

We derive the the equivalent control $\hat{u}_k$ that achieves $\dot{\sigma}_k = 0$:

$$\hat{u}_k = \left[\hat{\omega}_k^2 - sL_k(s)\right]q_k + 2\hat{\zeta}_k\hat{\omega}_k\dot{q}_k + \sum_{r=1, r\neq k}^{n} \hat{\mu}_{kr}\dot{q}_r - \hat{d}_k, \quad (6.36)$$

where $\hat{\omega}_k$, $\hat{\zeta}_k$, $\hat{d}_k$, and $\hat{\mu}_{kr}$ are, respectively, desired values chosen for the kth modal frequency, modal damping, disturbance, and modal coupling from the damping matrix.

Now, we can obtain the FSSMC using (6.28) as

$$u = \left[\hat{\omega}_k^2 - sL_k(s)\right]q_k + 2\hat{\zeta}_k\hat{\omega}_k\dot{q}_k + \sum_{r=1, r\neq k}^{n} \hat{\mu}_{kr}\dot{q}_r - \hat{d}_k - \beta_k \,\mathrm{sgn}(\sigma). \quad (6.37)$$

Here, the control law (6.37) results in the Lyapunov function (6.24) decreases all the time in which $\beta_k \geq \varrho_k + \eta_k$ is selected as large enough to guarantee the condition (6.29).

6.3.3 Simulation results and discussion

In this section, a three-storey (each storey with SDoF: one displacement) building model of mass $M = M^{\mathrm{T}} > 0$, viscous damping $C = C^{\mathrm{T}} > 0$, and lateral stiffness $K = K^{\mathrm{T}} > 0$ is considered as an application example. Two identical semiactive

control devices are rigidly placed on the first floor. Numerical values of the structural model parameters are given in Appendix A.1.

For the case of the three-storey building model that satisfies assumptions $(A\,7.1.)$ - $(A\,7.3.)$, we can write from (6.3):

$$
\begin{bmatrix}
\frac{k_1+k_2}{m_1} & \frac{-k_2}{m_1} & 0 \\
\frac{-k_2}{m_2} & \frac{k_2+k_3}{m_2} & \frac{-k_3}{m_2} \\
0 & \frac{-k_3}{m_3} & \frac{k_3}{m_3}
\end{bmatrix} = \Phi\Lambda\Phi^{-1}.
$$

The obtained mode shape vectors are

$$
\upsilon_1 = [-0.3738, -0.5907, -0.7151]^{\mathrm{T}},
$$

$$
\upsilon_2 = [0.7556, 0.2532, -0.6041]^{\mathrm{T}}, \quad \upsilon_3 = [-0.5379, 0.7661, -0.3517]^{\mathrm{T}}.
$$

The Λ, Υ, Ω, and damping matrices are

$$
\Lambda =
\begin{bmatrix}
1211.1 & 0 & 0 \\
0 & 9875.4 & 0 \\
0 & 0 & 22118
\end{bmatrix}, \quad
\Upsilon =
\begin{bmatrix}
-0.0038 & -0.006 & -0.0073 \\
0.0077 & 0.0026 & -0.0061 \\
-0.0055 & 0.0078 & -0.0036
\end{bmatrix},
$$

$$
\Omega =
\begin{bmatrix}
-0.0038 & 0 & 0 \\
0.0077 & 0 & 0 \\
-0.0055 & 0 & 0
\end{bmatrix}, \quad
\Phi^{-1}M^{-1}C\Phi =
\begin{bmatrix}
0.2095 & -0.2494 & 0.1826 \\
-0.2494 & 1.2283 & -0.3626 \\
0.1826 & -0.3626 & 1.8685
\end{bmatrix}.
$$

The obtained modal frequencies $\omega_k/2\pi = 5.53, 15.8, 23.65$ Hz and damping ratios $\zeta_k = 0.0189, 0.0389, 0.0395$. The FRF matrix is given by

$$
H(j\omega) = \Phi
\begin{bmatrix}
\delta_{11} & 0 & 0 \\
0 & \delta_{22} & 0 \\
0 & 0 & \delta_{33}
\end{bmatrix}
\Upsilon,
$$

where

$$
\delta_{11} = \frac{1}{\omega_1^2 - \omega^2 + 2j\zeta_1\omega\omega_1 + \frac{Ne^{j\phi}}{49.15}},
$$

$$
\delta_{22} = \frac{1}{\omega_2^2 - \omega^2 + 2j\zeta_2\omega\omega_2}, \quad \delta_{33} = \frac{1}{\omega_3^2 - \omega^2 + 2j\zeta_3\omega\omega_3}.
$$
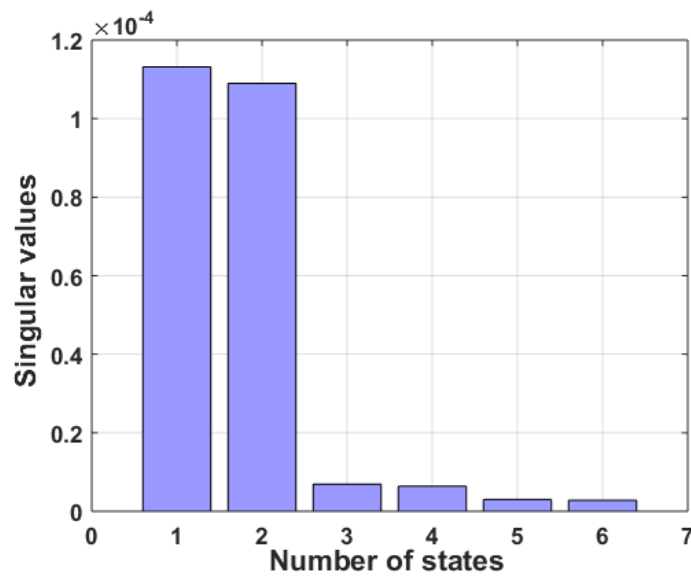
Figure 6.2 : Hankel singular values of the resulting system.
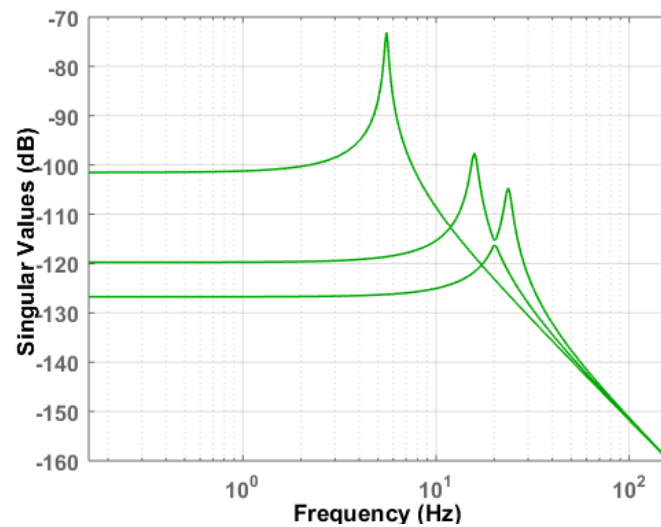
Figure 6.3 : Open-loop singular value plot for $H(j\omega)$.

The Hankel singular value (HSV) plot shown in Figure 6.2 suggests that there are two dominant modes in this system where most of its energy stored in the first and second states (each state represents a displacement or its rate of change). However, we take into account the contributions of the remaining modes as well for the controller design and implementation to the three-dof system.

Figure 6.3 illustrates the amplitude of input-output gain of the whole system as a function of frequency. Transfer functions (TFs) from input to the first, second and third floors displacement are shown in Figures 6.4(a), (b) and (c), respectively. These frequency responses confirm that the significant dynamics of the system rest in the frequency range of 5 to 24 Hz while the magnitude drops in the high-frequency ranges, and it remains almost similar in the low-frequency ranges.

We design the controller based on modal decomposition and a frequency shaped sliding surface for vibration suppression of the intelligent structure. We take $b_1 = 0$ in (6.34), $L_1(s) = (b_1 s + b_0)/(a_1 s + a_0)$, to place the zero at infinity. Hence (6.34) becomes

$$\sigma_1 = \frac{b_0}{a_1 s + a_0} q_1 + \dot{q}_1,$$

where $a_1 = 1, a_0 = 2\zeta_1\omega_1 = 1.313$ and $b_0 = 5.51$. We select $\kappa_1 = 0.2, \sum_{r=1}^{n} \hat{\mu}_{1r} = 0$, and replace $\text{sgn}(\sigma_1)$ by a sigmoid-like function $\frac{\sigma_1}{(|\sigma_1|+0.005)}$.

Since $u_k = \Omega f_{\text{MR}(k)}$, reciprocally, the damping force can be computed as $f_{\text{MR}(k)} = \Omega^{-1} u_k$. To derive a magnetization current i corresponding to a damping force f_{MR}, an approximate expression is obtained

$$i_k = p_0 + p_1 f_{\text{MR}(k)} + p_2 f_{\text{MR}(k)}^2, \tag{6.38}$$

whose coefficients $p_0 = 0.127, p_1 = -0.00094, p_2 = 0.0000021$ are determined by the *cftool* (see Figure 6.6). The quality of the resulting fit is evaluated using R^2 and RMSE. The current resulting from (6.38) supplied to excitation coils of MRD is constrained between a known interval $i \in [0 \ i_{\text{M}}], i_{\text{M}} = 2$ A, that is

$$i = \begin{cases} |i_k| & |i_k| < i_{\text{M}} \\ 0 & |i_k| \geq i_{\text{M}}. \end{cases} \tag{6.39}$$

To demonstrate the effectiveness of the designed controller, the ground seismic acceleration of four benchmark earthquakes (two far field: El-Centro & Hachinohe
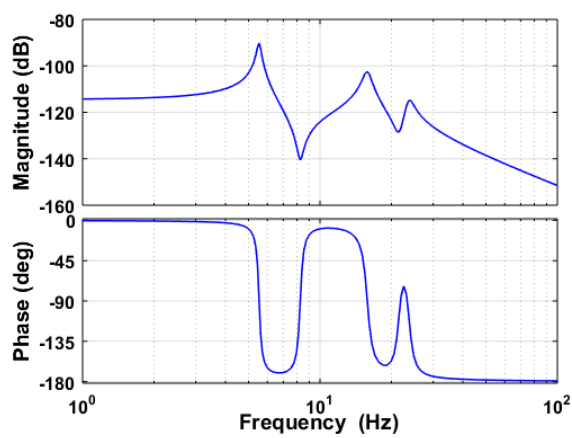
(a) First floor
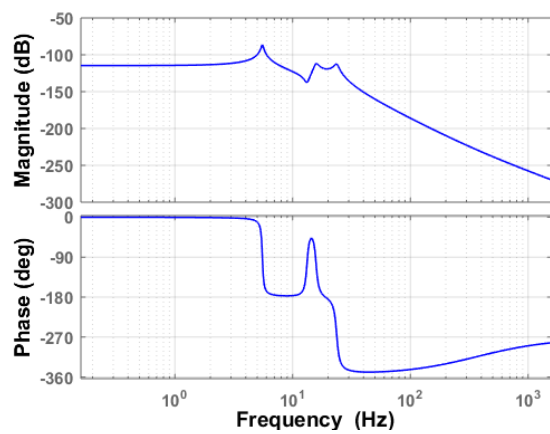
(b) Second floor
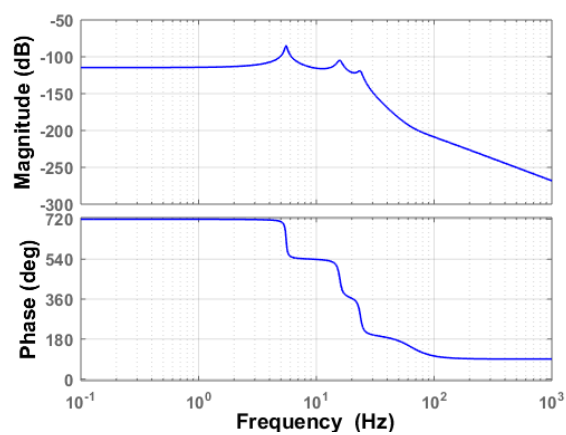
(c) Third floor

Figure 6.4 : TF from input to the floors displacements.

(a) El-Centro 1940

(b) Hachinohe 1968

(c) Northridge 1994

(d) Kobe 1995
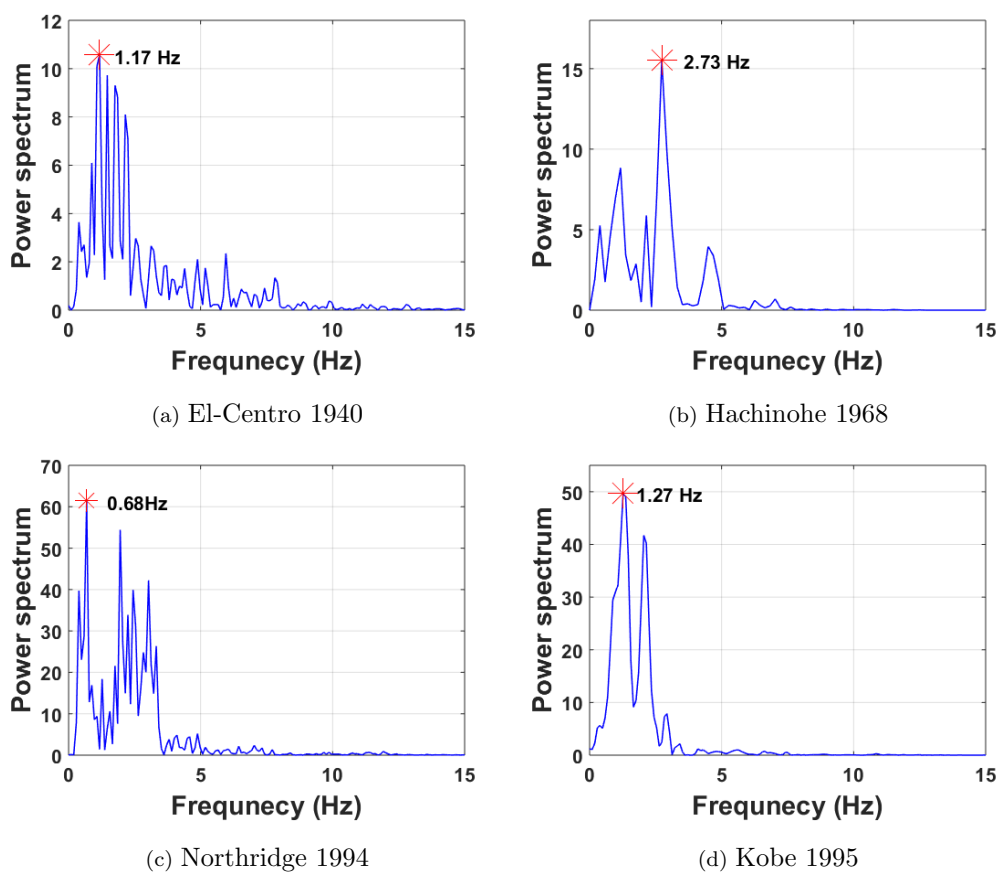
Figure 6.5 : Illustration of the quake-prone frequency range.
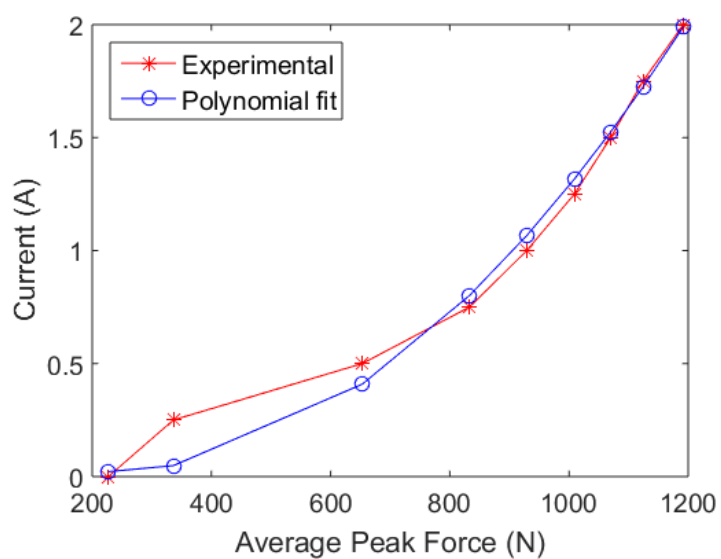
Figure 6.6 : Damper current corresponding to average peak force.
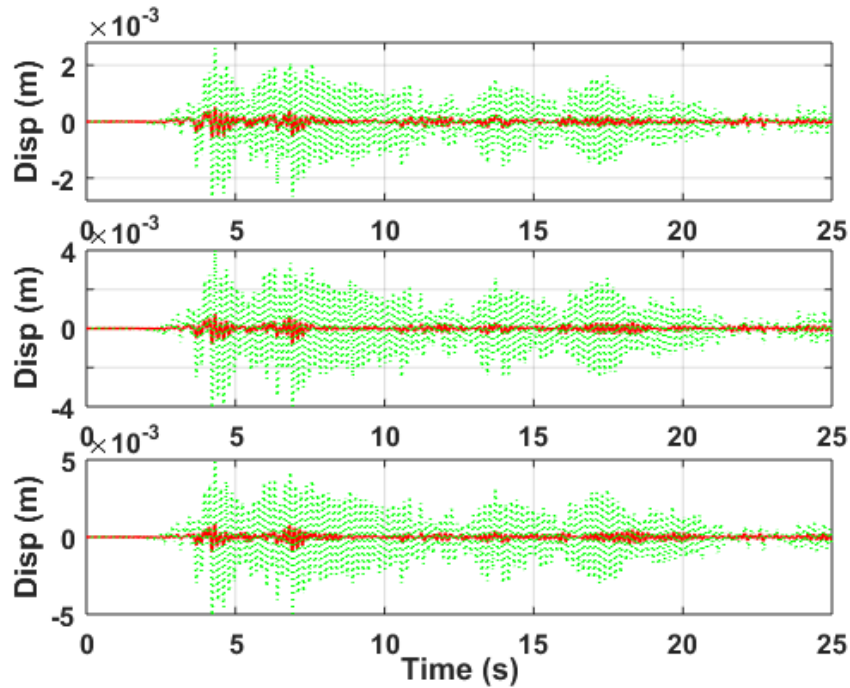
Figure 6.7 : Time responses of $x_1(t)$: first floor (top), $x_2(t)$: second floor (middle) and $x_3(t)$: third floor (bottom) with FSSM control (red-solid) and without (green-dot) control.

and two near field: Northridge & Kobe) record are used to excite the resulting smart structure in simulations. The power spectra of these earthquakes are shown in Figure 6.5 to illustrate the quake-prone frequency range.

Figure 6.7 shows the time responses of the system at zero initial conditions with and without control under a 50% scale down record of the El-Centro earthquake where its active frequency range is shown in Figure 6.5(a). From the uncontrolled time responses, two approximate displacement readings for the first, second and third floors are respectively -0.00263 m to 0.0026 m, -0.0041 m to 0.00409 m, and -0.00489 m to 0.00493 m at 4.3 sec and 6.9 sec. The controlled approximate readings for the first, second and third floors are respectively -0.00053 m to 0.00052 m, -0.0008 m to 0.00072 m, and -0.0009 m to 0.00091 m at 4.3 sec and 6.9 sec. A negative polarity represents right-to-left movement of the structure.

6.4   FS2SMC for Smart Suspension Systems

Smart structures can find many applications in vehicle suspensions, offshore plat-forms, or built infrastructure such as buildings and bridges. To further verify the merits of the proposed control strategy in engineering structure, described in the previous section, a four-dof half car model (HCM) with inbuilt active hydraulically interconnected suspension (HIS) system available at the University of Technology Sydney (UTS) Laboratory is considered in this section as an example of an applica-tion. The HCM simulates vehicle lateral dynamics and roll angle response to lateral acceleration. The active HIS system is a promising candidate for rollover prevention of heavy vehicles, driverless cars, and unmanned ground vehicles (UGVs), which is one of the prominent priorities in vehicle safety and handling control. During turning maneuver, when the car body inclines, a differential pressure results in the HIS system producing a counter roll moment to oppose that of the centrifugal force.

Autonomous driverless cars and UGVs are becoming a reality, thanks to the robotics community. These vehicles can be used in complex envrionments and off-road navigation, and are subject to nonlinear dynamic forces and moments because of complex terrain behavior and uneven traversing surface [133, 134]. Due to un-structured terrain irregularities and size of the wheeled off-road vehicles, they can be considered among the primary sources of energy dissipation and pollutant emission; they should overcome as well as their performing tasks. Having discussed the mer-its of frequency shaped sliding mode control in Section 2.5 and Section 6.3, in the following a frequency-shaped second-order sliding mode controller (FS2SMC) is de-veloped to directly adjust the structural frequency response and improve robustness performance.

6.4.1 FS2SMC design

We consider the following two-dimensional, single-input nonlinear system to illustrate the control design methodology:

$$\dot{x} = h(x) + g(x)u, \tag{6.40}$$

where $h(x)$ and $g(x) \geq g_0 > 0$, $\forall x \in \mathbb{R}^2$, are some smooth nonlinear functions, and $u \in \mathbb{R}$ is the control input. Our main goal is to design a robustly stabilizing control law $u = U(x_1, x_2)$.

We design the dynamic sliding surface (is a type of dynamic manifold) with a second-order LPF:

$$\sigma = \frac{b_0}{s^2 + a_1 s + a_0} x_1 + x_2, \tag{6.41}$$

since we want to make the rolloff of $|L(j\omega)|$, $\omega \in [0, \infty)$ large for large ω. The choice $L(s) = \frac{b_0}{s^2 + a_1 s + a_0}$ gives us a $|L(j\omega)|$ with 2-pole rolloff (asymptotic slope of -40 dB/decade) at high frequencies.

Then, from (6.41) we obtain

$$\ddot{\sigma} + \sigma(a_1 s + a_0) = \ddot{x}_2 + x_2(a_1 s + a_0) + b_0 x_1$$

$$\Rightarrow \ddot{\sigma} = \ddot{x}_2 - (a_1 s + a_0)\left(\frac{b_0}{s^2 + a_1 s + a_0}\right) x_1 + b_0 x_1$$

$$\Rightarrow \ddot{\sigma} = \frac{\partial h}{\partial x}(h + gu) + \frac{\partial g}{\partial x}(h + gu)u + g(x)\dot{u} + b_0 x_1\left(1 - \frac{a_1 s + a_0}{s^2 + a_1 s + a_0}\right) \tag{6.42}$$

$$\Rightarrow \ddot{\sigma} = H(x, u) + g(x)v + b_0 x_1\left(\frac{s^2}{s^2 + a_1 s + a_0}\right)$$

$$\Rightarrow \ddot{\sigma} = H(x, u) + s^2 L(s)x_1 + g(x)v,$$

where $H(x, u) = \frac{\partial h}{\partial x}(h + gu) + \frac{\partial g}{\partial x}(h + gu)u$ and $v = \dot{u}$ is prescribed as the new control [135]. Let $\hat{g}$ and $\hat{H}$ be nominal models of g and H, respectively. Taking

$$\hat{v} = -\hat{g}(x)^{-1}\left[\hat{H} + s^2 L(s)x_1\right] + v_R \tag{6.43}$$

results in

$$
\begin{aligned}
\ddot{\sigma} &= H + s^2 L(s)x_1 + g(x)\Big[-\frac{\hat{H} + s^2 L(s)x_1}{\hat{g}(x)} + v_R\Big] \\
&= H - \frac{g(x)}{\hat{g}(x)}\hat{H} + s^2 L(s)x_1\Big[1 - \frac{g(x)}{\hat{g}(x)}\Big] + g(x)v_R \\
&= \delta(x) + g(x)v_R,
\end{aligned}
\tag{6.44}
$$

where $\delta(x)$ denotes the perturbation term by $\delta(x) := H - \frac{g(x)}{\hat{g}(x)}\hat{H} + s^2 L(s)x_1\big[1 - \frac{g(x)}{\hat{g}(x)}\big]$.

Suppose $\delta(x)$ satisfies the inequality

$$
\big|g(x)^{-1}\delta(x)\big| \leq \varrho(x)
\tag{6.45}
$$

for some known function $\varrho(x)$.

We consider a Lyapunov function candidate $V = \frac{1}{2}\dot{\sigma}^2$ for $\ddot{\sigma} = H(x,u) + s^2 L(s)x_1 + g(x)v$. Taking into account the inequality (6.45), the time derivative of V can be computed as

$$
\dot{V} = \dot{\sigma}\ddot{\sigma} = \dot{\sigma}\big[\delta(x) + g(x)v_R\big] \leq g(x)|\dot{\sigma}|\varrho(x) + g(x)\dot{\sigma}v_R.
\tag{6.46}
$$

To achieve our goal, we take v_R as

$$
v_R = -\beta(x)\operatorname{sgn}(\dot{\sigma}) - \kappa\dot{\sigma}, \ \ \kappa > 0,
\tag{6.47}
$$

with $\beta(x) \geq \varrho(x) + \eta$, $\eta > 0$, so that the term $g(x)\dot{\sigma}v_R$ is negative and dominates over the residual (positive) term $g(x)|\dot{\sigma}|\varrho(x)$ when $\dot{\sigma} \neq 0$, and the net results (negative) to force $|\dot{\sigma}|$ to reach zero in finite term. Finally, the controller is obtained as

$$
v = -\hat{g}(x)^{-1}\big[\hat{H} + s^2 L(s)x_1\big] - \beta(x)\operatorname{sgn}(\dot{\sigma}) - \kappa\dot{\sigma}.
\tag{6.48}
$$

Substituting (6.47) into (6.46) results in

$$
\begin{aligned}
\dot{V} &\leq g(x)|\dot{\sigma}|\varrho(x) - g(x)\beta(x)\dot{\sigma}\operatorname{sgn}(\dot{\sigma}) - g(x)\kappa\dot{\sigma}^2 \\
&\leq g(x)|\dot{\sigma}|\varrho(x) - g(x)(\varrho(x) + \eta)|\dot{\sigma}| - g(x)\kappa\dot{\sigma}^2 \\
&\leq -g(x)\eta|\dot{\sigma}| - g(x)\kappa\dot{\sigma}^2 \leq -g_0\eta|\dot{\sigma}| - g_0\kappa\dot{\sigma}^2 \\
&\leq -g_0\kappa\dot{\sigma}^2 = -2g_0\kappa V,
\end{aligned}
\tag{6.49}
$$

where g_0 is defined in (6.40). By separating the variables and integrating the differential inequality over the time interval $t_0 \leq \tau \leq t$, we obtain

$$V(t) \leq V(t_0)e^{-2\kappa g_0(t-t_0)}. \tag{6.50}$$

According to the above inequality, we see that $V(t)$ will tend to zero exponentially in which the exponential decay rate is determined by the parameter κ. In (6.49), we established

$$\dot{\sigma}\ddot{\sigma} \leq -g_0\eta|\dot{\sigma}| - g_0\kappa\dot{\sigma}^2. \tag{6.51}$$

Since $g_0\kappa\dot{\sigma}^2 \geq 0$, an η-reachability condition has been established and a sliding motion will take place. By neglecting the nonlinear term in (6.51) yields

$$\frac{d}{dt}|\dot{\sigma}(t)| \leq -g_0\kappa|\dot{\sigma}(t)|, \tag{6.52}$$

which implies that

$$|\dot{\sigma}(t)| \leq |\dot{\sigma}(t_0)|e^{-\kappa g_0(t-t_0)}. \tag{6.53}$$

Here, $|\dot{\sigma}(t_0)|$ represents the initial distance away from the sliding surface, and κ is the decay rate at which the sliding surface is attained.

During the sliding phase, the motion is completely independent of g and H, and we only need the information of the upper bound $\varrho(x)$ which is likely to be smaller than an upper bound on the whole function. As a result, the amplitude of the switching component, $\varrho(x) + \eta$ to $-\varrho(x) - \eta$, will be reduced. The parameters η and κ are positive tuning parameters to be chosen to obtain a desired closed-loop performance.

6.4.2 Vehicle suspension structure control

The proposed FS2SMC technique is now applied to a four-dof HCM with an inbuilt active HIS system, see Figures 6.8(a) and (b). Input and output variables of the system are, respectively, $u = v_a$ and $y = [z_1, z_2, z_s, \theta]^{\mathrm{T}}$. v_a is the hydraulic

fluid volumetric displacement produced by the actuator. z_1, z_2, z_3, z_4 denote left and right deflections of the tire and sprung mass, respectively. The body bounce and roll angle can be given as $z_s = \frac{z_3+z_4}{2}$ and $\theta = \frac{z_4-z_3}{2l}$, respectively.

Using the Lagrange principle or Newton's law, the equations of motion can be described by

$$M\ddot{z} + C\dot{z} + Kz = B_u u + W_d f_d, \tag{6.54}$$

where $z = [z_1, z_2, z_3, z_4]^{\text{T}}$, $u = [f_1, f_2]^{\text{T}}$, $f_d = [f_{d1}, f_{d2}, a_c]^{\text{T}}$. f_1, f_2 represent the forces produced by the active HIS. Two road disturbance inputs and the centrifugal acceleration are denoted by f_{d1}, f_{d2} and a_c, respectively. The inertia, damping, stiffness, active HIS input and the disturbances input are, respectively, given by

$$M = \begin{bmatrix} m_u & 0 & 0 & 0 \\ 0 & m_u & 0 & 0 \\ 0 & 0 & \frac{m_s+\frac{I_s}{l^2}}{4} & \frac{m_s-\frac{I_s}{l^2}}{4} \\ 0 & 0 & \frac{m_s-\frac{I_s}{l^2}}{4} & \frac{m_s+\frac{I_s}{l^2}}{4} \end{bmatrix} \text{kg},$$

$$C = \begin{bmatrix} c_s & 0 & -c_s & 0 \\ 0 & c_s & 0 & -c_s \\ -c_s & 0 & c_s & 0 \\ 0 & -c_s & 0 & c_s \end{bmatrix} \text{Ns/m},$$

$$K = \begin{bmatrix} k_s + k_t & 0 & -k_s & 0 \\ 0 & k_s + k_t & 0 & -k_s 0 \\ -k_s & 0 & k_s & 0 \\ 0 & -k_s & 0 & k_s \end{bmatrix} \text{N/m},$$

$$B_u = \begin{bmatrix} -1 & 0 \\ 0 & -1 \\ 1 & 0 \\ 0 & 1 \end{bmatrix}, \quad W_d = \begin{bmatrix} k_t & 0 & 0 \\ 0 & k_t & 0 \\ 0 & 0 & -\frac{m_s h_g}{l} \\ 0 & 0 & \frac{m_s h_g}{l} \end{bmatrix}.$$
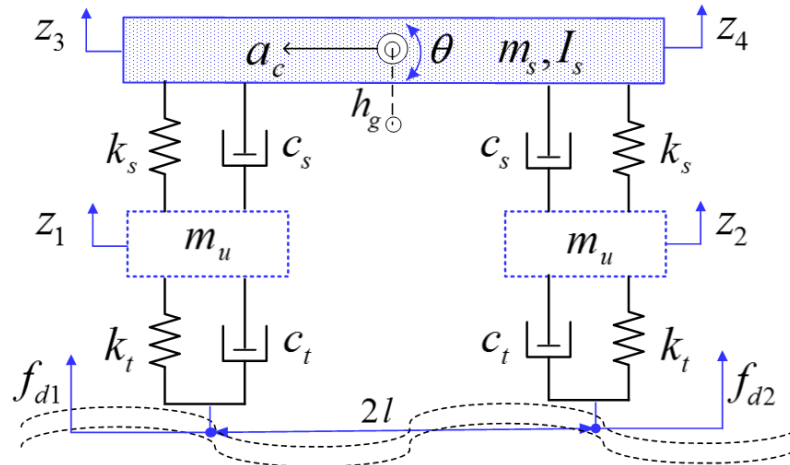
(a) Schematic diagram of a HCM
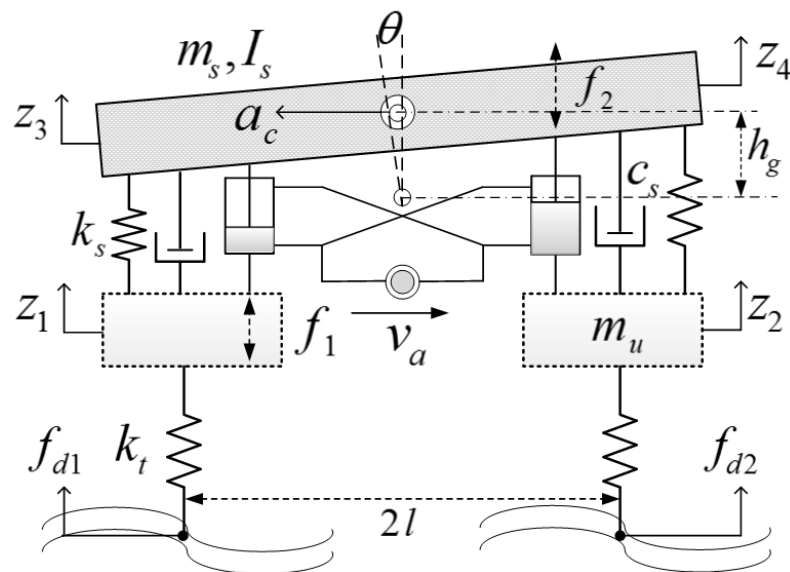
(b) HCM integrated with HIS system

Figure 6.8 : The forces produced by the active HIS, two road disturbance inputs, centrifugal acceleration, body bounce and roll angle are f_1, f_2, f_{d1}, f_{d2}, a_c, $z_s = \frac{z_3 + z_4}{2}$ and $\theta = \frac{z_4 - z_3}{2l}$, respectively. Input variable $u = v_a$ is the hydraulic fluid volumetric displacement produced by the actuator.

The HIS output is given by

$$u = M_h \ddot{z} + C_h \dot{z} + K_h z + M_{ha} \ddot{v}_a + C_{ha} \dot{v}_a + K_{ha} v_a, \qquad (6.55)$$

where M_h, C_h, and K_h are the fluid inertia, damping and stiffness matrices, respectively, associated with the passive behavior of the HIS system. M_{ha}, C_{ha}, and K_{ha} are, respectively, the fluid inertia, damping and stiffness matrices associated with the hydraulic actuator input.

Neglecting the higher-order terms of the actuator input in (6.55), we have

$$u = M_h \ddot{z} + C_h \dot{z} + K_h z + K_{ha} v_a. \qquad (6.56)$$

Substituing (6.56) into (6.54) results in

$$(M - M_h)\ddot{z} + (C - C_h)\dot{z} + (K - K_h)z = K_{ha} v_a + W_d f_d. \qquad (6.57)$$

where the inertia, damping and stiffness matrices of the combined system are, respectively, given by

$$\mathbf{M} = M - M_h, \ \mathbf{C} = C - C_h, \ \mathbf{K} = K - K_h. \qquad (6.58)$$

The state variables $(x_1, x_2) := (z, \dot{z})$ transform the combined system (6.57) into the form

$$\dot{x} = Ax + Bu + W f_d,$$
$$y = \overline{C}x, \qquad (6.59)$$

where

$$A = \begin{bmatrix} \mathbf{0}^{4 \times 4} & \mathbf{I}^{4 \times 4} \\ -\mathbf{M}^{-1}\mathbf{K} & -\mathbf{M}^{-1}\mathbf{C} \end{bmatrix},$$

$$B = \mathbf{M}^{-1} K_{ha}, \ W = \mathbf{M}^{-1} W_d,$$

$$\overline{C} = \begin{bmatrix} -1 & 0 & 1 & 0 & 0 & 0 & 0 & 0 \\ 0 & -1 & 0 & 1 & 0 & 0 & 0 & 0 \\ 0 & 0 & 1/2 & 1/2 & 0 & 0 & 0 & 0 \\ 0 & 0 & -1/(2l) & 1/(2l) & 0 & 0 & 0 & 0 \end{bmatrix}.$$
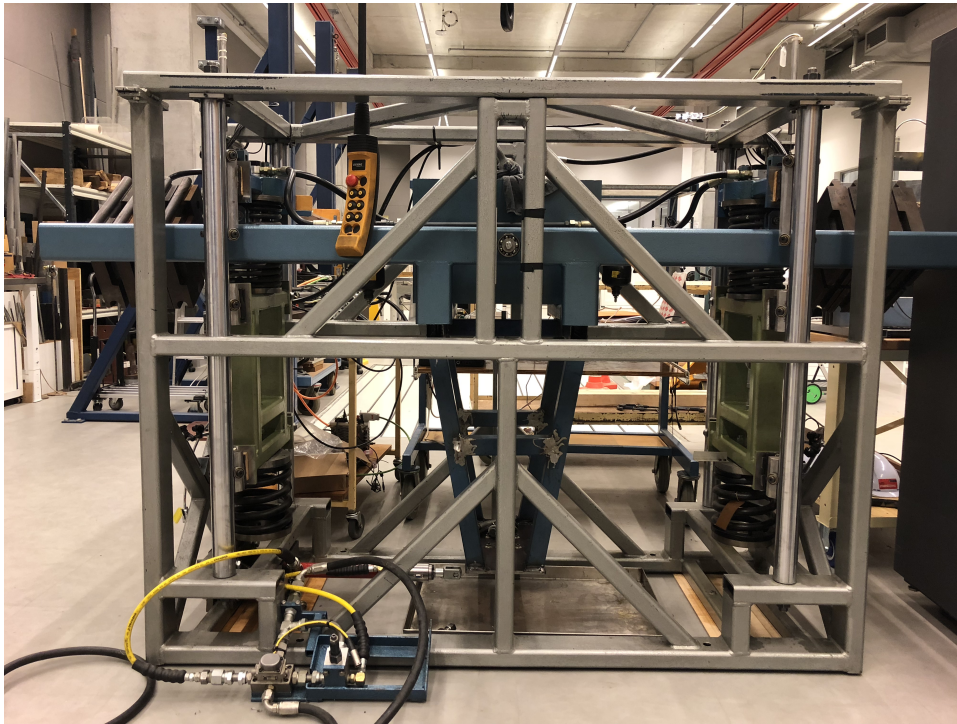
Figure 6.9 : Front view photograph of the combined system.

6.4.3   Simulation results

The following cases are taken into account in the simulation study:

(*C1.*) the HCM with active suspension control using the proposed FS2SMC,

(*C2.*) the HCM with passive HIS (without any hydraulic actuation), and

(*C3.*) the conventional HCM (without any suspension modifications).

The HCM parameters are identified as follows: the vehicle body (sprung) mass, wheel (unsprung) mass and rotational inertia are $m_s = 475$ kg, $m_u = 35$ kg and $I_s = 120$ kgm^2, respectively; the suspesion spring and tire stiffness are $k_s = 20$ and $k_t = 172$ kN/m, respectively, and the suspesion damping is $c_s = 240$ Ns/m. The distance between the roll center and the center of gravity (CoG) is $h_g = 0.5$ m, and the wheel track width is $2l = 0.7$ m. The active HIS system parameters are adopted from [136]. A photograph of the integrated system, available at the

University of Technology Sydney (UTS) Laboratory, is shown in Figure 6.9. Then the inertia, damping, stiffness, active HIS input and the disturbances input matrices are, respectively, given by

$$
M = \begin{bmatrix} 35 & 0 & 0 & 0 \\ 0 & 35 & 0 & 0 \\ 0 & 0 & 179.97 & 57.53 \\ 0 & 0 & 57.53 & 179.97 \end{bmatrix} \text{kg,}
$$

$$
C = \begin{bmatrix} 240 & 0 & -240 & 0 \\ 0 & 240 & 0 & -240 \\ -240 & 0 & 240 & 0 \\ 0 & -240 & 0 & 240 \end{bmatrix} \text{Ns/m,}
$$

$$
K = \begin{bmatrix} 192000 & 0 & -20000 & 0 \\ 0 & 192000 & 0 & -20000 \\ -20000 & 0 & 20000 & 0 \\ 0 & -20000 & 0 & 20000 \end{bmatrix} \text{N/m,}
$$

$$
B_u = \begin{bmatrix} -1 & 0 \\ 0 & -1 \\ 1 & 0 \\ 0 & 1 \end{bmatrix}, \ W_d = \begin{bmatrix} 172000 & 0 & 0 \\ 0 & 172000 & 0 \\ 0 & 0 & -340 \\ 0 & 0 & 340 \end{bmatrix}.
$$

To compute the passive HIS, we set the hydraulic actuator input $v_a = 0$ in (6.59). We take $\eta = 0.25$ and a Butterworth filter

$$
\sigma = \frac{1}{s^2 + 1.4142s + 1}\theta + \dot{\theta},
$$

to design the sliding variable and FS2SMC.

To determine the resonant frequencies and mode shapes of the combined structure, we diagonalized the matrix $\mathbf{M}^{-1}\mathbf{K}$ as $\mathbf{M}^{-1}\mathbf{K} = \Phi\Lambda\Phi^{-1}$, where the orthogonal

(a) Roll angle

(b) Actuator displacement
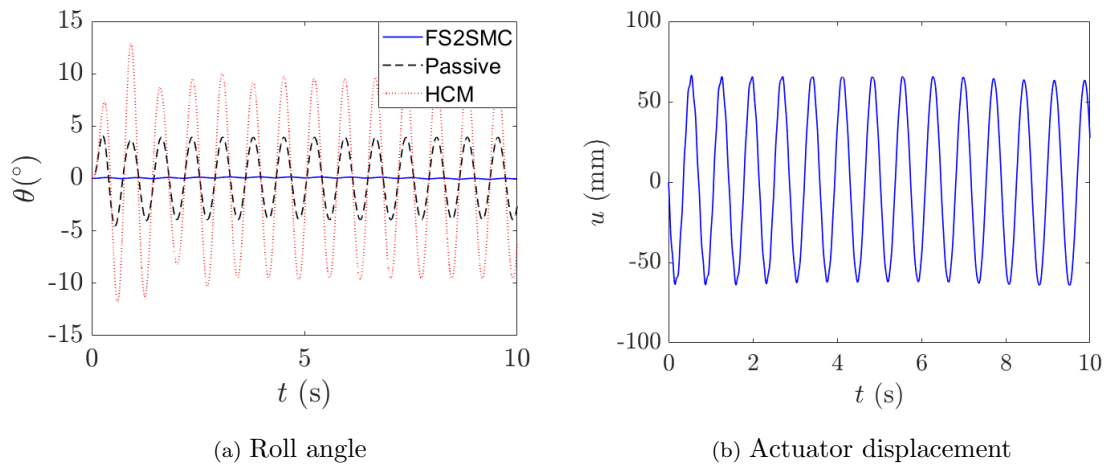
Figure 6.10 : Under lateral acceleration $3\sin(1.392 \times 2\pi t)$ m/s^2.

matrix Φ is formed from the associated eigenvectors and the diagonal frequency matrix Λ is listing the eigenvalues, $\lambda(\mathbf{M}^{-1}\mathbf{K})$. The principal diagonals entry of the damping matrix are $\Phi^{-1}\mathbf{M}^{-1}\mathbf{C}\Phi = 2\zeta\omega_n$. The obtained modal frequencies and damping ratios are, respectively, 1.392, 2.476, 11.808, 12.33 Hz and 0.041, 0.1841, 1.789, 9.0352.

The responses of the integrated system under harmonic excitation (consider as a disturbance) at zero initial conditions for three cases (*C1*) - (*C3*) are shown in Figure 6.10 (a). We observe that the roll angle in the FS2SMC case (blue-solid) is greatly attenuated compare to conventional suspension (black-dash) and passive HIS system (red-dot).

Figure 6.10(b) shows the actuator volumetric displacement

$$v_a = \int v(t)dt,$$

where a *back-information* antiwindup concept is employed, i.e. the difference between the saturated and the unsaturated output (control signal) is used to generate a feedback signal to act on the integrator input.

The roll angle spectrum of the system, excited at low frequency 0.5 Hz and
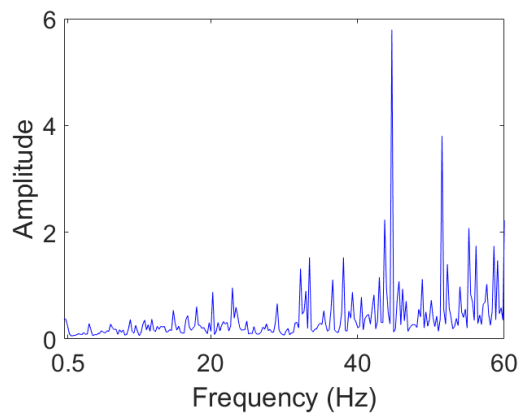
(a) Lateral acceleration $3\sin(0.5 \times 2\pi t)$ m/s^2
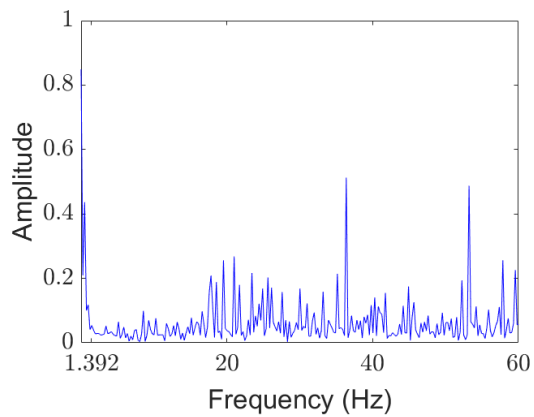
(b) $3\sin(1.392 \times 2\pi t)$ m/s^2
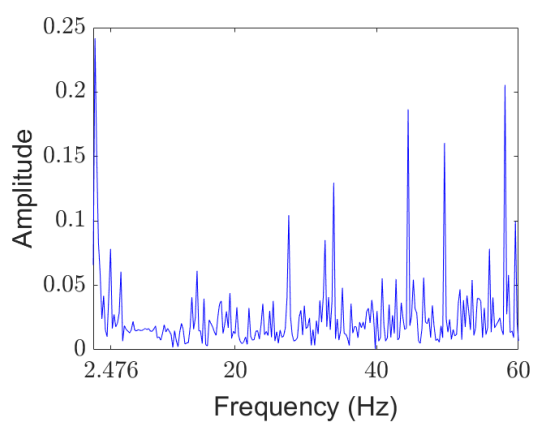
(c) $3\sin(2.476 \times 2\pi t)$ m/s^2

Figure 6.11 : Roll angle spectrums of the integrated system.

resonant frequencies 1.392 Hz and 2.476 Hz, are shown in Figures 6.11(a), (b) and (c), respectively. From these figures, we observe that the resonant frequencies are shifted further to prevent natural modes of the system to be excited.

6.4.4 Discussion

Although frequency-shaped sliding control has the advantage of attenuating the effect of high-frequency unmodeled dynamics [110], making the following substitution in the corresponding discontinuous ones with their equivalence: $\text{sgn}(\dot{\sigma})$ with $\text{sat}(\frac{\dot{\sigma}}{\varepsilon})$, $\text{sgn}(\dot{\sigma})$ with $\tanh(\frac{\dot{\sigma}}{\varepsilon})$, $\text{sgn}(\dot{\sigma})$ with $\frac{\dot{\sigma}}{|\dot{\sigma}|+\varepsilon}$, a continuous control law can be obtained in order to alleviate the chattering phenomena by smoothing out the control discontinuity in a thin boundary layer, $B_\varepsilon = \{\|\dot{\sigma}\| \leq \varepsilon\}$, neighboring the switching surface [73, 82, 106]. Here, we substitute the signum nonlinearity by $\text{sat}(\dot{\sigma}/\varepsilon)$:

$$v_R = -(\varrho + \eta)\,\text{sat}(\dot{\sigma}/\varepsilon) - \kappa\dot{\sigma}, \tag{6.60}$$

in which a good approximation of $\text{sgn}(\cdot)$ nonlinearity may need a small ε.

Outside the boundary layer, the system dynamics are the same as the switching control

$$v = v_E + v_R, \quad \|\dot{\sigma}\| \geq \varepsilon. \tag{6.61}$$

Inside the boundary layer

$$\dot{\sigma}(t) = sL(s)\theta + \ddot{\theta} = \phi(t) \leq \varepsilon$$
$$\Rightarrow \theta(t) = \frac{1}{sL(s) + s^2}\phi(t), \tag{6.62}$$

which represents the system dynamics of $\theta(t)$ under $\phi(t)$. Due to the boundary layer interpolation, after transients the roll angle error is bounded by

$$|e_\theta(t)|_\phi = |\int_0^t f(\tau)\phi(t - \tau)d\tau| \leq \varepsilon \int_0^\infty f(\tau)d\tau = \varepsilon\|f(t)\|_1, \tag{6.63}$$

where $f(t)$ is the impulse response of $\frac{1}{sL(s)+s^2}$ (see Figure 6.12).
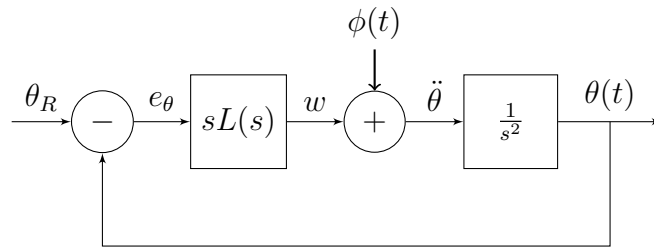
Figure 6.12 : Feedback system defined by FS2SM; $L(s) = \frac{1}{s^2+1.4142s+1}$ but extensions to more orders with an equal number of poles and zeros (or less zeros) can also be made.
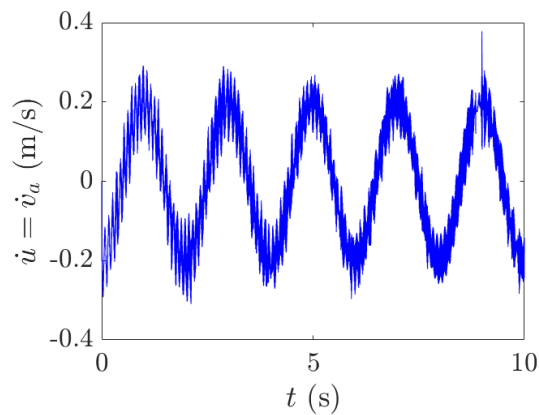
(a) $\varepsilon = \frac{0.05°}{\|f(t)\|_1}, \kappa = 5$
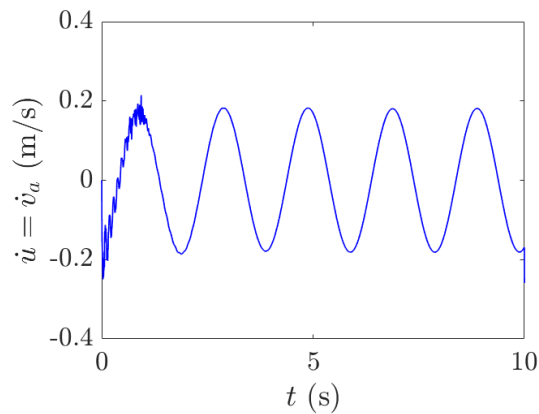
(b) $\varepsilon = \frac{0.5°}{\|f(t)\|_1}, \kappa = 0.5$

Figure 6.13 : Actuator velocity due to a (a) thin boundary and (b) thick boundary under lateral acceleration $3\sin(0.5 \times 2\pi t)$ m/s²; $\eta = 0.25$.

Figures 6.13(a) and 6.14(a) illustrate that

$$v_R = -(\varrho + \eta)\,\text{sat}(\dot{\sigma}/\varepsilon) - \kappa\dot{\sigma}$$
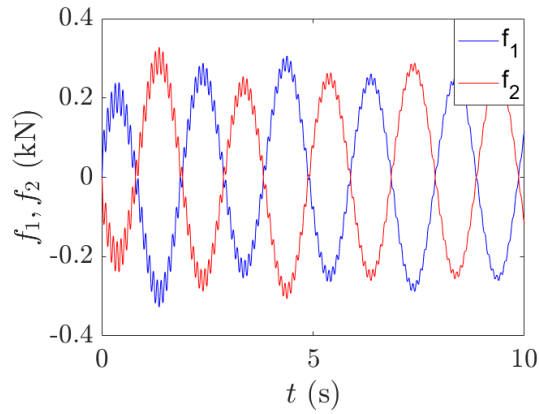
(a) $\varepsilon = \frac{0.05°}{\|f(t)\|_1}, \kappa = 5$
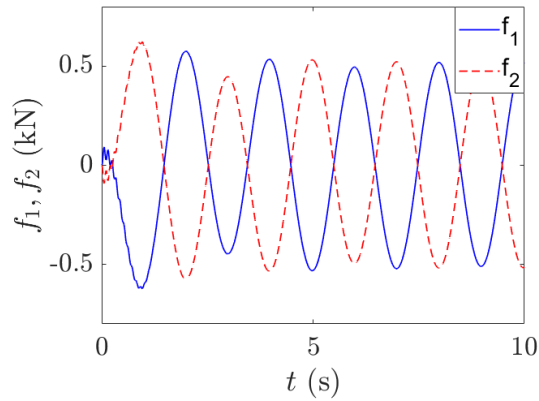
(b) $\varepsilon = \frac{0.5°}{\|f(t)\|_1}, \kappa = 0.5$

Figure 6.14 : Actuator force due to a (a) thin boundary and (b) thick boundary under lateral acceleration $3\sin(0.5 \times 2\pi t)$ m/s^2; $\eta = 0.25$.

is over-calculated during computer simulation because of thin boundary layer

$$\varepsilon = \frac{0.05°}{\|f(t)\|_1}, \ \kappa = 5, \ \eta = 0.25.$$

By increasing the boundary layer thickness

$$\varepsilon = \frac{0.5°}{\|f(t)\|_1}, \ \kappa = 0.5, \ \eta = 0.25,$$

we can achieve smooth responses in term of chattering amplitude attenuation as shown in Figures 6.13(b) and 6.14(b).

According to [72, 80], while dealing with uncertain systems, it may not possible to vanish the uncertain terms at the equilibrium but can bring the trajectories

(a) $\varepsilon = \frac{0.05°}{\|f(t)\|_1}, \kappa = 5$ (b) $\varepsilon = \frac{0.5°}{\|f(t)\|_1}, \kappa = 0.5$
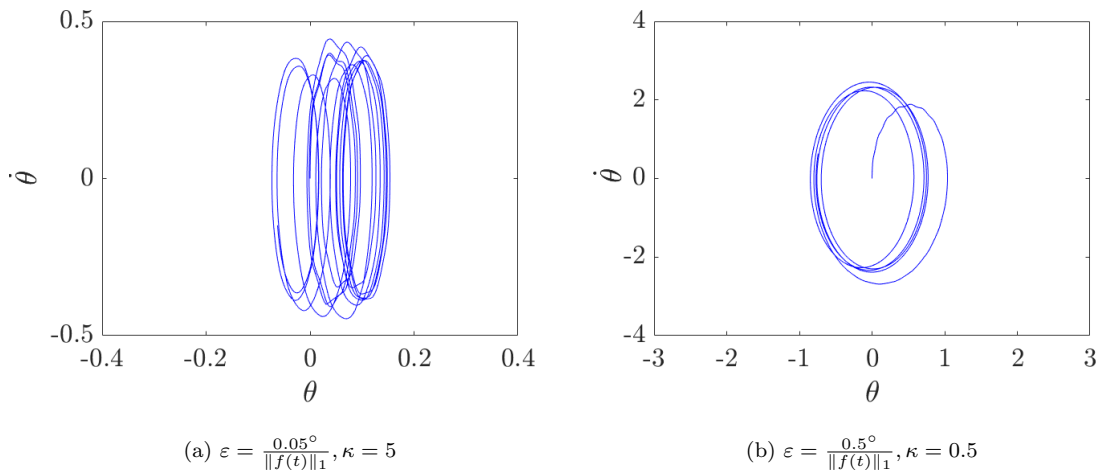
Figure 6.15 : Phase portrait.

arbitrarily close to it. This is known as practical stabilization. Hence, ultimate boundedness of trajectories to within an ε, κ-dependent neighborhood of the origin is guaranteed as shown in Figures 6.15(a) and (b). Figure 6.15(a) show that the peak error due to a thin boundary layer, $\varepsilon = \frac{0.05°}{\|f(t)\|_1}, \kappa = 5$:

$$|e_\theta(t)|_\phi = |-\theta(t)|_\phi = \varepsilon\|f(t)\|_1 < 0.2°,$$

results in an elliptical trajectories with major and minor axes $0.4°$ and $0.04°$, respectively. In Figure 6.15(b), ultimately the phase portrait is an enclosed ellipse with major and minor axes $2.2°$ and $0.7°$, respectively, together with the thick boundary $(\varepsilon = \frac{0.5°}{\|f(t)\|_1}, \kappa = 0.5)$ for $\dot{\sigma}$ around zero.

We see that (6.62) is equivalent to a feedback control problem as shown in Figure 6.12 and it can also be rearranged in linear fractional transformation (LFT) form (see Figure 6.16) as

$$\begin{bmatrix} \theta \\ e_\theta \end{bmatrix} = \overbrace{\begin{bmatrix} \frac{1}{s^2} & 0 & \frac{1}{s^2} \\ -\frac{1}{s^2} & 1 & -\frac{1}{s^2} \end{bmatrix}}^{G(s)} \begin{bmatrix} \phi \\ \theta_R \\ w \end{bmatrix}, \tag{6.64}$$

where $G(s)$ is the generalized plant and $w = sL(s)e_\theta$. Hence, the commonly-used
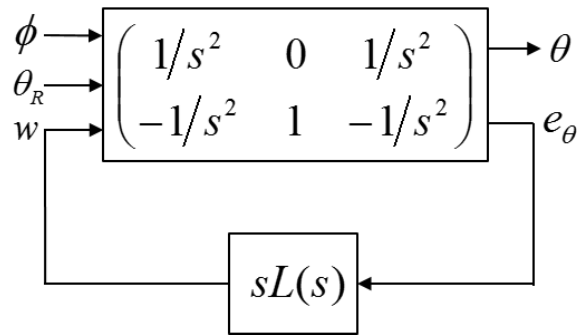
Figure 6.16 : LFT representation.

state space LQG, $\mathcal{H}_\infty$ techniques can also be employed to design the sliding surface.

6.5 Summary

In the first part of this chapter, we have encapsulated the current-dependent DFs in the frequency response of the control plant to analyze the input-output responses. The objective is to provide a strategy in the frequency domain as an alternative to state space designs in the time domain for structural control and health monitoring purposes. The controller designed uses a frequency shaped sliding surface. To do this, the system matrices are diagonalized via modal decomposition to obtain a set of n second-order systems in modal coordinates. The obtained results illustrate the effectiveness of the proposed controller for vibration suppression of MR smart structure systems.

A frequency-shaped second-order sliding mode controller (FS2SMC) has been presented in the second part. The FS2SMC is designed by incorporating a second-order Butterworth function into the sliding surface (identical to a feedback control problem) to shape the frequency characteristics of the equivalent dynamics. The sliding surface has been taken as a manifold modeled by a dynamic linear operator to suppress frequency components of the sliding mode response in a designated

frequency band. The system's closed loop performances demonstrate that the proposed control scheme is able to not only reduce the roll angle, but also to shape its spectrum, owing to the inclusion of a filter in the frequency domain. This makes the active HIS system more useful for control performance improvements of heavy vehicles, driverless cars, and UGVs.

Chapter 7

Low-Energy Structures Embedded with Smart Dampers

7.1   Introduction

Having discussed the frequency domain advantages (in Section 2.5 and Chapter 6) and cyclic energy dissipation in smart dampers (in Section 3.2), in this chapter the emphasis now shifts to the problem of energy balance in an MR based building structure subject to hostile dynamic loadings or external disturbances. Magnetorheological (MR) devices are widely used for energy-efficient protection of engineering structures to effectively withstand severe dynamic loadings. The smart device considered herein is the MR fluid damper (MRD), a semi-active device. The MRD can be controlled to adjust the damping and stiffness characteristics of the system under a low-power control signal, as well as fail-safe operations while a large amount of energy induced from external disturbance is dissipated in the fluid.

The level of possible damage of individual structural members, for example, beams, columns and roof/floor slabs can be determined by the transmitted external dynamic loading into structural vibrations. The earthquake input energy (IE) transmitted into a building from the ground motion can be decomposed into different forms: kinetic energy (KE), elastic strain energy (SE) and damping energy (DE). Here, two methods for computing the IE have been applied with one based on the absolute motion and the other on relative motion.

In the second part of this chapter, a frequency-shaped second-order sliding mode control (FS2SMC) is designed along with a low-pass filter (LPF) to implement the

desired dynamic sliding surface. The control signal exploits an equivalent control containing a frequency shaping filter and a robust signal to drive the system dynamics to the desired mechanical modes shifted away from the resonance region. For analysis of the energy flow in the smart structure, the mechanical output energy, including relative KE, DE, SE and the electrical control energy (CE) for magnetization are used as metrics for comparison.

Simulation results for a 10-floor building model equipped with current-controlled MRDs, subject to horizontal seismic excitations validate the proposed technique for low-energy structures with smart devices. The frequency responses of the hysteretic damper and combined structure are represented by its obtained describing functions (DFs) and modal decomposition, respectively, to facilitate the semi-active structural system analysis in the frequency domain. The closed-loop performance and comparison in terms of energy signals indicate that the proposed method allows not only to reduce induced vibrations and input energy, but also its spectrum can be adjusted to prevent natural modes of the structure under external excitations.

7.2 Energy balance equations of buildings with smart devices

Given an n degree-of-freedom (dof) shear structure of mass M, stiffness K, and viscous damping C, embedded with n MRDs subjected to dynamic loading sources with acceleration vector $\ddot{x}_g$, the governing equation can be described by

$$M\ddot{x} + C\dot{x} + Kx = \Gamma f_{\mathrm{MR}}(x, i) - M\ddot{x}_g, \tag{7.1}$$

where $x = r - x_g$ denotes the relative displacement between the ground and each mass and contain the dof of the system as shown in Figure 7.1. Here, r describe the vibrational absolute displacements of each floor with respect to a reference frame $xx - yy$. x_g represents the absolute ground displacement with respect to an inertial
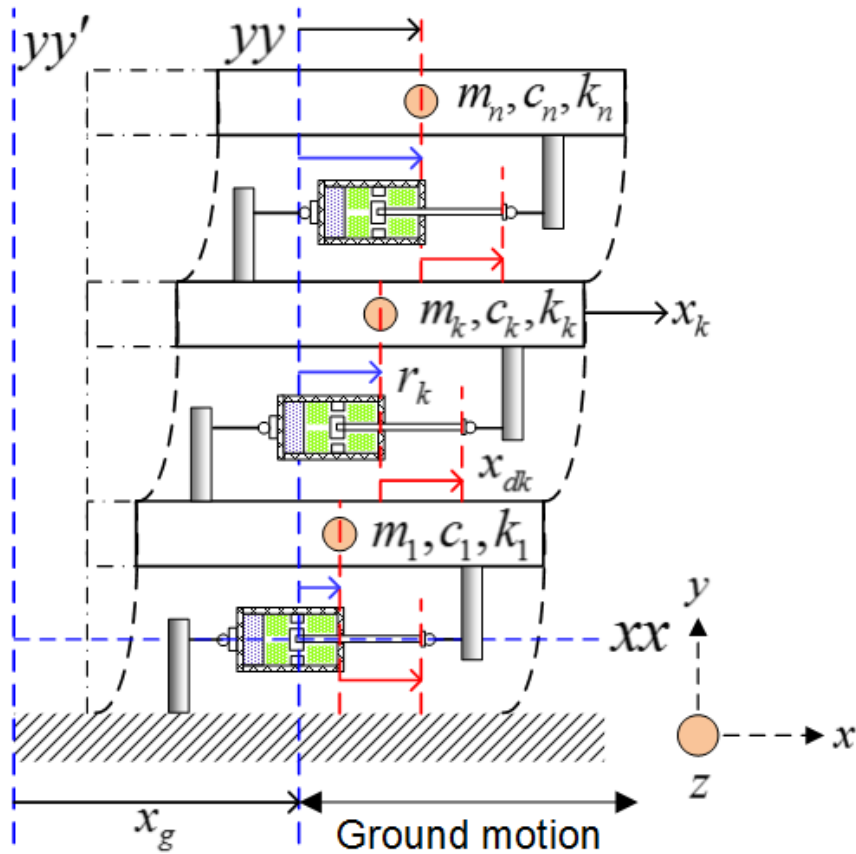
Figure 7.1 : Smart building integrated with energy-dissipative devices; $x_{dk} = x_k, k = 1, 2, \cdots, n.$

frame $xx - yy'$. The intelligent devices are rigidly mounted to the fixtures between each floor. The midpoint of each damper coincides with the intersection of axes xx and yy, i.e. the MRD's stroke $x_{dk} = x_k$ for the k-th floor; $1 \leq k \leq n$. $\Gamma \in \mathbb{R}^{n \times n}$ is a factor matrix taking into account the location and number of MRDs. $f_{\mathrm{MR}}(x, i)$ is the controllable damping force vector.

Suppose the model (7.1) satisfies the following assumptions:

($A8.1.$) the structure's M is invertible and $M^{-1}K$ has a set of n linearly indepen-
dent eigenvectors $v_1, v_2, \ldots, v_n$, i.e., all the eigenvalues $\lambda_k(M^{-1}K)$, $k = 1, 2, \cdots, n$,
are distinct and positive.

($A8.2.$) the unknown dynamic disturbance $f_d(t) = -M\ddot{x}_g$ and its time-derivative

are bounded for $t \in [0 \ \infty)$,

$(A8.3.)$ zero initial conditions, i.e., $x(t_0) = 0$, $\dot{r}(t_0) = 0$, and

$(A8.4.)$ $x = [x_1, \ldots, x_n]^{\mathrm{T}}$, $\dot{x} = [\dot{x}_1, \ldots, \dot{x}_n]^{\mathrm{T}}$ and $\ddot{x} = [\ddot{x}_1, \ldots, \ddot{x}_n]^{\mathrm{T}}$ are available for on-line measurement.

7.2.1 Relative energy balance equation

By integrating both sides of (7.1) over the structural response path from t_0 (when the ground motion excitation starts) to t, we obtain

$$\int_{x(t_0)}^{x(t)} \ddot{x}^{\mathrm{T}} M dx + \int_{x(t_0)}^{x(t)} \dot{x}^{\mathrm{T}} C dx + \int_{x(t_0)}^{x(t)} x^{\mathrm{T}} K dx = \int_{x(t_0)}^{x(t)} (\Gamma f_{\mathrm{MR}})^{\mathrm{T}} dx - \int_{x(t_0)}^{x(t)} \ddot{x}_g^{\mathrm{T}} M dx$$

$$\Rightarrow \int_{x(t_0)}^{x(t)} \dot{x}^{\mathrm{T}} M d\dot{x} + \int_{t_0}^{t} \dot{x}^{\mathrm{T}} C \dot{x} dt + \int_{x(t_0)}^{x(t)} x^{\mathrm{T}} K dx = \int_{t_0}^{t} f_{\mathrm{MR}}^{\mathrm{T}} \Gamma^{\mathrm{T}} \dot{x} dt - \int_{t_0}^{t} \ddot{x}_g^{\mathrm{T}} M \dot{x} dt$$

$$\Rightarrow \frac{1}{2} \dot{x}^{\mathrm{T}} M \dot{x} + \int_{t_0}^{t} \dot{x}^{\mathrm{T}} C \dot{x} dt + \frac{1}{2} x^{\mathrm{T}} K x = \int_{t_0}^{t} f_{\mathrm{MR}}^{\mathrm{T}} \Gamma^{\mathrm{T}} \dot{x} dt - \int_{t_0}^{t} \ddot{x}_g^{\mathrm{T}} M \dot{x} dt,$$

where $dx = \dot{x} dt$. Thus,

$$E_k + E_\zeta + E_s = E_{\mathrm{MR}} - E_i, \tag{7.2}$$

where the relative kinetic energy (KE):

$$E_k = \frac{1}{2} \dot{x}^{\mathrm{T}} M \dot{x},$$

the relative damping energy (DE):

$$E_\zeta = \int_{t_0}^{t} \dot{x}^{\mathrm{T}} C \dot{x} dt,$$

the relative strain energy (SE):

$$E_s = \frac{1}{2} x^{\mathrm{T}} K x,$$

and the relative input energy (IE):

$$E_i = \int_{t_0}^{t} \ddot{x}_g^{\mathrm{T}} M \dot{x} dt.$$

The MRD dissipated energy is given by

$$E_{\mathrm{MR}} = \int_{t_0}^{t} f_{\mathrm{MR}}^{\mathrm{T}} \Gamma^{\mathrm{T}} \dot{x} dt.$$

7.2.2 Absolute energy balance equation

The absolute KE and IE, respectively, can also be defined by

$$E_k' = \frac{1}{2}\dot{r}^{\mathrm{T}}M\dot{r}$$

and

$$E_i' = \int_{t_0}^{t} \ddot{r}^{\mathrm{T}}M\dot{x}_g dt,$$

where r is the vibrational absolute (or total) displacement, $\dot{r}$ is absolute velocity and $\ddot{r}$ denotes the absolute acceleration such that

$$r = x + x_g, \ \dot{r} = \dot{x} + \dot{x}_g, \ \ddot{r} = \ddot{x} + \ddot{x}_g.$$

The residual absolute energy terms can be derived similarly as (7.2). The absolute energy equation is then expressed as

$$E_k' + E_\zeta + E_s = E_{\mathrm{MR}} - E_i'. \tag{7.3}$$

7.3 FS2SMC of low-energy structures

After having established the energy relations of a building structure embedded with smart dampers, we now proceed with the robust control design to inject a small amount of control energy to dissipate vibration energy induced by external disturbances to the structure. To directly adjust the structural frequency response and to improve robustness performance, the second-order sliding mode control (2SMC) method is adopted here to achieve resilience of smart structures. Indeed, by incorporating the frequency response functions (FRFs) of the embedded devices, the control design can be proceeded in the frequency domain to facilitate the low-energy structure analysis. Thus, in the following a frequency-shaped (FS) second-order sliding mode controller (FS2SMC) is developed and applied to the structural model of buildings embedded with intelligent dissipation devices.

7.3.1 Energy-aware design

It can be shown that the nonlinear non-affine dynamic system (7.1) of a single-input embedded smart structure can be rendered to an n-th order nonlinear system of the form [21]

$$\dot{z} = h(z) + g(z, u), \tag{7.4}$$

where $z \in \mathbb{R}^n$ is the state, $u \in \mathbb{R}$ is the control input, $h(\cdot)$ and $g(\cdot, \cdot) \geq g_0 > 0$ are some smooth nonlinear functions. Our goal is to design a robustly stabilizing control $u = U(z)$ that steers the trajectories onto the manifold (or surface) $\sigma \equiv 0$ in finite time.

In order to dynamically shape the frequency response of the equivalent dynamics, the sliding function is cast by using a dynamic linear operator $L(s)$, a function of s. The dynamic sliding surface is designed with a second-order LPF as

$$\sigma = \mathcal{L}(s)z = \sum_{k=1}^{n-1} L(s)z_k + z_n, \tag{7.5}$$

where $\mathcal{L}(s) = [L(s), \dots, L(s), 1]$, for example, to get a steeper rolloff of $|L(j\omega)|$, $\omega \in [0, \infty)$ for large values of ω. Herein, $L(s) = \frac{b_0}{s^2 + a_1 s + a_0}$ gives a $|L(j\omega)|$ with an asymptotic slope of -40 dB/decade above cut-off frequency.

The algebraic manipulation of (7.5) gives

$$\sigma = \frac{b_0}{s^2 + a_1 s + a_0} z_1 + \cdots + \frac{b_0}{s^2 + a_1 s + a_0} x_{n-1} + z_n$$

$$\Rightarrow \ddot{\sigma} + \sigma(a_1 s + a_0) = b_0 \big(z_1 + \cdots + z_{n-1}\big) + \ddot{z}_n + x_n(a_1 s + a_0)$$

$$\Rightarrow \ddot{\sigma} = b_0 \sum_{k=1}^{n-1} z_k + \ddot{z}_n - (a_1 s + a_0)\big(\sigma - z_n\big)$$

$$\Rightarrow \ddot{\sigma} = b_0 \sum_{k=1}^{n-1} z_k + \ddot{z}_n - (a_1 s + a_0)\Big(\frac{b_0 \sum_{k=1}^{n-1} z_k}{s^2 + a_1 s + a_0}\Big)$$

$$\Rightarrow \ddot{\sigma} = b_0 \Big(\frac{s^2}{s^2 + a_1 s + a_0}\Big) \sum_{k=1}^{n-1} z_k + \frac{\partial h}{\partial z}\dot{z} + \frac{\partial g}{\partial z}\dot{z} + g(z)\dot{u}.$$

Now, we have

$$\ddot{\sigma} = s^2 L(s) z_1 + \cdots + s^2 L(s) z_{n-1} + H(z, u) + g(z) v, \qquad (7.6)$$

where $H = \frac{\partial h}{\partial z} \dot{z} + \frac{\partial g}{\partial z} \dot{z}$ and $v = \dot{u}$ is denoted as the new control variable [135].

Let $\hat{g}$ and $\hat{H}$ be nominal models of g and H, respectively. Taking

$$v = -\frac{s^2 L(s) z_1 + \cdots + s^2 L(s) z_{n-1} + \hat{H}}{\hat{g}} + v_R$$

results in

$$
\begin{aligned}
\ddot{\sigma} &= \sum_{k=1}^{n-1} s^2 L(s) z_k + H - \frac{g(z)}{\hat{g}(z)} \sum_{k=1}^{n-1} s^2 L(s) z_k - \frac{g(z)}{\hat{g}(z)} \hat{H} + g(z) v_R \\
&= H - \frac{g(z)}{\hat{g}(z)} \hat{H} + \sum_{k=1}^{n-1} s^2 L(s) z_k \left[1 - \frac{g(z)}{\hat{g}(z)} \right] + g(z) v_R \qquad (7.7) \\
&= \delta(z) + g(z) v_R,
\end{aligned}
$$

where $\delta(z) := H - \frac{g(z)}{\hat{g}(z)} \hat{H} + \sum_{k=1}^{n-1} s^2 L(s) z_k \left[1 - \frac{g(z)}{\hat{g}(z)} \right]$.

Suppose the perturbation term $\delta(z)$ satisfies the inequality

$$\left| \frac{\delta(z)}{g(z)} \right| \leq \varrho(z) \qquad (7.8)$$

for some known positive definite function $\varrho(z)$.

With $V = \frac{1}{2} \dot{\sigma}^2$ chosen as a Lyapunov function candidate for (7.6), the time derivative of V can be computed as

$$\dot{V} = \dot{\sigma} \ddot{\sigma} = \dot{\sigma} \left[\delta(z) + g(z) v_R \right] \leq g(z) |\dot{\sigma}| \varrho(z) + g(z) \dot{\sigma} v_R. \qquad (7.9)$$

To achieve the control objective, the robust signal v_R is selected as

$$v_R = -\beta(z) \operatorname{sgn}(\dot{\sigma}) - \kappa \dot{\sigma}, \ \ \kappa > 0, \qquad (7.10)$$

with

$$\beta(z) \geq \varrho(z) + \eta, \ \ \eta > 0,$$

so that the term $g(z)\dot{\sigma}v_R$ is negative and dominates over the residual term $g(z)|\dot{\sigma}|\varrho(x)$ when $\dot{\sigma} \neq 0$, giving the net results to force $|\dot{\sigma}|$ to reach zero. Finally, we have

$$v = -\frac{s^2 L(s)z_1 + \cdots + s^2 L(s)z_{n-1} + \hat{H}}{\hat{g}(z)} - \beta(z)\,\mathrm{sgn}(\dot{\sigma}) - \kappa\dot{\sigma}. \qquad (7.11)$$

Substituting (7.10) into (7.9) yields

$$\dot{V} \leq g(z)|\dot{\sigma}|\varrho(z) - g(x)\beta(z)\dot{\sigma}\,\mathrm{sgn}(\dot{\sigma}) - g(z)\kappa\dot{\sigma}^2$$

$$\leq g(z)|\dot{\sigma}|\varrho(z) - g(z)\big(\varrho(z) + \eta\big)|\dot{\sigma}| - g(z)\kappa\dot{\sigma}^2 = -g(z)\eta|\dot{\sigma}| - g(z)\kappa\dot{\sigma}^2 \qquad (7.12)$$

$$\leq -g_0\eta|\dot{\sigma}| - g_0\kappa\dot{\sigma}^2 \leq -g_0\kappa\dot{\sigma}^2 = -2g_0\kappa V.$$

where g_0 is defined in (7.4). By separating the variables and integrating the differential inequality over the time interval $t_0 \leq \tau \leq t$, we obtain

$$V(t) \leq V(t_0)e^{-2\kappa g_0(t-t_0)}. \qquad (7.13)$$

Thus, $V(t)$ will tend to zero exponentially where κ is the decay rate at which the sliding surface is attained. From (7.9) and (7.12), we obtain

$$\dot{\sigma}\ddot{\sigma} \leq -g_0\eta|\dot{\sigma}| - g_0\kappa\dot{\sigma}^2. \qquad (7.14)$$

Since $g_0\kappa\dot{\sigma}^2 \geq 0$, and by neglecting the nonlinear term, we also have

$$\frac{d}{dt}|\dot{\sigma}(t)| \leq -g_0\kappa|\dot{\sigma}(t)| \Rightarrow |\dot{\sigma}(t)| \leq |\dot{\sigma}(t_0)|e^{-\kappa g_0(t-t_0)} \qquad (7.15)$$

to substantially reduce the amplitude of the switching term in the control and hence, the commonly encountered chattering problem associated with sliding mode control.

7.3.2 Smart structural control

To further implement the proposed FS2SMC strategy (stated in the previous section) to low-energy MRD-embedded structures, a modal transformation (described in Section 6.2.1 of the previous chapter) is first applied to the structure dynamics, e.g. of a multi-floor building. Take the transformation [106],[137],

$$x = \sum_{k=1}^{n} v_k q_k(t) = \Phi q, \qquad (7.16)$$

where

$$\Phi = \begin{bmatrix} | & | & \cdots & | \\ v_1 & v_2 & \cdots & v_n \\ | & | & \cdots & | \end{bmatrix} = \begin{bmatrix} v_{11} & v_{12} & \cdots & v_{1n} \\ v_{21} & v_{22} & \cdots & v_{2n} \\ \vdots & \vdots & \ddots & \vdots \\ v_{n1} & v_{n2} & \cdots & v_{nn} \end{bmatrix}$$

is called the modal transformation matrix (MTM); $\vec{v}$ is the mode shape or eigen-vectors; and $q = [q_1, q_2, \ldots, q_n]^{\mathrm{T}}$ is the real-valued modal coordinate vector.

Then, we can obtain a set of n second-order motion equations decoupled from (7.1) for each mode, $m \in [1, n]$, as:

$$\ddot{q}_m + 2\zeta_m \omega_m \dot{q}_m + \sum_{r=1, r \neq m}^{n} \mu_{mr} \dot{q}_r + \omega_m^2 q_m = u_m + d_m, \tag{7.17}$$

where ω_m, ζ_m, u_m, q_m, d_m, and μ_{mr} are respectively the m-th modal frequency, damping ratio, entry of the modal control,

$$u = \Phi^{-1} M^{-1} \Gamma f_{\mathrm{MR}} = \Omega f_{\mathrm{MR}}, \tag{7.18}$$

modal coordinate, disturbance component and the mrth modal coupling term of the damping matrix. Here, $\Omega = \Phi^{-1} M^{-1} \Gamma f_{\mathrm{MR}}$ is called the mode participation matrix (MPM).

From (7.5) and (7.6), the following frequency-shaped sliding function is designed:

$$\begin{aligned} \sigma_m &= \frac{b_0}{s^2 + a_1 s + a_0} q_m + \dot{q}_m = L_m(s) q_m + \dot{q}_m \\ \Rightarrow \ddot{\sigma}_m &= s^2 L_m(s) q_m - 2\zeta_m \omega_m \ddot{q}_m - \sum_{r=1, r \neq m}^{n} \mu_{mr} \ddot{q}_r - \omega_m^2 \dot{q}_m + v_m + \dot{d}_m, \end{aligned} \tag{7.19}$$

where $v_m = \dot{u}_m$ is the new control instead of the modal control u_m.

We derive the equivalent control $\hat{v}_m$ to achieve $\ddot{\sigma}_m = 0$ as follows

$$\hat{v}_m = \hat{\omega}_m^2 \dot{q}_m + 2\hat{\zeta}_m \hat{\omega}_m \ddot{q}_m + \sum_{r=1, r \neq m}^{n} \hat{\mu}_{mr} \ddot{q}_r - \hat{\dot{d}}_m - s^2 L_m(s) q_m, \tag{7.20}$$

where $\hat{\omega}_m, \hat{\zeta}_m, \hat{\dot{d}}_m$, and $\hat{\mu}_{mr}$ are desired values chosen for the m-th modal frequency, modal damping, first derivative of the disturbance, and modal coupling from the damping matrix, respectively.

By applying the control law (7.11) for $v_m = \hat{v}_m + v_{Rm}$, we obtain the following FS2SMC:

$$v_m = \hat{\omega}_m^2 \dot{q}_m + 2\hat{\zeta}_m \hat{\omega}_m \ddot{q}_m + \sum_{r=1}^{n} \hat{\mu}_{mr} \ddot{q}_r - s^2 L_m(s) q_m - \hat{\dot{d}}_m - \beta_m \operatorname{sgn}(\dot{\sigma}_m) - \kappa_m \dot{\sigma}_m, \quad (7.21)$$

that can ensure the condition

$$\dot{\sigma}_m \ddot{\sigma}_m \leq -\eta_m |\dot{\sigma}_m| - \kappa_m \dot{\sigma}_m^2$$

as in (7.12), by taking $\beta_m = \varrho_m + \eta_m$ sufficiently large.

7.4 Application and simulation

In this section, the FS2SMC designed in Section 7.3.2 is applied to a 10-storey shear building model [138] with identical values for floor mass m_k, damping c_k, and stiffness k_k of each floor. This structure is assumed to be satisfied assumptions (*A8.1.*) - (*A8.4.*) with the following equation:

$$M\ddot{x} + C\dot{x} + Kx = \Gamma f_{\mathrm{MR}} + f_d, \quad (7.22)$$

where the positive-definite mass (in kg), damping (in Ns/m) and stiffness (in N/m) matrices are respectively given by

$$M = \begin{bmatrix} 360000 & 0 & 0 & \cdots & 0 \\ 0 & 360000 & 0 & \cdots & 0 \\ 0 & 0 & 360000 & \cdots & 0 \\ \vdots & \vdots & \vdots & \ddots & \vdots \\ 0 & 0 & 0 & \cdots & 360000 \end{bmatrix} \in \mathbb{R}^{10 \times 10},$$

$$C = \begin{bmatrix} 12.4 & -6.2 & 0 & 0 & 0 & 0 & 0 & 0 & 0 & 0 \\ -6.2 & 12.4 & -6.2 & 0 & 0 & 0 & 0 & 0 & 0 & 0 \\ 0 & -6.2 & 12.4 & -6.2 & 0 & 0 & 0 & 0 & 0 & 0 \\ 0 & 0 & -6.2 & 12.4 & -6.2 & 0 & 0 & 0 & 0 & 0 \\ 0 & 0 & 0 & -6.2 & 12.4 & -6.2 & 0 & 0 & 0 & 0 \\ 0 & 0 & 0 & 0 & -6.2 & 12.4 & -6.2 & 0 & 0 & 0 \\ 0 & 0 & 0 & 0 & 0 & -6.2 & 12.4 & -6.2 & 0 & 0 \\ 0 & 0 & 0 & 0 & 0 & 0 & -6.2 & 12.4 & -6.2 & 0 \\ 0 & 0 & 0 & 0 & 0 & 0 & 0 & -6.2 & 12.4 & -6.2 \\ 0 & 0 & 0 & 0 & 0 & 0 & 0 & 0 & -6.2 & 6.2 \end{bmatrix} \times 10^6,$$

and

$$K = \begin{bmatrix} 1300 & -650 & 0 & 0 & 0 & 0 & 0 & 0 & 0 & 0 \\ -650 & 1300 & -650 & 0 & 0 & 0 & 0 & 0 & 0 & 0 \\ 0 & -650 & 1300 & -650 & 0 & 0 & 0 & 0 & 0 & 0 \\ 0 & 0 & -650 & 1300 & -650 & 0 & 0 & 0 & 0 & 0 \\ 0 & 0 & 0 & -650 & 1300 & -650 & 0 & 0 & 0 & 0 \\ 0 & 0 & 0 & 0 & -650 & 1300 & -650 & 0 & 0 & 0 \\ 0 & 0 & 0 & 0 & 0 & -650 & 1300 & -650 & 0 & 0 \\ 0 & 0 & 0 & 0 & 0 & 0 & -650 & 1300 & -650 & 0 \\ 0 & 0 & 0 & 0 & 0 & 0 & 0 & -650 & 1300 & -650 \\ 0 & 0 & 0 & 0 & 0 & 0 & 0 & 0 & -650 & 650 \end{bmatrix} \times 10^6.$$

Notably, using full-scale MRDs [18], one can reach an output damping force of 182.1 kN and a controllable force of 164.38 kN in conjunction with appropriate control strategy.

7.4.1 Modal decomposition and control design

Since the mass matrix

$$M = \text{diag}\,(m_k) = M^{\text{T}} > 0, \ k = 1, 2, \ldots, 10,$$

is nonsingular, (7.22) is written for this case as

$$\ddot{x} + M^{-1}C\dot{x} + M^{-1}Kx = M^{-1}\Gamma f_{\text{MR}} + M^{-1}f_d, \ x \in \mathbb{R}^{10}, \tag{7.23}$$

where

$$M^{-1}K = \begin{bmatrix} \frac{k_1+k_2}{m_1} & \frac{-k_2}{m_1} & 0 & \cdots & \cdots & 0 \\ \frac{-k_2}{m_2} & \frac{k_2+k_3}{m_2} & \frac{-k_3}{m_2} & 0 & \cdots & \vdots \\ 0 & \frac{-k_3}{m_3} & \ddots & \ddots & \ddots & \vdots \\ \vdots & 0 & \ddots & \ddots & \frac{-k_9}{m_8} & 0 \\ \vdots & \vdots & \ddots & \frac{-k_9}{m_9} & \frac{k_9+k_{10}}{m_9} & \frac{-k_{10}}{m_9} \\ 0 & \cdots & \cdots & 0 & \frac{-k_{10}}{m_{10}} & \frac{k_{10}}{m_{10}} \end{bmatrix} = \Phi\Lambda\Phi^{-1} \in \mathbb{R}^{10\times 10};$$

$$\Lambda = \begin{bmatrix} 40.33 & 0 & 0 & 0 & 0 & 0 & 0 & 0 & 0 & 0 \\ 0 & 357.61 & 0 & 0 & 0 & 0 & 0 & 0 & 0 & 0 \\ 0 & 0 & 963.98 & 0 & 0 & 0 & 0 & 0 & 0 & 0 \\ 0 & 0 & 0 & 1805.56 & 0 & 0 & 0 & 0 & 0 & 0 \\ 0 & 0 & 0 & 0 & 2807.56 & 0 & 0 & 0 & 0 & 0 \\ 0 & 0 & 0 & 0 & 0 & 3880.97 & 0 & 0 & 0 & 0 \\ 0 & 0 & 0 & 0 & 0 & 0 & 4930.39 & 0 & 0 & 0 \\ 0 & 0 & 0 & 0 & 0 & 0 & 0 & 5862.60 & 0 & 0 \\ 0 & 0 & 0 & 0 & 0 & 0 & 0 & 0 & 6594.75 & 0 \\ 0 & 0 & 0 & 0 & 0 & 0 & 0 & 0 & 0 & 7061.79 \end{bmatrix}$$

is formed from the eigenvalues of $M^{-1}K$. The orthogonal matrix Φ is formed from the associated eigenvectors:

$$\upsilon_1 = [0.065, 0.129, 0.189, 0.246, 0.297, 0.341, 0.378, 0.406, 0.426, 0.435]^{\mathrm{T}},$$

$$\upsilon_2 = [-0.189, -0.341, -0.426, -0.426, -0.341, -0.189, 0, 0.189, 0.341, 0.426]^{\mathrm{T}},$$

$$\upsilon_3 = [-0.297 - 0.435 - 0.341 - 0.0650.2460.4260.3780.129 - 0.189 - 0.406]^{\mathrm{T}},$$

$$\upsilon_4 = [0.378, 0.378, 0, -0.378, -0.378, 0, 0.378, 0.378, 0, -0.378]^{\mathrm{T}},$$

$$\upsilon_5 = [-0.426, -0.189, 0.341, 0.341, -0.189, -0.426, 0, 0.426, 0.189, -0.341]^{\mathrm{T}},$$

$$\upsilon_6 = [0.435, -0.065, -0.426, 0.129, 0.406, -0.189, -0.378, 0.246, 0.341, -0.297]^{\mathrm{T}},$$

$$\upsilon_7 = [-0.406, 0.297, 0.189, -0.435, 0.129, 0.341, -0.378, -0.065, 0.426, -0.246]^{\mathrm{T}},$$

$$\upsilon_8 = [0.341, -0.426, 0.189, 0.189, -0.426, 0.341, 0, -0.341, 0.426, -0.189]^{\mathrm{T}},$$

$$\upsilon_9 = [0.246, -0.406, 0.426, -0.297, 0.065, 0.189, -0.378, 0.435, -0.341, 0.129]^{\mathrm{T}},$$

$$\upsilon_{10} = [-0.129, 0.246, -0.341, 0.406, -0.435, 0.426, -0.378, 0.297, -0.189, 0.065]^{\mathrm{T}}.$$

The diagonal and modal coupling terms of the damping matrix, i.e. $2\zeta_k\omega_k$ and μ_{kr}, can be respectively obtained, for $r \neq k$ with no dampers attached, as

$$\frac{\omega_k}{2\pi} = 1.01, 3.01, 4.94, 6.76, 8.43, 9.91, 11.18, 12.19, 12.93, 13.37 \text{ Hz (see Figure 7.2)},$$

$$\zeta_k = 0.19, 0.57, 0.93, 1.27, 1.59, 1.87, 2.1, 2.29, 2.43, 2.52.$$

The off-diagonal damping is bounded by

$$\mu_{kr} \in [-1.27 \times 10^{-14}, 2.39 \times 10^{-14}].$$

Hence, the off-diagonal damping is taken as the lower bound of the diagonal elements, i.e.

$$\mu_{kr} = \min(2\zeta_k\omega_k) = 0.38,$$
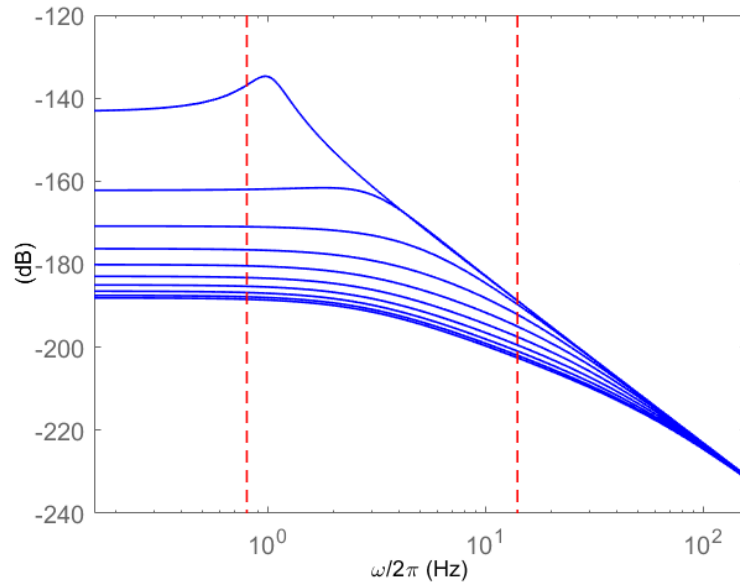
while designing the FS2SMC.

Figure 7.2 : Singular value plot of $H(j\omega)$.

Under a harmonic excitation at an angular frequency ω, the controlled smart devices $\Gamma f_{\mathrm{MR}}(q,i)$ can be modelled in the frequency domain as $DF_{\mathrm{MR}}Q(j\omega) \in \mathbb{C}^{10}$:

$$
\Gamma f_{\mathrm{MR}}(q,i) \rightarrow
\begin{bmatrix}
\gamma_1 N_1 e^{j\phi_1} & \varepsilon_{1,2} & \varepsilon_{1,3} & \cdots & \varepsilon_{1,10} \\
\varepsilon_{2,1} & \gamma_2 N_2 e^{j\phi_2} & \varepsilon_{2,3} & \cdots & \varepsilon_{2,10} \\
\varepsilon_{3,1} & \varepsilon_{3,2} & \gamma_3 N_3 e^{j\phi_3} & \cdots & \varepsilon_{3,10} \\
\vdots & \vdots & \vdots & \ddots & \vdots \\
\varepsilon_{10,1} & \varepsilon_{10,2} & \varepsilon_{10,3} & \cdots & \gamma_{10} N_{10} e^{j\phi_{10}}
\end{bmatrix}
\begin{bmatrix}
q_1(j\omega) \\
q_2(j\omega) \\
q_3(j\omega) \\
\vdots \\
q_{10}(j\omega)
\end{bmatrix},
$$

where

$$
\varepsilon_{k,r} \in [0 \quad \gamma_k N_k e^{j\phi_k}]; \; k \neq r, \; 1 \leq (k,r) \leq 10,
$$

denotes inter-floor damping from the MRDs mounted between the k-th and $(k-1)$-th floors and γ_k is a factor taking into account the placement and number of MRDs.

Thus,

$$\left[-\omega^2 + 2j\omega\zeta_k\omega_k + \omega_k^2\right]q_k(j\omega) + \sum_{r=1,r\neq k}^{10}\mu_{kr}j\omega q_r(j\omega) = -$$

$$\left[\frac{\gamma_k N_k e^{j\phi_k}}{m_k}q_k(j\omega) + \sum_{r=1,r\neq k}^{10}\frac{\varepsilon_{kr}}{m_k}q_r(j\omega)\right] + \Upsilon F_d(j\omega),\ \Upsilon = \Phi^{-1}M^{-1},$$

(7.24)

Equation (7.24) can be rewritten as

$$\left[-\omega^2 + 2j\omega\zeta_k\omega_k + \omega_k^2 + \frac{\gamma_k N_k e^{j\phi_k}}{m_k}\right]\Phi^{-1}x_k(j\omega)$$

$$+ \left[\sum_{r=1,r\neq k}^{10}\mu_{kr}j\omega + \sum_{r=1,r\neq k}^{10}\frac{\varepsilon_{kr}}{m_k}\right]\Phi^{-1}x_r(j\omega) = \Upsilon F_d(j\omega).$$

(7.25)

Since the damping capability always takes its strongest effect at the level where the MRDs are installed, DF_{MR} can be considered as diagonally dominant, thus including only terms $\gamma_k N_k e^{j\phi_k}$. Other the coupling terms from the residual modes and modal decomposition errors can be lumped to disturbance d_k.

Taking the assumption of Rayleigh damping [31, 33], the frequency response function (FRF) matrix, $H(j\omega)$, of the smart structure is therefore obtained as .

$$H(j\omega) =$$

$$\Phi\begin{bmatrix} \frac{1}{\omega_1^2-\omega^2+2j\zeta_1\omega\omega_1+\frac{\gamma_1 N_1 e^{j\phi_1}}{m_1}} & 0 & \cdots & 0 \\ 0 & \frac{1}{\omega_2^2-\omega^2+2j\zeta_2\omega\omega_2+\frac{\gamma_2 N_2 e^{j\phi_2}}{m_2}} & \ddots & \vdots \\ \vdots & 0 & \ddots & 0 \\ 0 & \cdots & 0 & \frac{1}{\omega_{10}^2-\omega^2+2j\zeta_{10}\omega\omega_{10}+\frac{\gamma_{10} N_{10} e^{j\phi_{10}}}{m_{10}}} \end{bmatrix}\Upsilon.$$

(7.26)

The transfer function of the DF model is approximated as

$$N_k e^{j\phi_k} \simeq N_k(1 + \tau_k s),$$

(7.27)

where the MRD equivalent time constant,

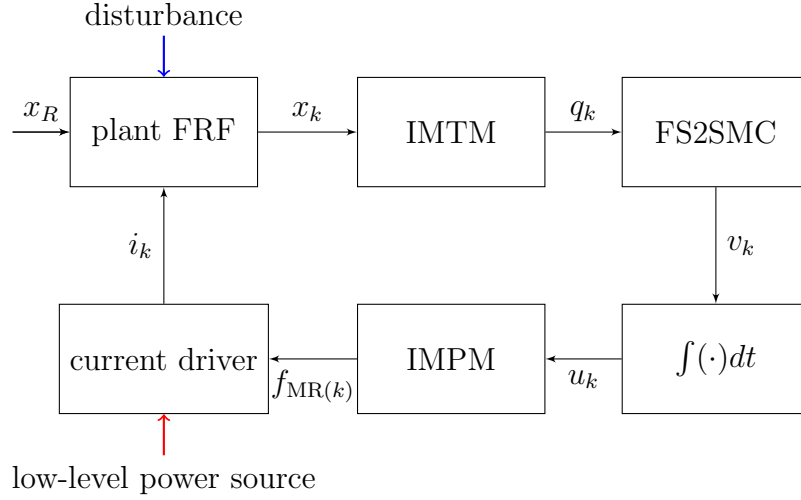$$\tau_k = \frac{\phi_{0k}}{\omega_k N_{0k}},$$

(7.28)

Figure 7.3 : Closed-loop block diagram of the modal FS2SMC of the smart structure.

is estimated at normalized values of amplitude $E = 1$, current $i = 1$ and first modal frequency $\omega_1 = 1$. Hence, the FRF of the smart structure is

$$H(j\omega) = \sum_{k=1}^{10} \frac{\Phi_k \Upsilon_k^{\mathrm{T}}}{\omega_k^2 - \omega^2 + \frac{\gamma_k N_k}{m_k} + j\omega\left(2\zeta_k\omega_k + \frac{\gamma_k N_k \tau_k}{m_k}\right)}. \tag{7.29}$$

The amplitude of input-output gain of the system as a function of frequency $(\omega/2\pi)$ is shown in Figure 7.2.

In our design, the controller parameters are chosen as $\kappa_k = 10, \eta_k = 1.25$ and $L(s)$ is a Butterworth filter, i.e. $L(s) = \frac{1}{s^2 + 1.4142s + 1}$. Notably, for the control law (7.21), a boundary layer [81] may be used in lieu of the signum function to smooth the response if necessary.

From the modal control, i.e.

$$u_k = \int v_k(t)dt, \tag{7.30}$$

the damping force can be computed as

$$f_{\mathrm{MR}(k)} = \Omega^{-1}u_k, \tag{7.31}$$

in which Ω^{-1} is the inverse mode participation matrix (IMPM). The controllable force range should be constrained by the maximum capacity, i_{M} and the residual

force at zero current in the passive control case. For example, the relation between magnetization current and damping force has the following form:

$$i_k = \begin{cases} |p_0 + p_1 f_{\mathrm{MR}(k)} + p_2 f_{\mathrm{MR}(k)}^2|, & |i_k| < i_{\mathrm{M}}, \\ 0, & |i_k| \geq i_{\mathrm{M}}, \end{cases} \tag{7.32}$$

where $p_0 = 0.127$, $p_1 = -0.00094$ and $p_2 = 0.0000021$ for the RD-8041-1 at $i_{\mathrm{M}} = 2$ A. A schematic block diagram of the modal FS2SMC procedure for the multi-dof smart structure system is shown in Figure 7.3 where as $q(t) = \Phi^{-1} x(t)$; Φ^{-1} is the inverse modal transformation matrix (IMTM).

7.4.2 Simulation results

In the simulation, four benchmark earthquake records (El-Centro 1940, Hachinohe 1968, Northridge 1994, Kobe 1995) are considered to excite the system as external disturbances. We normalized the structural dynamics and all quake records to a maximum acceleration level of $0.3g$ so that we have

$$x_{dk} = x_k < 15 \text{ mm}$$

corresponding to the operational stroke and capacity of the experimental dampers RD-8041-1. Extensive simulation was conducted with the scaled-down four benchmark quake records.

Typical results are shown in Figure 7.4 for the first floor's phase portrait of the uncontrolled and closed-loop motion under $0.3g$ record of the El-Centro earthquake. Also, the spectrum of the first, fourth, sixth, eight and top floor modes for the controlled case is depicted in Figure 7.5. It can be seen that not only a significant reduction in displacement and velocity trajectories are observed with the proposed controller, but also the system resonant frequencies are shifted further due to the proposed FS2SMC to avoid building collapse from frequency resonance.

Feasibility of the proposed controller is verified via the time responses of the controlled current signals, which are positive and constrained to 2 A, of the MRDs
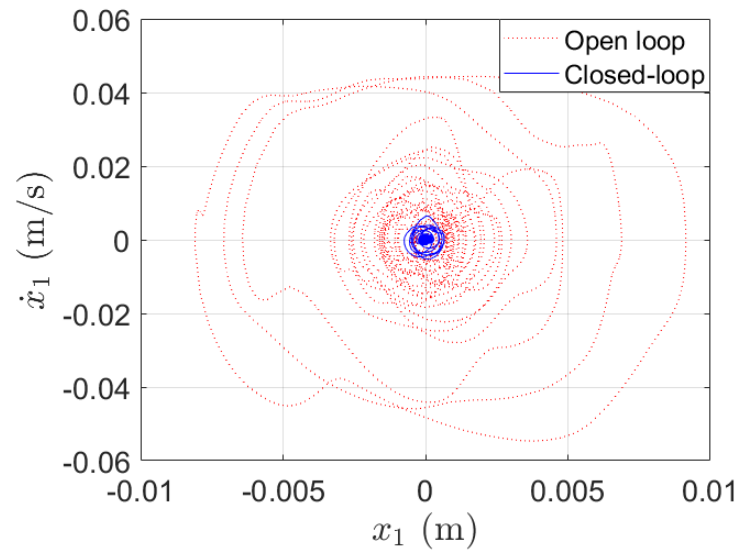
Figure 7.4 : Closed-loop and open-loop phase portrait.
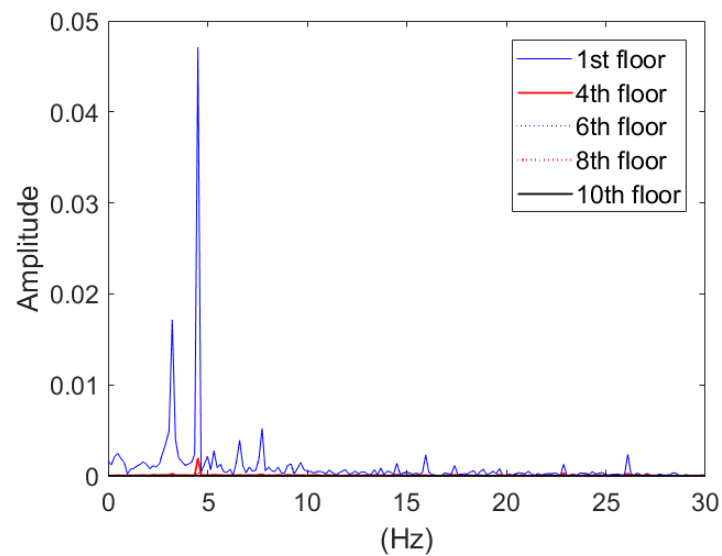
Figure 7.5 : The spectrum of the first, fourth, sixth, eight and top floor modes for the controlled case.

attached to the first and top floors, as plotted in Figure 7.6. Under the frequency shaped robust control strategy, not only seismic vibrations can be effectively suppressed but also the structural control responses involved can be kept at a low-energy level. Indeed, the conjugate force-displacement trajectory of the MRD under the

Figure 7.6 : MRD current.

Figure 7.7 : MRD force-displacement trajectory

scaled-down seismic disturbance is depicted in Figure 7.7, in which

$$x_{d1} = x_1$$

and

$$f_{\text{MR}(1)} = \Omega^{-1} u_1.$$

The associated kinetic, damping, strain and input energy processes are analyzed in the next section.

7.5   Discussion

Since internal forces within an engineering structure can be derived using relative displacements and velocities, we herein compute the input energy (IE) in terms of the relative motion as stated in the Section 7.2.1.

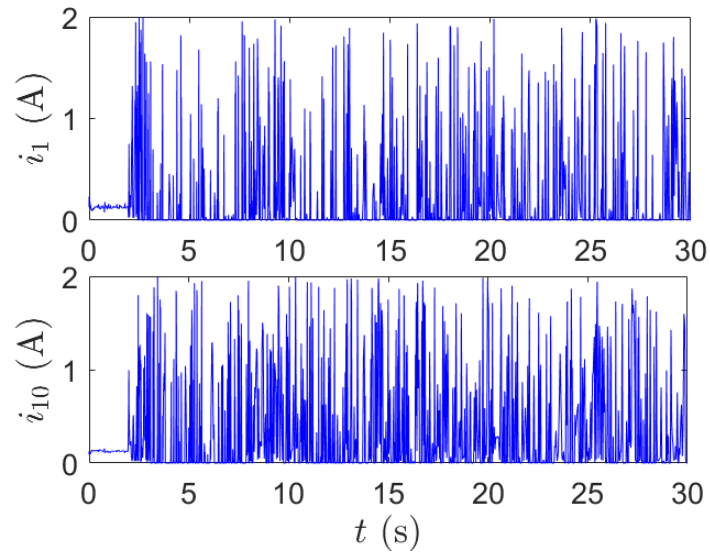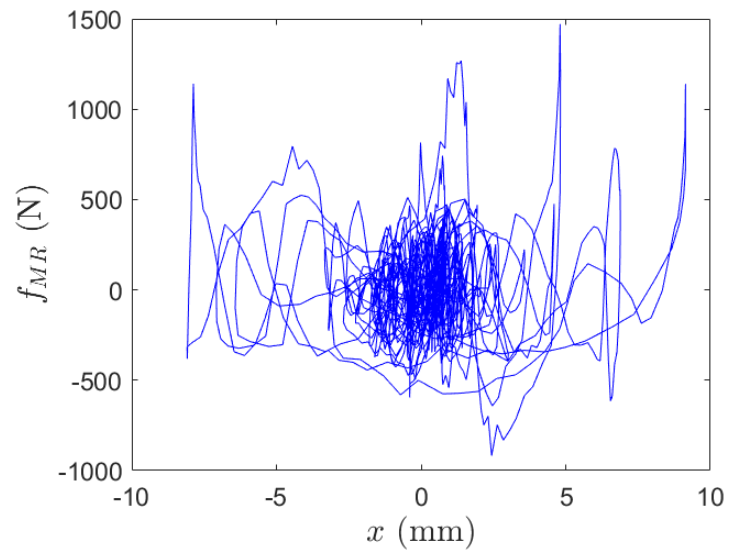For analysis of the energy flow in the smart structure, we present in Figures 7.8 and 7.9 the relative kinetic energy (KE), damping energy (DE), strain energy (SE), and IE signals with respect to displacement and velocity under $0.3g$ record of the El-Centro earthquake in both uncontrolled and controlled cases, respectively. Generally, from zero initial conditions,

$$x_k(t_0) = \dot{r}_k(t_0) = 0,$$

output energy (OE) components, i.e., E_k, E_ζ, E_s, and E_i begin to increase from zero when $t \in [t_0 \ \infty)$ under a horizontal ground motion excitation $\ddot{x}_g$ starting at t_0.

In the uncontrolled case, the input energy received from the external disturbance transmitted through the foundation of the smart structural system. The induced energy signal distributes to the kinetic, passive damping, and strain energy of the structure as mechanical OE, i.e. E_k, E_ζ, E_s and consequently, may exceed a permissible threshold causing structural damage when the magnitude of seismic input is too large. Indeed, due to excessive lateral motion results in structural inability to dissipate the intrinsic E_k, E_ζ, E_s, constituted from the transmitted E_i signal, which may eventually lead to serious structural damage.

For the controlled case, the reference is ideally set at $x_R = 0$ with

$$L(s) = \frac{1}{s^2 + 1.4142s + 1}, \ \kappa_k = 10, \ \text{and} \ \eta_k = 1.25.$$

(a) Open-loop E_k

(b) Open-loop E_ζ

(c) Open-loop E_s

(d) Open-loop E_i
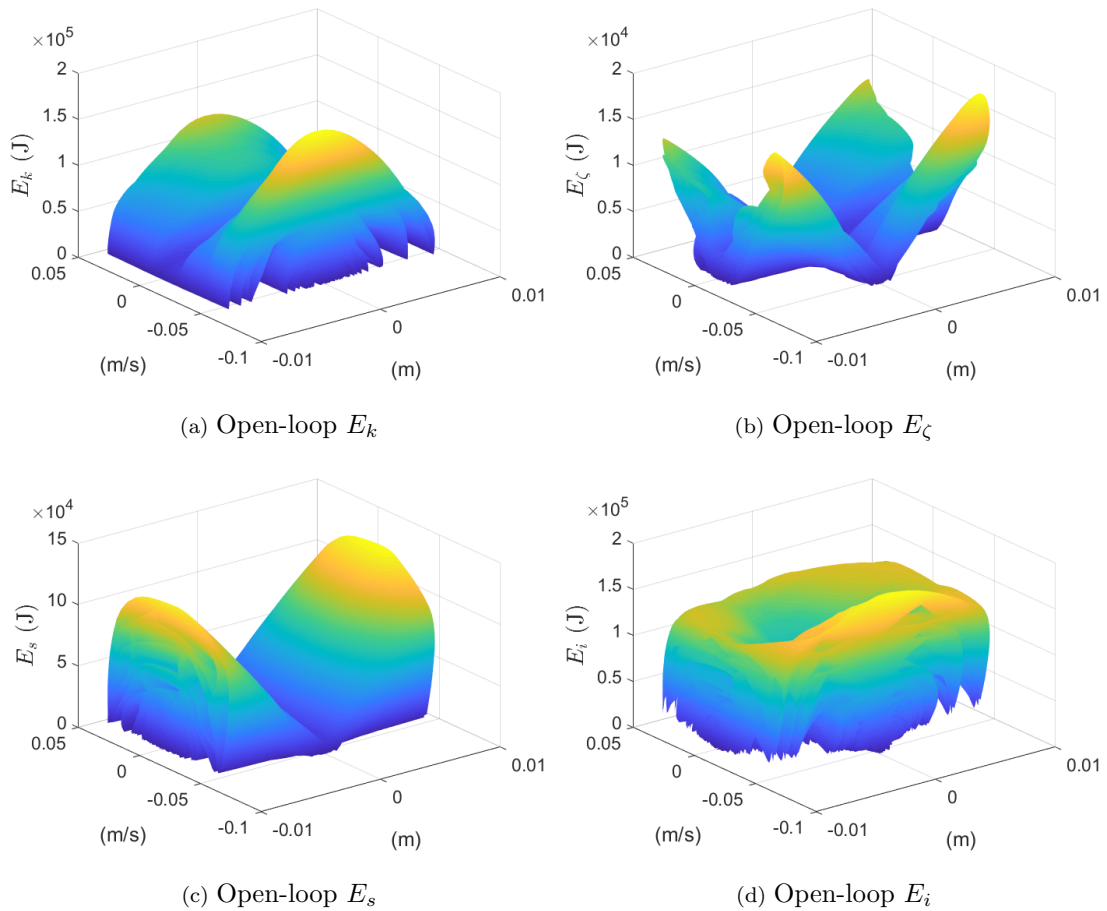
Figure 7.8 : Uncontrolled relative energy signals under seismic disturbance, $E_i \rightarrow E_k, E_\zeta, E_s$.

By controlling the capability of absorbing excitation energy via the use of MR fluid yield stress to ultimately mitigate the overall structural vibrations under seismic disturbances, a low-energy smart structure can be achieved to withstand dynamic loading source. Figure 7.9 of the flow of energy under current control of the embedded MRDs attached to the structure, i.e. E_k, E_ζ, E_s and the control energy E_c under the proposed control, where it can be seen that a small control electrical energy for magnetizing the fluid in the smart devices can substantially reduce the mechanical energy components in the presence of hostile loading sources.

Thus, in semi-active control with FS2SMC, by injecting a control energy (CE) for magnetization, the MRDs can dissipate a large amount of seismic energy imparted

(a) Controlled kinetic energy E_k

(b) Controlled damping energy E_ζ

(c) Controlled strain energy E_s

(d) Controlled trajectory including E_c
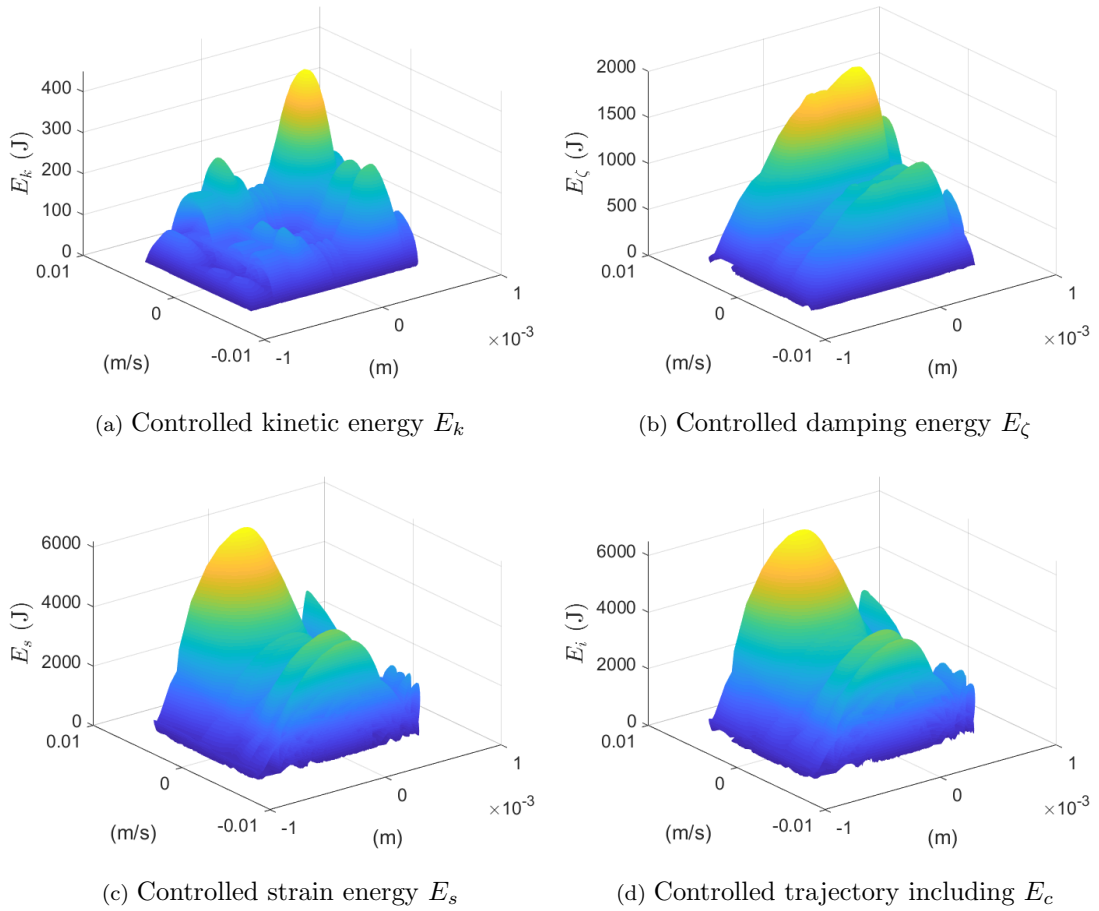
Figure 7.9 : Controlled relative energy signals under seismic disturbance for: $E_k, E_\zeta, E_s \to E_i$.

to the building structure. Under the robustly controlled magnetic field, the resulting damping force over a finite displacement of MRDs can adjust mechanical parameters of the seismically excited structure and dissipates the induced IE into heat through the MR fluid itself. This heat is, in turns, transferred to the environment via conduction and convection mechanisms. A schematic diagram of the energy flow in the multi-dof smart structure system under external excitation by a dynamic loading source is illustrated in Figure 7.10.

We now show effectiveness of the proposed FS2SMC by comparing its performance, in terms of output energies, with a Lyapunov-based control (LC) scheme, designed by employing an optimization algorithm to search for a suitable current
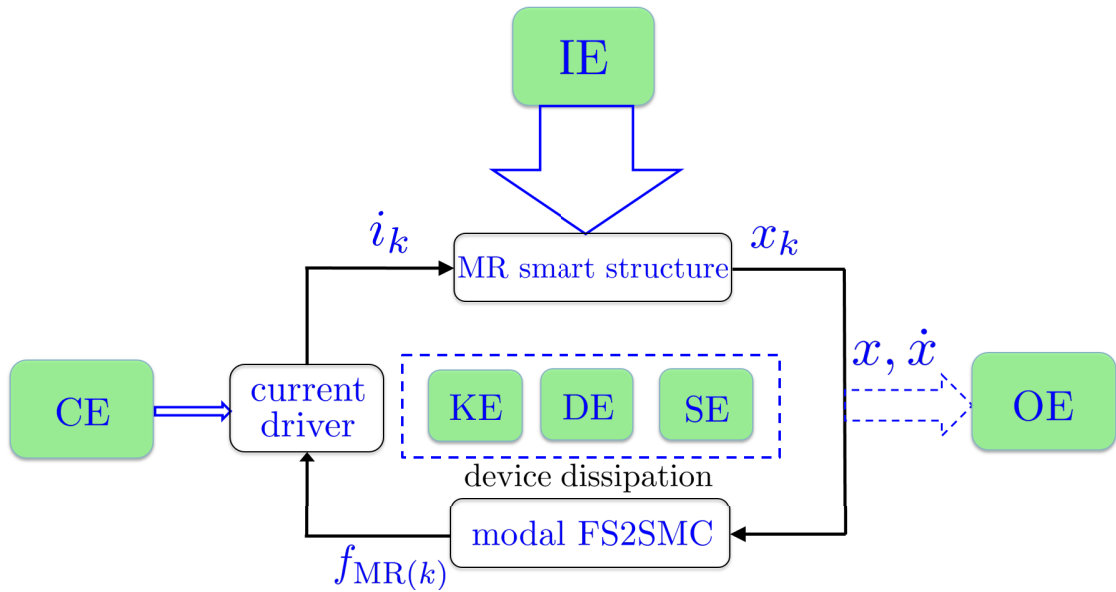
Figure 7.10 : Energy flow in the low-energy smart structure system under external excitation.

value for MRDs while minimizing the time rate of change of a chosen Lyapunov function,

$$V = y^T P y,$$

where P is a symmetric positive definite matrix, and y is the system state [52]. The peak responses of the relative energy signals for the uncontrolled (UC), LC, and FS2SMC cases under four benchmark scaled ($0.3g$) seismic records, the El-Centro, Hachinohe, Northridge and Kobe earthquakes, are provided in Table 7.1. For all excitation records, improvements can be noticed in the ability to suppress seismic vibrations via the controlled yield stress of the MRDs under control with FS2SMC or LC. It can be seen that for the controlled case, the output energies, namely E_k, E_ζ, E_s can be substantially reduced more than in the uncontrolled case with MRDs used in the fail-safe passive mode. While both controllers are effective for vibration suppression, the FS2SMC is more energy-efficient than the LC since it requires a smaller amount of control energy E_c but results in more absorption of input energy with less stiffness, damping and strain energies at the output. Indeed, owing to

Table 7.1 : Peak relative energy responses (J) under various seismic disturbances.

	El-Centro			Hachinohe		
	UC	LC	FS2SMC	UC	LC	FS2SMC
E_k	$161.9{\times}10^3$	534.144	406.81	$53.48{\times}10^3$	137.89	106.9
E_s	$126.1{\times}10^3$	8580.7	6042.7	$56.01{\times}10^3$	2779.7	1985.5
E_ζ	$17.1{\times}10^3$	1865.8	1863.9	6628.9	534.89	509.42
E_c	-	8815.1	6296.5	-	3065.3	2114.1
	Northridge			Kobe		
	UC	LC	FS2SMC	UC	LC	FS2SMC
E_k	$380.3{\times}10^3$	2893.8	2261.2	$926.97{\times}10^3$	1695.4	1280.2
E_s	$293.8{\times}10^3$	34143.9	29691	$924.15{\times}10^3$	40834.9	34089
E_ζ	$38.06{\times}10^3$	11528	9606.4	$112.11{\times}10^3$	9211.3	7676
E_c	-	39074.3	31011	-	45789	35232

the incorporation of the frequency-depending relationships of force-displacement and force-velocity of the smart devices into the system model and control design, and hence, the ability to effectively shape the frequency responses of the overall smart structure, the proposed controller can adjust the embodied energy to alter its spectrum in a desired bandwidth, roll off from the resonance region to limit the peak value of the mechanical and transmitted input energy terms, resulting in a low-energy structure while avoiding natural modes of the integrated structural system in dealing with any external loading source.

7.6 Summary

We have presented a frequency domain-based method for modeling and control of low-energy structures embedded with smart devices to mitigate the structural vi-

brations and dissipate the energy induced under external excitations. The controlled smart devices, here magnetorheological fluid dampers, are represented by describing functions of amplitude, frequency and control signal. The overall frequency response of the structure is obtained via a modal transformation. A frequency-shaped second-order sliding mode control is then proposed to achieve the control objective of maintaining structural resilience against any dynamic loading sources at a low control energy level. The control signal is a combination of an equivalent control containing a frequency shaping filter, and a robust control to drive the system dynamics to the desired mechanical modes shifted away from the resonance region. Experimental characterization of a laboratory MRD as well as a seismic building structure simulation have been conducted. The structural responses of a 10-floor building subject to benchmark earthquakes and comparison results on kinetic, damping, strain and input energies have indicated effectiveness and feasibility of the proposed method.

Chapter 8

Thesis Contributions, Conclusions and Future Works

This chapter presents a summary of the results drawn from this study, thesis contributions and future works.

8.1 Summary

Experimental characterization and cyclic energy dissipation of a laboratory magnetorheological (MR) damper (MRD) have been conducted for analysis of low-energy resilient structures integrated with smart dampers in Chapter 3. This work has presented multi-variable hysteresis models for semi-active structural members, namely MR pin joint (MRP) and MR elastomer base isolator (MRE). At first, the unique responses of MR devices are analyzed through a large quantity of experimental testing under various loading conditions. Then, the modeling and characterization are presented to show the current-dependent hysteretic relationships between the damping force (torque) and the linear (rotary) displacement. Model identification is considered here as solving a minimization optimization problem, and realized using the PSO algorithm. Furthermore, the relationships between model parameters and applied magnetic fields are also explored for the control application.

In Chapter 4, the problem of hysteresis in mechatronic smart devices such as MRD, MRP and MRE, in the frequency domain has been addressed. The describing function (DF) approach is applied to represent the nonlinear element of a smart device hysteresis by a gain and a phase. Approximate closed forms of the DFs gain

and phase as functions of amplitude, frequency and current are obtained by using curve-fitting technique, to facilitate the semi-active structural system analysis in the frequency domain.

A second-order sliding mode controller is designed in Chapter 5, to provide a real-time feedback control of MR devices for structural vibration mitigation. The effectiveness and feasibility of the controller for vibration control in building structures are discussed. Response comparisons of top floor acceleration, inter-storey drift and peak acceleration at each floor between passive and controlled structures are stated to evaluate the performance of the proposed technique in the simulation of a seismically excited three-storey benchmark building model.

In Chapter 6, the frequency domain-based method has been presented for modeling and control of structures embedded with smart devices to mitigate the structural vibrations and dissipate the energy induced under external excitations. Frequency-shaped sliding mode controllers are designed along with low-pass filters to implement the desired dynamic sliding surface and shape the frequency characteristics of the equivalent dynamics. The control signal exploits an equivalent control containing a frequency shaping filter and a robust signal to drive the system dynamics to the desired mechanical modes shifted away from the resonance region. The half-car model (HCM) with active suspension control using the proposed technique, HCM with passive HIS, and conventional HCM systems are taken into account in the simulation at zero initial conditions.

The energy equations for a building structure embedded with smart devices are established in Chapter 7. Two methods are used for deriving the input energy: one based on the absolute motion and the other on relative motion. A frequency-shaped second-order sliding mode controller (FS2SMC) is then proposed and designed for buildings embedded with dampers to inject a small amount of control energy to dissi-

pate vibration energy induced by external disturbances to the structure. The energy spectra of of a 10-floor building, subject to benchmark earthquakes, are compared between the uncontrolled case, Lyapynov-based control and proposed FS2SMC to illustrate the capability of a low-energy smart structure in suppressing quake-induced vibrations.

8.2 Thesis contributions

The contributions of this study are summarized as follows:

- Novel hysteresis models for MR fluid and elastomer based devices, namely MR damper (MRD), MR pin joint (MRP) and MR elastomer base isolator (MRE), have been proposed to describe the highly-nonlinear hysteretic relationship between input/output variables [25, 124]. These models are capable of effectively working in a wide scale of exciting variables. The relationships between the applied current and model parameters are also established for the current-controlled method for MR device integrated smart structures.

- New frequency-based hysteresis models for MR devices using the describing function (DF) method have been developed to obtain the overall structural frequency responses via a modal transformation for control and analysis of hysteretic behaviors in MR device-based smart structures [103]. Analysis and experimental validation of the energy dissipation process in the MR fluid of smart dampers in moving towards low-energy resilient structures embedded with MR devices have been also presented [21].

- A second-order sliding mode controller (2SMC) in conjunction with the field-dependent model is proposed to implement the semi-active control of MR devices. To extend sliding mode control (SMC) design to the frequency domain, frequency-shaped (FS) SMC (FSSMC) and FS2SMC have been developed.

These controllers are applied to various mechanical systems including active suspension [139] and smart structure systems [21, 59, 124, 137] to achieve the control objective of maintaining structural resilience against dynamic loadings under a low-power control signal and fail-safe operations.

8.3 Future works

The studies presented in this thesis were aimed to apply modeling and control techniques to resiliently preserve structural health and function with a low energy cost during extreme events or severe loadings. Following works in the energy-aware design of smart structure systems can be explored:

- While developing the design approach for energy-aware protection of MR based systems, the structural motion and ground floor were assumed to remain linear elastic and axially rigid, respectively. The effect of nonlinear and hysteretic structures, bi-directional and rotational ground motions should be investigated. For instance, soil-structure systems exhibit complex nonlinear hysteretic behavior. Consider the $(n + 2)$-dof soil-structure system of mass M and height H embedded with n MR devices subjected to dynamic loading sources with acceleration vector $\ddot{x}_g$ of the form

$$M\ddot{x} + g(x, \dot{x}, x_b, \dot{x}_b, \theta, \dot{\theta}) = \Gamma f_{\mathrm{MR}}(x, i) - M\ddot{x}_g, \tag{8.1}$$

where $g(\cdot)$ represents the nonlinear restoring force vector including viscous damping effects and hysteretic behavior; x_b is the horizontal translation of the base with respect to a reference frame; and θ denotes the rotation of the base or rocking of the foundation around the axis perpendicular to the horizontal direction. Here, the horizontal displacement of the system r can be given by

$$r = x + x_g + H\theta + x_b. \tag{8.2}$$

Similarly as of (1.1) and (7.2), the energy equation can be expressed as

$$E_k + E_\zeta + E_s + E_h = E_{\text{MR}} - E_i. \tag{8.3}$$

- Response analysis for multi-support earthquake excitation should be further considered in assessing the damage potential and developing an energy-based control approach for low-energy structures embedded with smart devices.

  Refer to Section 3.2.3, it was shown that the dissipated cyclic energy by a smart damper is converted into heat, depending on the applied magnetization current, oscillation amplitude and excitation frequency. Hence, further studies would be highly desired to derive a closed-form expression for the temperature rise in controllable fluid dampers from a different type of input excitations under fluctuating magnetic field.

- The proposed FS2SMC was numerically verified in the simulation of a half-car model (HCM) with inbuilt active hydraulically interconnected suspension (HIS) system. Experimental validation of the proposed technique for vehicle suspension systems should be conducted as schematically depicted in Figure 8.1.

  The proposed FSSMC methodology is beneficial for specific applications where the system's natural frequencies and some frequency bandwidth must be avoided to prevent a structural failure. The control schedule can also be applied wherein a fixed switching frequency is preferred to reduce the embodied energy losses. The controller can be designed along with a notch filter to implement the desired dynamic sliding surface.
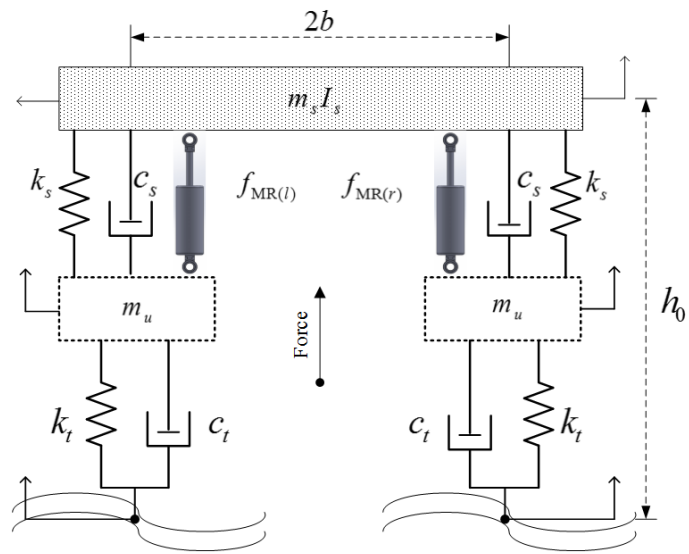
(a) HCM integrated with MRDs
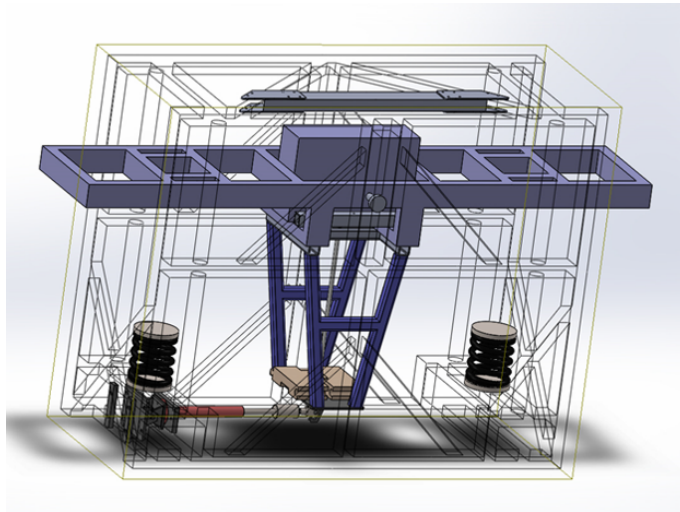
(b) CAD design schematic of Figure 6.9

Figure 8.1 : Semi-active suspension system.

Appendix A

Structure Model & MR Device Parameters

A.1. Building Structure Parameter:

The structural parameters of the 10-storey shear building model [138] are

Parameter	Description	Value	Unit
$m_{k=1,2,\ldots,10}$	mass	360	ton
$c_{k=1,2,\ldots,10}$	damping	6.2	MNs/m
$k_{k=1,2,\ldots,10}$	stiffness	650	MN/m

The structural parameters of the three-storey building model [58] are

Floor	m_k (kg)	c_k (Ns/m)	k_k (kN/m)
1	98.3	125	516
2	98.3	50	684
3	98.3	50	684

A.2. MRE Model Parameter:

$$f_e = c_e \dot{x} + k_e x + \alpha_e \sinh(\beta_e x), \tag{A.1}$$

where numerical values of the model parameters as functions of i are

$$
\begin{aligned}
c_e &= c_{e0} + c_{e1}i = 339.6 + 576.7i \text{ Ns/m,} \\
k_e &= k_{e0} + k_{e1}i = 3343.1 + 5816.1i \text{ N/m,} \\
\alpha_e &= \alpha_{e0} + \alpha_{e1}i = 8.11 + 4.981i, \\
\beta_e &= \beta_{e0} + \beta_{e1}i = 0.3463 + 0.1322i.
\end{aligned}
\tag{A.2}
$$

A.3. MRP Model Parameter:

$$T_p = c_p\dot{\theta} + k_p\theta + \alpha_p z_p + T_{p0}, \ \ z_p = \tanh(\beta_p\dot{\theta} + \delta_p \operatorname{sgn}\theta), \tag{A.3}$$

where numerical values of the model parameters as functions of i are

$$\begin{aligned}
c_p &= c_{p0} + c_{p1}i = 0.055 + 3.11i, \\
k_p &= k_{p0} + k_{p1}i = -5.3 + 60.3i, \\
\alpha_p &= \alpha_{p0} + \alpha_{p1}i + \alpha_{p1}i^2 = 0.8 + 6.2i - 0.6i^2, \\
\beta_p &= \beta_{p0} + \beta_{p1}i + \beta_{p2}i^2 = 11.11 + 5.33i - 2.1i^2, \\
\delta_p &= \delta_{p0} + \delta_{p1}i = 0.457 + 0.32i, \\
T_{p0} &= T_{p00} + T_{p01} = -0.16 + 0.009ii = 0.457 + 0.32i.
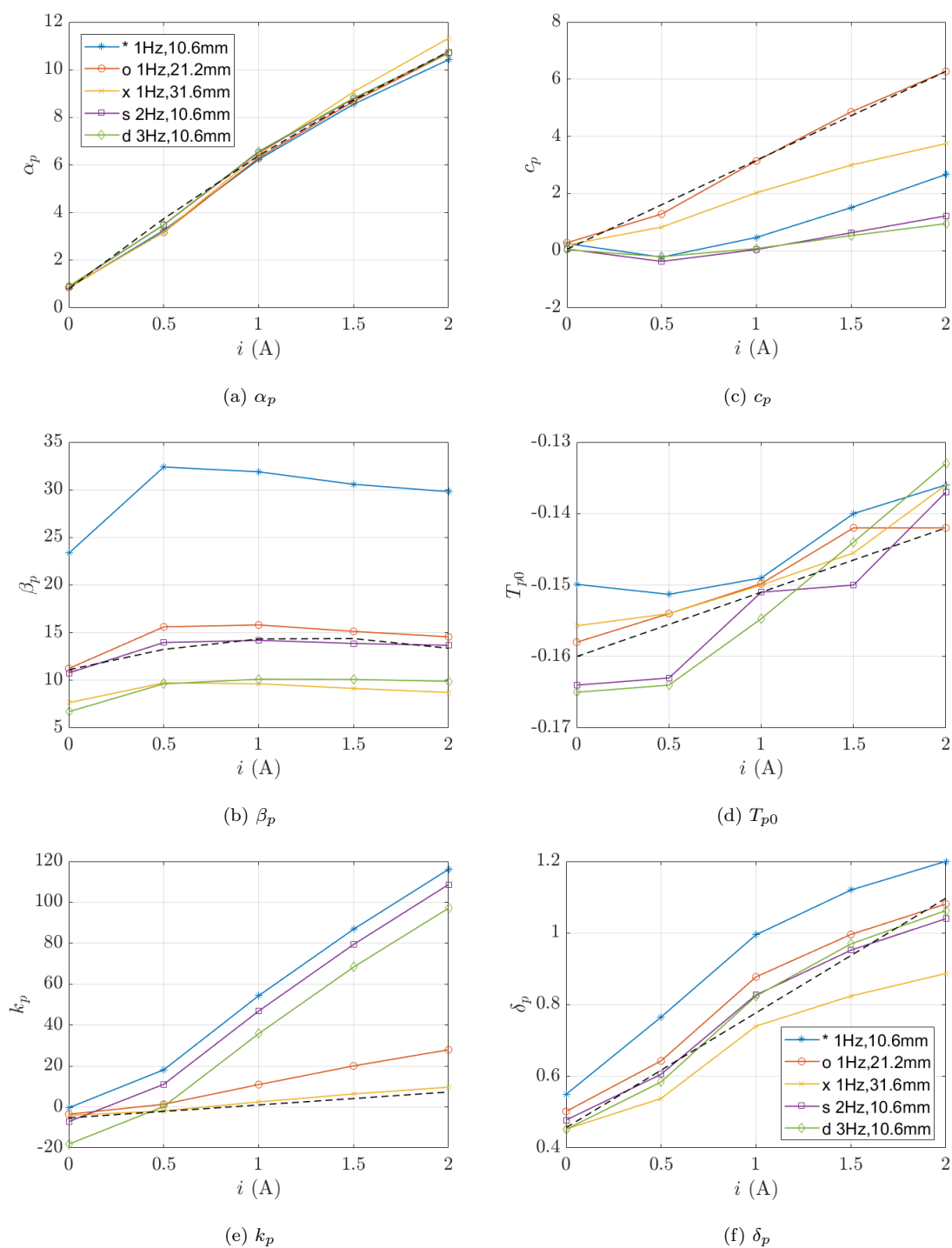\end{aligned} \tag{A.4}$$

Figure A.1 : MRP model parameter identification results (solid) and polynomial fitted results (dash).

Appendix B

# Half-car Test Rig Identification

B.1. Half-car Test Rig Identification:

Let y_s, y_t, and f represent the suspension displacement, tire displacement and applied force, respectively.

Raw measurements								
Force (N)	Left side (mm)				Right side (mm)			
f	y_{s1}	y_{s2}	y_{t1}	y_{t2}	y_{s1}	y_{s2}	y_{t1}	y_{t2}
0	82	86	30	33	89	84	31	31
250	100	99	29	31	102	97	30	30
500	113	113	28	30	117	112	28	28
750	126	126	26	29	129	124	27	26
1000	140	139	24	27	143	138	25	25

Relative measurements								Average		Actual	
Left side (mm)				Right side (mm)				(mm)		(mm)	
dy_{s1}	dy_{s2}	dy_{t1}	dy_{t2}	dy_{s1}	dy_{s2}	dy_{t1}	dy_{t2}	$\overline{dy_s}$	$\overline{dy_t}$	Y_s	Y_t
0	0	0	0	0	0	0	0	0	0	0	0
18	13	-1	-2	13	13	-1	-1	14.25	-1.25	13	1.25
31	27	-2	-3	28	28	-3	-3	28.5	-2.75	25.75	2.75
44	40	-4	-4	40	40	-4	-5	41	-4.25	36.75	4.25
58	53	-6	-6	54	54	-6	-6	54.75	-6	48.75	6
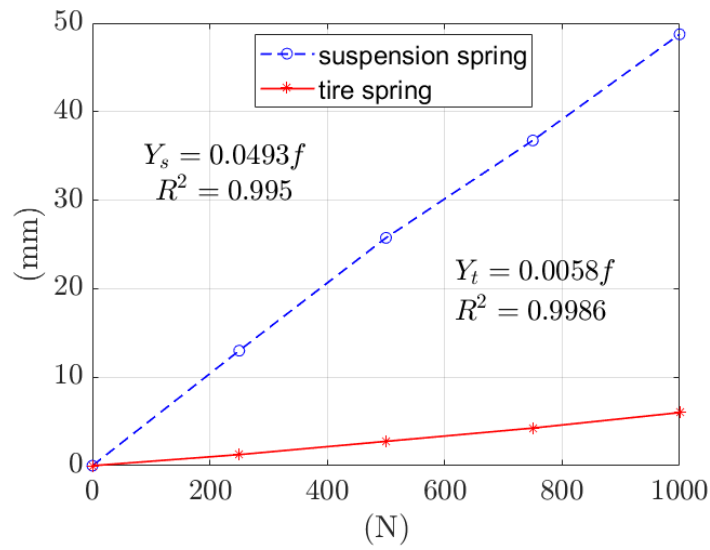
The suspension spring stiffness is calculated as

$$k_s = \frac{1}{0.0493} = \frac{f}{Y_s} = 20.28 \quad \text{kN/m},$$

Tire stiffness is obtained as

$$k_s = \frac{1}{0.0058} = \frac{f}{Y_t} = 172.41 \quad \text{kN/m}.$$

Hence, stiffness is

$$k = \frac{k_s k_t}{k_s + k_t} = 18146 \quad \text{N/m}.$$

B.2. Step Input Response & HCM Parameter:

t (sec)	x (mm)	$|\exp(1-x)|$	$T/2$ (sec)
0	0	1	0.35
0.35	1.83	0.83	0.36
0.71	0.31	0.69	0.37
1.08	1.57	0.57	0.37
1.45	0.51	0.49	0.36
1.81	1.40	0.4	0.37
2.18	0.67	0.33	0.36
2.54	1.26	0.26	0.36
2.9	0.82	0.18	0.36
3.26	1.11	0.11	0.36
3.62	0.94	0.06	0.36

$$\ddot{x} + \frac{c}{m}\dot{x} + \frac{k}{m}x = 0$$

$$\therefore r_{1,2} = -\frac{c}{2m} \pm \sqrt{\frac{c^2 - 4mk}{4m^2}} = -\frac{c}{2m} \pm j\sqrt{\frac{k}{m} - \left(\frac{c}{2m}\right)^2} = -\gamma + j\omega$$

$$x(t) = Ae^{-\zeta\omega_n}\sin(\omega_n\sqrt{1-\zeta^2}t) = Ae^{-\zeta\omega_n}\sin(\omega t)$$

$$\Rightarrow x(t) = \exp(-\gamma t) = \exp(-0.507t), \ \gamma = \frac{c}{2m} = \zeta\omega_n.$$

Now, we have

$$\gamma = 0.507 \ \ 1/\text{sec}, \ T/2 = 0.36 \ \ \text{sec}, \ \omega = \frac{2\pi}{T} = 8.726 \ \ \text{rad/sec},$$

$$\omega_n = \sqrt{\omega^2 + \gamma^2} = \sqrt{8.726^2 + 0.507^2} = 8.741 \ \ \text{rad/sec},$$

$$m = \frac{k}{\omega_n^2} = 237.5 \ \ \text{kg},$$

$$m_s = 2m = 475 \ \ \text{kg},$$

$$c_s = 2m_s\gamma = 240.84 \ \ \text{Ns/m}.$$

The HCM parameters are identified as

Parameter	Description	Value	Unit
m	quarter car (sprung) mass	237.5	kg
m_s	vehicle body (sprung) mass	475	kg
m_u	wheel (unsprung) mass	35	kg
I_s	rotational inertia	120	kgm^2
k_s	suspension spring stiffness	20	kN/m
k_t	tire stiffness	172	kN/m
c_s	suspension damping	240	Ns/m

The HIS system parameters are adopted from [136].

Appendix C

Testo 875-2i Report

C.1. Testo 875-2i Report on Heating Effect of RD-8041-1 MR Damper

Heating of MR Damper

Company	University of Technology Sydney

	Phone:	0431412691
	E-Mail:	sayed.royel@uts.edu.au

Device	Testo 875-2i	Serial No.:	2808788

Customer	Sayed Royel

Measuring Site:	CB11.B4.105 Dynamics & Mechanics Lab

Task	Experimental study on heat generation and dissipation of MRD

Sine wave, 1A, 12mm, 2Hz, 300sec

File:	IV_00040_IRSoft.bmt			**Date:**	2/05/2018
lens type:	Standard 32°	**lens serial no.:**	20381883	**Time:**	4:24:34 PM
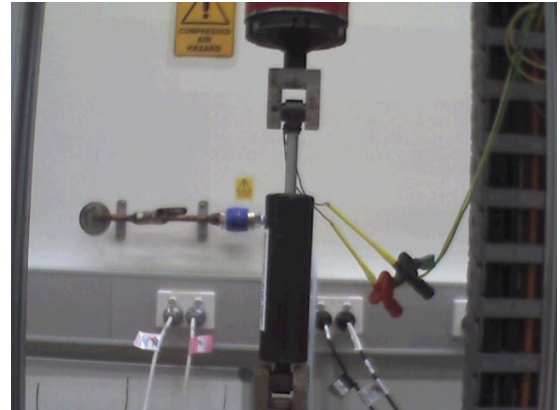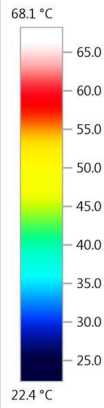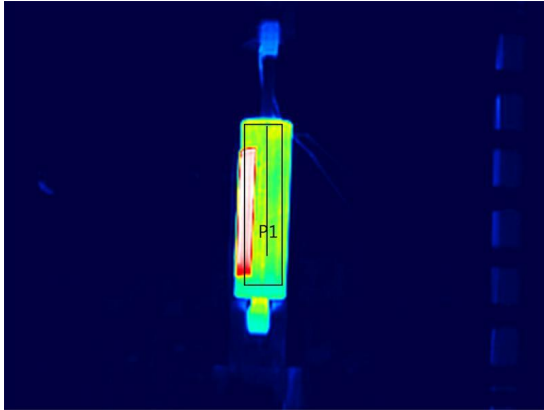
Picture parameters:
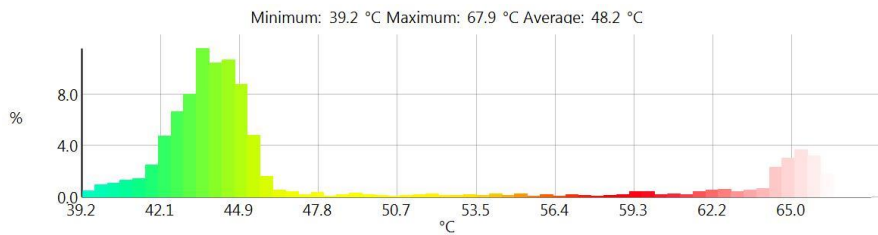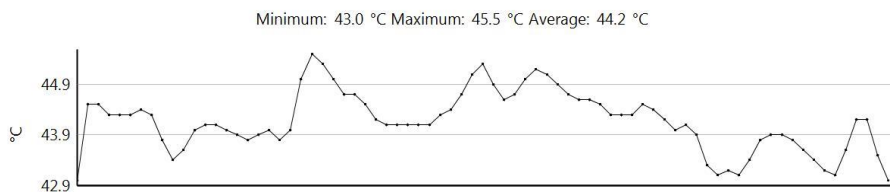
Emissivity: 0.95
Refl. temp. [°C]: 20.0

Histogram:

Minimum: 39.2 °C Maximum: 67.9 °C Average: 48.2 °C

Profile line:

Minimum: 43.0 °C Maximum: 45.5 °C Average: 44.2 °C

Heating of MR Damper

					Date:	2/05/2018
File:	IV_00032.BMT					
lens type:	Standard 32°	**lens serial no.:**	20381883		**Time:**	1:45:55 PM
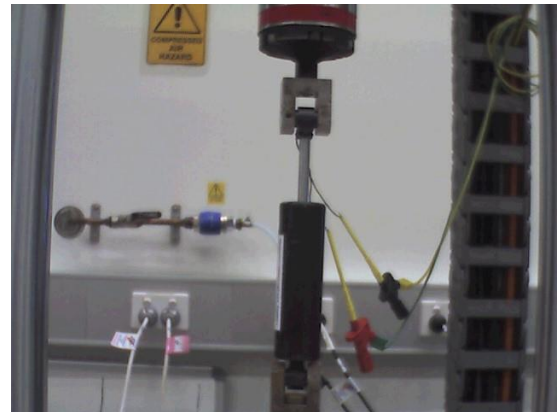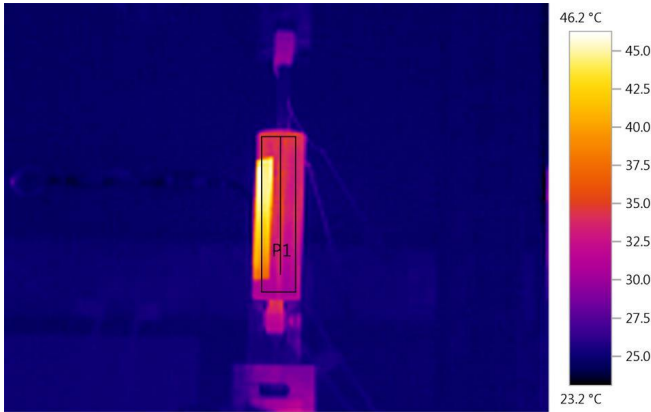
46.2 °C
- 45.0
- 42.5
- 40.0
- 37.5
- 35.0
- 32.5
- 30.0
- 27.5
- 25.0

23.2 °C

Picture parameters:

Emissivity: 0.95
Refl. temp. [°C]:   20.0

Histogram:

Minimum: 30.1 °C Maximum: 45.6 °C Average: 35.4 °C

Profile line:

Minimum: 32.5 °C Maximum: 35.2 °C Average: 34.2 °C
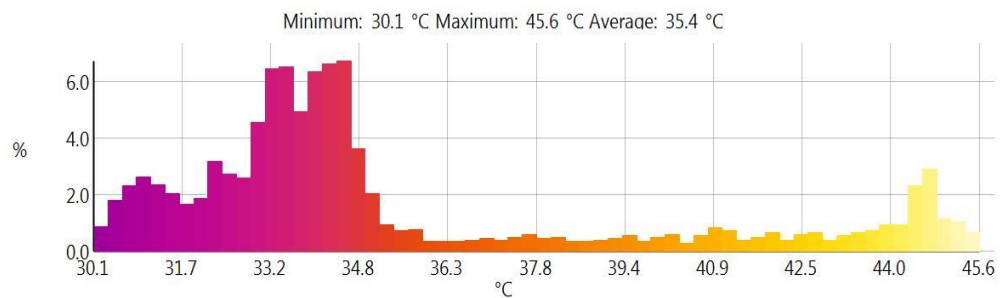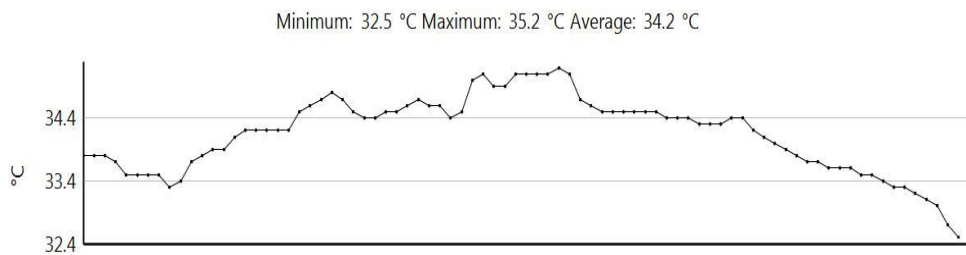
Heating of MR Damper

File: IV_00029.BMT

lens type: Standard 32° **lens serial no.:** 20381883

Date: 2/05/2018

Time: 1:38:30 PM

Picture parameters:

Emissivity: 0.95
Refl. temp. [°C]: 20.0

Histogram:

Minimum: 25.7 °C Maximum: 33.5 °C Average: 28.5 °C

Profile line:

Minimum: 28.2 °C Maximum: 30.5 °C Average: 29.5 °C
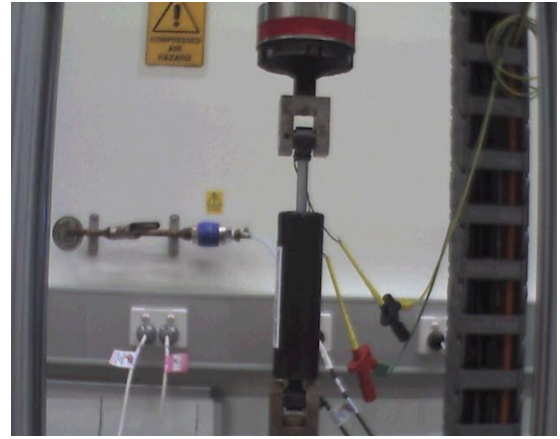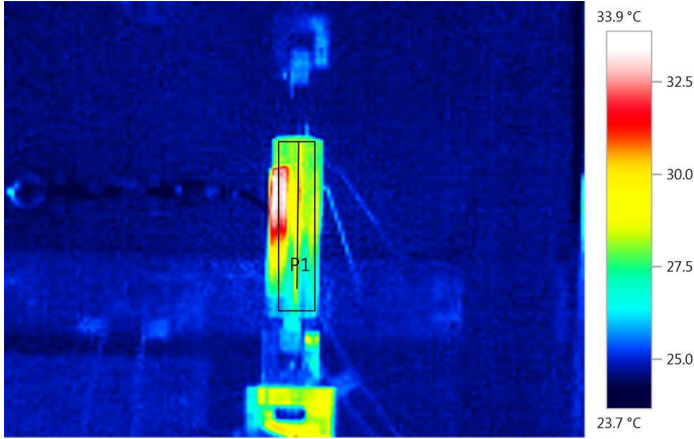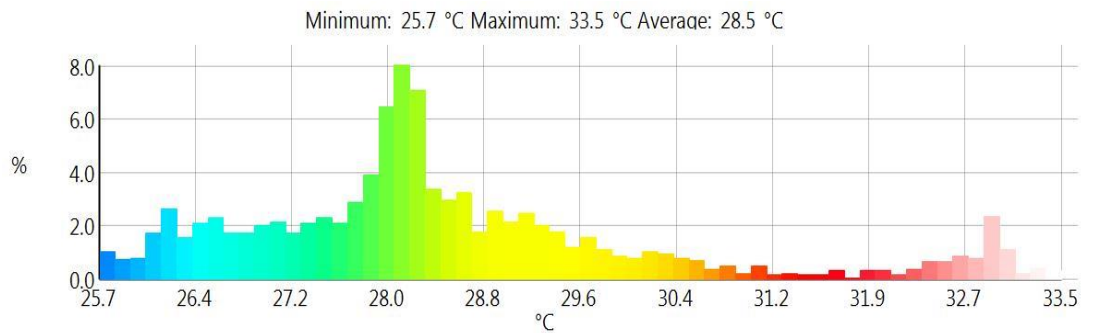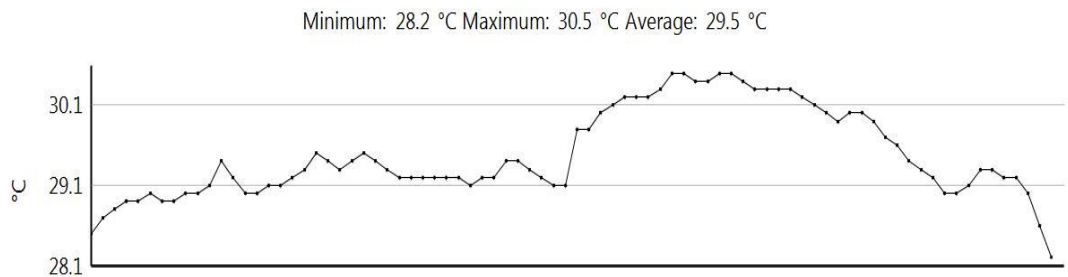
Heating of MR Damper

File: IV_00033_IRSoft.bmt   **Date:** 2/05/2018

lens type: Standard 32°   **lens serial no.:**   20381883   **Time:** 1:50:02 PM
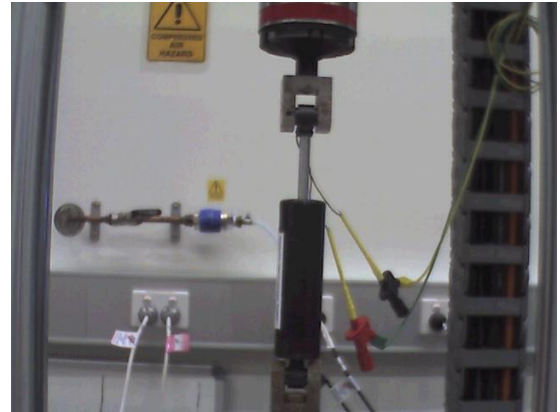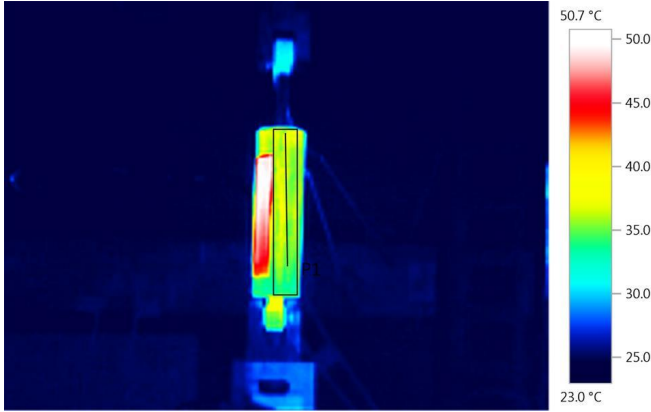
Picture parameters:

Emissivity: 0.95
Refl. temp. [°C]:   20.0

Histogram:

Minimum: 32.8 °C Maximum: 38.1 °C Average: 35.7 °C

Profile line:

Minimum: 34.7 °C Maximum: 37.5 °C Average: 36.0 °C
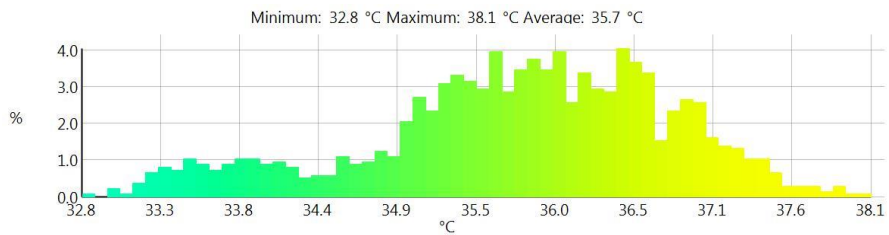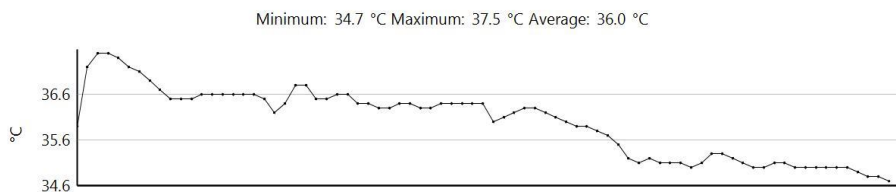
Heating of MR Damper

File:	IV_00041_IRSoft.bmt			**Date:**	2/05/2018
lens type:	Standard 32°	**lens serial no.:**	20381883	**Time:**	5:05:02 PM
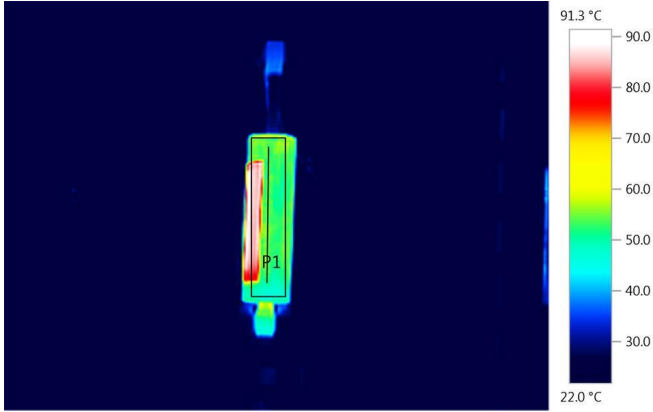
Picture parameters:

Emissivity: 0.95
Refl. temp. [°C]: 20.0

Histogram:

Minimum: 46.6 °C Maximum: 88.9 °C Average: 60.0 °C

Profile line:

Minimum: 50.8 °C Maximum: 55.8 °C Average: 54.1 °C
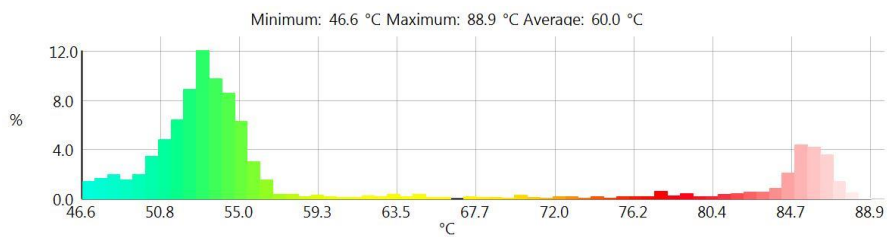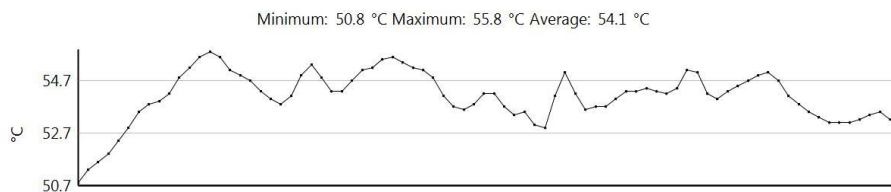
9/05/2018 ,

Bibliography

[1] https://en.wikipedia.org/wiki/List_of_tallest_buildings_and_structures

[2] A. Lago, D. Trabucco, and A. Wood, *Damping Technologies for Tall Buildings*, Butterworth-Heinemann, 2018.

[3] F. Cheng, H. Jiang, and K. Lou, *Smart Structures: Innovative Systems for Seismic Response Control*, CRC Press, Taylor & Francis Group, 2008.

[4] P. Castaldo, *Integrated Seismic Design of Structure and Control Systems*, Springer, 2014.

[5] Y. Xu, and J. He, *Smart Civil Structures*, CRC Press, Taylor & Francis Group, 2017.

[6] I. Sartori and A. Hestnes, "Energy use in the life cycle of conventional and low-energy buildings: A review article" *Energy and Buildings*, vol. 39, no. 3, pp. 249-257, 2007, doi: 10.1016/j.enbuild.2006.07.001.

[7] M. Liu and B. Mi, "Life cycle cost analysis of energy-efficient buildings subjected to earthquakes," *Energy and Buildings*, vol. 154, pp. 581-589, 2017, doi: 10.1016/j.enbuild.2017.08.056.

[8] A. Belleri and A. Marini, "Does seismic risk affect the environmental impact of existing buildings?" *Energy and Buildings*, vol. 110, pp. 149-158, 2016, doi: 10.1016/j.enbuild.2015.10.048.

[9] A. Nezhad and J. Xiao, "Estimation and minimization of embodied carbon of buildings: a review," *Buildings*, vol. 7, no. 1, 2017, doi: 10.3390/buildings7010005.

[10] T. Alqado, G. Nikolakopoulos and J. Jonasson, "Comfort level identification for irregular multi-storey building," *Automation in Construction*, vol. 50, pp. 40-49, 2015, doi: 10.1016/j.autcon.2014.10.009.

[11] Y. L. Xu and B. Chen, "Integrated vibration control and health monitoring of building structures using semi-active friction dampers: Part I- methodology," *Engineering Structures*, vol. 30, no. 7, pp. 1789-1801, 2008, doi: 10.1016/j.engstruct.2007.11.013.

[12] M. M. Ali and K. S. Moon, "Structural developments in tall buildings: current trends and future prospects," *Architectural Science Review*, vol. 50, no. 3, pp. 205-223, 2007, doi:10.3763/asre.2007.5027.

[13] B. F. Spencer and S. Nagarajaiah, "State of the art of structural control," *Journal of Structural Engineering*, vol. 129, no. 7, 2003, doi: 10.1061/(ASCE)0733-9445(2003)129:7(845).

[14] R. Smith, R. Merello, and M. Willford, "Intrinsic and supplementary damping in tall buildings" *Proc. of the Institution of Civil Engineers: Structures and Buildings*, vol. 163, no. 2, pp. 111-118, 2010, doi: 10.1680/stbu.2010.163.2.111.

[15] T. Soong and B. F. Spencer, "Supplemental energy dissipation: state-of-the-art and state-of-the-practice," *Engineering Structures*, vol. 24, pp. 243-259, 2002, doi: 10.1016/S0141-0296(01)00092-X.

[16] C. Spelta, F. Previdi, S. Savaresi, G. Fraternale, and N. Gaudiano, "Control of magnetorheological dampers for vibration reduction in a washing machine," *Mechatronics*, vol. 19, pp. 410-421, 2009, doi: 10.1016/j.mechatronics.2008.09.006.

[17] F. Weber, H. Distl, and M. Motavalli, "Cycle energy control of magnetorheological dampers on cables," *Smart Materials and Structures*, vol. 18, pp. 1123-1149, 2009, doi: 10.1088/0964-1726/18/1/015005.

[18] G. Yang, B. Spencer Jr., J. Carlson and M. K. Sain, "Large-scale MR fluid dampers: modeling and dynamic performance considerations," *Engineering Structures*, 24(3), pp. 309-323, 2002, doi: 10.1016/S0141-0296(01)00097-9.

[19] G. Yang, B. F. Spencer Jr, F. Billie, H. J. Jung, and J. D. Carlson, "Dynamic modelling of large scale magnetorheological damper systems for civil engineering applications," *Journal of Eng. Mechanics*, vol. 130, no. 9, pp. 1107-1114, 2004, doi: 10.1061/(ASCE)0733-9399(2004)130:9(1107).

[20] H. Li, and J. Wang, "Experimental investigation of the seismic control of a nonlinear soil-structure system using MR dampers," *Smart Materials and Structures*, 20(8):085026, 2011, doi:10.1088/0964-1726/20/8/085026.

[21] Q. P. Ha, S. Royel, and C. Balaguer, "Low-energy Structures Embedded With Smart Dampers," *Energy and Buildings*, vol. 177, pp. 375-384, 2018, doi: 10.1016/j.enbuild.2018.08.016.

[22] Q. P. Ha, M. T. Nguyen, J. Li, and N. M. Kwok, "Smart structures with

current-driven MR dampers: modelling and second-order sliding mode control," *IEEE/ASME Trans. on Mechatronics*, vol. 18, no. 6, pp. 1702-1711, 2013.

[23] Y. Li, J. Li, W. Li and H. Du, "A state-of-the-art review on magnetorheological elastomer devices," *Smart Materials and Structure*, vol. 23, 2014, doi:10.1088/0964-1726/23/12/123001.

[24] Y. Yu, Y. Li, and J. Li, "Parameter identification of a novel strain stiffening model for magnetorheological elastomer base isolator utilizing enhanced particle swarm optimization," *Journal of Intelligent Material Systems and Structures*, 2014, doi: 10.1177/1045389×14556166.

[25] S. Royel, Y. Yu, Y. Li, J. Li, and Q. P. Ha, "A hysteresis model and parameter identification for MR pin joints using immune particle swarm optimization," *Proc. 2015 IEEE International Conference on Automation Science and Engineering*, pp. 1319-1324, Gothenburg, Sweden, 24-28 August 2015, doi: 10.1109/CoASE.2015.7294281.

[26] Y. Li, J. Li, and B. Samali, "Dynamic performance of a novel magnetorheological pin joint," *Journal of System Design and Dynamics*, vol. 5, No. 5, pp. 706-715, 2011, doi: 10.1299/jsdd.5.706.

[27] Y. Li and J. Li, "Dynamic characteristics of a magnetorheological pin joint for civil structures," *Frontiers of Mechanical Engineering*, vol. 9, no. 1, pp. 15-33, 2014, doi: 10.1007/s11465-014-0283-0.

[28] F. Gordaninejad and D. Breese, "Heating of magnetorheological fluid dampers," *Journal of Intelligent Material Systems and Structures*, vol. 10, pp. 634-645, 1999, doi: 10.1106/55D1-XAXP-YFH6-B2FB.

[29] J. Hogsberg and A. Krenk "Energy dissipation control of magnetorheological

damper," *Probabilistic Engineering Mechanics*, vol. 23, pp.188-197, 2008, doi: 10.1016/j.probengmech.2007.12.007.

[30] R. Zalewski, J. Nachman, M. Shillor, and J. Bajkowski, "Dynamic model for a magnetorheological damper," *Applied Mathematical Modelling*, vol. 38, pp. 2366-2376, 2014, doi: 10.1016/j.apm.2013.10.050.

[31] A. K. Chopra and F. McKenna, "Modeling viscous damping in nonlinear response history analysis of buildings for earthquake excitation," *Earthquake Engineering and Structural Dynamics*, vol. 45, pp. 193-211, 2016, doi: 10.1002/eqe.2622.

[32] F. Ikhouane, V. Manosa, and J. Rodellar, "Adaptive control of a hysteretic structural system," *Automatica*, vol. 41, pp. 225-231, 2005, doi: 10.1016/j.automatica.2004.08.018.

[33] J. E. Luco, "A note on classical damping matrices," *Earthquake Engineering and Structural Dynamics*, vol. 37, pp. 615-626, 2008, doi: 10.1002/eqe.776.

[34] C. Uang and V. Bertero, "Evaluation of seismic energy in structures," *Earthquake Engineering and Structural Dynamics*, vol. 19, pp. 77-90, 1990, doi: 10.1002/eqe.4290190108.

[35] https://en.wikipedia.org/wiki/Millennium_Bridge,_London

[36] B. Culshaw, "Smart structures-a concept or a reality?," *Proc. of the Institution of Mechanical Engineers*, vol. 206, no. 1, pp. 1-8, 1992, doi: 10.1243/PIME_PROC_1992_206_302_02.

[37] E. F. Crawley, "Intelligent structures for aerospace: a technology overview and assessment," *AIAA Journal*, vol. 32, no. 8, pp. 1689-1699, 1994, doi: 10.2514/3.12161.

[38] I. Chopra and J. Sirohi, *Smart Structures Theory*, Cambridge University Press, 2013.

[39] G. Bossis and S. Lacis, "Magnetorheological fluids," *Journal of Magnetism and Magnetic Materials*, vol. 252, pp. 224-228, 2002, doi: 10.1016/S0304-8853(02)00680-7.

[40] J. Harvey "Smart materials," *Mechanical Engineers' Handbook*, 2015, doi: 10.1002/9781118985960.meh111.

[41] S. Hurlebaus and L. Gaul, "Smart structure dynamics," *Mechanical Systems and Signal Processing*, vol. 20, no. 2, pp. 255-281, 2006, doi: 10.1016/j.ymssp.2005.08.025.

[42] G. W. Housner, A. L. Bergman, T. K. Caughey, A. G. Chassiakos, R. O. Claus, S. F. Masri, R. E. Skeleton, T. T. Soong, B. F. Spencer, and J. T. P. Yao, "Structural control: past, present and future," *Journal of Engineering Mechanics*, vol. 123, no. 9, pp. 897-971, 1997, doi: 10.1061/(ASCE)0733-9399(1997)123:9(897).

[43] Z. Xu, Y. Guo, J. Zhu and F. Xu, *Intelligent Vibration Control in Civil Engineering Structures*, Zhejiang University Press, Elsevier Inc., 2017.

[44] S. Royel, "Semi-active control of structures using current-controlled MR fluid damper," *Master Thesis*, UTS, 2012.

[45] H. P. Gavin, "Control of seismically excited vibration using electrorheological materials and lyapunov methods," *IEEE Trans. on Control System Technology*, vol. 9, no. 1, pp. 27-36, 2001, doi: 10.1109/87.896743.

[46] B. F. Spencer, "Benchmark structural control problems for seismic and wind-excited structures: Editorial," *Journal of Engineering Mechanics*, vol. 130, no. 4, pp. 363-365, 2004, doi: 10.1061/(ASCE)0733-9399(2004)130:4(363).

[47] C. J. Lin, H. T. Yau, C. Y. Lee, and K. H. Tung, "System identification and semi active control of a squeeze mode magnetorheological damper," *IEEE/ASME Transactions on Mechatronics*, vol. 18, no. 6, pp. 1691-1701, 2013, doi: 10.1109/TMECH.2013.2279852.

[48] M. Canale, M. Milanese, and C. Novara, "Semi-active suspension control using fast model predictive techniques," *IEEE Transactions on Control Systems Technology*, vol. 14, pp. 1063-6536, 2006, doi: 10.1109/ACC.2005.1469945.

[49] M. M. Polycarpou and P. A. Ioannou, "A robust adaptive nonlinear control design," *Automatica*, vol. 32, no. 3, pp. 423-427, 1996, doi: 10.1016/0005-1098(95)00147-6.

[50] M. Zapateiro, F. Pozo, H. R. Karimi, and N. Luo, "Semiactive control methodologies for suspension control with magnetorheological dampers," *IEEE/ASME Transactions on Mechatronics*, vol. 17, no. 2, pp. 370-380, 2012, doi: 10.1109/TMECH.2011.2107331.

[51] N. Luo, J. Rodellar, D. De la Sen, J. Vehi, "Output feedback sliding mode control of base isolated structures," *Journal of the Franklin Institute*, vol. 337, pp. 555-577, 2000, doi: 10.1016/S0016-0032(00)00024-7.

[52] Q. P. Ha, N. M. Kwok, M. T. Nguyen, J. Li, and B. Samali, "Mitigation of seismic responses of building structures using MR dampers with lyapunov-based control," *Struc. Control and Health Monit.*, vol. 15, no. 6, pp. 604-621, 2008, doi: 10.1002/stc.218.

[53] R. Jimenez and L. Alvarez-Icaza, "A real-time estimation scheme for buildings with intelligent dissipation devices," *Mechanical Systems and Signal Processing*, vol. 21, pp. 2427-2440, 2007, doi: 10.1016/j.ymssp.2006.12.003.

[54] R. Jimenez and L. Alvarez-Icaza, "An adaptive observer for a shear building with an energy-dissipation device," *Control Engineering Practice*, vol. 18, pp. 331-338, 2010, doi: 10.1016/j.conengprac.2009.11.012.

[55] B. F. Spencer Jr., and M. K. Sain, "Controlling buildings: a new frontier in feedback," *IEEE Control System Magazine*, vol. 17. No. 6, pp. 19-35, 1997, doi: 10.1109/37.642972.

[56] J. Vicente, D. Klingenberg, and R. Alvarez"Magnetorheological fluids: a review," *Soft Matter*, vol. 7, pp. 3701-3710, doi: 10.1039/c0sm01221a.

[57] D. H. Wang, and W. H. Liao, "Magnetorheological fluid dampers: a review of parametric modelling," *Smart Materials and Structures*, vol. 20, no. 2, 2011, doi: 10.1088/0964-1726/20/2/023001.

[58] S. J. Dyke, B. F. Spencer Jr., M. K. Sain, and J. D. Carlson, "Modeling and control of magnetorheological dampers for seismic response reduction," *Smart Materials and Structures*, vol. 5, no. 5, pp. 565-575, 1996, doi: 10.1088/0964-1726/5/5/006.

[59] S. Royel, Z. Movassaghi, N. M. Kwok, and Q. P. Ha, "Smart structures using MR dampers with second order sliding mode control," *Proc. 2012 IEEE International Conference on Control, Automation and Information Sciences*, pp. 170-175, Ho Chi Minh, Vietnam, 26-29 Nov. 2012, doi: 10.1109/IC-CAIS.2012.6466580.

[60] S. McManus, K. Clair, P. Boileau, and J. Boutin, "Evaluation of vibration and shock attenuation performance of a suspension seat with a semi-active magnetorheological fluid damper," *Journal of Sound and Vibration*, vol. 253, no. 1, pp. 313-327, 2002, doi: 10.1006/jsvi.2001.4262.

[61] N. Caterino, "Semi-active control of a wind turbine via magnetorheological dampers," *Journal of Sound and Vibration*, vol. 345, pp. 1-17, 2015, doi: 10.1016/j.jsv.2015.01.022.

[62] A. Spaggiari, "Properties and applications of magnetorheological fluids," *Frattura ed Integrità Strutturale*, vol. 23, pp. 57-61, 2013, doi: 10.3221/IGF-ESIS.23.06.

[63] A. Dominiguez, R. Sedaghati, and I. Stiharu, "A new dynamic hysteresis model for magnetorheological dampers," *Smart Materials and Structures*, vol. 15, no. 5, pp. 1179-1189, 2006, doi: 0.1088/0964-1726/15/5/004.

[64] B. F. Spencer Jr., S. J. Dyke, M. K. Sain, and J. D. Carlson, "Phenomenological model of a magnetorheological damper," *Journal of Engineering Mechanics*, vol. 123, no. 3, pp. 230-238, 1997, doi: 10.1061/(ASCE)0733-9399(1997)123:3(230).

[65] C. C. Chang and P. Roschke, "Neural network modeling of a magnetorheological damper," *Journal of Intelligent Material Systems and Structures*, vol. 9, pp. 755-764, 1998, doi: 10.1177/1045389X9800900908.

[66] N. Kwok, Q. Ha, T. Nguyen, J. Li, and B. Samali, "A novel hysteretic model for magnetorheological fluid dampers and parameter identification using particle swarm optimization," *Sensors and Actuators A: Physical*, vol. 132, no. 2, pp.441-451, 2006, doi: 10.1016/j.sna.2006.03.015.

[67] N. M. Kwok, Q. P. Ha, M. T. Nguyen, J. Li, and B. Samali, "Bouc–Wen model parameter identification for a MRF damper using computationally efficient GA," *ISA Transactions*, vol. 46, no. 2, pp. 167-179, 2007, doi: 10.1016/j.isatra.2006.08.005.

[68] N. M. Wereley, L. Pang, and G. M. Kamath, "Idealized hysteresis modeling of electrorheological and magnetorheological dampers," *Journal of Intel-*

ligent Material Systems and Structures, vol. 9, no. 8, pp. 642-649, 1998, doi: 10.1177/1045389X9800900810.

[69] R. Jimenez and L. Alvarez-Icaza, "LuGre frinction model for a magnetorheological damper," *Structural Control and Health Monitoring*, vol. 12, no. 1, pp. 91-116, 2005, doi: 10.1002/stc.58.

[70] S. B. Choi and S. K. Lee, "A hysteresis model for the field-dependent damping force of a magnetorheological damper," *Journal of Sound and Vibration*, vol. 245, no. 2, pp. 375-383, 2001, doi: 10.1006/jsvi.2000.3539.

[71] T. Butz and O.von Stryk, "Modelling and simulation of electro- and magnetorheological fluid dampers," *Journal of Applied Mathematics and Mechanics*, vol. 82, no. 1, pp. 3-20, 2002, doi: 10.1002/1521-4001(200201)82.

[72] C. Edwards and S. K. Spurgeon, *Sliding Mode Control: Theory and Applications*, Taylor and Francis, London, 1998.

[73] R. DeCarlo, S. Zak, and G. Matthews, "Variable structural control of nonlinear multivariable systems: A tutorial," *Proceedings of the IEEE*, Vol. 76, no. 3, pp. 212-232, 1988, doi: 10.1109/5.4400.

[74] S. Oucheriah, "Robust exponential convergence of a class of linear delayed systems with bounded controllers and disturbances," *Automatica*, vol. 42, pp. 1863-1867, 2006, doi: 10.1016/j.automatica.2006.05.023.

[75] H. Obeid, L. Fridman, S. Laghrouche, M. Harmouche and M. Golkani, "Adaptation of Levant's differentiator based on barrier function," *International Journal of Control*, vol. 91, pp. 2019-2027, 2018, doi: 10.1080/00207179.2017.1406149.

[76] T. Sanchez, J. Moreno, and L. Fridman, "Output feedback Continuous Twisting Algorithm," *Automatica*, vol. 96, pp. 298-305, 2018, doi: 10.1016/j.automatica.2018.06.049.

[77] Y. Shtessel, C. Edwards, L. Fridman and A. Levant, *Sliding Mode Control and Observation*, Birkhauser Boston Inc, 2014.

[78] K. Furuta and Y. Pan, "Variable structure control with sliding sector," *Automatica*, vol. 36, pp. 211-228, 2000, doi: 10.1016/S0005-1098(99)00116-8.

[79] V. Utkin, "Discussion Aspects of High-Order Sliding Mode Control," *IEEE Transactions on Automatic Control*, vol. 61, no. 3, pp. 829-833, 2016, doi: 10.1109/TAC.2015.2450571.

[80] H. K. Khalil, *Nonlinear Systems*, 3rd ed., NJ, USA: Prentice Hall, 2002.

[81] J. J. E. Slotine and W. Li, *Applied Nonlinear Control*, Prentice-Hall, Englewood Cliffs, New Jersey, 1991.

[82] J. Liu, *Sliding Mode Control Using MATLAB*, Elsevier Inc, 2017.

[83] A. F. Filippov, *Differential Equations with Discontinuous Right-Hand Sides*. Math. and Its App., Kluwer Academic Publishers, Dordrecht, 1988.

[84] A. Mehta and B. Bandyopadhay, *Frequency-Shaped and Observer-Based Discrete-time Sliding Mode Control*, Springer, ISBN:978-81-322-2237-8, 2015.

[85] C. Fallaha, M. Saad, H. Y. Kanaan, and K. Al-Haddad, "Sliding mode robot control with exponential reaching law," *IEEE Transactions on Industrial Electronics*, vol. 58, no. 2, pp. 600-610, 2010, doi: 10.1109/TIE.2010.2045995.

[86] J. Liu and X. Wang, *Advanced Sliding Mode Control for Mechanical Systems: Design, Analysis and MATLAB Simulation*, Springer, Berlin Heidelberg, 2011.

[87] K. D. Young, V. I. Utkin, and U. Ozguner, "A control engineer's guide to sliding mode control," *IEEE Transactions on Control Systems Technology*, vol. 7, no. 3, pp. 328-342, 1999, doi: 10.1109/87.761053.

[88] K. B. Park, and T. Tsuji, "Terminal sliding mode control of second-order nonlinear uncertain systems," *International Journal of Robust and Nonlinear Control*, vol.9, no. 11, pp. 769-780, 1999, doi: 10.1002/(SICI)1099-1239(199909)9.

[89] M. Zhihong, A. P. Paplinski, and H. R. Wu, "A robust MIMO terminal sliding mode control for rigid robotic manipulators," *IEEE Transactions on Automatic Control*, vol. 39, pp. 2464-2469, 1994, doi: 10.1109/9.362847.

[90] X. Yu and M. Zhihong, "Fast terminal sliding mode control design for nonlinear dynamical systems," *IEEE Transactions on Circuits & Systems-I*, vol. 49, no. 2, pp. 261-264, 2002, doi: 10.1109/81.983876.

[91] Y. Feng, X. Yu, and M. Zhihong, "Non-singular terminal sliding mode control of rigid manipulators," *Automatica*, vol. 38, pp. 2159-2167, 2002, doi: 10.1016/S0005-1098(02)00147-4.

[92] H. Choi, Y. Park, Y. Cho and M. Lee, "Global sliding mode control," *IEEE Control Magazine*, vol. 21, no. 3, pp. 27-35, 2001, doi: 10.1109/37.924795.

[93] A. Levant, "Homogeneity approach to high-order sliding mode design," *Automatica*, vol. 41, no. 5, pp. 823-830, 2005, doi: 10.1016/j.automatica.2004.11.029.

[94] A. Levant, "Quasi-continuous high-order sliding-mode controllers," *IEEE Transactions on Automatic Control*, vol. 50, no. 11, pp. 1812-1816, 2005, doi: 10.1109/TAC.2005.858646.

[95] A. Levant, "Principles of 2-sliding mode design," *Automatica*, vol. 43, no. 4, pp. 576-586, 2007, doi: 10.1016/j.automatica.2006.10.008.

[96] A. Levant, "Generalized homogeneous quasi-continuous controllers," *International Journal of Robust and Nonlinear Contr*, vol. 18, pp. 385-398, 2008, doi: 10.1002/rnc.1199.

[97] A. Pisano and E. Usai, "Sliding mode control: a survey with applications in math," *Mathematics and Computers in Simulation*, vol. 81, pp. 954-979, 2011, doi: 10.1016/j.matcom.2010.10.003.

[98] Y. Shtessel, L. Fridman & A. Zinober, "Higher Order Sliding Modes," *International Journal of Robust and Nonlinear Control*, vol. 18, no. 4-5, pp. 381-384, 2008, doi: 10.1002/rnc.1229.

[99] S. Ding, A. Levant and S. Li, "Simple homogeneous sliding-mode controller," *Automatica*, vol. 67, pp. 22-32, 2016, doi: 10.1016/j.automatica.2016.01.017.

[100] Q. Huang, Y. Xu, J. Li, Z. Su, and H. Liu, "Structural damage detection of controlled building structures using frequency response functions," *Journal of Sound and Vibration*, vol. 331, no. 11, pp. 3476-3492, 2012, doi: 10.1016/j.jsv.2012.03.001.

[101] M. Nayyerloo, J. G. Chase, G. A. MacRae and X. Q. Chen, "LMS-based approach to structural health monitoring of nonlinear hysteretic structures," *Structural Health Monitoring*, vol. 10, no. 4, pp. 429-444, 2011, doi: 10.1177/1475921710379519.

[102] R. P. Bandara, T. H. T. Chan and D. P. Thambiratnam, "Structural damage detection method using frequency response functions," *Structural Health Monitoring*, vol. 13, no. 4, pp. 418-429, 2014, doi: 10.1177/1475921714522847.

[103] Q. P. Ha, S. Royel, J. Li, and Y. Li, "Hysteresis modeling of smart structure MR devices using describing functions," *IEEE/ASME Transactions on Mechatronics*, vol. 21, no. 1, pp. 44-50, 2016, doi: 10.1109/TMECH.2015.2506539.

[104] N. K. Gupta, "Frequency-shaped cost functionals: extension of linear-Quadratic-Gaussian design methods," *Journal of Guidance, Control and Dynamics*, vol. 3, no. 6, pp. 529-535, 1980, doi: 10.2514/3.19722.

[105] K. C. Cheok, H. X. Hu, and N. K. Loh, "Optimal output feedback regulation with frequency shaped cost functionals," *International Journal of Control*, vol. 47, no. 6, pp. 1665-1681, 1988, doi: 10.1080/00207178808906128.

[106] L. Zuo and J. J. E. Slotine, "Robust vibration isolation via frequency-shaped sliding control and modal decomposition," *Journal of Sound and Vibration*, vol. 285, pp. 1123-1149, 2005, doi: 10.1016/j.jsv.2004.09.014.

[107] A. Koshkouei and A. Zinober, "Robust frequency shaping sliding mode control," *IEE Proceedings - Control Theory and Applications*, vol. 147, no. 3, pp. 312-320, 2000, doi: 10.1049/ip-cta:20000378.

[108] B. D. Anderson, J. B. Moore, and D. L. Mongori, "Relations between frequency dependent control and state weighing in LQG problems," *Optim. Control Appl. Methods*, vol. 8, pp. 109-127, 1987, doi: 10.1002/oca.4660080202.

[109] J. X. Xu and W. J. Cao, "Synthesized sliding mode control of a single-link flexible robot," *International Journal of Control*, vol. 73, no. 3, pp. 197-209, 2000, doi: 10.1080/002071700219740.

[110] K. D. Young and U. Ozguner, "Frequency shaping compensator design for sliding mode," *International Journal of Control*, vol. 57, no. 5, pp. 1005-1019, 1993, doi: 10.1080/00207179308934427.

[111] K. C. Cheok, H. X. Hu, and N. K. Loh, "Discrete-time frequency-shaping parametric LQ control with application to active seat suspension control," *IEEE Trans. on Industrial Electronics*, vol. 36, no. 3, pp. 383-390, 1989, doi: 10.1109/41.31501.

[112] H. Yanada and H. Ohnishi, "Frequency-shaped sliding mode control of an electrohydraulic servo-motor," *Proc. of the Institution of Mechanical Engineers,*

Part I: Journal of Systems and Control Engineering, vol. 213, no. 6, pp. 441-448, 1999, doi: 10.1243/0959651991540269.

[113] W. C. Wu and T. Liu, "Frequency-shaped sliding mode control for flying height of pickup head in near-field optical disk drives," *IEEE Transactions on Magnetics*, vol. 41, no. 2, pp. 1061-1063, 2005, doi: 10.1109/TMAG.2004.842020.

[114] M. Zheng and M. Tomizuka, "A frequency-shaping methodology for discrete-time sliding mode control," *International Journal of Control*, 2017, doi: 10.1080/00207179.2017.1406148.

[115] A. Mehta and B. Bandyopadhay, "Frequency-shaped sliding mode control using output sampled measurements," *IEEE Trans. on Industrial Electronics*, vol. 56, no. 1, pp. 28-35, 2009, doi: 10.1109/TIE.2008.2006946.

[116] T. Acarman and U. Ozguner, "Frequency shaping compensation for backstepping sliding mode control," *IFAC Proceedings Volumes*, vol. 35, no. 1, pp. 37-42, 2002, doi: 10.3182/20020721-6-ES-1901.01077.

[117] J. B. Moore and D. L. Minigori, "Robust frequency-shaped LQ control," *Automatica*, vol. 23, no.5, pp. 641-645, 1987, doi: 10.1016/0005-1098(87)90060-4.

[118] S. Hong, M. Nguyen, N. Kwok, Q. Ha, and J. Li, "Hysteretic model for magnetorheological fluid dampers using a curve fitting approach," *Journal of Japanese Society of Applied Electromagnetics and Mechanics*, vol. 15, pp. 176-179, 2007.

[119] J. Kennedy and R. Eberhart, "Particle swarm optimization," *Proc. of the Fourth IEEE International Conference on Neural Networks*, pp. 1942-1948, Perth, Australia, 1995, doi: 10.1109/ICNN.1995.488968.

[120] Z. Zhang, "Immune optimization algorithm for constrained nonlinear multi-objective optimization problems," *Applied Soft Computing*, vol. 7, no. 3, pp. 840-857, 2007, doi: 10.1016/j.asoc.2006.02.008.

[121] Y. Li, J. Li, T. Tian, and W. Li, "A highly adjustable magnetorheological elastomer base isolator for applications of real-time adaptive control," *Smart Materials and Structures*, vol. 22, no. 9, 2013, doi:10.1088/0964-1726/22/9/095020.

[122] Y. Li, J. Li, W. Li, and B. Samali, "Development and characterization of a magnetorheological elastomer based adaptive seismic isolator," *Smart Materials and Structures*, vol. 22, no. 3, 2013, doi:10.1088/0964-1726/22/3/035005.

[123] Y. Yu, Y. Li, J. Li, X. Gu, and S. Royel, "Nonlinear Characterisation of the MRE Isolator Using Binary-coded Discrete CSO and ELM," *International Journal of Structural Stability and Dynamics*, vol 18, no 8, doi: 10.1142/S0219455418400072, 2018.

[124] Y. Yu, S. Royel, J. Li, Y. Li and Q. P. Ha, "Magnetorheological elastomer base isolator for earthquake response mitigation on building structures: modeling and second-order sliding mode control," *Earthquakes and Structures*, vol. 11, no. 6, pp. 943-966, 2016, doi: 10.12989/eas.2016.11.6.943.

[125] Y. Yu, Y. Li, J. Li, X. Gu, S. Royel, and A. Pokhrel, "Nonlinear and hysteretic modelling of magnetorheological elastomer base isolator using adaptive neuro-fuzzy inference system," *Applied Mechanics and Materials*, vol. 846, pp. 258-263, 2016, doi: 10.4028/www.scientific.net/AMM.846.258.

[126] Y. Yu, Y. Li, and J. Li, "Parameter identification and sensitivity analysis of an improved LuGre friction model for magnetorheological elastomer base isolator," *Meccanica*, 50(11), pp. 2691-2707, 2015, doi: 10.1007/s11012-015-0179-z.

[127] W. Pan, "Mixed modified fruit fly optimization algorithm with general regression neural network to build oil and gold prices forecasting model," *Kybernetes*, vol. 43, no. 7, pp. 1053-1063, 2014, doi: 10.1108/K-02-2014-0024.

[128] F. Duarte and J. T. Machado, "Fractional describing function of systems with coulomb friction," *Nonlinear Dynamics*, vol. 56, pp. 381-387, 2009, doi: 10.1007/s11071-008-9405-8.

[129] J. T. Machado, "Fractional order describing functions," *Signal Processing*, vol. 107, pp. 389-394, 2015, doi: 10.1016/j.sigpro.2014.05.012.

[130] M. Nordin and P. O. Gutman, "Controlling mechanical systems with backlash - a survey," *Automatica*, vol. 38, pp. 1633-1649, 2002, doi: 10.1016/S0005-1098(02)00047-X.

[131] C. Schwartz and R. Gran, "Describing function analysis using MATLAB and Simulink," *IEEE Control Systems Magazine*, vol. 21, no. 9, pp. 19-26, 2001, doi: 10.1109/37.939940.

[132] A. Cavallo, C. Natale, S. Pirozzi, and C. Visone, "Limit cycles in control systems employing smart actuators with hysteresis," *IEEE/ASME Transactions on Mechatronics*, vol. 10, no. 2, pp. 172-180, 2005, doi: 10.1109/TMECH.2005.844711.

[133] H. Taghavifar and A. Mardani, *Off-road Vehicle Dynamics: Analysis, Modelling and Optimization*, Springer International Publisher Science, Switzerland, 2017.

[134] R. N. Jazar, *Vehicle Dynamics: Theory and Application*, Springer Science & Business Media, New York, 2014.

[135] G. Bartolini, A. Ferrara & E. Usai, "Chattering avoidance by second-order sliding mode control," *IEEE Transactions on Automatic Control*, 43(2), pp. 241-246, 1998, doi: 10.1109/9.661074.

[136] A. Tkachev and N. Zhang, "Active hydraulically interconnected suspension modeling and simulation," *SAE Tech. Paper*, 2017-01-1561, 2017, doi: 10.4271/2017-01-1561.

[137] S. Royel and Q. P. Ha, "Frequency-shaped sliding mode control of magnetorheological smart structure systems," *Proc. IEEE International Conference on Mechatronics*, pp. 117-122, Australia, Feb. 13-15, 2017, doi: 10.1109/ICMECH.2017.7921090.

[138] M. Hadi, and Y. Arfiadi, "Optimum design of absorber for MDOF structures," *Journal of Structural Engineering*, vol. 124, no. 11, pp. 1272-1280, 1998, doi: 10.1061/(ASCE)0733-9445(1998)124:11(1272).

[139] S. Royel, Q. Ha. and R. P. Aguilera, "Frequency-shaped second-order sliding mode control for smart suspension systems," *Proc. 2018 International Conference on Control, Automation, Robotics and Vision (ICARCV 2018)*, pp. 907-912, Singapore, Nov. 18 - 21, 2018, doi: 10.1109/ICARCV.2018.8581139.